CONTROLS ON NICKEL ISOTOPE COMPOSITIONS OF MODERN SEAWATERS AND MARINE SEDIMENTS



Tzu-Hao Wang

Department of Earth Sciences
Wolfson College
University of Oxford

Thesis submitted for the degree of
Doctor of Philosophy in Earth Sciences

Michaelmas 2022

Table of Contents

Declaration iv
Acknowledgements v
Abstract vii
Extended Abstract viii
List of Tables xiii
List of Figures xv
1 Introduction 2
1.1 Geochemistry of nickel 2
1.2 Oceanic Ni biogeochemistry 3
1.3 Isotope geochemistry of Ni 6
1.4 Motivation for this thesis 14
1.5 References 16
2 Isotopic evidence for a biologically limiting nickel pool in the ocean 24
2.1 Introduction 24
2.2 Methods 26
2.2.1 Phytoplankton strains 26
2.2.2 Reagents and laboratory equipment 27
2.2.3 Culturing techniques and Ni concentration 28
2.2.4 Whole cell digestion and three-cellular-fraction separation 31
2.2.5 Ni concentration and Ni isotope analysis 32
2.3 Results and Discussion 35
2.3.1 Assessment of instrumental biases under low-Ni conditions 35
2.3.2 Ni isotope fractionation during phytoplankton growth 36
2.3.3 Bioavailability of Ni in cultures 40
2.3.4 Mechanism controlling Ni isotope fractionation in phytoplankton 42
2.3.5 Evaluation of relative binding strengths in three phytoplankton species by amino acid compositions 48
2.3.6 Implications on global Ni biogeochemistry 51
2.4 Conclusions 59
2.5 References 60
3 Factors regulating Ni isotope fractionation in cosmopolitan phytoplankton 68
3.1 Introduction 68
3.2 Materials and methods 71
3.2.1 Phytoplankton strains 71
3.2.2 Reagents and laboratory equipment 72

3.2.3 Culturing techniques 73
3.2.4 Elemental and Ni isotope analysis 73
3.3 Results 75
3.4 Discussion 83
3.4.1 Variations of metal uptake characteristics among phytoplankton 83
3.4.2 Factors influencing Ni isotope fractionation among phytoplankton 88
3.4.3 Biological isotope fractionations in Ni, Cu and Zn systems 96
3.5 Concluding remarks 101
3.6 References 102
4 Ni isotope fractionation during the formation of amorphous nickel sulfides 109
4.1 Introduction 109
4.2 Previous work on Ni-sulfide precipitation experiments 111
4.3 Materials and Methods 113
4.3.1 Nickel sulfide precipitation experiments 113
4.3.2 X-ray diffraction (XRD) analysis 115
4.3.3 Ni concentration and isotope analysis 116
4.4 Results 118
4.4.1 Ni-sulfide mineral characterization 118
4.4.2 Isotope fractionation during "time-series" Ni-sulfide precipitation 121
4.4.3 Ni-sulfide precipitation under varying Ni/S ratios 123
4.5 Discussion 124
4.5.1 Ni isotope fractionation during amorphous nickel sulfide precipitation 124
4.5.2 Implications for Ni-sulfide formation mechanism 132
4.5.3 Link to modern sediment settings 137
4.5.4 Implications for global oceanic Ni mass balance 139
4.6 Conclusions 142
4.7 References 144
5 Controls on Ni isotope compositions of organic-rich sediments from Namibian margin 153
5.1. Introduction 153
5.2 Materials and methods 156
5.2.1 Study area 156
5.2.2 Sample collection 160
5.2.3 Sample digestion 162
5.2.4 Elemental concentration measurement 163
5.2.5 Ni isotope analysis 164
5.3 Results 166

5.3.1 Seawaters and particulates 166
5.3.2 Sediments and porewaters 172
5.4 Discussion 177
5.4.1 Regional water mass mixing versus local redox changes 177
5.4.2 Evidence for a benthic input of Ni from sulfidic sediments 179
5.4.3 Detrital versus authigenic controls on Ni in the sediments 181
5.4.4 Sulfide formation dominates the diagenetic cycling of Ni in BUS sediments 187
5.4.5 Implications for the oceanic budget of Ni and its isotopes 195
5.5. Conclusions 198
5.6 References 200
6 Outlook 209
6.1 Potential application of Ni isotopes 209
6.2 Future work 216
6.3 References 218
Appendix A. Methodology 222
A.1 Introduction 222
A.2 Sample collection 223
A.3 Reagents and laboratory equipment 231
A.4 Sample digestion 231
A.5 Purification of Ni in geological samples 235
A.6 Analysis 243
A.7 Reference 280
Appendix B. Phytoplankton culturing 287
B.1 Phytoplankton growth rate 287
Appendix C. Sulfide precipitation experiments 290
C.1 Ni speciation modelling 290
Appendix D. Namibian samples 291
D.1. Analytical errors 291
D.2. Particulate data 292
D.3. Porewater data 293
D.4. Sediment data 294
D.5. Enrichment factors in sediments 298
D.6. Correlations between trace metals and different mineral fractions 300
D.7. Local bedrocks 302

Declaration

The contents of this thesis are all my own work, except where otherwise stated. The views and interpretations expressed herein are mine and not necessarily those of any other person or group unless so attributed.

Tzu-Hao Wang

Acknowledgements

It is a bit touching and indescribable that my thesis finally come to this page. This thesis would not be completed without the support and help from many people. First of all, I would like to thank my supervisor Gideon Henderson for giving me the opportunity to study in Oxford for my DPhil, and for all the support and advice over the years. They are always timely and essential. I appreciate that he always reminds me to go back to the fundamental part of the science and deliver the key messages as simply as possible. I would also like to thank my supervisor Yu-Te Alan Hsieh for his help on countless issues about isotope analysis. I enjoy the chat with him and can always feel his passion for research. I am very grateful to Qiong Zhang and Rosalind Rickaby, my collaborators from the OceanBug group, for their support on culturing experiments and insightful advices from biological perspectives. Also, thanks to Jane Barling, cleansuite manager, for always being there for any lab-related issues and the weekly trips to get amazing chai. I appreciate that her carefulness always reminds me that the devil is in details. I would like to thank Phil Holdship, ICPMS manager, for his help with loads of concentration measurements. I would also like to thank Luke Bridgestock, previous group member, for guiding me during the shipboard sampling in Namibia during the first year. I thank Julie Cosmidis for sharing the glovebox facility to enable my anoxic experiments and Nick Belshaw for saving my day on P4 many times. Thanks to Chen-Feng You and Peter Yuan for inspiring my interest in Earth Sciences and Geochemistry during my undergraduate years. I would also like to thank my two examiners Don Porcelli and Susan Little for their insightful discussion and comments on my thesis.

The Earth Sciences Department at Oxford has been a great place to work, with many excellent and interesting minds around. I thank OUTSS for giving me an opportunity to

meet Wayne, Mi-Jun, Gu-Lung, Chee, Albert, Jeff, Cindy, Mu-Huan, No-No, Wendy, Steven, Monica, A-Tsung and so on. I am grateful for their organized trips, hosts, homemade dinners, company, CSGO sections, laughter and hilarious (or bad) jokes. I would like to thank Aart, David, Richard, Annika, Kirsty, Ethan, Michael, Chris (and Chris), Joyce, Hamish, Sean, Craig, James, May, Steven (and Steven), Kristina and so on, my officemates and colleagues, for their company, help, chat and all kinds of entertainment in the department. Big thanks to Rafael, Annie, Adina, Xiaoxu, Stergios, Alba, Ana, Jess for the epic trip to Wales, the routine gatherings, weekly tennis and squash sections ending with Sunday roasts. I would like to thank Tugce, Claudiu, Pauline and Rafa, my roommates, for their company, delicious food, help and laughter in my daily life. Thanks to AY and other guys for the company during the gym time, and special thanks to AY for the delicious homemade chicken meals. I would also like to thank my friends in Taiwan, HW, YL, Leo, Martin, YP, WC, CH, SJ, PJ, JT, JH, XY, WL, SMJ and so on, for the endless fun and the gathering every time when I am around. Thanks to Han-Wen and A-Gan in the Netherlands for their host during the visit. Also, thanks to Der-Hui in Japan for the long chats from time to time.

Finally, I would like to express my biggest thanks to my beloved parents and partner Yun-Ting, for their endless support and love. Without them, I will not have persistent motivation and confidence to finish this thesis.

Abstract

In this thesis, Ni isotope fractionation during marine phytoplankton uptake and amorphous Ni-sulfide formation are characterized, to improve the understanding of biogeochemistry of Ni and its isotopes in the ocean, from the surface to the bottom of the ocean. The first direct Ni isotope measurement in phytoplankton cells suggests that marine phytoplankton preferentially take up heavy Ni isotopes from the culturing medium with species-dependent isotope fractionation factors. This finding contrasts to previous hypothesis in the community that biological activity consumes isotopically light Ni in the surface ocean where the enrichment of isotopically heavy Ni is observed. The contradiction inspires a new framework of considering relative binding strength between biological metal acquisition mechanism and ambient ligands, which reconciles findings from culturing and the modern ocean. Coccolithophores show an enhancement of Fe, depletions of Co and Cu, and a decreasing isotopic pattern; with increasing Ni availability in the media, which are not seen in cultures of other species. The distinct Ni/Co efflux proteins for regulating excess cellular Ni shown in coccolithophores may cause their contrasting isotopic pattern. The Ni isotope fractionation during amorphous sulfide formation and the mineral transformation from amorphous to crystalline sulfides; suggest a potential benthic flux of isotopically heavy Ni from sulfide-containing sediments in euxinic ocean settings. This diagenetic remobilization of Ni is supported by the slightly lighter Ni isotope compositions found in nearshore euxinic sediments off Namibian margin; compared to the offshore sediments, which are anoxic but not euxinic according to the porewater chemistry. This thesis addresses important processes in the biogeochemical cycling of Ni and its isotopes in the modern ocean, demonstrating the potential and limitation of its application as a novel geochemical tracer.

Extended Abstract

The biogeochemistry of Ni and its isotope in the modern ocean has received increasing attention in recent decades because of its importance to biological processes and the potential for being a powerful geochemical tracer. However, the magnitudes and controlling mechanisms of isotope fractionation during phytoplankton uptake in the surface ocean and formation of Ni-sulfide at the sea floor have not been clearly investigated, as critical aspects in marine biogeochemical cycling of Ni. The aim of this thesis is to address these knowledge gaps with laboratory experiments and direct Ni isotope measurements, further applying these newly developed hypotheses to natural samples in the modern ocean, and assessing the robustness and limitation of Ni isotopes as a proxy for biogeochemical processes.

Chapter 1 introduces the characteristics of Ni and its isotopes, reviewing the development of Ni isotopes as a tracer in marine biogeochemistry. This chapter pinpoints currently unsolved issues related to oceanic Ni system, including the excess/residual Ni at the surface oceans compared to other nutrients, the regionally-variable Ni isotope fractionations in the surface seawaters and the imbalance of elemental and isotopic Ni oceanic budget, which hinders further applications. This thesis then builds on these debated issues, designing experiments and projects to provide key but currently lacking insights to the community.

Chapter 2 characterizes the Ni isotope fractionation during the biological uptake of marine phytoplankton dinoflagellate, diatom and cyanobacteria. The results suggest that marine phytoplankton preferentially take up heavy Ni isotopes from the culturing medium with species-dependent isotope fractionation factors, which is contrasting to

previous argument that biology utilizes isotopically light Ni for the regionally-variable Ni isotope fractionation towards heavy composition observed in the surface oceans. A new framework of considering the relative binding strength between biological metal acquisition system and ambient ligands is proposed, which controls the directions of Ni isotope fractionations in both culturing condition and modern ocean, and suggests the binding strength of EDTA < phytoplankton < strong oceanic ligands. Based on a combination of seawater Ni data, results from incubation experiments and marine gene biogeography, we suggest a potential limitation of biological available Ni in the mid-latitude surface ocean, which is characterized by low Ni concentrations and high δ^{60}Ni values. This study points out the importance of Ni supply and bioavailability for ocean productivity and global carbon cycling.

Chapter 3 compares the physiological responses among four phytoplankton species, by adding observations on coccolithophores, discussing the factors controlling different elemental and Ni isotopic patterns among species. With increasing Ni availability in the media, coccolithophores show an enhancement of cellular Fe and inhibited uptake patterns of Co and Cu, which are not seen in other phytoplankton and explained by its sole high-affinity Ni transport system, while others have a combination of low- and high-affinity pathways. All phytoplankton species show an enrichment of heavy Ni isotopes relative to medium, while the coccolithophores display decreasing δ^{60}Ni values with increasing Ni availability, which contrast to the increasing trends obtained in other species. This characteristic isotopic pattern in the coccolithophores is likely caused by its unique Ni/Co system which removes isotopically heavy Ni from the cells via protein binding to regulate excess cellular Ni. This chapter suggests that the relative binding strength between cells and extracellular ligands may control the directions of biological

Ni isotope fractionations, while the processes of transportation, storage and enzymatic activity inside the cells may induce a redistribution of Ni isotopes inside the cells but not result in a net change. This hypothesis may also apply to the isotope system of Cu and Zn which have high complex stability.

Chapter 4 characterizes Ni isotope fractionation during the formation of amorphous Ni-sulfides and discusses its potential implications to oceanic Ni cycling. The results show that the Ni isotope fractionation between the solid and liquid phases ($\varepsilon_{S\text{-}L}$) during the formation of amorphous Ni-sulfides develops with time. The $\varepsilon_{S\text{-}L}$ is about –0.22 ~ –0.26‰, under both oxic and anoxic conditions after 10 min reaction time, following Rayleigh fractionation process. While $\varepsilon_{S\text{-}L}$ changes to about –0.50‰ after 6 h of reaction time, following equilibrium fractionation process. Combing with literatures, it suggests a development from early-stage amorphous Ni-sulfides which record the kinetic effect of nucleation events ($\varepsilon_{S\text{-}L}$ = –0.22 ~ –0.26‰), to an intermediate stage when amorphous Ni-sulfides reach isotope equilibrium ($\varepsilon_{S\text{-}L}$ = –0.50‰), to later crystalline Ni-sulfides which record an equilibrium isotope effect ($\varepsilon_{S\text{-}L}$ = –0.73 ± 0.08‰; Parigi et al., 2022a) of re-crystallization controlled by the bond-length of mineral phases and the resultant binding strengths with Ni. Combined with the increasing solubility of sulfides under the decreasing pH induced by sulfate-reducing bacteria, these isotope data indicate a potential flux of isotopically heavy Ni from sulfides to ambient environments during the mineral development of Ni-sulfides.

Chapter 5 investigates the controls of Ni isotope compositions in organic-rich Namibian sediments, with complementary trace metal data in porewaters, seawater and particulates. The δ^{60}Ni values in the nearshore euxinic sediments (0.82~1.14‰) are

~0.2‰ lighter than the values in offshore dysoxic sediments (0.97~1.20‰), with the Ni/Al ratios are lower in the nearshore sediments, which support that a diagenetic transformation of Ni-sulfides may lead to a remobilization of isotopically heavy Ni from sulfide-containing sediments. Nickel and its isotopes in the nearshore Namibian sediments are mainly governed by local redox changes; while in the offshore sediments, the signals reflects mainly the regional water mass mixing of South Atlantic Central Water (SACW). The calculation here agrees that the δ^{60}Ni in the authigenic fraction of organic-rich sediments can reflect the chemistry of deep ocean, with limited isotope fractionations. Our findings evidence that sulfide formation and cycling may dominate Ni and its isotopes in Namibian sediments, especially in euxinic settings; which is different to the Mn oxide cycling thought to control Ni cycling in oxic ocean settings. The Ni-TOC relationship suggests that the Namibian region with the presence of H_2S, may undergo different Ni cycling processes, compared to other upwelling regions (e.g., Peru and Chile). The oceanic Ni budget is revisited with the new data provided here, which suggests an average δ^{60}Ni of 1.45‰ for marine organic-rich sediments, a δ^{60}Ni of 3.23‰ for the diagenetic benthic flux and a residence time of 21~22 kyr for Ni in the ocean.

Chapter 6 discusses the potential application of Ni isotopes in banded iron formations (BIFs) as an indicator for early photosynthesis and the future work inspired by this thesis. With the Ni isotope fractionation during Ni sorption onto ferrihydrite considered ($\Delta^{60}Ni_{solution\text{-}solid}$ = 0.16‰; Wang and Wasylenki, 2017; Chi Fru et al., 2016), the difference between the δ^{60}Ni of seawater in modern ocean (δ^{60}Ni = 1.44 ± 0.15‰; Cameron et al., 2009) and 3.75 Ga ocean (average δ^{60}Ni = 0.62‰, 0.54~0.70‰; Gueguen et al., 2013) can be explained by the biological activity of cyanobacteria ($\Delta^{60}Ni_{cell\text{-}meidum}$ = 0.86‰) under higher Ni availability (~340 nM) at that time. The sparce oxygen generated by

cyanobacteria may lead to the formation of ferrihydrite particles which record the chemistry of ambient seawater in the photic zone. This proposed mechanism suggests the potential of Ni isotopes in BIFs as a tracer for biological activity in the photic zone back in Archean, while more Ni isotope data in BIFs and further characterization of isotope fractionation during the growth of chemolithotrophic bacteria are required for a convincing story. Alternatively, the absence of both Mn-oxides in oxic sediments and the subsequent diagenetic remobilization of Ni could lead to a lower δ^{60}Ni (estimated to be 1.06‰) in the anoxic Archean ocean. Finally, future works beneficial to this research field are suggested, including characterization of Ni isotope fractionation during Ni binding to organic ligands and varying enzymatic activities in marine phytoplankton, and further understanding of Ni isotope signals influenced by early diagenesis in marine sediments under varying ocean settings.

Appendix includes the general methodology applied in this thesis, and the extended data and figures related to above chapters, in order to follow the page limit and also to clarify the main stories for each chapter.

List of Tables

Table 2.1. Ni contents and speciation in this study 29
Table 2.2. Compilation of growth rates, Ni quotas and $\Delta^{60}Ni_{cell\text{-}medium}$ for whole cell analyses performed on three species of phytoplankton 39
Table 2.3. $\Delta^{60}Ni_{fraction\text{-}medium}$ in three subcellular fractions of dinoflagellate cultured under [Ni'] of 7.821 pM. 44
Table 2.4. Ni quotas in three cellular fractions (P, CD and MRG) of dinoflagellate P. minimum normalized to whole cell P and relative proportions under varying Ni bioavailability 46
Table 2.5. Protein sequences for representative diatom, cyanobacteria and dinoflagellate extracted from UniProt, with normalized cysteine and histidine abundance (total =1) 49
Table 3.1. Compilation of growth rate, metal quotas and $\Delta^{60}Ni_{cell\text{-}medium}$ for four cosmopolitan phytoplankton cultured under varying Ni availability. 79
Table 3.2. Responses of metal quotas to increasing Ni availability in four species of phytoplankton. 80
Table 3.3. Coefficient of determination (R^2 value) and statistical significance (p value, t-test) of covariations between Ni/P ratios and other metal quotas for four cosmopolitan phytoplankton species. 80
Table 3.4. Protein analysis for Ni-related proteins in representative coccolithophore, diatom and cyanobacteria. 85
Table 4.1. Compilation of Ni precipitated fractions and Ni isotope compositions under varying ionic strengths in oxic condition (O_2~21‰, laminar flow hood) for oxic "time-series" experiments. 120
Table 4.2. Compilation of Ni precipitated fractions and Ni isotope compositions under varying ionic strengths in anoxic condition (O_2 <2ppmv, glovebox) for anoxic "time-series" experiments.. 121
Table 4.3. Compilation of Ni precipitated fractions and Ni isotope compositions of liquid ($\delta^{60}Ni_L$) and solid ($\delta^{60}Ni_S$) phases for "Ni/S ratio" experiments under both oxic and anoxic settings. 124
Table 5.1. Seawater profiles of O_2 concentration, temperature, salinity and Ni concentration at stations 23005 and 23070. 167
Table 5.2. Ni concentrations in 10m-depth seawaters collected by pump and CTD at various station off Namibian margin. 170
Table 5.3. Major and trace element concentration in particulate samples filtered from surface seawaters at stations 23005 and 23070. 171
Table 5.4. Geochemical profiles of sediment cores 23010 and 23060, including bottom water oxygen (BWO) concentrations, TOC contents, element/Al ratios and Ni isotope compositions. 174
Table 5.5. Depth profiles of sulfate and trace metal concentrations in porewater samples extracted from sediment cores 23010 and 23060. 176
Table 5.6. Estimated authigenic Ni fraction and Ni isotope composition in Namibian sediment cores 23010 and 23060. 184
Table 5.7. Budget for Ni and its isotopes in the modern ocean. 195
Table A.1. Location of stations along 20°S and 23°S transect off Namibian margin. 225

Table A.2. Dimensions of column moulds used in this study for making Teflon columns. 239
Table A.3. Summary of chemical procedure for a three-step ion exchange chromatography separating Ni from biological and geological samples in this study. 240
Table A.4. Elemental concentration for standards processed with Ni purification technique. 242
Table A.5. Total Ni procedural blanks accumulated from the entire sample processing in sediments, biological and sulfide samples, with details of double-spikes applied for the calculation. 243
Table A.6. Potential elemental and polyatomic interferences on the mass of five Ni stable isotopes and ^{57}Fe. 262
Table A.7. The normal (top) and adapted (bottom) detector array of Nu plasma-HR MC-ICP-MS at the Department of Earth Sciences, University of Oxford. 265
Table A.8. Typical instrumental settings for Ni isotope analysis on Nu Plasma-HR MC-ICP-MS. 265
Table A.9. Compilation of reproducibility and accuracy of Ni isotope measurement carried out in this study with published values for various reference materials. 276
Table D.1. Analytical results and certified values for river water standard SLRS-6 measured by quadrupole ICP-MS with normal introduction system. 291
Table D.2. Analytical results and certified values for seawater standard NASS-7 measured by quadrupole ICP-MS connected with seaFAST preconcentration system. 291
Table D.3. Elemental concentrations in particulate samples filtered from ~10 m depth seawaters off Namibian margin at stations along transect 20°S and 23°S. 292
Table D.4. Porewater profiles of trace metals and sulfate in sediment cores collected off Namibian margin along transect 20°S and 23°S. 293
Table D.5. Certified, measured elemental values and elemental recoveries for standard SGR-1b. 294
Table D.6. Certified, measured elemental values and elemental recoveries for standard SDO-1. 295
Table D.7. Depth profiles of elemental/Al ratios, carbon contents, authigenic fraction estimation and $\delta^{60}Ni$ values in Namibian sediment cores 23010 and 23060. 296
Table D.8. Enrichment factors of elements in sediment cores 23010 and 23060. 298

List of Figures

Figure 1.1. Compilation of published $\delta^{60}Ni$ data for terrestrial samples. The grey shade represents the range of estimated $\delta^{60}Ni$ of bulk silicate earth. 8
Figure 1.2. Depth profiles of (A) Ni concentrations and (B) Ni isotope compositions of seawater collected at five different stations (E-4W, A3-2, E-5, F-L and R2) in the Indian Sector of the Southern Ocean. 10
Figure 1.3. Depth profiles of (A) Ni concentrations and (B) Ni isotope compositions of seawater collected at various locations in the Pacific Ocean and Atlantic Ocean. 10
Figure 1.4. (A) Locations of currently available Ni isotope data in seawaters and (B) the correlation between Ni concentration and $\delta^{60}Ni$ values in seawaters. 11
Figure 2.1. Assessment of instrumental biases during Ni isotope analysis with varying sample-to-standard intensity ratio 36
Figure 2.2. Ni isotope fractionation between collected cells and culturing medium under varying Ni availability. 37
Figure 2.3. Ni/P ratios in harvested phytoplankton cells under varying Ni availabilities. 38
Figure 2.4. Overall trend between $\Delta^{60}Ni_{cell\text{-}medium}$ and proportion of $[Ni]_{total}$ taken by phytoplankton. 38
Figure 2.5. Assessment of Ni bioavailability in cultures. 41
Figure 2.6. Subcellular Ni isotope analysis on dinoflagellate P. minimum (RCC291) under [Ni'] of 7.821 pM. 44
Figure 2.7. Ni quotas normalized to whole cell P in three subcellular fractions of dinoflagellate P. minimum under varying [Ni']. 45
Figure 2.8. Relative proportion of Ni in three cellular fractions of dinoflagellate P. minimum under varying [Ni']. 46
Figure 2.9. Abundance of amino acids cysteine (sulfur-binding) and histidine (nitrogen-binding) within high-affinity Ni transporters in representative dinoflagellate, diatom and cyanobacteria species. 50
Figure 2.10. Conceptual model of mechanisms causing Ni isotope fractionation in the culturing medium and the modern ocean, and demonstrating how the relative binding strength of phytoplankton uptake system versus ligands controls the direction of isotope fractionations. 52
Figure 2.11. Global perspectives of Ni and its isotopes in seawater 54
Figure 3.1 Metal quotas (Ni/P, Fe/P, Zn/P, Mn/P, Cu/P and Co/P) of four species of phytoplankton under varying Ni availability. 77
Figure 3.2. Covariations between Ni/P ratios and other metal/P ratios in four species of phytoplankton under varying Ni availability. 78
Figure 3.3. Physiological responses of four phytoplankton species under varying Ni availability. (A) cellular Ni/P ratios; (B) $\Delta^{60}Ni_{cell\text{-}medium}$. 82
Figure 3.4. $\Delta^{60}Ni_{cell\text{-}medium}$ versus Ni/P ratios for four species of phytoplankton with potential physiological mechanisms 91

Figure 3.5. Schematic diagram for processes causing Ni isotope fractionations in cultured coccolithophores E. huxleyi. 94
Figure 3.6. Schematic comparison of biological isotope fractionations in multiple isotope systems. 97
Figure 4.1. X-ray diffraction patterns of Ni precipitates from "time-series" experiments in media (A) 0.5SW and (B) SW under anoxic condition for 48 h. 119
Figure 4.2. "Time-series" experiments – Ni-sulfide precipitation from media with different ionic strengths under oxic (A) and anoxic (C) conditions, and precipitated Ni fraction and $\Delta^{60}Ni_{final-initial}$ in the solution during Ni-sulfide precipitations in MQ under oxic condition (B), in MQ (D) and SW (E) under anoxic conditions. 122
Figure 4.3. Oxic "Ni/S ratio" experiments – Ni-sulfide precipitation in MQ under oxic condition with 10 min equilibrium time 128
Figure 4.4. Anoxic "Ni/S ratio" experiments – Ni-sulfide precipitation in MQ under anoxic condition with (A) 10 min and (B) 6 h equilibrium time 129
Figure 4.5. Schematic diagram of the development of Ni-sulfides and related reported Ni isotope fractionations under euxinic ocean settings. 134
Figure 5.1. (A) Sampling area (red square) plotted with regional ocean currents impacting Benguela upwelling system (BUS). (B) Sampling sites (yellow) with bottom water oxygen concentrations along the sampling transect (23°S). 157
Figure 5.2. Depth profiles of dissolved Ni and oxygen level for seawaters collected at stations 23005 (blue squares) and 23070 (orange squares). 167
Figure 5.3. Seawater profiles of oxygen concentration (μmol/kg) along the 23°S transect with the stations where the sediment (brown) and seawater (blue) samples were sampled. 168
Figure 5.4. Seawater profiles of salinity (‰) along the 23°S transect with the stations where the sediment (brown) and seawater (blue) samples were sampled. 168
Figure 5.5. Seawater profiles of temperature (℃) along the 23°S transect with the stations where the sediment (brown) and seawater (blue) samples were sampled. 169
Figure 5.6. Comparison of Ni concentrations in 10m-depth seawaters collected by pump and CTD at various stations off Namibian margin. 170
Figure 5.7. Elemental concentrations in particulate samples filtered from surface seawaters (~10 m depth) at stations 23005 and 23070. 171
Figure 5.8. Depth profiles of element/Al ratios, TOC and Ni isotope compositions in sediment samples collected at stations 23010 (blue) and 23060 (orange). 174
Figure 5.9. Depth profiles of sulfate and trace metal (Fe, Mn and Ni) concentration in porewater samples extracted from sediment cores 23010 (blue) and 23060 (orange). 176
Figure 5.10. Local effect versus water mass mixing for seawaters collected at stations 23005 and 23070. 177
Figure 5.11. Depth profiles of calculated authigenic Ni fraction and Ni isotope composition in Namibian sediment cores 23010 and 23060. 183

Figure 5.12. δ^{60}Ni values of bulk sediments and authigenic phase plotted with Ni/Al ratios for sediment samples in this study and previously reported sediments under varying environmental settings. 186
Figure 5.13. Relationship between Ni isotope compositions of authigenic Ni fraction, metal/Al ratios and TOC contents in Namibian sediment cores 23010 and 23060. 189
Figure 5.14. δ^{60}Ni of authigenic Ni fraction in sediment samples plotted with TOC contents. 190
Figure 5.15. δ^{60}Ni values plotted with Mn/Ni ratios for sediment samples in this study and Mn-/Fe-related processes in the ocean reported in previous studies. 192
Figure 5.16. Ni abundances plotted with TOC contents in Namibian sediments (this study) and other organic-rich sediments. 194
Figure 6.1. Cellular Ni/P ratios and Δ^{60}Ni of cultured cyanobacteria Synechococcus sp. under varying Ni availability. 211
Figure 6.2. Compilation of processes potentially influencing the signals recorded in BIFs around 3.75 Ga. 212
Figure 6.3. Conceptual mechanism linking the δ^{60}Ni signals recorded in ferrihydrite particles (precursor of BIF) and cyanobacterial photosynthesis. 213
Figure A.1. (a) Map of sampling sites of this study off Namibian margin. In the red square are transect 20°S and 23°S. (b) Sampling strategy for a comprehensive set of samples including sediments, porewater extracted from sediments, seawater and particulate matters filtered from seawater. 224
Figure A.2. Schematic diagram of standard-sample-bracketing technique used in this study during Ni isotopic analysis. 257
Figure A.3. Schematic diagram of the double-spike technique. 260
Figure A.4. Relationship between Ar sweep gas flow rate and normalized argon index (NAI) with duplication. 271
Figure A.5. NAI vs. Ar sweep gas flow rate with different nebulizer Ar gas flow rates 271
Figure A.6. Analytical sensitivity of $^{58}Ni^{+}$ under different NAIs after sensitivity optimization. 272
Figure A.7. Ni isotope measurement of standards (A) SRM986, (B) Kambalda (Kam, in-house) and (C) Nod-P-1 under different NAIs for the test of non-spectral matrix effect. 274
Figure A.8. Comparison of Ni isotope composition for various reference materials between measurements in this study and previously reported values. 277
Figure A.9. Long-term instrumental reproducibility monitored by repeatedly measuring in-house sulfide standards (Kam and Sud, (A and B)) and USGS Mn-nodule standard Nod-P-1 I during each run for over 30 months. 279
Figure B.1. Growth rates for (A) cyanobacteria Synechococcus sp., (B) diatom T. weissfloggi, and (C) dinoflagellate P. minimum under concentration from 0 to 2 μg/L. 288
Figure B.2. Growth rates for (A) cyanobacteria Synechococcus sp., (B) diatom T. weissfloggi, and (C) dinoflagellate P. minimum under concentrations of 0, 20 and 200 μg/L. 289
Figure C.1. Proportions of major Ni species and calculated lnβ under varying ionic strengths. 290
Figure D.1. Enrichment factors for elements in Namibian core 23010. 299

Figure D.2. Enrichment factors for elements in Namibian core 23060. 299
Figure D.3. Correlations between trace metals and Ca (representing carbonate fraction) in Namibian sediments. 300
Figure D.4. Correlations between trace metals and Mn (representing Fe-Mn oxyhydroxide fraction) in Namibian sediments. 300
Figure D.5. Correlations between trace metals and TOC (representing organic-sulfide fraction) in Namibian sediments. 301
Figure D.6. Correlations between trace metals and Al (representing silicate fraction) in Namibian sediments. 301
Figure D.7. (A) Geological map of southwest Africa (map is adopted from the Fig.2 in Garzanti et al., 2012) with (B) Ni/Al ratios in local bedrocks and the Namibian sediments collected in this study. 303

CHAPTER 1
Introduction

1 Introduction

1.1 Geochemistry of nickel

Nickel (Ni) is a first-row transition metal, having five stable isotopes ^{58}Ni, ^{60}Ni, ^{61}Ni, ^{62}Ni and ^{64}Ni, with respective abundance of 68.08%, 26.22%, 1.14%, 3.63% and 0.93% (Gramlich et al., 1989). The name "nickel", the German for "demon", is allegedly derived from the frustration of miners due to the contamination of copper sulfide deposits with nickel (Zamble et al., 2017), that the Ni ore was called "kupfernickel" and now called "nickeline" (Nicholls, 1974). High-pressure experiments have suggested that the core of Earth is likely consisted of Fe-Ni alloy which contains over 90% of the total Ni on Earth (McDonough and Sun, 1995). Despite this heterogeneous distribution, Ni is still the 15th most abundant element (0.008 wt%) in the continental crust but rarely occurs as a pure metal (Nicholls, 1974). The remaining Ni on Earth is mainly bound in silicates (e.g., olivine, pyroxene and spinel) with an average concentration of ~2000 μg/g in the mantle, by substituting for Fe and Mg in common silicate structures (McDonough, 2014). As Ni is a highly compatible element, mantle rocks usually contain higher Ni contents than oceanic crust (~150 μg/g) and continental crust (~50 μg/g) (Rauch and Pacyna, 2009). It has been observed in both natural and experimental samples that Ni preferentially enters the sulfide melt during sulfide-silicate segregation, which can lead to highly Ni-enriched sulfide depositions (Peach et al., 1990).

The oxidation state of Ni is mostly +2 under the surface redox states on Earth, which makes Ni to be largely insensitive to environmental redox changes (Nicholls, 1974). Under certain biological processes, other oxidation states of Ni can be found rarely, e.g., +2 and +3 in Ni superoxide dismutase (Ni-SOD); +1, +2 and +3 in methyl-coenzyme M

reductase (MCR) (Ragsdale, 2009). Nickel behaves similarly to iron (Fe) as first-row transition metals but has a distinct characteristic for being unaffected by oxidation states, which gives an advantage of studying Ni in natural samples.

Seawater profiles of dissolved Ni generally show a nutrient-type pattern inferring biological utilization at the surface and remineralization at depths, with a concentration range of 2∼12 nM (Archer et al., 2020; Bruland, 1980; Cameron and Vance, 2014; Lemaitre et al., 2022; Middag et al., 2020a; Sclater et al., 1976; Takano et al., 2017, 2020; R. M. Wang et al., 2019; Yang et al., 2020, 2021). The residence time of Ni in the ocean has been estimated to be around 10∼21 kyr (Little et al., 2020; Sclater et al., 1976). Dissolved Ni concentrations in the water column correlate with macronutrients, e.g., with phosphate in the upper ocean, and with silicate in the deep ocean, showing a characteristic of Ni as a bioactive metal (Sclater et al., 1976). In the modern ocean, the inorganic Ni species are calculated in mole fractions of Ni^{2+} (20%), $NiCl^{+}$ (57%), $NiCO_3$ (19%), $NiHCO_3^{+}$ (2%) and $NiSO_4$ (2%) (Fujii et al., 2011). Nickel has also been reported to form strong complexes with ligands in the ocean (Mackey et al., 2002; van den Berg and Nimmo, 1987). The $3d^8$ electronic configuration of Ni^{2+} favours square planar coordination, which leads to the high stability of any Ni-containing compound with this coordination, e.g., Ni-tetrapyrrole complexes found in sediments and petroleum deposits (Mackey et al., 2002).

1.2 Oceanic Ni biogeochemistry

Nickel is the metal center for various enzyme systems due to its extreme plasticity in coordination and redox chemistry (e.g., Ni(+1), NI(+2), Ni(+3)) in biological processes (Ragsdale, 2009). Seven of eight known Ni-containing enzymes are involved in the

production and utilization of gases (O_2, H_2, CO, CO_2, CH_4, NH_3) which play important roles controlling global carbon, oxygen and nitrogen cycles (Mulrooney and Hausinger, 2003; Ragsdale, 2009). It has been reported that Ni is utilized by marine phytoplankton as the metal center in urease, which facilitates the breakdown of urea to NH_3 and CO_2 (Price and Morel, 1991). A Ni-containing superoxide dismutase (SOD) has also been found to be encoded in many marine cyanobacterial genomes, which catalyzes the breakdown of reactive oxygen species (superoxide) generated from both photosynthesis and respiration, into hydrogen peroxide and molecular oxygen, functioning like other Fe-, Mn- and Cu/Zn-containing isoforms (Dupont et al., 2008; Fridovich, 1997; Palenik et al., 2003). The utilization of Ni-SOD is also regarded as a strategy for conserving limited iron availability (Palenik et al., 2003). The NiFe hydrogenase (HupL) found in diazotrophic cyanobacteria controls the use and production of H_2 (Li et al., 2022), which has been regarded as the main cause of surprisingly varying ratios of N_2 fixation rate : H_2 net production rate (0.003∼0.48) observed in both field and laboratory studies (Punshon and Moore, 2008; Schropp et al., 1987; Wilson et al., 2010), with an assumption that the ratio should equal to 1 following the reaction below, where P_i stands for inorganic phosphate.

$$1N_2 + 16ATP + 8H^+ + 8e^- \rightarrow 2NH_3 + 1H_2 + 16P_i + 16ADP \quad (1.1)$$

Another important Ni-containing enzyme is the methyl-coenzyme M reductase (MCR), which Ni is involved in its catalytic center as a nickel hydrocorphin called coenzyme F_{430} (Ragsdale, 2009). All biologically generated methane on Earth derives from the catalytic activity of MCR in methanogens which have essential Ni requirement (Ragsdale, 2009). Due to the importance of Ni in methane-producing enzymes, significant decreases of

Ni/Fe ratios recorded in banded iron formations (BIFs) about 2.5 Ga and 2.0 Ga have suggested a Ni famine to methanogens in the ocean and a subsequent decline in biogenic methane production (Konhauser et al., 2009). These decreased Ni/Fe ratios were explained by the reduced Ni flux to the ocean, likely caused by the cooling of upper-mantle temperature and the decreased eruption of nickel-rich ultramafic rocks at the time (Konhauser et al., 2009). As methane may have played a key role maintaining the warm climate on the early Earth and preventing a permanent icehouse, this observation prompts considerable interests in developing Ni and its isotopes as a biomarker for methanogenesis (Cameron et al., 2009; S. J. Wang et al., 2019).

The metal center in SOD has been reported to process with potential spanning from +890 to –160 mV (Miller, 2008), while in MCR, the potential can be as low as –600 mV (Holliger et al., 1993), which shows a wide range of ~1.5 V in Ni-containing enzymes performing redox chemistry.

The bioavailability of Ni in the ocean has been actively debated in the community. On one hand, Ni has been regarded as biologically sufficient, as its concentration at the surface ocean is never fully depleted and rarely falls below 2 nM (Bruland, 1980; Sclater et al., 1976). It has been suggested that the microbes which have higher Ni demand are no longer dominant in the modern ocean, for instance methanogens and microorganisms preforming anaerobic metabolisms, compared to the limited use by eukaryotes (Zhang et al., 2009), further indicating that the biological function of Ni may be evolutionary relicts of the anoxic Archean (Zamble et al., 2017). This argument is supported by the observations that the Ni concentration for optimal growth in marine microalgae (5~100 nM) is lower than the Ni concentration in cyanobacteria (15~1500 nM), while

methanogenic archaea require slightly higher Ni concentration (200~2000 nM) (complied in Zamble et al., 2017). The residual Ni at the surface oceans in subtropical gyres has been alternatively explained by the slow depletion of Ni relative to macronutrients in the upwelling regions (John et al., 2022).

On the other hand, Ni has been regarded as biologically limiting, that a fraction of dissolved Ni is not bioavailable (Archer et al., 2020; Mackey et al., 2002; Middag et al., 2020b), due to the observations that Ni can form strong complexes with ligands (Irving and Williams, 1953) in the ocean which limit the access of Ni to marine microorganisms (Mackey et al., 2002; van den Berg and Nimmo, 1987).

1.3 Isotope geochemistry of Ni

At the early stage, Ni isotope studies mainly focused on the nucleosynthetic origins of different meteoritic components, investigating mass-independent isotopic variations, both radiogenic and non-radiogenic (Elliott and Steele, 2017). As ^{60}Ni is the radiogenic daughter of ^{60}Fe, a short-lived nuclide ($t_{1/2}$ = 2.62 Ma; Rugel et al., 2009) which has potential to be both an important heat source and chronometer in the early solar system, early studies of Ni isotopes were aimed to provide evidence for the presence and abundance of formerly live ^{60}Fe, as a ^{60}Fe-^{60}Ni chronometer (Birck and Lugmair, 1988; Shukolyukov and Lugmair, 1993; Tachibana and Huss, 2003).

In recent decade or two, Ni isotope studies focusing on low-temperature biogeochemical cycling have become of interest for the community as Ni is a bio-essential element, leading to research investigating mass-dependent isotopic variations (Cameron et al., 2009; Elliott and Steele, 2017). This thesis will focus on the low-temperature Ni

biogeochemical cycling in the ocean, discussing processes and mechanisms fractionating Ni isotopes in a mass-dependent fashion.

The mass-dependent Ni isotopic variations are conventionally expressed in the delta notation, relative to established Ni isotopic standard SRM986 (high-purity Ni metal), in units of per mille (‰):

$$\delta^{60}Ni = (^{60}Ni/^{58}Ni_{sample} / {}^{60}Ni/^{58}Ni_{standard} - 1) \times 1000\ (‰) \quad (1.2)$$

Studies of mass dependent Ni isotope fractionation started around 2006, with the development of MC-ICP-MS (Tanimizu and Hirata, 2006). The Ni isotope compositions in low-temperature materials display a wide range of variations, as low as –1.5‰ in cultured methanogens (Cameron et al., 2009) and up to 2.8‰ in lherzolite separates (Elliott and Steele, 2017; Gall et al., 2017; Saunders et al., 2020). A compilation of published $\delta^{60}Ni$ values for terrestrial samples is shown in Figure 1.1.

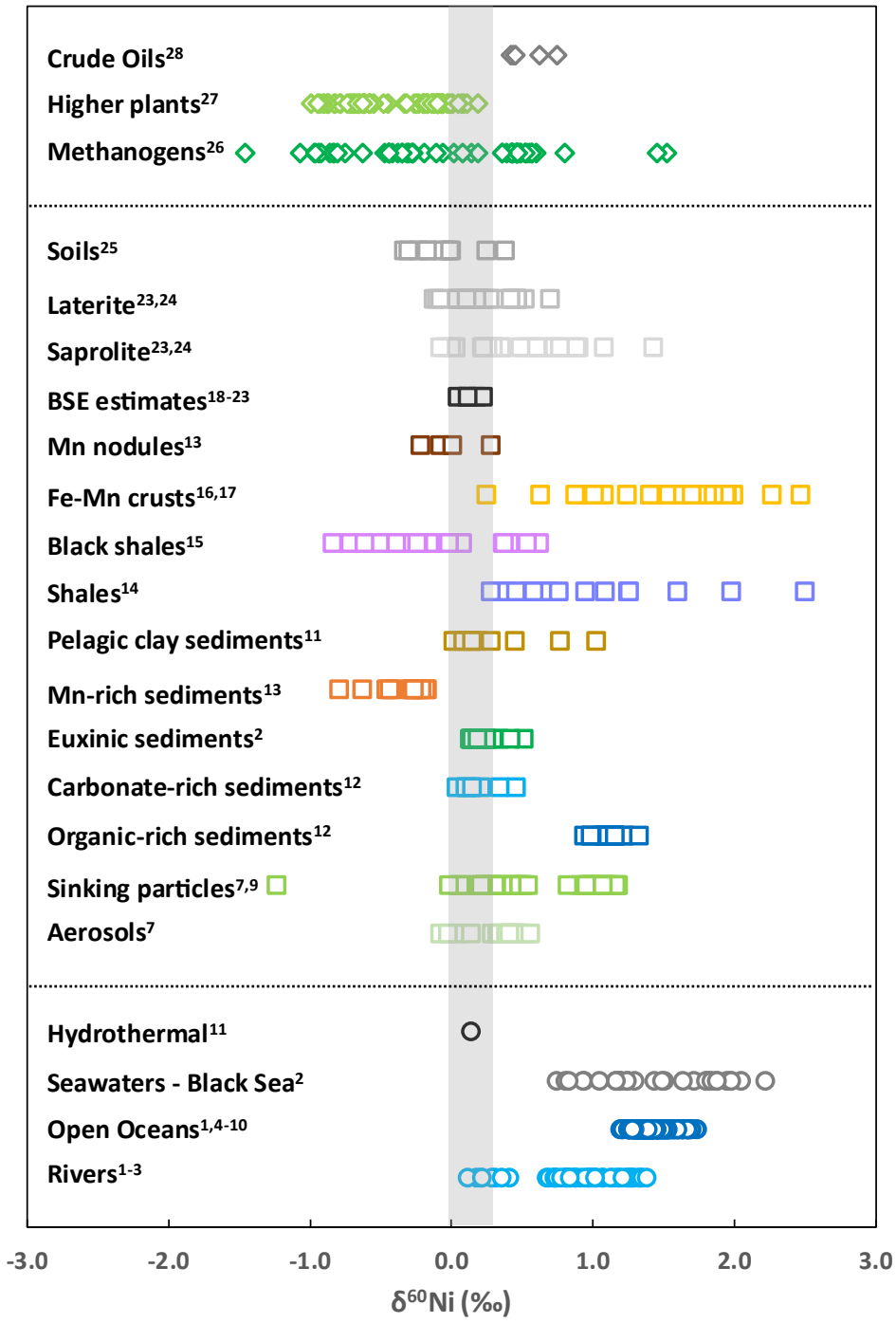


Figure 1.1. Compilation of published δ^{60}Ni data for terrestrial samples. The grey shade represents the range of estimated δ^{60}Ni of bulk silicate earth. Data source: [1](Cameron and Vance, 2014); [2](Vance et al., 2016); [3](Revels et al., 2020); [4](R. M. Wang et al., 2019); [5](Takano et al., 2017); [6](Archer et al., 2020); [7](Takano et al., 2020); [8](Yang et al., 2020); [9](Yang et al., 2021); [10](Lemaitre et al., 2022); [11](Gueguen and Rouxel, 2021); [12](Ciscato et al., 2018); [13](Little et al., 2020); [14](Porter et al., 2014); [15](Pašava et al., 2019); [16](Gall et al., 2013); [17](Gueguen et al., 2016); [18](Elliott and Steele, 2017); [19](Gueguen et al., 2013); [20](Steele et al., 2011); [21](Gall et al., 2017); [22](Klaver et al., 2020); [23](Spivak-Birndorf et al., 2018);

[24](Ratié et al., 2018); [25](Estrade et al., 2015); [26](Cameron et al., 2009); [27](Deng et al., 2014); [28](Ventura et al., 2015).

The average δ^{60}Ni of modern ocean is around 1.39‰ (Cameron and Vance, 2014; Ciscato et al., 2018; Takano et al., 2017), while the average δ^{60}Ni of deep ocean (depths > 500 m) is about 1.33 ± 0.13‰ (2SD, n = 135) ((Lemaitre et al., 2022). The first Ni isotope data in seawaters suggested a homogeneous composition and a lack of isotopic shift associated with the drawdown of Ni at the surface (Cameron and Vance, 2014), which is in agreement with the homogeneous profiles reported in the Southern Ocean (R. M. Wang et al., 2019; Figure 1.2).The seawater δ^{60}Ni profiles with observable isotope fractionation towards higher δ^{60}Ni at the surface have later been reported in South Atlantic (Archer et al., 2020), North Atlantic (Lemaitre et al., 2022), South Pacific (Takano et al., 2017) and North Pacific (Yang et al., 2020, 2021), which are explained by the biological utilization in the surface ocean which preferentially takes up isotopically light Ni (Figure 1.3). A compilation of currently available Ni isotope data in seawater is shown in Figure 1.4.

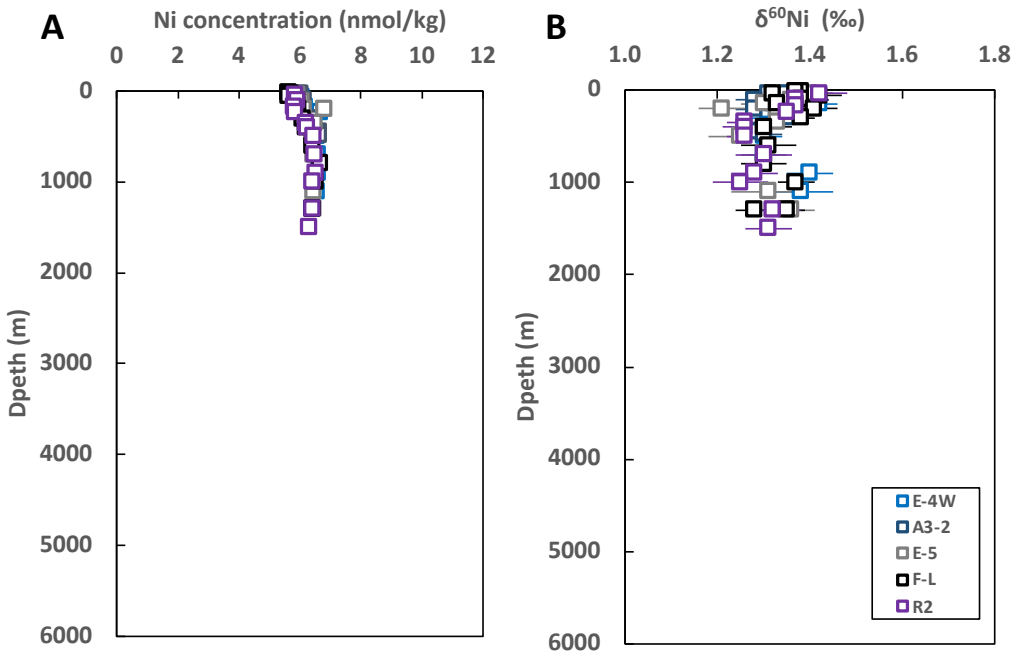


Figure 1.2. Depth profiles of (A) Ni concentrations and (B) Ni isotope compositions of seawater collected at five different stations (E-4W, A3-2, E-5, F-L and R2) in the Indian Sector of the Southern Ocean. Data source: (Wang et al., 2019).

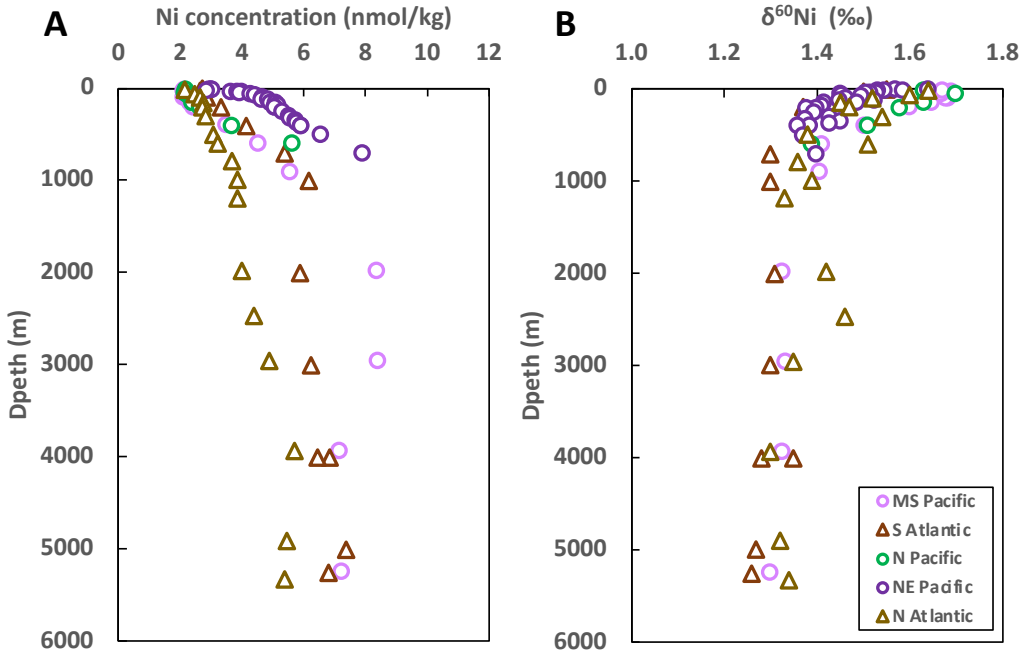


Figure 1.3. Depth profiles of (A) Ni concentrations and (B) Ni isotope compositions of seawater collected at various locations in the Pacific Ocean and Atlantic Ocean. Data source: Middle-South Pacific (Takano et al., 2017); South Atlantic (Archer et al., 2020); North Pacific (Yang et al., 2020); North-East Pacific (Yang et al., 2021); North Atlantic (Lemaitre et al., 2022).

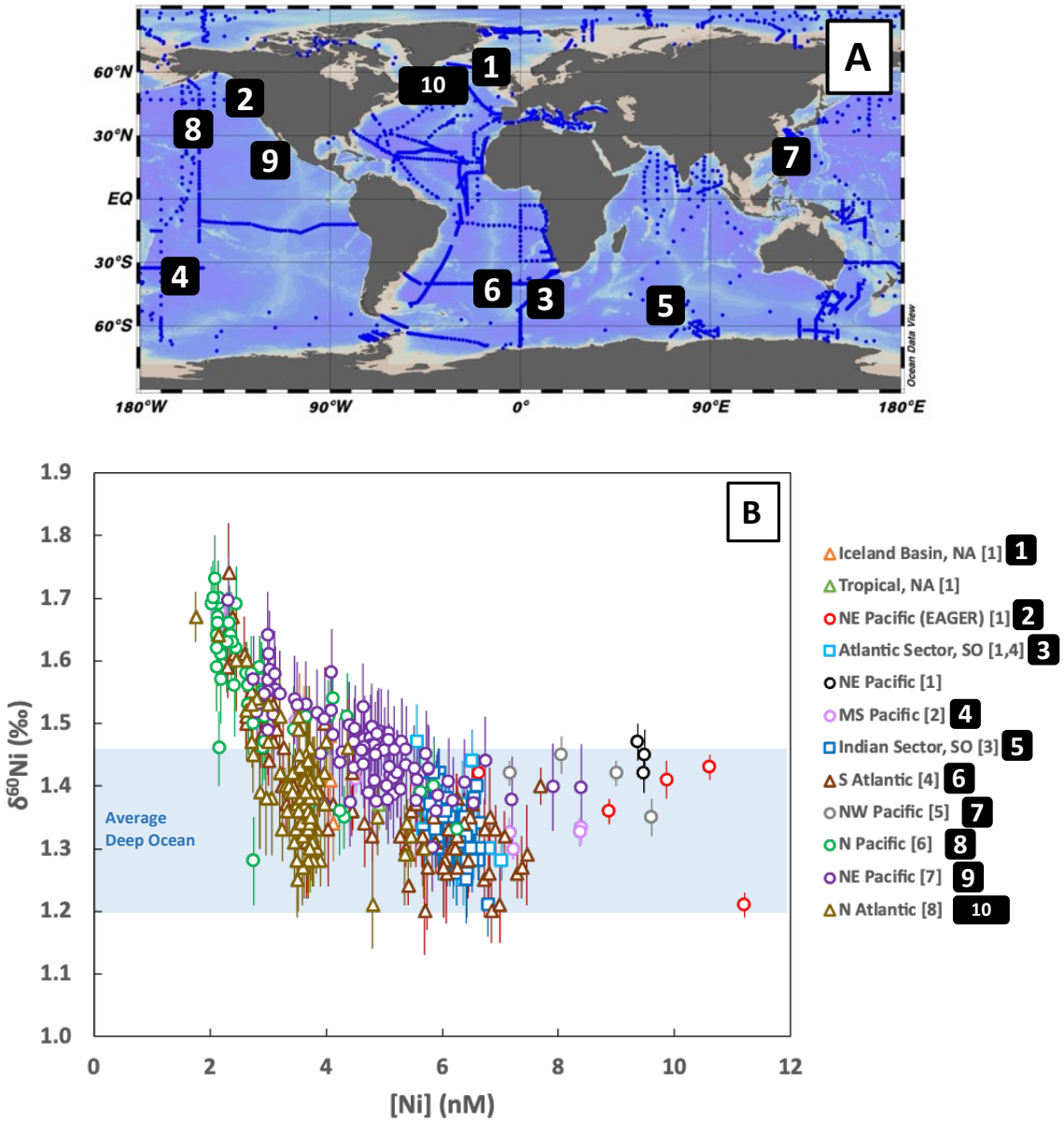


Figure 1.4. (A) Locations of currently available Ni isotope data in seawaters and (B) the correlation between Ni concentration and δ^{60}Ni values in seawaters. Numbers noted in (B) correspond to the locations in (A). Seawater samples from Atlantic Ocean, Pacific Ocean and Southern Ocean are denoted as triangles, circles and squares, respectively. The blue shade represents the average δ^{60}Ni (1.33 ± 0.13‰) of deep ocean (Lemaitre et al., 2022). Data source: [1](Cameron and Vance, 2014); [2] (Takano et al., 2017); [3](R. M. Wang et al., 2019); [4](Archer et al., 2020); [5](Takano et al., 2020); [6](Yang et al., 2020); [7](Yang et al., 2021);[8](Lemaitre et al., 2022).

The average Ni isotope composition of the modern ocean is heavier than the composition of rivers (average δ^{60}Ni = 0.8‰; Cameron and Vance, 2014; Gueguen and Rouxel, 2021),

while the Ni isotope composition of rivers is heavier than the bulk silicate earth (δ^{60}Ni = 0.05~0.23‰; Elliott and Steele, 2017; Gall et al., 2017; Gueguen et al., 2013; Klaver et al., 2020). Other reported Ni inputs to the ocean including atmospheric deposition (δ^{60}Ni = 0.14; Cameron et al., 2009; Ciscato et al., 2018; Desboeufs et al., 2005; Gueguen and Rouxel, 2021; Vance et al., 2016) and hydrothermal inputs (δ^{60}Ni = 0.14‰; Gueguen and Rouxel, 2021) are also reported to have lighter Ni isotope compositions than the modern ocean. Ferromanganese crusts are initially regarded as an important sink for Ni in the ocean under oxic conditions, via adsorption of Ni onto Fe-Mn oxides, which have a Ni isotope composition slightly heavier (average δ^{60}Ni = 1.6‰; Gall et al., 2013; Gueguen et al., 2016) than the dissolved Ni pool. Later, studies suggest that dispersed Fe-Mn oxides in oxic sediments are the important sink of dissolved Ni in the ocean (average δ^{60}Ni = 1.20‰; Gall et al., 2013; Gueguen and Rouxel, 2021; Little et al., 2020). In addition to Fe-Mn oxides in oxic sediments, carbonate sediments (average δ^{60}Ni = 1.29‰; Ciscato et al., 2018) and organic-rich sediments (average δ^{60}Ni = 1.22‰; Ciscato et al., 2018) as other sinks of Ni in the ocean, generally have similar δ^{60}Ni values compared to seawaters. The δ^{60}Ni values of sulfidic sediments from the Black Sea show a range of 0.13~0.51‰ (Vance et al., 2016). The δ^{60}Ni values of shale samples show a range from 0.28 to 1.60‰ for samples collected in Robin Hood's Bay, UK, and a range of 0.46 to 2.50‰ for samples collected in west Canada sedimentary basin (Porter et al., 2014). For organic-rich black shales, it has been reported that the δ^{60}Ni values range from –0.84 to +0.54‰ for samples collected from various locations (Pašava et al., 2019). The δ^{60}Ni values of crude oils within a range of source rock are reported to range from 0.42 to 0.75‰ (Ventura et al., 2015).

An imbalance on elemental and isotopic budget of Ni was brought up to discussion about a decade ago (Cameron and Vance, 2014), which would require isotopically heavy Ni

inputs and/or isotopically light outputs to reach the balance, and this issue has been continuously revisited since then (Ciscato et al., 2018; Gueguen and Rouxel, 2021; Little et al., 2020). Recently, a hypothetical benthic flux of isotopically heavy Ni ($\delta^{60}Ni$ = 3.03‰) has been proposed to be released from Mn-rich sediments with light isotope compositions ($\delta^{60}Ni$ = –0.2 ~ –0.8‰), by the diagenetic remobilization of Ni via Mn-oxide cycling or mineral transformation from birnessite to todorokite, which would possibly ameliorate the budget problem (Little et al., 2020). The calculated $\delta^{60}Ni$ of this benthic flux was later refined to $\delta^{60}Ni$ = 2.85‰, given new data considered (Gueguen and Rouxel, 2021).

Adsorption processes have been reported to generally cause preferential enhancements of isotopically light Ni in the solid products, for instance, the inorganic adsorption of Ni onto Fe oxyhydroxides ($\Delta^{60}Ni_{mineral\text{-}medium}$ = –0.23 ~ –0.77‰; Gueguen et al., 2018; Wasylenki et al., 2015), carbonates ($\Delta^{60}Ni_{mineral\text{-}medium}$ = –0.52 ± 0.16‰; Castillo Alvarez et al., 2020) and smectites ($\Delta^{60}Ni_{mineral\text{-}medium}$ = –0.11 ± 0.09‰; Spivak-Birndorf et al., 2018), and the surface complexation with birnessite ($\Delta^{60}Ni_{mineral\text{-}medium}$ = –2.76 ~ –3.35‰; Sorensen et al., 2020), in which experiments the minerals are all enriched in light Ni isotopes. Low temperature alteration processes have been shown to have similar enrichments of isotopically light Ni in the products, compared to pristine samples, for instance serpentinised peridotites (Gall, 2011; Gueguen et al., 2013), altered basalts (Gall, 2011) and altered dunites (Spivak-Birndorf et al., 2018). The $\delta^{60}Ni$ values of laterites, extreme weathering products of ultramafic rocks, show a range of –0.12 ~ +0.90‰ (Ratié et al., 2016, 2015). It has been reported that soil samples preferentially enrich light Ni isotopes ($\Delta^{60}Ni_{soil\text{-}rock}$ = –0.63‰) compared to the parent rocks (Estrade et al., 2015).

1.4 Motivation for this thesis

Many pioneering studies have suggested the great potential of Ni isotopes as a geochemical tracer to disentangle processes in the ocean by distinct isotope signals. In order to put Ni isotopes into applications with robustness, a comprehensive understanding of Ni cycling in the ocean and the controlling mechanism for the Ni isotope fractionations observed is necessary.

Two of the most puzzling observations in the ocean are that Ni is never fully depleted at the surface, and that Ni isotope fractionation in the surface ocean is regionally-variable. For the latter, the regionally-variable enrichment of heavy Ni isotopes has been commonly explained by the biological activity of microorganisms like phytoplankton, but there is no direct evidence from culturing or incubation experiments thus far. In Chapter 2, direct Ni isotope measurements in cultured phytoplankton cells are provided, which requires persistent accumulation of cell materials due to their low-Ni-content, low procedural blank and precise Ni isotopic analysis on low working concentration (Appendix A). With the results obtained in Chapter 2, the bioavailability of Ni in the ocean is revisited, given the new Ni isotope data in phytoplankton. While Chapter 2 focuses on the implication that how the new phytoplankton data can fit in the Ni cycling in the modern ocean, Chapter 3 discusses the controlling mechanism for the different isotope fractionation patterns observed among phytoplankton species and compares further with other trace metal isotope systems like Cu and Zn.

Ni isotope fractionation during sulfide formation and related mineral transformation in the ocean have not been clearly understood, as an important sink of Ni under anoxic

ocean settings. In chapter 4, Ni isotope fractionation during the formation of amorphous Ni-sulfide under varying ionic strengths are measured and presented, which is followed by discussion of the implication on how these observed isotope fractionations during mineral transformation can contribute to oceanic Ni cycling. Given the new Ni isotope data from lab-scale experiments for sulfide formation, it is crucial to evaluate whether these experimental data are relevant to sulfide-containing sediments in nature. In Chapter 5, the Ni isotope data in organic-rich sediments collected off the Namibian margin are provided, with complementary trace element data in ambient porewater, seawater and particulate samples reported. At the end of Chapter 5, the oceanic Ni budget for both Ni fluxes and isotopic compositions is revisited, with new data taken into consideration.

1.5 References

Archer, C., Vance, D., Milne, A., Lohan, M.C., 2020. The oceanic biogeochemistry of nickel and its isotopes : New data from the South Atlantic and the Southern Ocean biogeochemical divide. Earth Planet. Sci. Lett. 535, 116118. https://doi.org/10.1016/j.epsl.2020.116118

Birck, J.L., Lugmair, G.W., 1988. Nickel and chromium isotopes in Allende inclusions. Earth Planet. Sci. Lett. 90, 131–143. https://doi.org/10.1016/0012-821X(88)90096-9

Bruland, K.W., 1980. Oceanographic distributions of cadmium, zinc, nickel, and copper in the North Pacific. Earth Planet. Sci. Lett. 47, 176–198. https://doi.org/10.1016/0012-821X(80)90035-7

Cameron, V., Vance, D., 2014. Heavy nickel isotope compositions in rivers and the oceans. Geochim. Cosmochim. Acta 128, 195–211. https://doi.org/10.1016/j.gca.2013.12.007

Cameron, V., Vance, D., Archer, C., House, C.H., 2009. A biomarker based on the stable isotopes of nickel. Proc. Natl. Acad. Sci. 106, 10944–10948. https://doi.org/10.1073/pnas.0900726106

Castillo Alvarez, C., Quitté, G., Schott, J., Oelkers, E.H., 2020. Experimental determination of Ni isotope fractionation during Ni adsorption from an aqueous fluid onto calcite surfaces. Geochim. Cosmochim. Acta 273, 26–36. https://doi.org/10.1016/j.gca.2020.01.010

Ciscato, E.R., Bontognali, T.R.R., Vance, D., 2018. Nickel and its isotopes in organic-rich sediments: implications for oceanic budgets and a potential record of ancient seawater. Earth Planet. Sci. Lett. 494, 239–250. https://doi.org/10.1016/j.epsl.2018.04.061

Deng, T., Cloquet, C., Tang, Y.T., Sterckeman, T., Echevarria, G., Estrade, N., Morel, J.L., Qiu, R.-L., 2014. Nickel and Zinc Isotope Fractionation in Hyperaccumulating and Nonaccumulating Plants. Environ. Sci. Technol. 48, 11926–11933. https://doi.org/dx.doi.org/10.1021/es5020955

Desboeufs, K. V., Sofikitis, A., Losno, R., Colin, J.L., Ausset, P., 2005. Dissolution and solubility of trace metals from natural and anthropogenic aerosol particulate matter. Chemosphere 58, 195–203. https://doi.org/10.1016/j.chemosphere.2004.02.025

Dupont, C.L., Barbeau, K., Palenik, B., 2008. Ni uptake and limitation in marine Synechococcus strains. Appl. Environ. Microbiol. 74, 23–31. https://doi.org/10.1128/AEM.01007-07

Elliott, T., Steele, R.C.J., 2017. The Isotope Geochemistry of Ni. Rev. Mineral. Geochemistry 82, 511–542.

Estrade, N., Cloquet, C., Echevarria, G., Sterckeman, T., Deng, T., Tang, Y.T., Morel, J.L., 2015.

Weathering and vegetation controls on nickel isotope fractionation in surface ultramafic environments (Albania). Earth Planet. Sci. Lett. 423, 24–35. https://doi.org/10.1016/j.epsl.2015.04.018

Fridovich, I., 1997. Superoxide anion radical (O2/-·), superoxide dismutases, and related matters. J. Biol. Chem. 272, 18515–18517. https://doi.org/10.1074/jbc.272.30.18515

Fujii, T., Moynier, F., Dauphas, N., Abe, M., 2011. Theoretical and experimental investigation of nickel isotopic fractionation in species relevant to modern and ancient oceans. Geochim. Cosmochim. Acta 75, 469–482. https://doi.org/10.1016/j.gca.2010.11.003

Gall, L., 2011. Development and Application of Nickel Stable Isotopes as a New Geochemical Tracer. University of Oxford.

Gall, L., Williams, H.M., Halliday, A.N., Kerr, A.C., 2017. Nickel isotopic composition of the mantle. Geochim. Cosmochim. Acta 199, 196–209. https://doi.org/10.1016/j.gca.2016.11.016

Gall, L., Williams, H.M., Siebert, C., Halliday, A.N., Herrington, R.J., Hein, J.R., 2013. Nickel isotopic compositions of ferromanganese crusts and the constancy of deep ocean inputs and continental weathering effects over the Cenozoic. Earth Planet. Sci. Lett. 375, 148–155. https://doi.org/10.1016/j.epsl.2013.05.019

Gramlich, J.W., Machlan, L.A., Barnes, I.L., Paulsen, P.J., 1989. Absolute isotopic abundance ratios and atomic weight of a reference sample of nickel. J. Res. Natl. Inst. Stand. Technol. 94, 347–356. https://doi.org/10.6028/jres.094.034

Gueguen, B., Rouxel, O., 2021. The Nickel isotope composition of the authigenic sink and the diagenetic flux in modern oceans. Chem. Geol. 563, 120050. https://doi.org/10.1016/j.chemgeo.2020.120050

Gueguen, B., Rouxel, O., Ponzevera, E., Bekker, A., Fouquet, Y., 2013. Nickel Isotope Variations in Terrestrial Silicate Rocks and Geological Reference Materials Measured by MC-ICP-MS. https://doi.org/10.1111/j.1751-908X.2013.00209.x

Gueguen, B., Rouxel, O., Rouget, M.L., Bollinger, C., Ponzevera, E., Germain, Y., Fouquet, Y., 2016. Comparative geochemistry of four ferromanganese crusts from the Pacific Ocean and significance for the use of Ni isotopes as paleoceanographic tracers. Geochim. Cosmochim. Acta 189, 214–235. https://doi.org/10.1016/j.gca.2016.06.005

Gueguen, B., Sorensen, J. V., Lalonde, S. V., Peña, J., Toner, B.M., Rouxel, O., 2018. Variable Ni isotope fractionation between Fe-oxyhydroxides and implications for the use of Ni isotopes as geochemical tracers. Chem. Geol. 481, 38–52. https://doi.org/10.1016/j.chemgeo.2018.01.023

Holliger, C., Pierik, A.J., Hagen, W.R., Reijerse, E.J., 1993. A Spectroelectrochemical Study

of Factor F430 Nickel(II/I) from Methanogenic Bacteria in Aqueous Solution. J. Am. Chem. Soc. 115, 5651–5656. https://doi.org/10.1021/ja00066a034

John, S.G., Kelly, R.L., Bian, X., Fu, F., Smith, M.I., Nathan, T., Liang, H., Pasquier, B., Seelen, E.A., Holzer, M., Wasylenki, L., 2022. The biogeochemical balance of oceanic nickel cycling. Nat. Geosci. https://doi.org/10.1038/s41561-022-01045-7

Klaver, M., Ionov, D.A., Takazawa, E., Elliott, T., 2020. The non-chondritic Ni isotope composition of Earth's mantle. Geochim. Cosmochim. Acta 268, 405–421. https://doi.org/10.1016/j.gca.2019.10.017

Konhauser, K.O., Pecoits, E., Lalonde, S. V., Papineau, D., Nisbet, E.G., Barley, M.E., Arndt, N.T., Zahnle, K., Kamber, B.S., 2009. Oceanic nickel depletion and a methanogen famine before the Great Oxidation Event. Nature 458, 750–753. https://doi.org/10.1038/nature07858

Lemaitre, N., Du, J., de Souza, G.F., Archer, C., Vance, D., 2022. The essential bioactive role of nickel in the oceans: Evidence from nickel isotopes. Earth Planet. Sci. Lett. 584, 117513. https://doi.org/10.1016/j.epsl.2022.117513

Li, H.T., Tuo, S. how, Lu, M.C., Ho, T.Y., 2022. The effects of Ni availability on H2 production and N2 fixation in a model unicellular diazotroph: The expression of hydrogenase and nitrogenase. Limnol. Oceanogr. 1–11. https://doi.org/10.1002/lno.12151

Little, S.H., Archer, C., Mcmanus, J., Najorka, J., Wegorzewski, A. V, Vance, D., 2020. Towards balancing the oceanic Ni budget. Earth Planet. Sci. Lett. 547, 116461. https://doi.org/10.1016/j.epsl.2020.116461

Mackey, D.J., O'Sullivan, J.E., Watson, R.J., Pont, G.D., 2002. Trace metals in the Western Pacific: Temporal and spatial variability in the concentrations of Cd, Cu, Mn and Ni. Deep. Res. Part I Oceanogr. Res. Pap. 49, 2241–2259. https://doi.org/10.1016/S0967-0637(02)00124-3

McDonough, W.F., 2014. Compositional Model for the Earth's Core, in: Treatise on Geochemistry: Second Edition. Elsevier Ltd., pp. 559–576. https://doi.org/10.1016/B978-0-08-095975-7.00215-1

McDonough, W.F., Sun, S. s., 1995. The composition of the Earth. Chem. Geol. 120, 223–253. https://doi.org/10.1016/0009-2541(94)00140-4

Middag, R., Baar, H.J.W. De, Bruland, K.W., 2020a. The Distribution of Nickel in the West-Atlantic Ocean , Its Relationship With Phosphate and a Comparison to Cadmium and Zinc 7, 1–17. https://doi.org/10.3389/fmars.2020.00105

Middag, R., de Baar, H.J.W., Bruland, K.W., van Heuven, S.M.A.C., 2020b. The Distribution of Nickel in the West-Atlantic Ocean, Its Relationship With Phosphate and a Comparison to Cadmium and Zinc. Front. Mar. Sci. 7, 1–17. https://doi.org/10.3389/fmars.2020.00105

Miller, A.F., 2008. Redox tuning over almost 1 V in a structurally conserved active site: Lessons from Fe-containing superoxide dismutase. Acc. Chem. Res. 41, 501–510. https://doi.org/10.1021/ar700237u

Mulrooney, S.B., Hausinger, R.P., 2003. Nickel uptake and utilization by microorganisms. FEMS Microbiol. Rev. 27, 239–261. https://doi.org/10.1016/S0168-6445(03)00042-1

Nicholls, D., 1974. Complexes and First-Row Transition Elements, 1st ed. Red Globe Press London. https://doi.org/https://doi.org/10.1007/978-1-349-02335-6

Palenik, B., Brahamsha, B., Larimer, F.W., Land, M., Hauser, L., Chain, P., Lamerdin, J., Regala, W., Allen, E.E., McCarren, J., Paulsen, I., Dufresne, A., Partensky, F., Webb, E.A., Waterbury, J., 2003. The genome of a motile marine Synechococcus. Nature 424, 1037–1042. https://doi.org/10.1038/nature01943

Pašava, J., Chrastný, V., Loukola-Ruskeeniemi, K., Šebek, O., 2019. Nickel isotopic variation in black shales from Bohemia, China, Canada, and Finland: a reconnaissance study. Miner. Depos. 54, 719–742. https://doi.org/10.1007/s00126-018-0839-8

Peach, C.L., Mathez, E.A., Keays, R.R., 1990. Sulfide melt-silicate melt distribution coefficients for noble metals and other chalcophile elements as deduced from MORB: Implications for partial melting. Geochim. Cosmochim. Acta 54, 3379–3389. https://doi.org/10.1177/009430610903800504

Porter, S.J., Selby, D., Cameron, V., 2014. Characterising the nickel isotopic composition of organic-rich marine sediments. Chem. Geol. 387, 12–21. https://doi.org/10.1016/j.chemgeo.2014.07.017

Price, N.M., Morel, F.M.M., 1991. Colimitation of phytoplankton nickel and nitrogen. Limnol. Oceanogr. 36, 1071–1077.

Punshon, S., Moore, R.M., 2008. Aerobic hydrogen production and dinitrogen fixation in the marine cyanobacterium Trichodesmium erythraeum IMS101. Limnol. Oceanogr. 53, 2749–2753. https://doi.org/10.4319/lo.2008.53.6.2749

Ragsdale, S.W., 2009. Nickel-based enzyme systems. J. Biol. Chem. 284, 18571–18575. https://doi.org/10.1074/jbc.R900020200

Ratié, G., Garnier, J., Calmels, D., Vantelon, D., Guimarães, E., Monvoisin, G., Nouet, J., Ponzevera, E., Quantin, C., 2018. Nickel distribution and isotopic fractionation in a Brazilian lateritic regolith: Coupling Ni isotopes and Ni K-edge XANES. Geochim. Cosmochim. Acta 230, 137–154. https://doi.org/10.1016/j.gca.2018.03.026

Ratié, G., Jouvin, D., Garnier, J., Rouxel, O., Miska, S., Guimarães, E., Cruz Vieira, L., Sivry, Y., Zelano, I., Montarges-Pelletier, E., Thil, F., Quantin, C., 2015. Nickel isotope fractionation during tropical weathering of ultramafic rocks. Chem. Geol. 402, 68–76. https://doi.org/10.1016/j.chemgeo.2015.02.039

Ratié, G., Quantin, C., Jouvin, D., Calmels, D., Ettler, V., Sivry, Y., Vieira, L.C., Ponzevera, E., Garnier, J., 2016. Nickel isotope fractionation during laterite Ni ore smelting and refining: Implications for tracing the sources of Ni in smelter-affected soils. Appl. Geochemistry 64, 136–145. https://doi.org/10.1016/j.apgeochem.2015.09.005

Rauch, J.N., Pacyna, J.M., 2009. Earth's global Ag, Al, Cr, Cu, Fe, Ni, Pb, and Zn cycles. Global Biogeochem. Cycles 23, 1–16. https://doi.org/10.1029/2008GB003376

Revels, B.N., Rickli, J., Moura, A. V, Vance, D., 2020. Nickel and its isotopes in the Amazon Basin: the impact of the weathering regime and delivery to the oceans. Geochim. Cosmochim. Acta. https://doi.org/10.1016/j.gca.2020.11.005

Rugel, G., Faestermann, T., Knie, K., Korschinek, G., Poutivtsev, M., Schumann, D., Kivel, N., Günther-Leopold, I., Weinreich, R., Wohlmuther, M., 2009. New measurement of the Fe60 half-life. Phys. Rev. Lett. 103, 14–17. https://doi.org/10.1103/PhysRevLett.103.072502

Saunders, N.J., Barling, J., Harvey, J., Halliday, A.N., Saunders, N.J., Barling, J., Harvey, J., Halliday, A.N., 2020. Heterogeneous nickel isotopic compositions in the terrestrial mantle - Part 1. Geochim. Cosmochim. Acta. https://doi.org/10.1016/j.gca.2020.06.029

Schropp, S.J., Scranton, M.I., Schwarz, J.R., 1987. Dissolved hydrogen, facultatively anaerobic, hydrogen-producing bacteria, and potential hydrogen production rates in the western North Atlantic Ocean and Gulf of Mexico,. Limnol. Oceanogr. 32, 396–402. https://doi.org/10.4319/lo.1987.32.2.0396

Sclater, F.R., Boyle, E., Edmond, J.M., 1976. On the marine geochemistry of nickel. Earth Planet. Sci. Lett. 31, 119–128. https://doi.org/10.1038/263042a0

Shukolyukov, A.A., Lugmair, G.W., 1993. Live Iron-60 in the Early Solar System. Science (80-.). 259, 1138–1142.

Sorensen, V., Gueguen, B., Stewart, B.D., Peña, J., Rouxel, O., Toner, B.M., 2020. Large nickel isotope fractionation caused by surface complexation reactions with hexagonal birnessite 537. https://doi.org/10.1016/j.chemgeo.2020.119481

Spivak-Birndorf, L.J., Wang, S.J., Bish, D.L., Wasylenki, L.E., 2018. Nickel isotope fractionation during continental weathering. Chem. Geol. 476, 316–326. https://doi.org/10.1016/j.chemgeo.2017.11.028

Steele, R.C.J., Elliott, T., Coath, C.D., Regelous, M., 2011. Confirmation of mass-independent Ni isotopic variability in iron meteorites. Geochim. Cosmochim. Acta 75, 7906–7925. https://doi.org/10.1016/j.gca.2011.08.030

Tachibana, S., Huss, G.R., 2003. The Initial Abundance of 60 Fe in the Solar System . Astrophys. J. 588, L41–L44. https://doi.org/10.1086/375362

Takano, S., Liao, W., Tian, H., Huang, K., Ho, T., 2020. Sources of particulate Ni and Cu in

the water column of the northern South China Sea : Evidence from elemental and isotope ratios in aerosols and sinking particles. Mar. Chem. 219, 103751. https://doi.org/10.1016/j.marchem.2020.103751

Takano, S., Tanimizu, M., Hirata, T., Shin, K.C., Fukami, Y., Suzuki, K., Sohrin, Y., 2017. A simple and rapid method for isotopic analysis of nickel, copper, and zinc in seawater using chelating extraction and anion exchange. Anal. Chim. Acta 967, 1–11. https://doi.org/10.1016/j.aca.2017.03.010

Tanimizu, M., Hirata, T., 2006. Determination of natural isotopic variation in nickel using inductively coupled plasma mass spectrometry. J. Anal. At. Spectrom. 21, 1423–1426. https://doi.org/10.1039/b609543g

van den Berg, C.M.G., Nimmo, M., 1987. Determination of interactions of nickel with dissolved organic material in seawater using cathodic stripping voltammetry. Sci. Total Environ. 60, 185–195. https://doi.org/10.1016/0048-9697(87)90415-3

Vance, D., Little, S.H., Archer, C., Cameron, V., Andersen, M.B., Rijkenberg, M.J.A., Lyons, T.W., 2016. The oceanic budgets of nickel and zinc isotopes: The importance of sulfdic environments as illustrated by the Black Sea. Philos. Trans. R. Soc. A Math. Phys. Eng. Sci. 374. https://doi.org/10.1098/rsta.2015.0294

Ventura, G.T., Gall, L., Siebert, C., Prytulak, J., Szatmari, P., Hürlimann, M., Halliday, A.N., 2015. The stable isotope composition of vanadium, nickel, and molybdenum in crude oils. Appl. Geochemistry 59, 104–117. https://doi.org/10.1016/j.apgeochem.2015.04.009

Wang, R.M., Archer, C., Bowie, A.R., Vance, D., 2019. Zinc and nickel isotopes in seawater from the Indian Sector of the Southern Ocean: The impact of natural iron fertilization versus Southern Ocean hydrography and biogeochemistry. Chem. Geol. 511, 452–464. https://doi.org/10.1016/j.chemgeo.2018.09.010

Wang, S.J., Rudnick, R.L., Gaschnig, R.M., Wang, H., Wasylenki, L.E., 2019. Methanogenesis sustained by sulfide weathering during the Great Oxidation Event. Nat. Geosci. https://doi.org/10.1038/s41561-019-0320-z

Wasylenki, L.E., Howe, H.D., Spivak-Birndorf, L.J., Bish, D.L., 2015. Ni isotope fractionation during sorption to ferrihydrite: Implications for Ni in banded iron formations. Chem. Geol. 400, 56–64. https://doi.org/10.1016/j.chemgeo.2015.02.007

Wilson, S.T., Foster, R.A., Zehr, J.P., Karl, D.M., 2010. Hydrogen production by Trichodesmium erythraeum Cyanothece sp. and Crocosphaera watsonii. Aquat. Microb. Ecol. 59, 197–206. https://doi.org/10.3354/ame01407

Yang, S., Hawco, N.J., Pinedo-gonzález, P., Bian, X., Huang, K., Zhang, R., John, S.G., 2020. A new purification method for Ni and Cu stable isotopes in seawater provides evidence for widespread Ni isotope fractionation by phytoplankton in the North Pacific. Chem. Geol. 547, 119662. https://doi.org/10.1016/j.chemgeo.2020.119662

Yang, S.C., Kelly, R.L., Bian, X., Conway, T.M., Huang, K.F., Ho, T.Y., Neibauer, J.A., Keil, R.G., Moffett, J.W., John, S.G., 2021. Lack of redox cycling for nickel in the water column of the Eastern tropical north pacific oxygen deficient zone: Insight from dissolved and particulate nickel isotopes. Geochim. Cosmochim. Acta 309, 235–250. https://doi.org/10.1016/j.gca.2021.07.004

Zamble, D., Rowinska-Zyrek, M., Kozlowski, H., 2017. The Biological Chemistry of Nickel. Royal Society of Chemistry. https://doi.org/10.1039/9781788010580-FP007

Zhang, Y., Rodionov, D.A., Gelfand, M.S., Gladyshev, V.N., 2009. Comparative genomic analyses of nickel, cobalt and vitamin B12 utilization. BMC Genomics 10. https://doi.org/10.1186/1471-2164-10-78

CHAPTER 2
Isotopic evidence for a biologically limiting nickel pool in the ocean

(This chapter is submitted as:
Isotopic evidence for a biologically limiting nickel pool in the ocean.
T.H. Wang, Q. Zhang, Y.T. Hsieh, G.M. Henderson, R.E.M. Rickaby. In revision)

2 Isotopic evidence for a biologically limiting nickel pool in the ocean

2.1 Introduction

Nickel (Ni) plays key roles in various important enzyme systems because of its plasticity in coordination, redox chemistry and catalyzing potential (Mulrooney and Hausinger, 2003; Ragsdale, 2009). Seven of eight known Ni-containing enzymes are critically involved in the production and/or utilization of ubiquitous gases (e.g., O_2, H_2, CO, CO_2, CH_4, NH_3) controlling global carbon, nitrogen and oxygen cycles.

Despite its enzymatic importance, the concentration of Ni in the oceanic photic zone is higher than that of many other transition metals with similar biological functions (e.g., Fe, Zn) and is rarely lower than 2 nM (Archer et al., 2020; Bruland, 1980; Cameron and Vance, 2014; Middag et al., 2020; Sclater et al., 1976; Takano et al., 2020, 2017; Wang et al., 2019; Yang et al., 2020, 2021). This has led to the suggestion that either Ni is not limiting biological processes in the surface ocean or that a fraction of dissolved Ni in seawater is not bioavailable (Archer et al., 2020; Mackey et al., 2002; Middag et al., 2020). An alternative explanation has been proposed that the residual Ni at the surface ocean is biologically labile and resulted from the slow depletion of Ni relative to macronutrients in upwelling regions (John et al., 2022).

Seawater Ni isotope data indicate that the isotope fractionation observed in the surface ocean is regionally variable (Archer et al., 2020; Cameron and Vance, 2014; Lemaitre et al., 2022; Takano et al., 2020, 2017; Wang et al., 2019; Yang et al., 2020, 2021). The surface ocean is generally either similar to or offset toward isotopically heavier values than the deep ocean, which has an average δ^{60}Ni of 1.33 ± 0.13 ‰ (Lemaitre et al., 2022). Four

particular regions display low Ni concentration (~2nM) coupled with a heavy Ni isotope composition (δ^{60}Ni up to 1.75‰) in the surface ocean: the mid-latitudes of the South Atlantic (30-40°S) (Archer et al., 2020), North Atlantic (40-60°N) (Lemaitre et al., 2022), South Pacific (~30°S) (Takano et al., 2017) and North Pacific (20-30°N) (Yang et al., 2020, 2021). To explain these high δ^{60}Ni of surface seawater, it has been proposed that biological activity in the surface ocean preferentially takes up isotopically light Ni (Archer et al., 2020; Lemaitre et al., 2022; Takano et al., 2017; Yang et al., 2020, 2021). Alternatively, there may be no biological fractionation but an equilibrium fractionation between bioavailable and non-bioavailable Ni species may occur that control Ni isotope compositions in seawater (Archer et al., 2020). In ocean regions where the seawater δ^{60}Ni profiles show a constant value along with depth (e.g., Southern Ocean) (Cameron and Vance, 2014; Wang et al., 2019), it has been suggested there is no significant biological Ni isotope fractionation occurring in the surface ocean.

The contrasting dominance of different phytoplankton could also contribute to the expression of regionally variable Ni isotope fractionations in the surface ocean (Archer et al., 2020; Lemaitre et al., 2022). South of the polar front in the Southern Ocean, the community dominated by diatoms uses modest amounts of Ni which leads to no isotope fractionation in the surface waters. By contrast, north of the polar front, the community is dominated by cyanobacteria with a high Ni requirement, which is suggested to cause high δ^{60}Ni of the surface seawaters (Archer et al., 2020). In the North Atlantic, south of the subarctic front, diazotrophic cyanobacteria have been proposed to explain the heavy δ^{60}Ni of the nitrate-depleted surface seawaters where the lack of fixed inorganic nitrogen may trigger a high Ni requirement for urease to convert urea into ammonium for N acquisition (Lemaitre et al., 2022).

Despite suggestions of a role for ligand binding and species-dependent Ni isotope signals, there is no direct evidence illustrating that biological activity is the cause of Ni isotope fractionation in the surface ocean. A lack of understanding of the interaction between Ni-binding ligands and dissolved Ni also hinders our knowledge of Ni bioavailability in the ocean. Here we address these knowledge gaps by direct measurement of Ni isotope fractionation during phytoplankton growth in the laboratory, which ultimately indicates that Ni is biologically limiting in some regions of the surface ocean.

2.2 Methods

2.2.1 Phytoplankton strains

Three species of cosmopolitan marine phytoplankton were chosen in this study to investigate the metal uptake mechanism and the associated Ni isotope fractionation. Dinoflagellate *Prorocentrum minimum* (RCC291) and diatom *Thalassiosira weissflogii* (RCC76) were obtained from the Roscoff Culture Collection (RCC) which is run by Sorbonne University and the French National Centre for Scientific Research at France. Cyanobacteria *Synechococcus sp*. (PCC8806) was obtained from the Pasteur Culture Collection of Cyanobacteria (PCC) which is supported by the Pasteur Institute at France. The diatom *Thalassiosira weissflogii* (RCC76) originates from Gardiners Island, northern Atlantic Ocean. The selected cyanobacteria *Synechococcus sp.* (PCC8806) originates from the margin of Port-Gentil, Gabon. Little is known about the origin of dinoflagellate *Prorocentrum minimum* (RCC291).

Sterile techniques were applied every time during the handling of cultures and medium in laminar flow hoods.

2.2.2 Reagents and laboratory equipment

All ultrapure deionized water (H_2O) used in this study was 18.2MΩ-grade from a Merck Millipore water purification system.

For bulk cell digestion, sub-boiled nitric acid (HNO_3, in-house sub-boiling distillation system) and commercial hydrogen peroxide (H_2O_2, Merck suprapur®) were used. For subcellular fraction separation, extraction buffer Tris-Cl (commercial) and sodium hydroxide (NaOH) prepared from crystalline commercial powders were used. For Ni column chemistry, sub-boiled HCl and HNO_3 were used. Solutions of dimethyglyoxime (DMG) and ammonium citrate ($(NH_4)_2C_6H_6O_7$ were prepared from crystalline commercial powders. Reagent grade acetone ($(CH_3)_2CO$), commercial Merck suprapur® reagents ammonia solution (NH_4OH, 25%) and hydrogen peroxide (H_2O_2) were also used.

All handling of cultures before collection was carried out in sterile laminar flow hoods in the OceanBug Laboratory at the Department of Earth Sciences, University of Oxford. After harvest, the subsequent sample preparation and chemistry were carried out in Class 100 laminar flow hood within the metal-free clean laboratories at the Department of Earth Sciences, University of Oxford.

2.2.3 Culturing techniques and Ni concentration

The cultures were all grown in sterile culture flasks with culturing medium Aquil* (National Center for Marine Algae and Microbiota) (Sunda et al., 2005). Medium Aquil* is the new version of the original Aquil medium (Morel et al., 1979; Price et al., 1989), which is a synthetic ocean seawater (SOW) enriched with macro- and micro-nutrients. The prepared SOW was adjusted to pH 8.1 and then passed through a chelating resin (Chelax® 100, Bio-Rad, USA) to remove impurities. After the chelating column, the nutrients were added to the SOW and sterilized by filtering through 0.22 **μ**m filters (Sunda et al., 2005).

The total Ni concentration in freshly prepared Aquil* was around 6.2 nM comparable to the modern open ocean (1.5-14.1 nM) (Archer et al., 2020; Bruland, 1980; Cameron and Vance, 2014; Lemaitre et al., 2022; Middag et al., 2020; Sclater et al., 1976; Takano et al., 2020, 2017; Wang et al., 2019; Yang et al., 2021, 2020), regarded as the control group representing the modern open ocean in the culturing experiments. Additional Ni was added as $NiCl_2$ solution prepared by dissolving commercial $NiCl_2 \cdot 6H_2O$ powders in deionized water with known Ni isotopic composition. In order to increase the quantity of metals in cultured cells, to aid precise analysis of Ni isotopes by mass spectrometry, higher Ni concentrations were applied in the medium in comparison with the controlled ones. The concentrations of added Ni were 0 **μ**gL^{-1}(control), 10 **μ**gL^{-1} (~170 nM), 20 **μ**gL^{-1} (~341 nM), 100 **μ**gL^{-1} (~1704 nM), 200 **μ**gL^{-1} (~3408 nM) and 500 **μ**gL^{-1} (~8519 nM). With the Ni in freshly prepared Aquil* taken into account, the Ni speciation for set Ni concentrations are shown in Table 2.1. Three phytoplankton species were initially cultured and compared at four concentrations, i.e., 0 **μ**gL^{-1}, 20 **μ**gL^{-1}, 100 **μ**gL^{-1} and 200 **μ**gL^{-1}. Based on the Ni contents preliminarily measured in three species, the dinoflagellate *P. minimum* was chosen to perform duplications and three-cellular-fraction

separation as it showed more tendency to accumulate enough Ni for precise Ni isotope analyses. Additionally, two duplications of the culturing for dinoflagellate *P. minimum* were carried out in 500 μgL^{-1} to see its physiological responses to increased/very high Ni availability.

Table 2.1. Ni contents and speciation in this study

Unit						
Total Ni (μgL^{-1})	0.366	10.366	20.366	100.366	200.366	500.366
Total Ni (nM)	6.236	176.613	346.990	1710.005	3413.774	8525.081
Ni' (pM)	0.014	0.405	0.795	3.917	7.821	19.530
Ni^{2+} (pM)	0.008	0.227	0.447	2.201	4.394	10.972
Total Ni (%)	100					
Ni' (%)	0.00023					
Ni^{2+} (%)	0.00013					

Medium Aquil* contains ~0.1mM ethylenediaminetetraacetic acid (EDTA) which acts as a metal buffering agent, prevents the formation of insoluble precipitates and maintains the metals at a fixed bioavailable concentration for phytoplankton uptake, despite the continuous utilization during phytoplankton growth. In terms of the bioavailability of trace metal for phytoplankton, previous studies suggested the free metal ion concentration as a main factor regulating the uptake, intracellular utilization and the toxicity of trace metals (Anderson and Morel, 1978, 1982; Anderson et al., 1978; Bates et al., 1982; Sunda, 1975). Given the total Ni concentration and the presence of ~0.1mM of EDTA, the concentration of free divalent Ni^{2+} and dissolved inorganic Ni species (noted as Ni', including mainly Ni^{2+}, $NiSO_{4(aq)}$, $NiCO_{3(aq)}$, $NiHCO_3^+$ and $NiCl^+$) can be calculated using the inorganic side reaction coefficient ($\alpha_M = [M']/[M^{n+}]$; $\alpha_{Ni} = 1.78$ at 20°C and a pH of 8.2) and the stability constant ($\text{Log } [M]_{total}/[M']$; $\text{Log } [Ni]_{total}/[Ni'] = 5.64$ at 20°C and a

pH of 8.2) (Sunda et al., 2005). These constants and corresponded speciation are pH– and temperature–dependent.

The ranges of [Ni'] and [Ni^{2+}] applied in this study were 0.014 - 19.530 pM and 0.008 – 10.972 pM, respectively (Table 2.1). The concentration of Ni' is ~0.00023% of total dissolved Ni, which is conventionally used in culturing studies (Ho et al., 2003; Sunda et al., 2005).

The algae were cultured in condition-controlled incubators at a constant temperature of 20 ± 1°C and illuminated with 100 **μ**mol photons $m^{-2}s^{-1}$ on a day to night cycle of 12:12 hours.

The cell numbers for determining growth rates (**μ**) for different species were measured by Beckman Coulter® electronic particle counter on a daily basis. The growth rates were calculated by the following equation: $N_2 = N_1e^{\mu t}$. N_1 represents the initial population. N_2 represents the current population after a time t with a growth rate **μ**.

All phytoplankton cells were acclimated to the given culturing conditions in 50-mL sterile flasks for at least three generations before being inoculated into 2L sterile polycarbonate bottles for the experiments. The cells were harvested before the end of exponential growth by centrifugation at 4700 rpm for 30 min. For bulk cell analysis, the collected cells were rinsed three times with chelex-cleaned SOW (Ho et al., 2003). For three-cellular-fraction separation, the harvested cells were rinsed two times with chelex-cleaned SOW and one time with Tris-Cl buffer (pH = 8) (Wilson et al., 2019). The rinses were for removing loosely bound metals on cell surfaces.

2.2.4 Whole cell digestion and three-cellular-fraction separation

The whole cell digestion was carried out to understand the uptake and partitioning of Ni into the cell. For this purpose, the collected cells were digested completely with concentrated HNO_3 and 30% H_2O_2 with a volumetric ratio 3:2. The aliquots were then dried down, dissolved in 2% HNO_3 and refluxed at 120°C on a hotplate before elemental analysis. Two certified biological standards from Sigma Aldrich, BCR-273 (single cell) and BCR-414 (plankton), were also processed along with the algal samples.

The three-cellular-fraction experiments were designed to investigate the distribution of Ni in different parts of the cell and understand the potential uptake and metal-regulating mechanisms. To that end, additional batches of culture for dinoflagellate *Prorocentrum minimum* (RCC 291) were harvested and separated into three procedurally defined cellular fractions, i.e., protein (P), cell debris (CD) and metal-rich granules (MRG) (Aharchaou et al., 2017; Wilson et al., 2019). Protein (P) fraction represents proteins and some organelles of the cell. Cell debris (CD) represents the cell wall and surface membrane. Metal-rich granules (MRG) represents the part of membrane which is resistant to NaOH.

The harvested cells were resuspended in 1 mL of extraction buffer (20 $mmolL^{-1}$ Tris-Cl, pH 8.0) and disrupted by ultrasonication. During the ultrasonication, the cells were put on ice to prevent the released heat denaturing the proteins. Each sample was disrupted with 20 s bursts for six times (pulse frequency of 0.4 s s^{-1}, magnitude of 70%), with 20 s intervals between bursts. The sample solution was then centrifuged for 30 min at 13,200 rpm and 4°C. The supernatant was then collected as protein (P) fraction and the residues

were used for next-step extraction. The residues were then boiled for 2 min with 0.5 mL of Milli-Q water. Then the solution was digested with 0.5 mL 1 M NaOH at 70°C for 60 min, left to cool down and centrifuged for another 30 min at 13,200 rpm and 4°C. The supernatant at this stage was collected as cell debris (CD) fraction and the residues were collected as metal-rich granules (MRG) fraction. In case for any incomplete separation, three fractions were all treated with concentrated HNO_3 and 30% H_2O_2 with a volumetric ratio 3:2 until fully dissolved. Solutions were dried down and dissolved in 2% HNO_3 before elemental analysis.

2.2.5 Ni concentration and Ni isotope analysis

The elemental analysis for whole cells and three separated subcellular fractions was carried out using a PerkinElmer NexION 350D quadrupole inductively coupled plasma mass spectrometer (ICP-MS) at the Department of Earth Sciences, University of Oxford. Three modes, i.e., standard mode, KED (Kinetic Energy Discrimination) mode and DRC (Dynamic Reaction Cell) mode, were available to be applied to optimize the signals and minimize the potential interferences on measured masses for various elements. KED mode with application of commercial grade helium gas (>99.999%) was applied for the measurement of ^{60}Ni for Ni concentration in samples. Potential polyatomic interferences like $^{24}Mg^{36}Ar^+$, $^{42}Ca^{18}O^+$, $^{44}Ca^{16}O^+$, $^{23}Na^{37}Cl^+$ and $^{43}Ca^{16}O^1H^+$ can be minimized. Precision and accuracy of the analytical method were verified with the long-term monitoring river water standard SLRS-6 (see Appendix D, Table D.2).

After the acquisition of Ni content in each sample, the dissolved samples were double-spiked to ensure that any isotopic fractionation induced by sample processing and mass spectrometry can be corrected for. There are five stable Ni isotopes: ^{58}Ni, ^{60}Ni, ^{61}Ni, ^{62}Ni

and ^{64}Ni, with respective abundance of 68.08%, 26.22%, 1.14%, 3.63% and 0.93% (Gramlich et al., 1989). The double-spike technique used in this study consisted of a ^{61}Ni:^{62}Ni ratio of 25:75 and was added into each dissolved sample at a sample-to-spike ratio of 0.4 before Ni purification (Gall et al., 2012). In Gall et al. (2012), a sample-to-spike ratio of 0.3 – 2.0 has been shown to yield accurate results, but a sample-to-spike ratio of 0.4 – 0.6 was recommended in the study due to the lower analytical errors.

Prior to Ni isotope analysis, the chemical purification for Ni was carried out in Class 100 laminar flow hood in the metal-free clean laboratory at the Department of Earth Sciences, University. A three-stage ion exchange method was applied (Gall et al., 2012). The first and second cation column exploits the ability of Ni to form strong complexes with ammonia and dimethylglyoxime (DMG), respectively. The third anion column was applied to separate any remaining Fe from Ni. The total procedural blanks for the sample digestion combined with Ni purification were assessed along with every batch of column chemistry and were usually less than 4.1 ng.

Nickel isotope compositions were measured on a Nu Plasma high resolution multi-collector inductively coupled plasma mass spectrometer (HR-MC-ICP-MS) at the Department of Earth Sciences, University of Oxford. All isotopic analyses were carried out in low resolution. Sample solutions of 200 ng/g total Ni were introduced into the plasma in 2% HNO_3 using a PFA nebulizer (ESI scientific, 50μLmin^{-1}) coupled with an Aridus II desolvating nebulizer system (TELEDYNE, CETAC Technologies). The desolvator can enhance the sensitivity and minimize oxide formation during ionization. The intensities of total Ni in standards and samples were all controlled at ~15 V. Each isotopic measurement consists of 40 cycles which have 10s integration time for acquiring ion

beam intensity. The potential interference of ^{58}Fe on ^{58}Ni was corrected by simultaneous measurement of ^{57}Fe. The normalized argon index (NAI) technique was used to quantify the thermal condition of plasma and minimize the possible interferences on Ni isotopes (Fietzke and Frische, 2016). This technique has been applied to Ba isotope analysis (Yu et al., 2020). The data reduction method for the deconvolution of the double-spike was performed online (Siebert et al., 2001).

The accuracy and precision of the analytical method were monitored long-term by repeated analysis of two in-house Fe-Ni sulfide standards (Kam, Sud) and one USGS reference material Nod-P-1 (Mn nodule). Phytoplankton standard BCR-414 was also chemically purified and measured along with the phytoplankton cells to verify the approach applied in this study.

All Ni isotope compositions reported in this study are represented as delta notation (δ) in per mil deviation (‰) relative to Ni isotope standard SRM 986 (high-purity Ni metal). Isotopic results for bulk cell analysis are reported as the fractionation between the collected cells and the initial culturing medium, which are expressed as $\Delta^{60}Ni_{cell\text{-}medium} = \delta^{60}Ni_{cell} - \delta^{60}Ni_{medium}$. While for subcellular analysis, isotopic results are reported as the fractionation between the subcellular fraction and the initial culturing medium, which are expressed as $\Delta^{60}Ni_{fraction\text{-}medium} = \delta^{60}Ni_{fraction} - \delta^{60}Ni_{medium}$.

$$\delta^{60}Ni = \left[\frac{(^{60}Ni/^{58}Ni)_{sample}}{(^{60}Ni/^{58}Ni)_{SRM986}} - 1\right] \times 1000\ (‰)\ (2.1)$$

The long-term reproducibilities of Kam, Sud and Nod-P-1 over 30 months were -0.88 ± 0.06‰ (n=43), 0.79 ± 0.06‰ (n=43) and 0.37 ± 0.07‰ (n=36), respectively. The results of BCR-414 (0.12 ± 0.05‰, n=4) was in good agreement with previous numbers published (0.11 ± 0.06‰, n=10, Takano et al., 2020; 0.07 ± 0.06‰, n=3, Yang et al., 2020). The Ni isotopic composition of the added $NiCl_2$ solution was 0.28 ± 0.06‰ (n=5).

The sample sizes in this study may occasionally deviated from the normal working sample size (~60 ng of Ni) due to the trace amount of Ni in phytoplankton, despite scaling up cultures in 2L sterile bottles. Consequently, an assessment of instrumental mass bias was conducted on two in-house Fe-Ni sulfide standards (Kam and Sud), considering varying intensity ratios between the sample and the standard.

2.3 Results and Discussion

2.3.1 Assessment of instrumental biases under low-Ni conditions

The accuracy and precision of Ni isotope analysis decreases with the decreasing sample size (Figure 2.1). Samples with total Ni content less than 10 ng were excluded from further discussion of their Ni isotopic composition and the curve fitting for Rayleigh distillation law, i.e., the data points of dinoflagellates and cyanobacteria grown under [Ni'] = 0.014 pM, because the low content of Ni may have influenced the quality of Ni isotopic analysis and caused potentially significant, scattered and irregular instrumental biases.

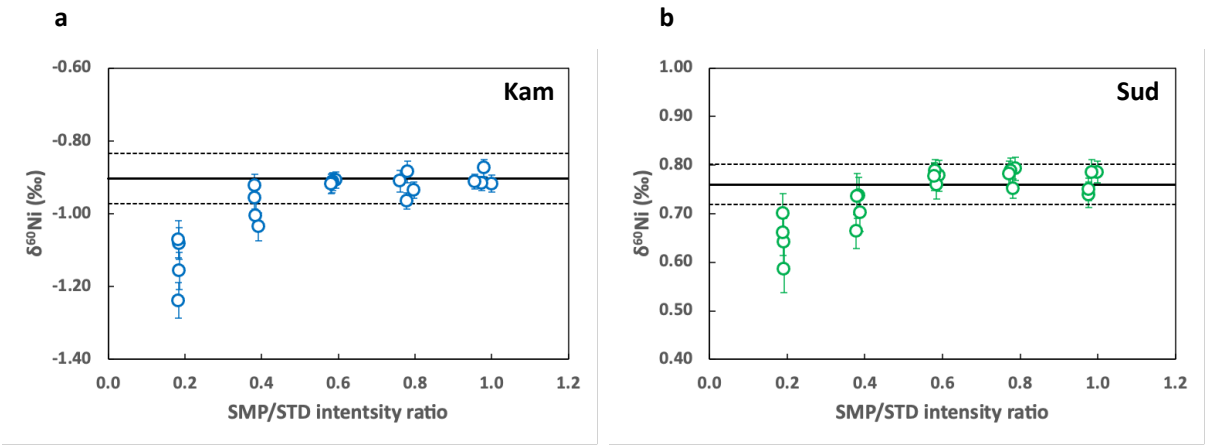


Figure 2.1. Assessment of instrumental biases during Ni isotope analysis with varying sample-to-standard intensity ratio. Intensity means the total intensity of ^{58}Ni, ^{60}Ni, ^{61}Ni and ^{62}Ni. the total Two in-house Fe-Ni sulfide standards Kam (a) and Sud (b) were measured repeatedly for 4 times at each sample/standard (SMP/STD) intensity ratio. The black solid lines represent the long-term monitored values and the dotted lines represent the 2 standard deviations (2SD) under intensity-matched circumstance. The long-term monitored δ^{60}Ni values were -0.90 ± 0.05‰ (n = 66) and 0.76± 0.05‰ (n = 52) for Kam and Sud, respectively. The averaged instrumental shifts caused by the unmatched concentration were ~ -0.2‰ and ~-0.1‰ for Kam and Sud when the total Ni intensity was about ~20% of the standard, respectively. Following the trend toward the low end, the data points seemed to be more scattered, and the analytical errors became larger.

2.3.2 Ni isotope fractionation during phytoplankton growth

We measured Ni isotope fractionation during the growth of cyanobacteria, diatoms and dinoflagellates under varying Ni bioavailability in well-controlled culturing experiments (see section 2.2.3). The results show that the phytoplankton cells overall preferentially take up isotopically heavy Ni, relative to the total dissolved Ni (Figure 2.2 and Table 2.2). This observation is in contrast to previous hypotheses that biological uptake in the surface ocean removes isotopically light Ni from seawater or causes no fractionation (Archer et al., 2020; Lemaitre et al., 2022; Takano et al., 2017; Yang et al., 2020, 2021). The utilization and accumulation of Ni within these phytoplankton are confirmed by the increasing cellular Ni/P ratios with the increasing Ni availability (Figure 2.3). The

differences between $\delta^{60}Ni$ of harvested cells and the medium ($\Delta^{60}Ni_{cell\text{-}medium}$) increase in parallel with the increasing Ni availability up to ~5‰ for cyanobacteria and dinoflagellates, and ~2‰ for diatoms, tending to the starting composition when more Ni is removed from the medium (Figure 2.4). The isotopic fractionations are large compared to any natural samples or processes reported so far (lowest $\delta^{60}Ni$ of ~-1.5‰ in methanogen; highest $\delta^{60}Ni$ of ~2.8‰ in lherzolite separates) (Cameron et al., 2009; Elliott and Steele, 2017; Gall et al., 2017; Saunders et al., 2020).

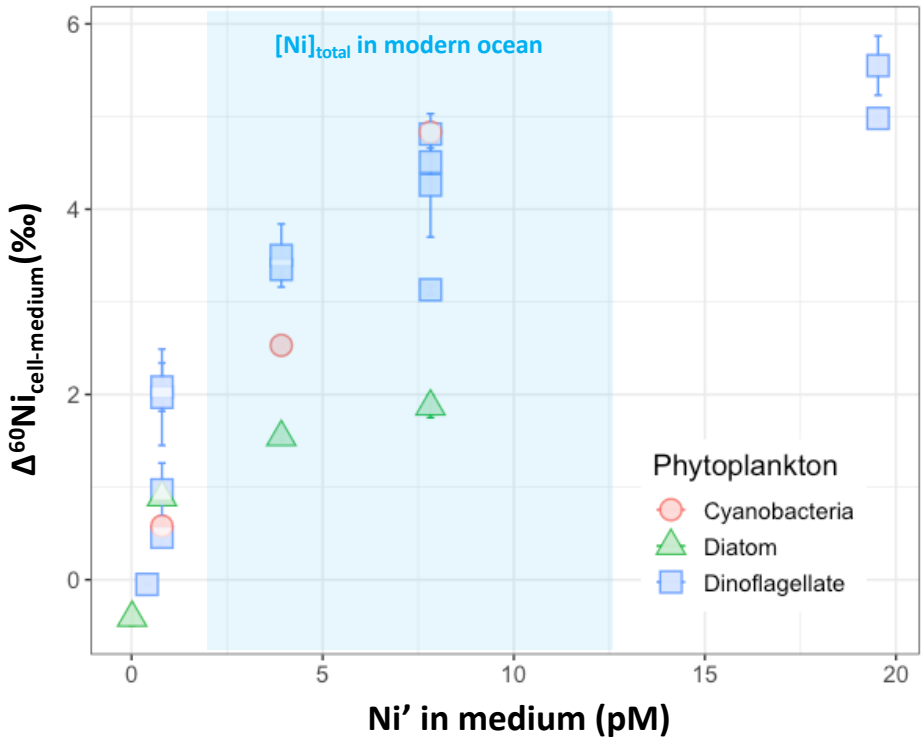


Figure 2.2. Ni isotope fractionation between collected cells and culturing medium under varying Ni availability. Cyanobacteria *Synechococcus sp.* (red circle), diatom *T. weissfloggi* (green triangle) and dinoflagellate *P. minimum* (blue square) were cultured and compared. Error bars represent the standard deviations (2SD) of measurements. The range of $[Ni]_{total}$ in modern ocean is shown as the blue shade.

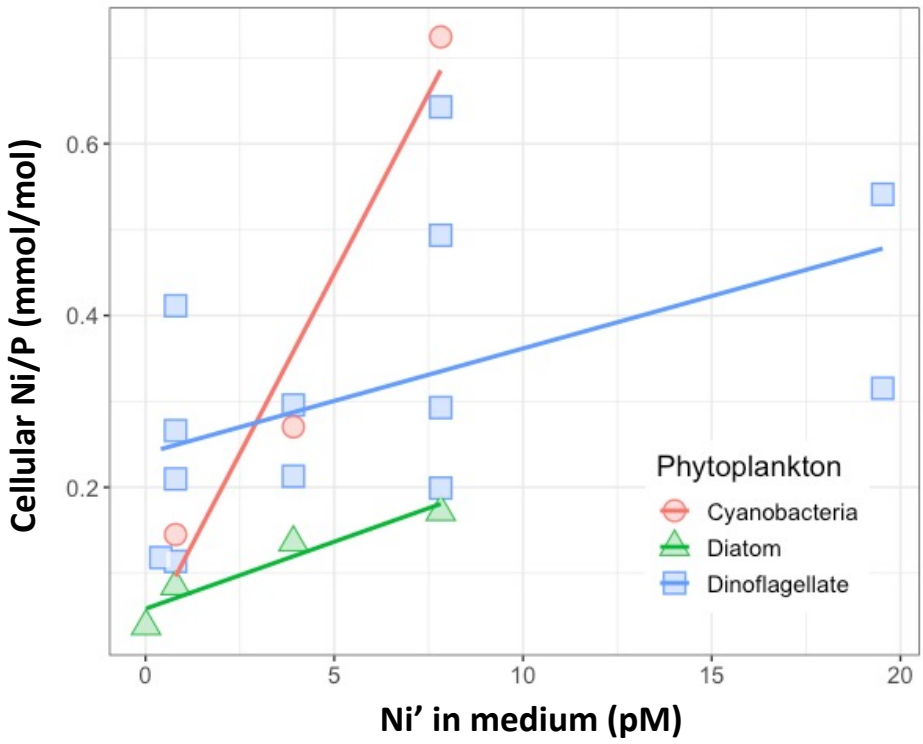


Figure 2.3. Ni/P ratios in harvested phytoplankton cells under varying Ni availabilities. Lines denote the trends for these phytoplankton.

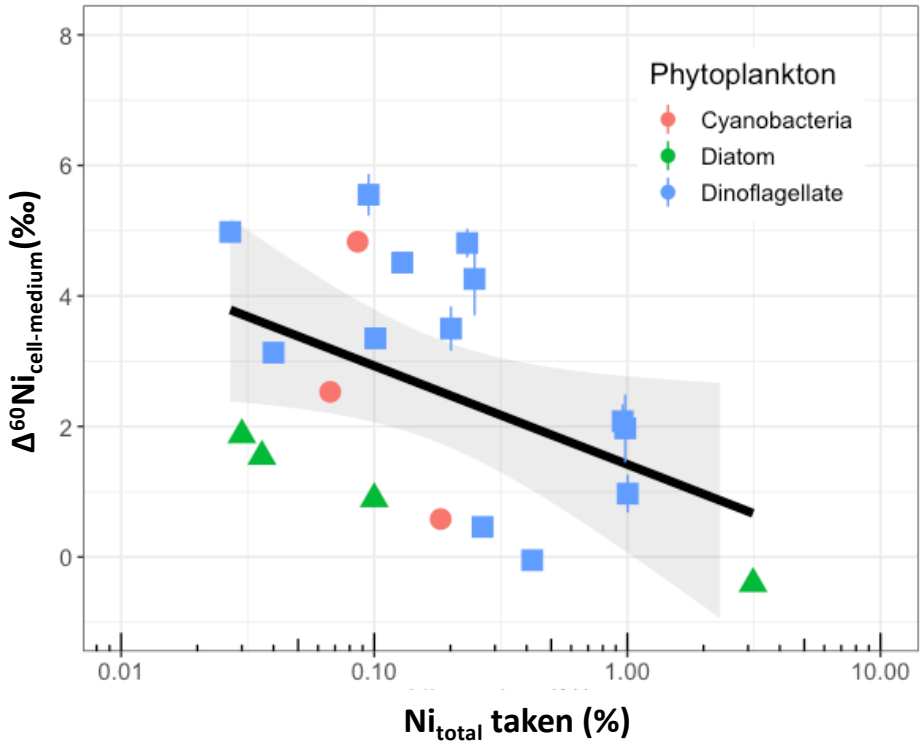


Figure 2.4. Overall trend between $\Delta^{60}Ni_{cell\text{-}medium}$ and proportion of $[Ni]_{total}$ taken by phytoplankton. Error bars represent the standard deviations (2SD) of duplicated measurements. The grey band denotes the 95% confidence interval. T-test ($p < 0.01$).

Table 2.2. Compilation of growth rates, Ni quotas and $\Delta^{60}Ni_{cell\text{-}medium}$ for whole cell analyses performed on three species of phytoplankton

Phytoplankton	Species	Strain	[Ni'] in medium(pM)	Growth rate μ (d^{-1})	Ni/P_{cell} (mmol/mol)	Δ^{60}Ni (‰)	2SD*	n
Dinoflagellate	*Prorocentrum minimum*	RCC 291	0.014	0.73	0.043	-0.35 **	0.04	2
			0.014		0.005	-2.17 **	0.12	2
			0.405		0.118	-0.05	0.01	2
			0.795	0.75	0.411	1.97	0.52	5
			0.795		0.210	0.97	0.29	5
			0.795		0.266	2.08	0.26	6
			0.795		0.114	0.46	0.09	3
			3.917		0.296	3.50	0.34	6
			3.917		0.213	3.35	0.09	3
			7.821	0.64	0.643	4.26	0.56	5
			7.821		0.293	4.51	0.15	6
			7.821		0.493	4.81	0.22	6
			7.821		0.199	3.13	0.05	2
			19.530		0.541	5.55	0.32	5
			19.530		0.315	4.98	0.03	4
Cyanobacteria	*Synechococcus sp.*	PCC 8806	0.014	0.62	0.006	-0.73 **	0.09	1
			0.795	0.47	0.145	0.58	0.10	2
			3.917		0.270	2.53	0.03	4
			7.821	0.47	0.724	4.83	0.04	4
Diatom	*Thalassiosira weissfloggi*	RCC 76	0.014	0.75	0.038	-0.41	0.08	1
			0.795	0.80	0.085	0.89	0.03	1
			3.917		0.136	1.54	0.04	2
			7.821	0.76	0.171	1.87	0.12	3

* The numbers represent the 2SD (standard deviation) of different independent analyses when n≥2, while numbers represent the 2SE (standard error) of 40 analytic cycles of one analysis when n=1.

** Excluded for further discussion as the low Ni contents may influence the quality of isotopic analysis (see section 2.3.1 and Figure 2.1).

2.3.3 Bioavailability of Ni in cultures

To assess the cause of observed biological Ni isotopic fractionations, it is critical to understand the bioavailability of Ni utilized by phytoplankton. For our culture experiments, we tested two possible forms of Ni bioavailability, (1) $[Ni]_{total}$: total dissolved Ni and (2) [Ni'] : dissolved Ni in inorganic forms (e.g., Ni^{2+}, $NiSO_{4(aq)}$), by plotting the observed difference between $\delta^{60}Ni$ in the cells and the medium ($\Delta^{60}Ni_{cell-medium}$) versus the utilized fraction by phytoplankton (see section 2.2.3 and Figure 2.5).

The scale of $[Ni]_{total}$ shows the estimated utilization percentages to be mostly less than 3%, which suggests that a small fraction of Ni is taken into phytoplankton during growth. (Figure 2.5a). While the scale of [Ni'] shows the estimated utilization percentages to be 2 to 4 orders of magnitude higher than 100%, which implies that Ni may be continuously released from the chelator EDTA and utilized by phytoplankton (Figure 2.5b). In general, the utilization percentages of [Ni'] is higher when Ni concentration is lower in the medium (Figure 2.5). As for the phytoplankton with high utilization percentages of [Ni'], there is no significant difference on their growth rate compared to higher Ni availability, which suggests that the replenishing rate of Ni from EDTA may be faster or comparable to the utilization rate of phytoplankton. This replenishment of Ni from the EDTA, as a metal buffering agent used to prevent toxicity or precipitation of metals and also maintain the metals at a fixed bioavailable concentration for phytoplankton uptake, on timescales equivalent to that of biological uptake, indicates that the bioavailable pool may have a constant Ni isotopic composition through the process.

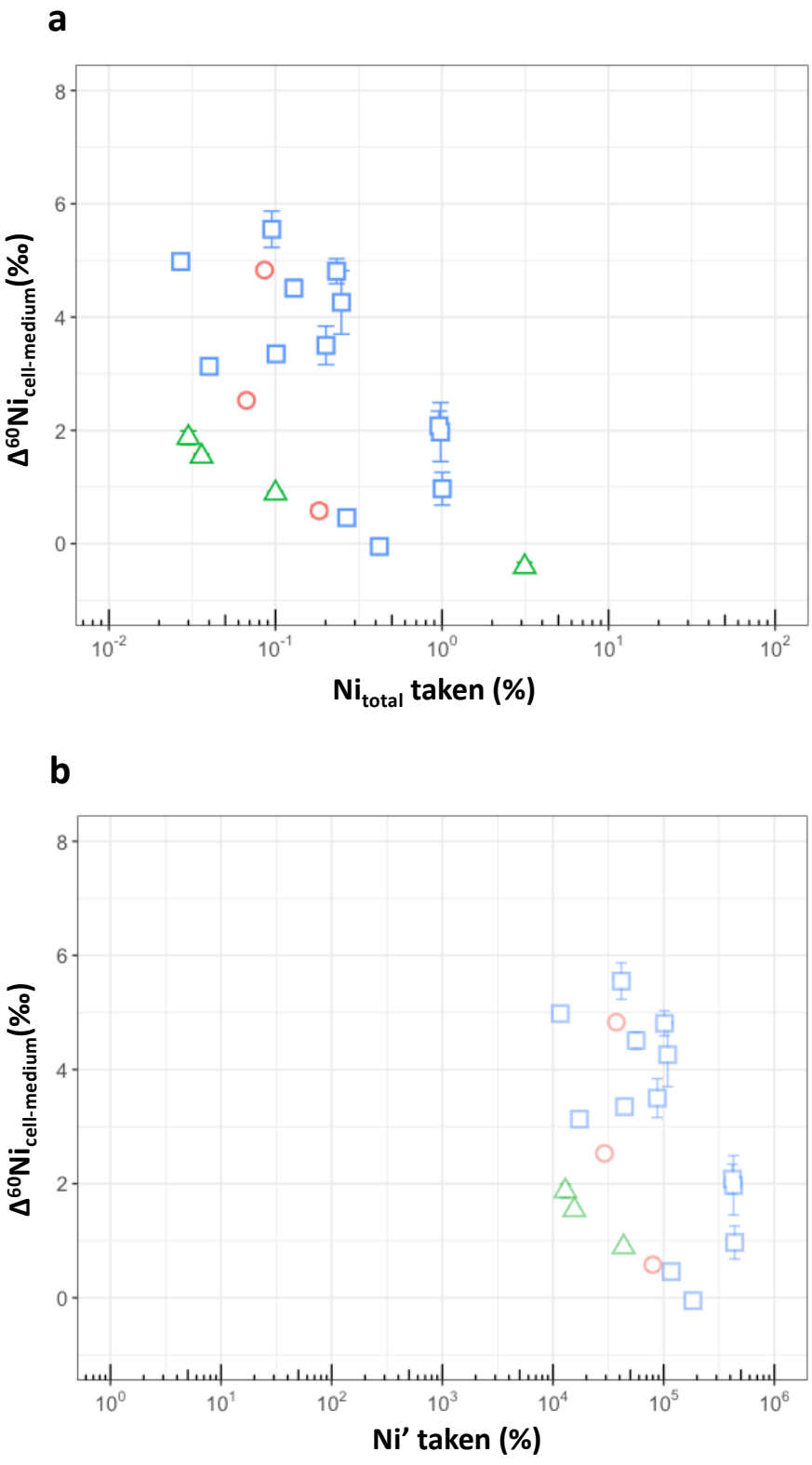


Figure 2.5. Assessment of Ni bioavailability in cultures. $\Delta^{60}Ni_{cell\text{-}medium}$ measured in three species of phytoplankton are plotted with the proportion of taken (a) $[Ni]_{total}$ and (b) [Ni'].

2.3.4 Mechanism controlling Ni isotope fractionation in phytoplankton

These positive Ni isotope fractionations between cells and medium ($\Delta^{60}Ni_{cell\text{-}medium}$) suggest that the binding strength during the Ni uptake of phytoplankton may be stronger than the binding strength of Ni species in the media, because heavy isotopes are generally enriched in stronger bonds if there is an equilibrium fractionation (Albarède, 2015; Irving and Williams, 1953). Ni isotope fractionation between harvested cells and medium varies with phytoplankton species and Ni availability (Figure 2.2). In general, larger and more positive fractionations are observed in all three species when Ni availability is higher. There are two potential explanations about this observation: (1) The uptake pathway of Ni in phytoplankton may change under changing Ni availability and cause different isotope fractionations, but the pathways all enrich heavy Ni isotopes; (2) The fractionation caused by uptake may be constant but dependent on the species. An additional metal regulation system such efflux pathway may impose another isotope fractionation effect on harvested cells. In this case, the efflux systems in all three species can impose a kinetic isotope effect, which transports isotopically lighter Ni out of cells and results in heavier Ni isotope compositions in cells. This efflux may occur more frequently and cause more isotope fractionation (i.e., increasing $\Delta^{60}Ni_{cell\text{-}medium}$) when Ni availability is higher in cultures, in order to regulate in vivo metal concentration. Both explanations do not mutually exclude one another, indicating potential complexity in the physiological responses of phytoplankton. The current evidence remains inconclusive.

The presence of EDTA in the cultures influenced the availability of Ni, and is likely to have induced an isotope fractionation between Ni-EDTA and free Ni during equilibration in the media before biological uptake. A similar issue was noted in experiments investigating

Zn isotopic fractionation by phytoplankton (Köbberich and Vance, 2019), with the conclusion that -0.16‰ ~ -0.33‰ of the observed $\Delta^{66}Zn_{biomass\text{-}medium}$ could be attributed to the equilibrium fractionation with heavy Zn isotopes preferentially bound to EDTA, leaving the remaining solution isotopically lighter. Similarly, an enrichment of heavy isotopes onto EDTA has also been observed during the chelation of Ni by EDTA (Nomura et al., 2013), with a reported Ni isotope fractionation of +0.5‰ between EDTA-bound Ni and free Ni. Though the experimental conditions such as temperature and pH in Nomura et al. (2013) were not completely identical to our cultures. This fractionation by binding to EDTA is likely to at most lead to fractionate the bioavailable Ni pool about 0.5‰ lighter than the $\delta^{60}Ni$ of bulk medium and result in larger isotope fractionations observed in phytoplankton cells. If the buffering rate of Ni from EDTA occurs on timescales equivalent to that of biological uptake, the observed $\Delta^{60}Ni_{cell\text{-}medium}$ should be a combined effect of the isotope fractionation between EDTA-bound Ni and bioavailable Ni pool (Ni^{2+}) and the isotope fractionation between bioavailable Ni pool (Ni^{2+}) and cells, where $\Delta^{60}Ni_{cell\text{-}medium} = \Delta^{60}Ni_{EDTA\text{-}Ni2+} + \Delta^{60}Ni_{cell\text{-}Ni2+}$, based on an assumption $\delta^{60}Ni_{medium} = \delta^{60}Ni_{EDTA}$.

Following the culture experiments for dinoflagellate *P. minimum,* we also separated cells into subcellular components for isotope analysis. This analysis confirms the uptake of isotopically heavy Ni into the cells and the distribution of this isotopic signal through the different subcellular fractions (Figure 2.6 and Table 2.3).

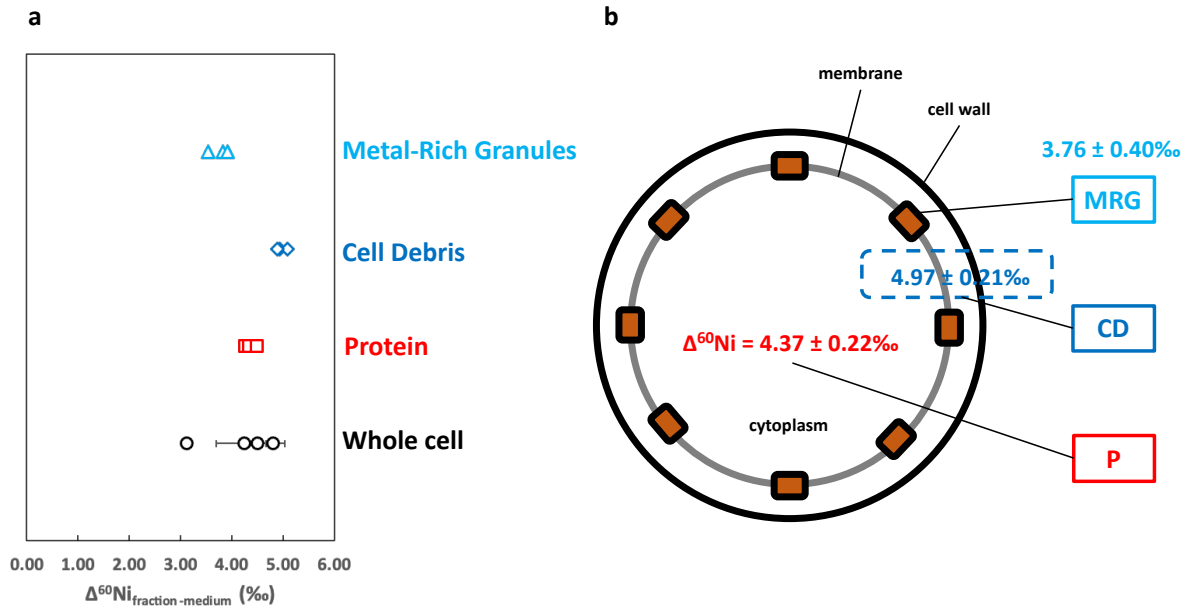


Figure 2.6. Subcellular Ni isotope analysis on dinoflagellate P. minimum (RCC291) under [Ni'] of 7.821 pM. The medium with high Ni availability was selected to accumulate enough Ni in cells for precise Ni isotope analysis. a, Comparison of $\Delta^{60}Ni_{cell\text{-}medium}$ in bulk cells and their subcellular units, i.e., protein (P), cell debris (CD) and metal-rich granules (MRG). b, Schematic diagram for the distribution of Ni isotopes in different fractions which are procedurally defined (see section 2.2.4). P fraction represents proteins and some organelles of the cell. CD fraction represents the cell wall and part of the membrane. MRG represents the rest part of the membrane which is resistant to NaOH.

Table 2.3. $\Delta^{60}Ni_{fraction\text{-}medium}$ in three subcellular fractions of dinoflagellate cultured under [Ni'] of 7.821 pM.

Fraction	Duplication	Δ^{60}Ni (‰)	2SD*	n
P	1	4.28	0.06	2
	2	4.34	0.03	1
	3	4.49	0.03	1
CD	1	4.93	0.05	2
	2	5.09	0.02	1
	3	4.90	0.04	1
MRG	1	3.82	0.07	2
	2	3.92	0.02	1
	3	3.54	0.03	1

The increasing Ni/P ratios in all fractions reflect the physiological responses to the increasing Ni availability in the media (Figure 2.7 and Table 2.4). There is a significant increase of the Ni in the protein fraction when [Ni'] increases from 0.014 pM to 0.795 pM (Figure 2.8).

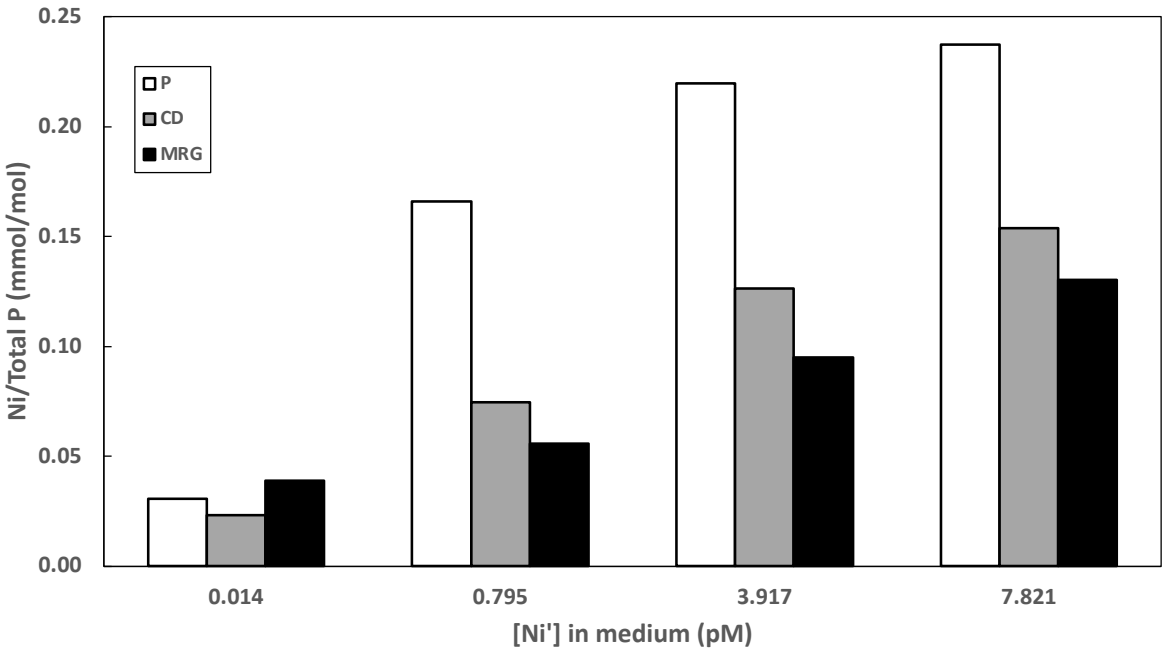


Figure 2.7. Ni quotas normalized to whole cell P in three subcellular fractions of dinoflagellate *P. minimum* under varying [Ni']. Each quota represents an average of three duplications. P: protein; CD: cell debris; MRG: metal-rich granules.

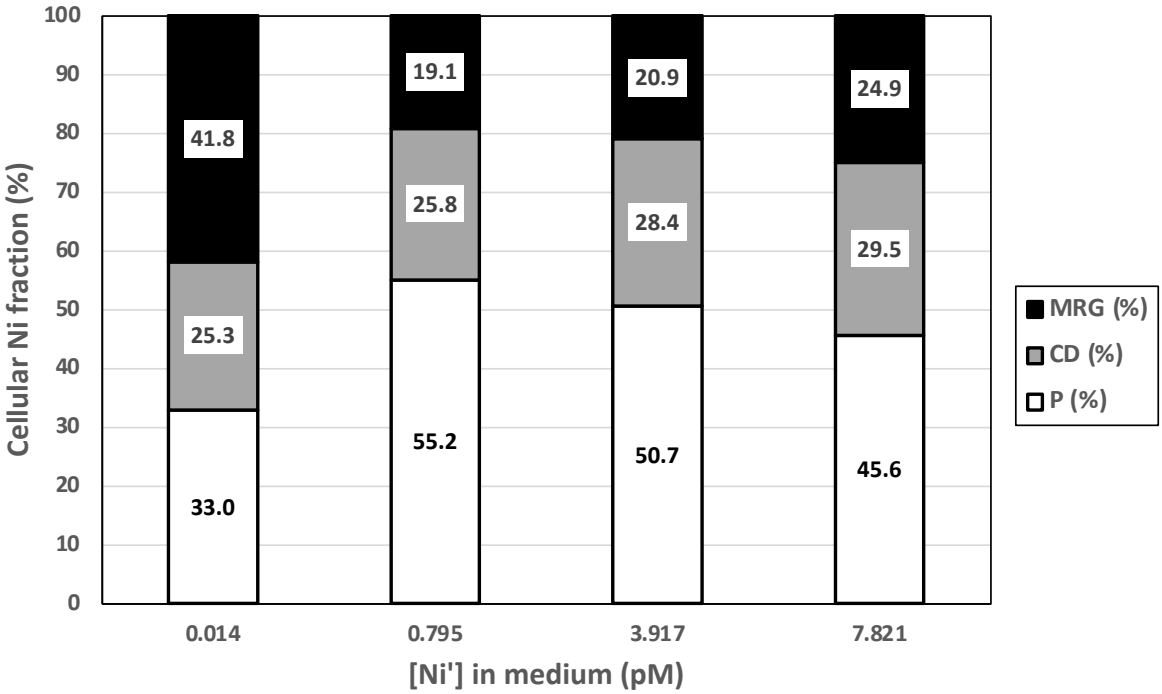


Figure 2.8. Relative proportion of Ni in three cellular fractions of dinoflagellate *P. minimum* under varying [Ni']. The proportions presented are an average of three duplications. P: protein; CD: cell debris; MRG: metal-rich granules.

Table 2.4. Ni quotas in three cellular fractions (P, CD and MRG) of dinoflagellate *P. minimum* normalized to whole cell P and relative proportions under varying Ni bioavailability

[Ni'] in medium (pM)	Duplication	Ni/P (mmol/mol)			Proportion of total Ni (%)		
		P	CD	MRG	P	CD	MRG
0.014	1	0.032	0.025	0.043	32.0	24.9	43.1
	2	0.031	0.022	0.039	33.5	23.9	42.6
	3	0.029	0.023	0.035	33.4	26.9	39.7
	AVG	0.031	0.023	0.039	33.0	25.3	41.8
	2SD	0.003	0.003	0.009	1.7	3.1	3.7
0.795	1	0.227	0.069	0.054	64.9	19.6	15.5
	2	0.139	0.082	0.060	49.5	29.1	21.4
	3	0.132	0.074	0.053	51.1	28.6	20.3
	AVG	0.166	0.075	0.056	55.2	25.8	19.1
	2SD	0.106	0.013	0.008	16.9	10.7	6.3
3.917	1	0.234	0.100	0.050	61.0	26.0	13.0
	2	0.224	0.127	0.098	49.9	28.2	21.9
	3	0.201	0.152	0.136	41.1	31.1	27.8
	AVG	0.220	0.126	0.095	50.7	28.4	20.9
	2SD	0.033	0.053	0.087	20.0	5.1	14.9
7.821	1	0.228	0.158	0.153	42.2	29.4	28.4
	2	0.233	0.150	0.134	45.0	29.0	25.9
	3	0.251	0.152	0.103	49.6	30.0	20.4
	AVG	0.237	0.154	0.130	45.6	29.5	24.9
	2SD	0.025	0.008	0.050	7.5	1.0	8.3

Above this concentration, there is a gradual shift of Ni from protein fraction to metal-rich granules fraction with increasing Ni availability, potentially showing increased storage or removal of Ni into unexchangeable Ni fractions away from cellular processes. The high $\Delta^{60}Ni_{cell\text{-}medium}$ signals are shown in different cellular components. One explanation for the preferential cellular binding of heavy Ni isotopes is that, since Ni chelation is generally strong, biological uptake exerts an equilibrium fractionation via the competitive strength of the binding protein compared to the weaker ligand binding with EDTA in the media (Walke et al., 2022). This leads to heavy Ni isotopes notably at the cellular surface (CD fraction) with $\Delta^{60}Ni_{CD\text{-}medium}$ = 4.97 ± 0.21‰ (n=3), then the transmembrane transport processes may exert a kinetic fractionation with a preferential uptake of light Ni isotopes into the cytosol (P fraction) with $\Delta^{60}Ni_{P\text{-}medium}$ = 4.37 ± 0.22 (n=3) for enzymatic and metabolic activities and/or further to periplasm (MRG fraction) for storage with $\Delta^{60}Ni_{MRG\text{-}medium}$ = 3.76 ± 0.40‰ (n=3). The enrichment of heavy Ni isotopes in all subcellular fractions rules out the possibility that the fractionations are caused by either scavenging or mineral precipitation onto the cell walls. Cleaning protocols were also applied during the harvest to minimize any non-biological components (see section 2.2.4). Furthermore, Ni isotopic fractionations ($\Delta^{60}Ni_{solid\text{-}liquid}$) during Ni adsorption onto different minerals are all found to preferentially enrich isotopically light Ni in the solid phase, e.g., -0.23∼-0.77‰ for Fe oxyhydroxide (Gueguen et al., 2018; Wasylenki et al., 2015), -0.52 ± 0.16‰ for carbonate (Castillo Alvarez et al., 2020), -0.11 ± 0.19‰ for smectite (Spivak-Birndorf et al., 2018), -2.76∼-3.35‰ for birnessite (Sorensen et al., 2020).

2.3.5 Evaluation of relative binding strengths in three phytoplankton species by amino acid compositions

Transmembrane transport processes may underpin the isotope fractionation into phytoplankton. As proposed above, the different magnitudes of Ni isotope fractionation between phytoplankton species may be related to contrasting binding strengths or affinity of their transporters to Ni. Such a proposal may be tested by considering a proxy for Ni-binding affinity of the transporters to be the proportion of cysteine- (sulfur-binding) and histidine-containing (nitrogen-binding) amino acids. As N-binding for Ni is stronger than S-binding (Albarède, 2015), phytoplankton which have a higher proportion of histidine in their transporters may have a higher binding strength to Ni.

As different magnitudes of Ni isotope fractionation between phytoplankton species may be related to their contrasting binding strengths or affinity of transporters, a proposed proxy for the Ni-binding affinity of the transporters was tested by comparing the proportion of cysteine- (sulfur-binding) and histidine-containing (nitrogen-binding) amino acids in different phytoplankton species (Zhang et al., 2022). Protein sequences of high-affinity Ni transporter families from the phytoplankton groups in this study were extracted from UniProt (www.uniprot.org), the universal protein knowledgebase (The UniProt Consortium, 2021). The compositions of amino acids were then determined by counting the elements forming each amino acid in the sequences. Histidine and cysteine were chosen to compare as the imidazole group of His side chains is the most common amino acid ligand of Ni, whereas the sulfur atoms of cysteine or methionine and the carboxylate groups of glutamic acid and aspartic acid take the residues (Sigel et al., 2007).

The accession numbers of the extracted protein sequences were A0A1Q9EGA0 for dinoflagellate *Symbiodinium microadriaticum*; K0RKT7, K0SMA1 and K0TLK4 for diatom *Thalassiosira oceanica*; Q7U5R9 and Q7V8K6 for cyanobacteria *Synechococcus sp.* and *Prochlorococcus marinus*, respectively. As there was no characterized protein sequence in the database for dinoflagellate *P. minimum* and diatom *T. weissfloggi*, sequences of similar phytoplankton group were applied.

A comparison of the abundance of histidine (nitrogen-binding) and cysteine (sulfur-binding) present in high-affinity Ni transporters (see section 2.2.6) indeed suggests that transporters with higher affinity, as found in the cyanobacteria compared to both dinoflagellates and diatoms, could explain the larger isotopic fractionation observed in cyanobacteria (Figure 2.9 and Table 2.5).

Table 2.5. Protein sequences for representative diatom, cyanobacteria and dinoflagellate extracted from UniProt, with normalized cysteine and histidine abundance (total =1)

Type	Species	Accession number	Total amino acid	Cysteine	Histidine	His/Cys
Diatom	*Thalassiosira oceanica*	K0RKT7	165	0.0424	0.0242	0.6
Diatom	*Thalassiosira oceanica*	K0SMA1	439	0.0205	0.0296	1.4
Diatom	*Thalassiosira oceanica*	K0TLK4	338	0.0207	0.0325	1.6
Avg.				0.0279	0.0288	
SD				0.0126	0.0042	
Cyanobacteria	*Synechococcus sp.* (WH 8102)	Q7U5R9	249	0.0040	0.0763	19.1
Cyanobacteria	*Prochlorococcus marinus* (MIT 9313)	Q7V8K6	254	0.0039	0.0787	20.2
Avg.				0.0040	0.0775	
SD				0.0001	0.0017	
Dinoflagellate	*Symbiodinium microadriaticum*	A0A1Q9EGA0	1021	0.0266	0.0285	1.1

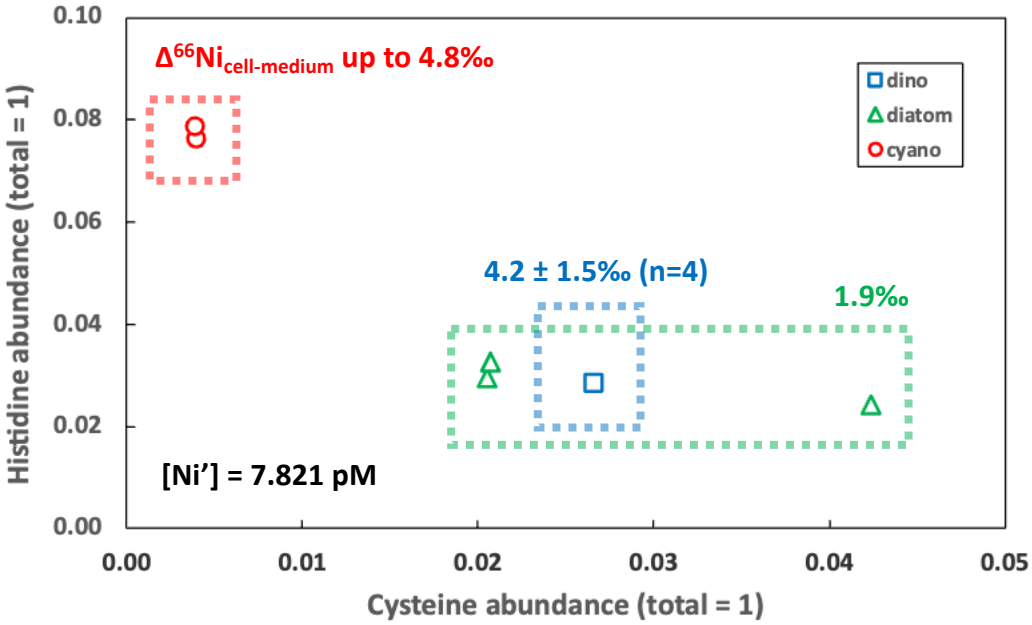


Figure 2.9. Abundance of amino acids cysteine (sulfur-binding) and histidine (nitrogen-binding) within high-affinity Ni transporters in representative dinoflagellate, diatom and cyanobacteria species. Abundance of histidine and cysteine in representative species. The dotted squares denote the patterns of each phytoplankton, with $\Delta^{60}Ni_{cell\text{-}medium}$ observed at high Ni availability.

Enrichment of heavy isotopes during biological isotopic fractionation has also been reported for Cu and Zn, in agreement with the observation that these three metals have the higher complex stabilities of the first-row transition metals (Balter et al., 2013; Irving and Williams, 1953; Köbberich and Vance, 2019). Similar enrichment of heavy isotopes in stronger bonds has been reported in the application of Cu isotopes in animals (Balter et al., 2013). Eleven out of twelve cultured phytoplankton (diatoms and cyanobacteria) enrich isotopically light Zn during their growth (Köbberich and Vance, 2019), in agreement with the activity of many isotope systems of biologically active elements (e.g., C, N, Si) (Cardinal et al., 2007; Fogel and Cifuentes, 1993; Sutton et al., 2013). But one cyanobacteria strain was enriched in the heavy isotopes of Zn (Köbberich and Vance, 2019). On the timescales of biological uptake and use, it allows the strength of element binding versus the transport rate to dictate whether isotopes are fractionated kinetically

or at equilibrium. The interaction between these metal acquisition systems and the ambient reservoirs may be a more appropriate conceptual model for understanding biological isotopic fractionation.

2.3.6 Implications on global Ni biogeochemistry

Our results reveal that phytoplankton preferentially take up heavy isotopes of Ni from the media during their growth. The direction of this fractionation is not intuitively consistent with the heavy Ni isotope compositions in parts of the surface ocean in Atlantic (Archer et al., 2020; Lemaitre et al., 2022) and Pacific (Takano et al., 2017; Yang et al., 2020, 2021), which suggest removal of isotopically light Ni from the photic zone.

Here we propose a new conceptual framework in which the isotope fractionation of Ni-ligand binding and of biological acquisition compete with one another to control the Ni isotope composition of cells. This framework reconciles isotopic observations from our culture experiments with those in surface seawaters (Archer et al., 2020; Cameron and Vance, 2014; Lemaitre et al., 2022; Takano et al., 2020, 2017; Wang et al., 2019; Yang et al., 2020, 2021). Biological uptake must be considered relative to the bioavailable Ni (i.e., that not ligand-bound with binding stronger than the cells). As ligand binding strength increases, the concentration of bioavailable Ni decreases and, because ligand binding favours heavy isotopes, this bioavailable Ni becomes isotopically lighter (Figure 2.10). In our culture experiments, the EDTA-Ni binding is relatively weak, the bioavailable Ni pool therefore not fractionated to particularly low δ^{60}Ni values, and the stronger binding by the cells causing a biological fractionation towards high δ^{60}Ni results in cells with a δ^{60}Ni above that of the medium. In the oceans, ligand binding to Ni may be stronger, leaving the bioavailable Ni pool fractionated to lower δ^{60}Ni, and results in phytoplankton cells with

a δ^{60}Ni still lower than the seawater (Figure 2.10). This conceptual framework provides a consistent explanation for the net positive cellular δ^{60}Ni in our cultures and the net negative cellular δ^{60}Ni in modern ocean. It is consistent with binding strengths of EDTA < phytoplankton < strong ligands in the ocean, relative to Ni. The hypothesis that biological metal acquisition is stronger than Ni binding to EDTA is supported by the increasing stability constants (K) of Ni-EDTA (Log K = 9.64 for Ni'; Sunda et al., 2005), cysteine (Log K = 2.16–33.44; Lihl et al., 2020) and histidine (Log K = 8–120; Valenti et al., 2006).

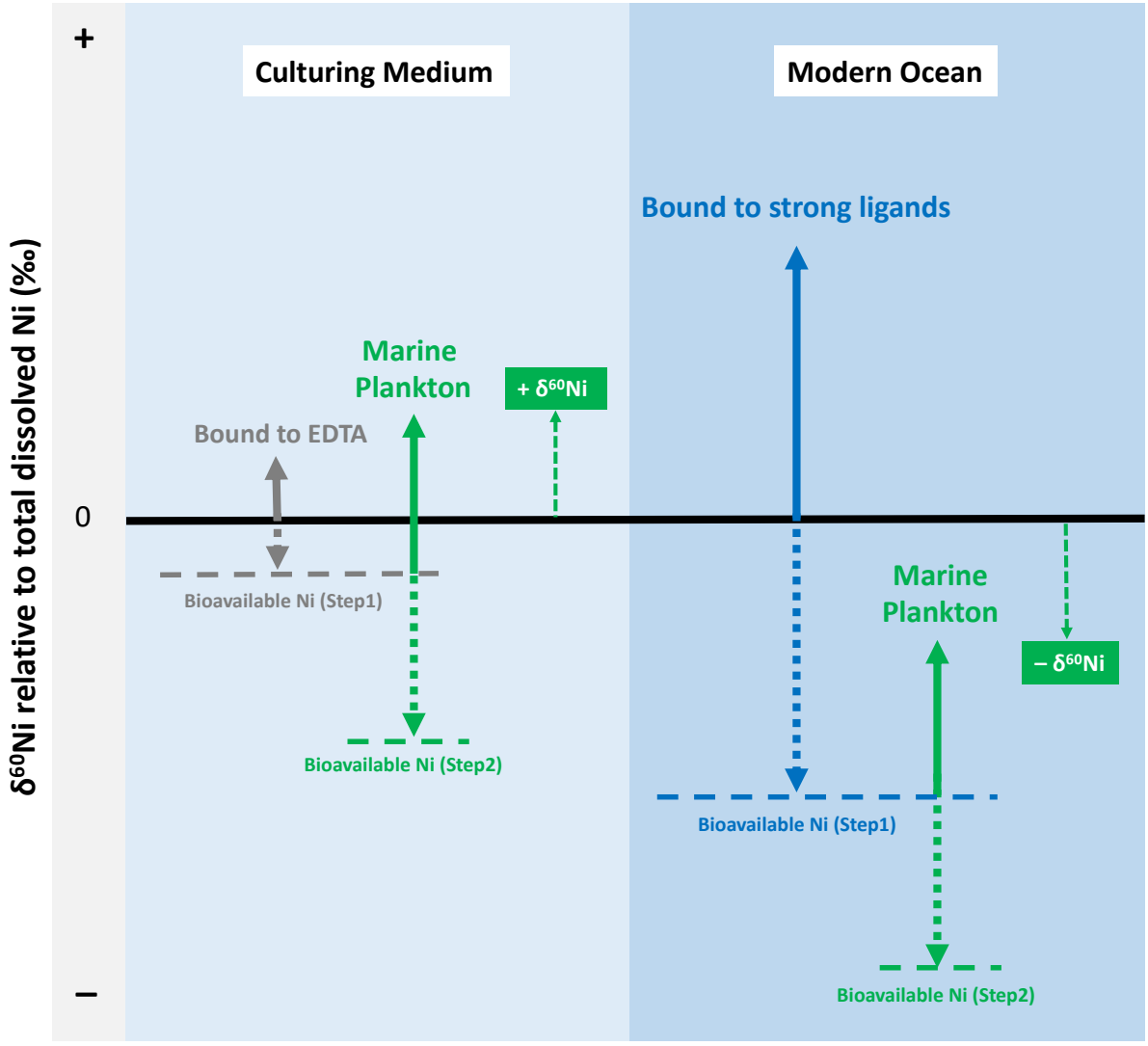


Figure 2.10. Conceptual model of mechanisms causing Ni isotope fractionation in the culturing medium and the modern ocean, and demonstrating how the relative

binding strength of phytoplankton uptake system versus ligands controls the direction of isotope fractionations. Colors of arrow represent different processes fractionating Ni isotopes, i.e., phytoplankton uptake (green), Ni binding to EDTA (grey) and Ni binding to strong ligands in the ocean (blue). Solid lines denote the directions of isotopic fractionation into ligands or cells, whereas the dotted lines denote for the residual bioavailable pool. Steps are hypothetically noted to emphasize the net isotopic fractionations in phytoplankton cells, as the steps may alternatively and repeatedly occur. In both culturing media and modern ocean, the isotope fractionations during phytoplankton uptake and Ni-EDTA binding compete with each other. With the assumed binding strengths of EDTA < phytoplankton < strong oceanic ligands and the prerequisite that biological uptake exerts from the bioavailable Ni pool, it results a net-positive cellular δ^{60}Ni compared to ambient medium in cultures and a net-negative cellular δ^{60}Ni compared to ambient seawater in modern ocean. These net biological fractionations leave the ambient medium towards low δ^{60}Ni in culturing, but leave the ambient seawater towards high δ^{60}Ni in the modern ocean. The removal of isotopically light Ni in the surface ocean has been supported by that the δ^{60}Ni of biogenic sinking particles are 0.3-0.7‰ lighter than dissolved seawater in northern South China Sea (Takano et al., 2020) and the particulates δ^{60}Ni are generally ~0.5‰ lighter than dissolved pool in Eastern Tropical North Pacific (Yang et al., 2021).

This conceptual framework depends on the concept that the δ^{60}Ni of total dissolved seawater combines the signals of ligand-bound Ni (non-bioavailable) and free Ni (bioavailable) (Figure 2.11b). This builds on previous understanding, including Ni mass balance calculation indicating a low [Ni], high δ^{60}Ni (1.7‰) non-bioavailable Ni pool and a low δ^{60}Ni (1.2‰) bioavailable Ni pool (Archer et al., 2020). When the bioavailable Ni is quantitatively taken up by phytoplankton, the remaining signal reflects the isotopically heavy Ni bound to the strongest ligands. Where there is a small amount of Ni being utilized, or the Ni is largely bioavailable and therefore unfractionated compared to the ligand pool, the δ^{60}Ni of surface ocean remains similar to the deep ocean. In contrast, in regions where surface seawaters have low [Ni] and high δ^{60}Ni, this reflects the high Ni demand by the local phytoplankton community as well as the competition between biological uptake and oceanic ligands (Figure 2.11).

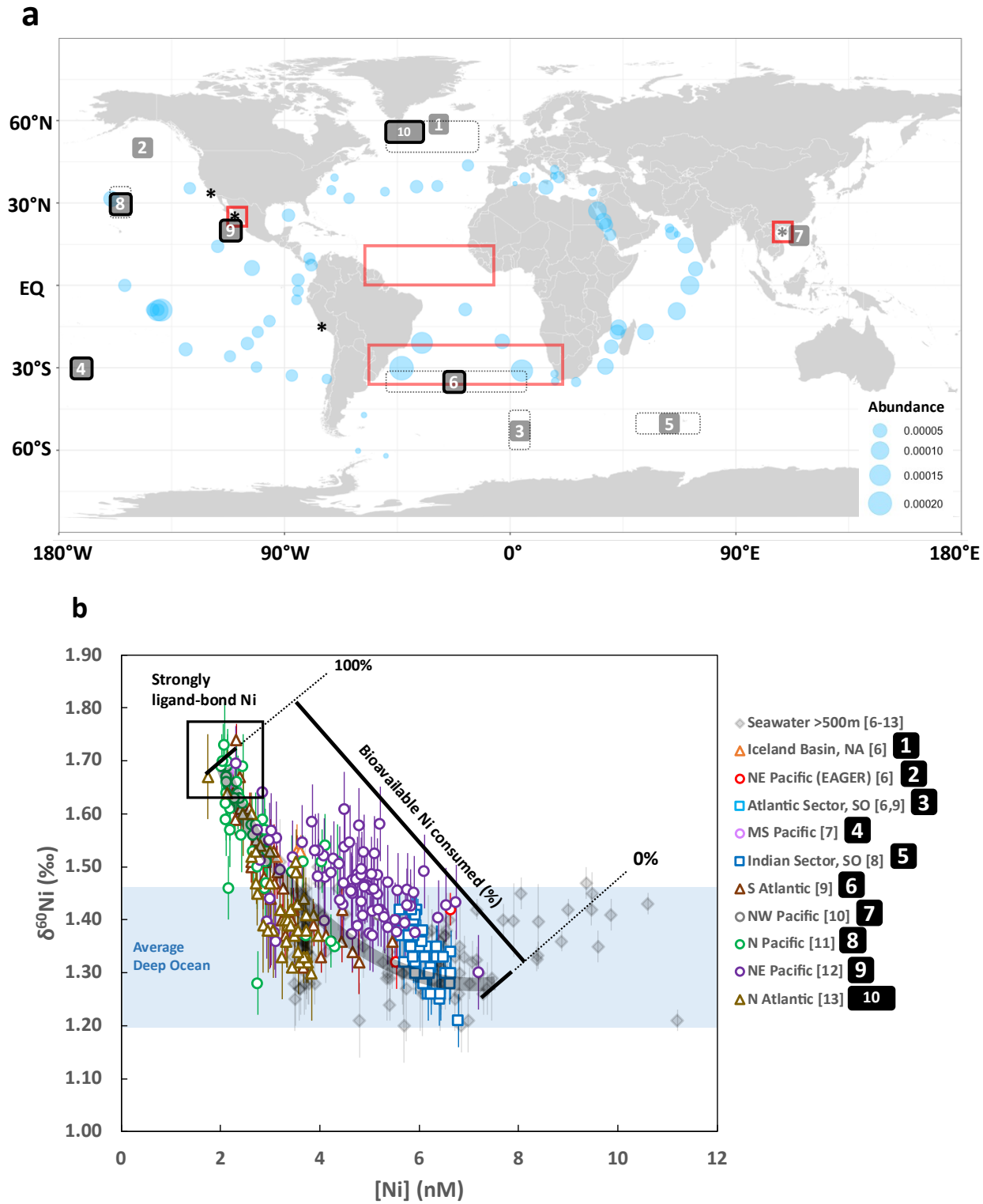


Figure 2.11. Global perspectives of Ni and its isotopes in seawater. a, Locations of currently available seawater δ^{60}Ni data. Numbers correspond to the sampling sites of studies in Figure 2.11b. Numbers with black bold outline represent regions with low [Ni] and high δ^{60}Ni. Back dotted lines represent the covered area in that study. Asterisks represent the Ni addition experiments done with seawater collected in situ in Gulf of California, Peru upwelling region (black asterisks)(Dupont et al., 2010) and north South China Sea (grey asterisk) (Ho, 2013). The red squares represent the region reported as

Ni limiting region (Dupont et al., 2010; Ho, 2013; Li et al., 2022). Blue circles denote the biogeography of high-affinity Ni transporters for cyanobacteria (see Methods), with sizes of circles represent the normalized abundance. b, Compilation of global seawater δ^{60}Ni data (Archer et al., 2020; Cameron and Vance, 2014; Lemaitre et al., 2022; Takano et al., 2020, 2017; Wang et al., 2019; Yang et al., 2020, 2021) with applied ligand-fractionating model proposed in this study. Seawaters collected >500m are denoted as grey diamonds. Seawater samples collected from Atlantic Ocean, Pacific Ocean and Southern Ocean are denoted as triangles, circles and squares, respectively. The blue shade represents the global deep ocean δ^{60}Ni value (1.33 ± 0.13‰) (Lemaitre et al., 2022). Relatively Ni-depleted regions (up-left) are the regions where the bioavailable Ni pool fractionated by strong ligands is utilized quantitatively, whereas the rest data points fall between the isotope signals of strongly ligand-bond Ni pool and average deep ocean. The controlling mechanisms of deep ocean seawaters are a combination of ocean circulation and Ni remineralization at depth.

The community of ligands with different structures and binding strengths may vary regionally and influence the δ^{60}Ni and availability of bioavailable Ni pool. It has been reported in Cu isotope system that the phytoplankton community is the major source and control of Cu-binding organic ligands (Croot et al., 2000; Leal et al., 1999; Moffett et al., 1990; Moffett and Brand, 1996; Pistocchi et al., 1997; Semeniuk et al., 2016; Vasconcelos et al., 2002). A similar mechanism may also apply to the Ni isotope system such that the geographical distribution of phytoplankton communities may influence the composition of ligands and Ni bioavailability. Nickel has been suggested to form strong complexes with ligands in the ocean and could be a limiting nutrient (Mackey et al., 2002; van den Berg and Nimmo, 1987). As the $3d^8$ electronic configuration of Ni^{2+} favours square planar coordination, any Ni-containing compound with this coordination (such as the Ni-tetrapyrrole complexes found in sediments and petroleum deposits) can be extremely stable (Mackey et al., 2002). One of the major Ni binding ligands in the eastern South Pacific Ocean was characterized to be $[C_{20}H_{21}N_4O_8S_2+M]^+$ (M=metal isotopes) which accounts for 5-8% of dissolved Ni and includes main fragments as $[C_{11}H_7N_2O_6+M]^+$ and $[C_9H_{13}N_2O_2S_2]^+$ (Boiteau et al., 2016). The nitrogen atoms in the first fragment serve as the electron donor of many strong Ni and Cu chelators like cyclic peptides and porphyrins

(Boiteau et al., 2016). That study proposed that nitrogen is a key metal binding moiety in terms of Ni-binding ligands, in agreement with our proposal that the binding strengths of bonds based on histidine content control the ability to retain Ni and further influence the availability and isotope fractionations.

Our experimental results and proposed conceptual understanding suggest that high δ^{60}Ni observed in the surface oceans may be a robust indication of Ni limitation (Figure 2.11). The isotopic fractionation recorded in phytoplankton δ^{60}Ni switches from a net-positive δ^{60}Ni effect in cultures to a net-negative δ^{60}Ni effect in the modern ocean, compared to total dissolved Ni, evidencing that phytoplankton encounter stronger competition for Ni in the surface seawaters by oceanic ligands. This strong binding by oceanic ligands may further inhibit the efficacy of cellular metal acquisition system and limit phytoplankton growth. During biological uptake, the phytoplankton take up isotopically heavy Ni relative to the bioavailable Ni pool (free Ni and ligand-bound Ni with relatively weak binding that phytoplankton can outcompete). Nonetheless, this biological utilization removes Ni which is isotopically lighter than the strongest bound ligand pool. As the Ni bioavailability decreases, the δ^{60}Ni of seawater increasingly reflects this strongest bound and isotopically heaviest Ni in seawater. The characterized seawater with low but not completely depleted Ni concentration (~2 nM) and high Ni δ^{60}Ni (~1.7‰) reflect the composition of the "winners" in the competition between biological uptake and ligand binding: remaining Ni-binding ligands with Ni-affinity stronger than the phytoplankton, which also limits their Ni acquisition.

This potential Ni-limitation is supported by field and laboratory data in various ocean settings (Dupont et al., 2010; Ho, 2013; Li et al., 2022). Nickel addition experiments in

seawater collected in situ showed that Ni can be limiting in at least three previous studies: the Gulf of California in terms of urease used by cyanobacteria and picoeukaryotes growing on urea (Dupont et al., 2010); the northern South China Sea in terms of Ni-SOD used by cyanobacteria (Ho, 2013); and the tropical Atlantic in terms of NiFe hydrogenase (HupL) used by diazotrophic and oxygenic cyanobacteria (Li et al., 2022). Culturing experiments also suggested that urea-grown diatoms can be limited by Ni but this limitation has not been reported in the real ocean (Egleston and Morel, 2008; Price and Morel, 1991). Among these reported regions of Ni-limitation, the Gulf of California and South Atlantic (20-40°S) display low Ni content and high δ^{60}Ni in the surface, implying that the bioavailable Ni pool may be considerably or quantitatively consumed by plankton in those areas (Figure 2.11a).

To acquire the global distribution of high-affinity Ni transporter families, related proteins from cyanobacteria *Prochlorococcus marinus* (accession number: Q7V8K6) was input to Ocean Gene Atlas (Vernette et al., 2022), as the regions reported to be Ni-limiting are all dominated by cyanobacteria (Dupont et al., 2010; Ho, 2013; Li et al., 2022) and there was no characterized protein sequence for *Synechococcus sp.* available. This biogeography of high-affinity Ni transporter families for cyanobacteria *P. marinus* was queried from database OM-RGC_v1 (Sunagawa et al., 2015). The abundance of high-affinity Ni transporter families was scaled as varying sizes of circles. The global distribution of high-affinity Ni transporter families in cyanobacteria represents the regions where cyanobacteria may face the shortage of Ni, which may induce those high-affinity Ni transporters expressed.

The global seawater data suggest that Ni in the mid-latitude Pacific Ocean (Takano et al.,

2017; Yang et al., 2020, 2021) and Atlantic Ocean (Archer et al., 2020; Lemaitre et al., 2022) have a tendency to be limiting for phytoplankton in the surface, and those regions are in line with the global biogeography of high-affinity Ni transporters expressed in cyanobacteria in the oceans (Vernette et al., 2022) (see section 2.2 and Figure 2.11a). High-affinity Ni transporters are developed to increase Ni uptake efficiency to cope with the potential shortage of Ni, that the phytoplankton community may face regionally. These proposed Ni-limiting regions with low [Ni] and high δ^{60}Ni are mostly dominated by cyanobacteria, in accordance with its high Ni requirement (Dupont et al., 2010; Ho, 2013; Li et al., 2022), and agrees with the global distribution of blooms for nitrogen-fixing cyanobacteria *Trichodesmium* (Westberry and Siegel, 2006).

These potential Ni-limiting areas are also global upwelling regions, where the residual Ni at the surface has been alternatively explained by the lower depletion rate of Ni relative to other macronutrients (e.g., silicate, phosphate) and suggested to be biologically labile (John et al., 2022). Our conceptual framework provides a mechanism leading to this slow/incomplete depletion of Ni but with an argument that part of the dissolved Ni can be non-bioavailable due to the competition with strong oceanic ligands. This concept is supported by the observation that higher ligand concentrations nearshore at the tropical eastern Pacific lead to higher total dissolved Ni concentrations and higher proportions of ligand-bound Ni (Boiteau et al., 2016), which suggests that more ligands may retain more dissolved Ni away from biological uptake, similarly for Cu in the ocean (Boiteau et al., 2016).

2.4 Conclusions

Our findings from phytoplankton culturing experiments indicate the dependence of the direction of Ni isotope fractionation on the relative binding strength between biological acquisition system and ligands. This provides a new framework with which to consider biogeochemical processes in the ocean and associated isotope fractionation. This framework suggests that surface waters characterized by low concentration but isotopically heavy Ni are indicative of Ni-limitation in the mid-latitude Atlantic and Pacific; an observation supported by in situ incubation experiments and the biogeography of Ni-limiting biomarkers/genes (Archer et al., 2020; Dupont et al., 2010; Ho, 2013; Lemaitre et al., 2022; Li et al., 2022; Takano et al., 2017; Vernette et al., 2022; Westberry and Siegel, 2006; Yang et al., 2020, 2021). From a global biogeochemical perspective, Ni may have been overlooked as a ubiquitous micronutrient in the ocean because its concentration is never fully depleted. With strong Ni-binding ligands fractionating the bioavailable Ni pool and limiting Ni availability, Ni should be considered an important factor influencing ocean productivity and carbon cycling.

2.5 References

Aharchaou, I., Rosabal, M., Liu, F., Battaglia, E., Vignati, D.A.L., Fortin, C., 2017. Bioaccumulation and subcellular partitioning of Cr(III) and Cr(VI) in the freshwater green alga Chlamydomonas reinhardtii. Aquat. Toxicol. 182, 49–57. https://doi.org/10.1016/j.aquatox.2016.11.004

Albarède, F., 2015. Metal Stable Isotopes in the Human Body: A Tribute of Geochemistry to Medicine, Elements Magazine.

Anderson, D., Morel, F., 1978. Copper sensitivity of Gonyaulax tamarensis. Limnol. Oceanogr. 23, 283–295.

Anderson, M.A., Morel, F.M.M., 1982. The influence of aqueous iron chemistry on the uptake of iron by the coastal diatom Thalassiosira weissflogii. Limnol. Oceanogr. 27, 789–813. https://doi.org/10.4319/lo.1982.27.5.0789

Anderson, M.A., Morel, F.M.M., Guillard, R.R.L., 1978. Growth limitation of a coastal diatom by low zinc ion activity [14]. Nature 276, 70–71. https://doi.org/10.1038/276070a0

Archer, C., Vance, D., Milne, A., Lohan, M.C., 2020. The oceanic biogeochemistry of nickel and its isotopes : New data from the South Atlantic and the Southern Ocean biogeochemical divide. Earth Planet. Sci. Lett. 535, 116118. https://doi.org/10.1016/j.epsl.2020.116118

Balter, V., Lamboux, A., Zazzo, A., Télouk, P., Leverrier, Y., Marvel, J., Moloney, A.P., Monahan, F.J., Schmidt, O., Albarède, F., 2013. Contrasting Cu, Fe, and Zn isotopic patterns in organs and body fluids of mice and sheep, with emphasis on cellular fractionation. Metallomics 5, 1470–1482. https://doi.org/10.1039/c3mt00151b

Bates, S.S., Tessier, A., Campbell, P.G.C., Buffle, J., 1982. ZINC ADSORPTION AND TRANSPORT BY CHLAMYDOMONAS VARUIABILIS AND SCENEDESMUS SUBSPICATUS (CHLOROPHYCEAE) GROWN IN SEMICONTINUOUS CULTURE. J. Phycol. 18, 521–529.

Boiteau, R.M., Till, C.P., Ruacho, A., Bundy, R.M., Hawco, N.J., McKenna, A.M., Barbeau, K.A., Bruland, K.W., Saito, M.A., Repeta, D.J., 2016. Structural characterization of natural nickel and copper binding ligands along the US GEOTRACES eastern Pacific zonal transect. Front. Mar. Sci. 3, 1–16. https://doi.org/10.3389/fmars.2016.00243

Bruland, K.W., 1980. Oceanographic distributions of cadmium, zinc, nickel, and copper in the North Pacific. Earth Planet. Sci. Lett. 47, 176–198. https://doi.org/10.1016/0012-821X(80)90035-7

Cameron, V., Vance, D., 2014. Heavy nickel isotope compositions in rivers and the oceans. Geochim. Cosmochim. Acta 128, 195–211. https://doi.org/10.1016/j.gca.2013.12.007

Cameron, V., Vance, D., Archer, C., House, C.H., 2009. A biomarker based on the stable

isotopes of nickel. Proc. Natl. Acad. Sci. 106, 10944–10948. https://doi.org/10.1073/pnas.0900726106

Cardinal, D., Savoye, N., Trull, T.W., Dehairs, F., Kopczynska, E.E., Fripiat, F., Tison, J.L., André, L., 2007. Silicon isotopes in spring Southern Ocean diatoms: Large zonal changes despite homogeneity among size fractions. Mar. Chem. 106, 46–62. https://doi.org/10.1016/j.marchem.2006.04.006

Castillo Alvarez, C., Quitté, G., Schott, J., Oelkers, E.H., 2020. Experimental determination of Ni isotope fractionation during Ni adsorption from an aqueous fluid onto calcite surfaces. Geochim. Cosmochim. Acta 273, 26–36. https://doi.org/10.1016/j.gca.2020.01.010

Croot, P.L., Moffett, J.W., Brand, L.E., 2000. Production of extracellular Cu complexing ligands by eucaryotic phytoplankton in response to Cu stress. Limnol. Oceanogr. 45, 619–627. https://doi.org/10.4319/lo.2000.45.3.0619

Dupont, C.L., Buck, K.N., Palenik, B., Barbeau, K., 2010. Nickel utilization in phytoplankton assemblages from contrasting oceanic regimes. Deep. Res. Part I Oceanogr. Res. Pap. 57, 553–566. https://doi.org/10.1016/j.dsr.2009.12.014

Egleston, E.S., Morel, F.M.M., 2008. Nickel limitation and zinc toxicity in a urea-grown diatom. Limnol. Oceanogr. 53, 2462–2471. https://doi.org/10.4319/lo.2008.53.6.2462

Elliott, T., Steele, R.C.J., 2017. The Isotope Geochemistry of Ni. Rev. Mineral. Geochemistry 82, 511–542.

Fietzke, J., Frische, M., 2016. Experimental evaluation of elemental behavior during LA-ICP-MS: Influences of plasma conditions and limits of plasma robustness. J. Anal. At. Spectrom. 31, 234–244. https://doi.org/10.1039/c5ja00253b

Fogel, M.L., Cifuentes, L.A., 1993. Isotope fractionation during primary production. Org. geochemistry Princ. Appl. 73–98. https://doi.org/10.1007/978-1-4615-2890-6_3

Gall, L., Williams, H., Siebert, C., Halliday, A., 2012. Determination of mass-dependent variations in nickel isotope compositions using double spiking and MC-ICPMS. J. Anal. At. Spectrom. 27, 137–145. https://doi.org/10.1039/c1ja10209e

Gall, L., Williams, H.M., Halliday, A.N., Kerr, A.C., 2017. Nickel isotopic composition of the mantle. Geochim. Cosmochim. Acta 199, 196–209. https://doi.org/10.1016/j.gca.2016.11.016

Gramlich, J.W., Machlan, L.A., Barnes, I.L., Paulsen, P.J., 1989. Absolute isotopic abundance ratios and atomic weight of a reference sample of nickel. J. Res. Natl. Inst. Stand. Technol. 94, 347–356. https://doi.org/10.6028/jres.094.034

Gueguen, B., Sorensen, J. V., Lalonde, S. V., Peña, J., Toner, B.M., Rouxel, O., 2018. Variable Ni isotope fractionation between Fe-oxyhydroxides and implications for the use of

Ni isotopes as geochemical tracers. Chem. Geol. 481, 38–52. https://doi.org/10.1016/j.chemgeo.2018.01.023

Gustafsson, J.P., 2017. Visual MINTEQ.

Ho, T.Y., 2013. Nickel limitation of nitrogen fixation in Trichodesmium. Limnol. Oceanogr. 58, 112–120. https://doi.org/10.4319/lo.2013.58.1.0112

Ho, T.Y., Quigg, A., Finkel, Z. V., Milligan, A.J., Wyman, K., Falkowski, P.G., Morel, F.M.M., 2003. The elemental composition of some marine phytoplankton. J. Phycol. 39, 1145–1159. https://doi.org/10.1111/j.0022-3646.2003.03-090.x

Irving, B.H., Williams, R.J.P., 1953. The stability of transition-metal complexes. J. Chem. Soc.

John, S.G., Kelly, R.L., Bian, X., Fu, F., Smith, M.I., Nathan, T., Liang, H., Pasquier, B., Seelen, E.A., Holzer, M., Wasylenki, L., 2022. The biogeochemical balance of oceanic nickel cycling. Nat. Geosci. https://doi.org/10.1038/s41561-022-01045-7

Köbberich, M., Vance, D., 2019. Zn isotope fractionation during uptake into marine phytoplankton: Implications for oceanic zinc isotopes. Chem. Geol. 523, 154–161. https://doi.org/10.1016/j.chemgeo.2019.04.004

Leal, M.F.C., Vasconcelos, M.T.S.D., Van Den Berg, C.M.G., 1999. Copper-induced release of complexing ligands similar to thiols by Emiliania huxleyi in seawater cultures. Limnol. Oceanogr. 44, 1750–1762. https://doi.org/10.4319/lo.1999.44.7.1750

Lemaitre, N., Du, J., de Souza, G.F., Archer, C., Vance, D., 2022. The essential bioactive role of nickel in the oceans: Evidence from nickel isotopes. Earth Planet. Sci. Lett. 584, 117513. https://doi.org/10.1016/j.epsl.2022.117513

Li, H.T., Tuo, S. how, Lu, M.C., Ho, T.Y., 2022. The effects of Ni availability on H2 production and N2 fixation in a model unicellular diazotroph: The expression of hydrogenase and nitrogenase. Limnol. Oceanogr. 1–11. https://doi.org/10.1002/lno.12151

Lihi, N., Kelemen, D., May, N. V., Fábián, I., 2020. The Role of the Cysteine Fragments of the Nickel Binding Loop in the Activity of the Ni(II)-Containing SOD Enzyme. Inorg. Chem. 59, 4772–4780. https://doi.org/10.1021/acs.inorgchem.0c00057

Mackey, D.J., O'Sullivan, J.E., Watson, R.J., Pont, G.D., 2002. Trace metals in the Western Pacific: Temporal and spatial variability in the concentrations of Cd, Cu, Mn and Ni. Deep. Res. Part I Oceanogr. Res. Pap. 49, 2241–2259. https://doi.org/10.1016/S0967-0637(02)00124-3

Middag, R., Baar, H.J.W. De, Bruland, K.W., 2020. The Distribution of Nickel in the West-Atlantic Ocean , Its Relationship With Phosphate and a Comparison to Cadmium and Zinc 7, 1–17. https://doi.org/10.3389/fmars.2020.00105

Moffett, J.W., Brand, L.E., 1996. Production of strong, extracellular Cu chelators by marine

cyanobacteria in response to Cu stress. Limnol. Oceanogr. 41, 388–395. https://doi.org/10.4319/lo.1996.41.3.0388

Moffett, J.W., Zika, R.G., Brand, L.E., 1990. Distribution and potential sources and sinks of copper chelators in the Sargasso Sea. Deep Sea Res. Part A, Oceanogr. Res. Pap. 37, 27–36. https://doi.org/10.1016/0198-0149(90)90027-S

Morel, F.M.M., Rueter, J.G., Anderson, D.M., Guillard, R.R.L., 1979. Aquil: a chemically definied phytoplankton culture medium for trace metal studies.pdf. J. Phycol. 15, 135–141.

Mulrooney, S.B., Hausinger, R.P., 2003. Nickel uptake and utilization by microorganisms. FEMS Microbiol. Rev. 27, 239–261. https://doi.org/10.1016/S0168-6445(03)00042-1

Nomura, M., Kudo, T., Adachi, A., Aida, M., Fujii, Y., 2013. fractionation of isotopes in Ni and Pb chelate complex formation reactions Mass-Dependent and -Independent Fractionation of Isotopes in Ni and Pb Chelate Complex Formation Reactions 2, 1–7. https://doi.org/10.1063/1.4833685

Pistocchi, R., Guerrini, F., Boni, L., Balboni, V., 1997. Copper toxicity and carbohydrate production in the microalgae cylindrotheca fusiformis and gymnodinium sp. Eur. J. Phycol. 32, 125–132. https://doi.org/10.1080/09670269710001737049

Price, N.M., Harrison, G.I., Hering, J.G., Hudson, R.J., Nirel, P.M. V., Palenik, B., Morel, F.M.M., 1989. Preparation and Chemistry of the Artificial Algal Culture Medium Aquil. Biol. Oceanogr. 6, 443–461. https://doi.org/10.1080/01965581.1988.10749544

Price, N.M., Morel, F.M.M., 1991. Colimitation of phytoplankton growth by nickel and nitrogen. Limnol. Oceanogr. 36, 1071–1077. https://doi.org/10.4319/lo.1991.36.6.1071

Ragsdale, S.W., 2009. Nickel-based enzyme systems. J. Biol. Chem. 284, 18571–18575. https://doi.org/10.1074/jbc.R900020200

Saunders, N.J., Barling, J., Harvey, J., Halliday, A.N., Saunders, N.J., Barling, J., Harvey, J., Halliday, A.N., 2020. Heterogeneous nickel isotopic compositions in the terrestrial mantle - Part 1. Geochim. Cosmochim. Acta. https://doi.org/10.1016/j.gca.2020.06.029

Sclater, F.R., Boyle, E., Edmond, J.M., 1976. On the marine geochemistry of nickel. Earth Planet. Sci. Lett. 31, 119–128. https://doi.org/10.1038/263042a0

Semeniuk, D.M., Bundy, R.M., Posacka, A.M., Robert, M., Barbeau, K.A., Maldonado, M.T., 2016. Using 67Cu to study the biogeochemical cycling of copper in the Northeast subarctic Pacific Ocean. Front. Mar. Sci. 3, 1–19. https://doi.org/10.3389/fmars.2016.00078

Siebert, C., Nägler, T.F., Kramers, J.D., 2001. Determination of molybdenum isotope

fractionation by double-spike multicollector inductively coupled plasma mass spectrometry. Geochemistry, Geophys. Geosystems 2. https://doi.org/10.1029/2000GC000124

Sigel, A., Sigel, H., Sigel, R.K.O. (Eds.), 2007. Nickel and its surprising impact in nature. Wiley.

Sorensen, V., Gueguen, B., Stewart, B.D., Peña, J., Rouxel, O., Toner, B.M., 2020. Large nickel isotope fractionation caused by surface complexation reactions with hexagonal birnessite 537. https://doi.org/10.1016/j.chemgeo.2020.119481

Spivak-Birndorf, L.J., Wang, S.J., Bish, D.L., Wasylenki, L.E., 2018. Nickel isotope fractionation during continental weathering. Chem. Geol. 476, 316–326. https://doi.org/10.1016/j.chemgeo.2017.11.028

Sunagawa, S., Coelho, L.P., Chaffron, S., Kultima, J.R., Labadie, K., Salazar, G., Djahanschiri, B., Zeller, G., Mende, D.R., Alberti, A., Cornejo-Castillo, F.M., Costea, P.I., Cruaud, C., D'Ovidio, F., Engelen, S., Ferrera, I., Gasol, J.M., Guidi, L., Hildebrand, F., Kokoszka, F., Lepoivre, C., Lima-Mendez, G., Poulain, J., Poulos, B.T., Royo-Llonch, M., Sarmento, H., Vieira-Silva, S., Dimier, C., Picheral, M., Searson, S., Kandels-Lewis, S., Boss, E., Follows, M., Karp-Boss, L., Krzic, U., Reynaud, E.G., Sardet, C., Sieracki, M., Velayoudon, D., Bowler, C., De Vargas, C., Gorsky, G., Grimsley, N., Hingamp, P., Iudicone, D., Jaillon, O., Not, F., Ogata, H., Pesant, S., Speich, S., Stemmann, L., Sullivan, M.B., Weissenbach, J., Wincker, P., Karsenti, E., Raes, J., Acinas, S.G., Bork, P., 2015. Structure and function of the global ocean microbiome. Science (80-.). 348, 1–10. https://doi.org/10.1126/science.1261359

Sunda, W., 1975. The relationship between cupric ion activity and the toxicity of copper to phytoplankton. Massachusetts Institute of Technology & Woods Hole Oceanographic Institution.

Sunda, W.G., Price, N.M., Morel, F.M.M., 2005. Trace Metal Ion Buffers and Their Use in Culture Studies. Algal Cult. Tech. 7, 35–63.

Sutton, J.N., Varela, D.E., Brzezinski, M.A., Beucher, C.P., 2013. Species-dependent silicon isotope fractionation by marine diatoms. Geochim. Cosmochim. Acta 104, 300–309. https://doi.org/10.1016/j.gca.2012.10.057

Takano, S., Liao, W., Tian, H., Huang, K., Ho, T., 2020. Sources of particulate Ni and Cu in the water column of the northern South China Sea : Evidence from elemental and isotope ratios in aerosols and sinking particles. Mar. Chem. 219, 103751. https://doi.org/10.1016/j.marchem.2020.103751

Takano, S., Tanimizu, M., Hirata, T., Shin, K.C., Fukami, Y., Suzuki, K., Sohrin, Y., 2017. A simple and rapid method for isotopic analysis of nickel, copper, and zinc in seawater using chelating extraction and anion exchange. Anal. Chim. Acta 967, 1–11. https://doi.org/10.1016/j.aca.2017.03.010

The UniProt Consortium, 2021. UniProt: the universal protein knowledgebase in 2021.

Nucleic Acids Res. 49, D480–D489. https://doi.org/10.1093/nar/gkaa1100

Valenti, L.E., De Pauli, C.P., Giacomelli, C.E., 2006. The binding of Ni(II) ions to hexahistidine as a model system of the interaction between nickel and His-tagged proteins. J. Inorg. Biochem. 100, 192–200. https://doi.org/10.1016/j.jinorgbio.2005.11.003

van den Berg, C.M.G., Nimmo, M., 1987. Determination of interactions of nickel with dissolved organic material in seawater using cathodic stripping voltammetry. Sci. Total Environ. 60, 185–195. https://doi.org/10.1016/0048-9697(87)90415-3

Vasconcelos, M.T.S.D., Leal, M.F.C., Van Den Berg, C.M.G., 2002. Influence of the nature of the exudates released by different marine algae on the growth, trace metal uptake and exudation of Emiliania huxleyi in natural seawater. Mar. Chem. 77, 187–210. https://doi.org/10.1016/S0304-4203(01)00087-1

Vernette, C., Lecubin, J., Pablo, S., Coordinators, T.O., Sunagawa, S., Delmont, T.O., Acinas, S.G., Pelletier, E., Hingamp, P., Lescot, M., 2022. The Ocean Gene Atlas v2 . 0 : online exploration of the biogeography and phylogeny of plankton genes 50, 516–526.

Walke, G., Aupič, J., Kashoua, H., Janoš, P., Meron, S., Shenberger, Y., Qasem, Z., Gevorkyan-Airapetov, L., Magistrato, A., Ruthstein, S., 2022. Dynamical interplay between the human high-affinity copper transporter hCtr1 and its cognate metal ion. Biophys. J. 121, 1194–1204. https://doi.org/10.1016/j.bpj.2022.02.033

Wang, R.M., Archer, C., Bowie, A.R., Vance, D., 2019. Zinc and nickel isotopes in seawater from the Indian Sector of the Southern Ocean: The impact of natural iron fertilization versus Southern Ocean hydrography and biogeochemistry. Chem. Geol. 511, 452–464. https://doi.org/10.1016/j.chemgeo.2018.09.010

Wasylenki, L.E., Howe, H.D., Spivak-birndorf, L.J., Bish, D.L., 2015. Ni isotope fractionation during sorption to ferrihydrite : Implications for Ni in banded iron formations. Chem. Geol. 400, 56–64. https://doi.org/10.1016/j.chemgeo.2015.02.007

Watt, R.K., Ludden, P.W., 1999. Nickel-binding proteins 56, 604–625.

Westberry, T.K., Siegel, D.A., 2006. Spatial and temporal distribution of Trichodesmium blooms in the world ' s oceans 20, 1–13. https://doi.org/10.1029/2005GB002673

Wilson, W., Zhang, Q., Rickaby, R.E.M., 2019. Susceptibility of algae to Cr toxicity reveals contrasting metal management strategies. Limnol. Oceanogr. 64, 2271–2282. https://doi.org/10.1002/lno.11183

Yang, S., Hawco, N.J., Pinedo-gonzález, P., Bian, X., Huang, K., Zhang, R., John, S.G., 2020. A new purification method for Ni and Cu stable isotopes in seawater provides evidence for widespread Ni isotope fractionation by phytoplankton in the North Pacific. Chem. Geol. 547, 119662. https://doi.org/10.1016/j.chemgeo.2020.119662

Yang, S.C., Kelly, R.L., Bian, X., Conway, T.M., Huang, K.F., Ho, T.Y., Neibauer, J.A., Keil, R.G.,

Moffett, J.W., John, S.G., 2021. Lack of redox cycling for nickel in the water column of the Eastern tropical north pacific oxygen deficient zone: Insight from dissolved and particulate nickel isotopes. Geochim. Cosmochim. Acta 309, 235–250. https://doi.org/10.1016/j.gca.2021.07.004

Yu, Y., Siebert, C., Fietzke, J., Goepfert, T., Hathorne, E., Cao, Z., Frank, M., 2020. The impact of MC-ICP-MS plasma conditions on the accuracy and precision of stable isotope measurements evaluated for barium isotopes. Chem. Geol. 549, 119697. https://doi.org/10.1016/j.chemgeo.2020.119697

Zhang, Q., Bendif, E.M., Zhou, Y., Nevado, B., Shafiee, R., Rickaby, R.E.M., 2022. Declining metal availability in the Mesozoic seawater reflected in phytoplankton succession. Nat. Geosci. 15, 932–941. https://doi.org/10.1038/s41561-022-01053-7

CHAPTER 3
Factors regulating Ni isotope fractionation in cosmopolitan phytoplankton

3 Factors regulating Ni isotope fractionation in cosmopolitan phytoplankton

3.1 Introduction

As a bioactive element, nickel (Ni) shows a nutrient-like pattern with depth in the modern ocean like many other bioactive transition metals, which is akin to phosphate and nitrate in the upper ocean and akin to silicate at depth. Nonetheless, the concentration of Ni in the surface seawaters is rarely determined to be below 2 nM (Bruland, 1980; Mackey et al., 2002; Sclater et al., 1976). Despite the incomplete consumption of Ni at the surface ocean, emerging evidence has argued that a component of dissolved Ni in the ocean is chelated to organic ligands and not biologically available (Archer et al., 2020; Boiteau et al., 2016; Dupont et al., 2010; Mackey et al., 2002; Middag et al., 2020; Wang et al., submitted). Such behavior seems plausible for an element, Ni, with the second highest complex stability among first-row transition metals (Irving and Williams, 1953). An alternative proposal is that the remaining Ni at the surface ocean may arise due to the limiting number of membrane proteins for Ni uptake per cell and the slow kinetics of Ni acquisition because of the relative inertness of the Ni^{2+} ions which have a lower water exchange rate than other divalent cations (e.g., Cu, Cd, Zn, Co, Mn, Fe) (Morel et al., 1991; Morse and Luther, 1999; Price and Morel, 1991). Furthermore, these relatively slow uptake kinetics and poor selectivity for Ni via divalent metal transport system (low-affinity Ni transport pathway) may lead to toxicity of other metals co-transported with Ni (Egleston and Morel, 2008). Thus, it has been argued that regardless of the requirement for Ni, marine phytoplankton may not be able to consume Ni to very low concentrations (Morel et al., 2014).

Nickel provides the metal centres in eight known enzymes essential for prokaryotic and eukaryotic organisms, which control global carbon, nitrogen and hydrogen cycles (Ragsdale, 2009). For instance, urease is utilized by phytoplankton to hydrolyse urea to yield ammonia, the produced urea is estimated to supply up to 50% of the fixed nitrogen required for oceanic primary production (Dupont et al., 2010; Ragsdale, 2009). Superoxide dismutase (SOD) for protecting nitrogenase from the irreversible damage by reactive oxygen species (ROS), are commonly found in marine phytoplankton in the form of various metal isoforms including Ni-SOD (Gallon, 1981). For NiFe hydrogenase, Ni serves as an essential cofactor to bind H_2 at its active site for H_2 oxidation (Volbeda et al., 1995). In culturing experiments of diatoms and cyanobacteria grown on urea as the only nitrogen source, the growth of these phytoplankton was shown to be limited by Ni availability, which pointed to a potential Ni-N co-limitation in some ocean settings (Dupont et al., 2008; Price and Morel, 1991). Nickel addition experiments carried out in seawater collected in situ has also showed that Ni can be limiting in Gulf of California in terms of urease utilized by cyanobacteria and picoeukaryotes growing on urea (Dupont et al., 2010), in northern South China Sea in terms of Ni-SOD used by cyanobacteria (Ho, 2013) and tropical Atlantic in terms of NiFe hydrogenase (HupL) used by diazotrophic and oxygenic cyanobacteria (Li et al., 2022), based on the boosted growth rate of the local phytoplankton after Ni addition with the presence of >2 nM Ni in the starting seawater.

Nickel isotopes have been applied to provide a new dimension of perspectives in understanding the oceanic Ni biogeochemical cycling and Ni bioavailability on phytoplankton growth. Nickel isotope data (δ^{60}Ni) in seawater have been reported to be globally homogeneous (δ^{60}Ni = 1.33 ± 0.13‰) in the deep ocean, showing regionally-

variable isotopic fractionations toward high δ^{60}Ni in the mid-latitude surface ocean and invariant depth profiles in the Southern Ocean (Archer et al., 2020; Cameron and Vance, 2014; Lemaitre et al., 2022; Takano et al., 2020; Wang et al., 2019; Yang et al., 2020, 2021). The enrichments of isotopically heavy Ni in the surface ocean are explained by the biological uptake which preferentially take up light isotopes of Ni (Archer et al., 2020; Lemaitre et al., 2022; Takano et al., 2017; Yang et al., 2020, 2021). Based on isotope data in seawater, it has been proposed that locally dominant phytoplankton species may control the isotopic variations observed at the surface ocean, but the physiological mechanisms remain unclear (Archer et al., 2020; Lemaitre et al., 2022).

In contrast to the above, culture experiments reported that dinoflagellate, cyanobacteria and diatom all preferentially take up isotopically heavy Ni from the media, following Rayleigh distillation isotope fractionation under varying Ni availability, with species-dependent fractionation factors (see Chapter 2). This study prompts the consideration of relative binding strengths between phytoplanktonic acquisition system and ligands in both culturing media and the modern ocean, in terms of the directions of isotope fractionation observed in phytoplankton cells and ligands (see Chapter 2). The difference between species were explained by the proportion of Ni-binding site at histidine (nitrogen-binding amino acid) and cysteine (sulfur-binding amino acid) in their high-affinity Ni transporters, given that the chelation by nitrogen is stronger than that of sulfur and may preferentially bind more heavy Ni isotopes because of the higher binding strength (Albarède, 2015). However, the similar proportion of histidine and cysteine could not fully justify the isotopic differences between dinoflagellates and diatoms (see Chapter 2).

As another cosmopolitan phytoplankton species in the global ocean, coccolithophores contribute significantly to the long-term sequestration of CO_2, which contribute up to 10% of the global carbon fixation (Bottini et al., 2020; Poulton et al., 2007). The coccolithophore *Emiliania huxleyi* has been observed to increasingly expand its range to polar oceans, likely due to changing ocean carbonate chemistry caused by the increasing level of CO_2 in the atmosphere, the subsequent acidification in the ocean, increasing surface temperature and salinity (Winter et al., 2014). Investigating the Ni isotopic signals during Ni uptake in coccolithophores and whether the signals reconcile with global seawater data where the regions are dominated by them, will significantly contribute to the understanding of the controlling factors for the regionally variable isotope signals in the surface ocean and further applications in oceanic biogeochemistry.

Here we culture coccolithophores and measure their metal quotas and cellular Ni isotope compositions. We present the first Ni isotope data in cultured coccolithophores, placing the isotope data and metal quotas in the context of other cosmopolitan phytoplankton species dinoflagellate, cyanobacteria and diatom previously reported to understand their characteristic physiological responses and the potential controlling factors.

3.2 Materials and methods

3.2.1 Phytoplankton strains

Four cosmopolitan phytoplankton species were selected in this study to compare the factors controlling the biological Ni isotope fractionations. The growth rate, Ni/P ratio and Ni isotope composition data of dinoflagellate *Prorocentrum minimum* (RCC291), diatom *Thalassiosira weissflogii* (RCC76) and cyanobacteria *Synechococcus sp.* (PCC8806)

were previously reported in Chapter 2. The coccolithophore *Emiliania huxleyi* (RCC911) was chosen to broaden the comparison among cosmopolitan species, which originates from Marquesas Islands, Pacific Ocean. The strains selected here for dinoflagellate, diatom and coccolithophore were obtained from the Roscoff Culture Collection (RCC) which is run by Sorbonne University and French National Centre for Scientific Research at France. While the strain for cyanobacteria was obtained from Pasteur Culture Collection of Cyanobacteria (PCC).

3.2.2 Reagents and laboratory equipment

All ultrapure deionized water (H_2O) used in this study was 18.2MΩ-grade from a Merck Milli-Q® lab water purification system. For cell digestion, sub-boiled nitric acid (HNO_3, in-house sub-boiling distillation system) and ultrapure hydrogen peroxide (H_2O_2, Merck suprapur®) were used. For Ni ion exchange chromatography, sub-boiled HCl and HNO_3 (in-house), solution of dimethyglyoxime (DMG) and ammonium citrate ($(NH_4)_2C_6H_6O_7$) prepared from commercial crystalline powders, reagent grade acetone ($(CH_3)_2CO$), commercial Merck suprapur® reagents ammonia solution (NH_4OH, 25%) and hydrogen peroxide (H_2O_2) were applied.

All handling of cultures and media before digestion was carried out in laminar flow hoods with sterile techniques in the OceanBug Laboratory at the Department of Earth Sciences, University of Oxford. After collection of cells, the subsequent sample preparation and chemistry were carried out in a Class 100 laminar flow hood within metal-free clean laboratory at the Department of Earth Sciences, University of Oxford.

3.2.3 Culturing techniques

The culturing conditions were similar to methods in Chapter 2. A short summary is given below. The cultures were all grown in sterile culturing flasks with medium Aquil* (Morel et al., 1979; Price et al., 1989; Sunda et al., 2005), cultured in incubators at 20 ± 1°C with 100 **μ**mol photons $m^{-2}s^{-1}$ on a day : night cycle of 12:12 hours.

The range of total Ni concentration was set between 0~200 μgL^{-1}, which was equivalent to bioavailable Ni (dissolved inorganic Ni species, Ni') of 0.014~7.821 pM, in order to provide varying Ni availabilities for the experiments. [Ni'] constitutes ~2.3×10^{-4} % of the total Ni speciation, with the presence of ~0.1 mM ethylenediaminetetraacetic acid (EDTA) (see Chapter 2). The Ni availability was adjusted using $NiCl_2$ solution prepared by dissolving commercial $NiCl_2 \cdot 6H_2O$ powders in deionized water.

All phytoplankton cells were acclimated to the given culturing conditions for at least three generations before being inoculated into 2L sterile polycarbonate bottles for the experiment and sufficient volume for harvest and analysis. The cells were harvested (separated from media) before the end of exponential growth by centrifugation at 4700 rpm for 30 min, rinsed three times with chelex-cleaned synthetic seawater (Zhang et al., 2018).

3.2.4 Elemental and Ni isotope analysis

The collected cells were digested completely with concentrated HNO_3 and 30% H_2O_2 in a volumetric ratio of 3:2. The aliquots were then evaporated completely, dissolved in 2% HNO_3 and refluxed on a hotplate at 120°C for 12 h before elemental analysis. Two

biological standards BCR-273 (single cell) and BCR-414 (plankton) were treated equally during the sample processing for comparison.

The procedures applied for elemental and Ni isotope analysis in this study are identical to those previously described in Chapter 2, which are briefly summarized below. The elemental analysis was carried out using a PerkinElmer NexION 350D quadrupole inductively coupled plasma mass spectrometer (ICP-MS) at the department of Earth Sciences, University of Oxford. The precision and accuracy of elemental analysis were monitored with river water standard SLRS-6 from National Research Council Canada, which the RSDs were usually < 4.5% for Ni, Cu, Co, Zn and Fe. After the acquisition of Ni content, digested cells were double-spiked by a ^{61}Ni-^{62}Ni mixture with the ratio of 25:75 and kept at a sample-to-spike ratio of 0.4 (Gall et al., 2012). Samples were purified by a three-step ion exchange chromatography to separate Ni from the matrix (Gall et al., 2012). Nickel isotope compositions were determined using a Nu Plasma high resolution multi-collector inductively coupled plasma mass spectrometer (MC-ICP-MS) at the Department of Earth Sciences, University of Oxford (see Chapter 2 and Appendix A). The total procedural blanks during sample digestion and Ni purification, estimated by isotope dilution analysis, were usually less than 4.1 ng. The precision and accuracy of Ni isotope analyses were monitored daily by repeatedly measuring two in-house Fe-Ni sulfide standards (Kam, Sud) and a USGS reference material Nod-P-1 (Mn nodule). Plankton standard BCR-414 was also chemically purified and measured to verify the method applied in this study.

All Ni isotope data presented here are given in standard delta notation (δ), in per mil deviation (‰), reported relative to Ni isotope standard SRM 986 (high-purity Ni metal).

All culturing results are reported as the fractionation between the collected cells and the initial culturing medium, which are expressed as $\Delta^{60}Ni$ (‰) = $\delta^{60}Ni_{cells} - \delta^{60}Ni_{medium}$.

$$\delta^{60}Ni = \left[\frac{(^{60}Ni/^{58}Ni)_{sample}}{(^{60}Ni/^{58}Ni)_{SRM986}} - 1\right] \times 1000\ (‰)$$

The long-term reproducibility of Kam, Sud and Nod-P-1 over 30 months are -0.88 ± 0.06‰ (n=43), 0.79 ± 0.06‰ (n=43) and 0.37 ± 0.07‰ (n=36), respectively. The $\delta^{60}Ni$ values of Nod-P-1 agree with the range ($\delta^{60}Ni$ = 0.328~0.41‰) of previously published values (Gueguen et al., 2018, 2016, 2013; Ratié et al., 2015; Wu et al., 2019).The $\delta^{60}Ni$ of BCR-414 (0.12 ± 0.05‰, n=4) are also in agreement with previous studies (0.11 ± 0.06‰, Takano et al., 2020; 0.07 ± 0.06‰, Yang et al., 2021). The Ni isotopic composition of the added $NiCl_2$ solution (i.e., initial medium composition) was 0.28 ± 0.06‰ (n=5).

3.3 Results

Metal concentrations in four phytoplankton species are normalized to the concentration of phosphorus (P) in this study to represent cellular metal quotas and compare with other studies (Figure 3.1–3.2, Table 3.1–3.3). P-normalized cellular trace metals (Ni, Fe, Mn, Zn, Co and Cu) measured in this study are generally in agreement with previous culture work at comparable bioavailable metal contents (Ho et al., 2003; Twining and Baines, 2013). The Ni/P ratios increase with the increasing Ni availability in all four species. The Fe/P ratios in the cultured dinoflagellates (R^2 = 0.7155, $p < 0.001$), diatoms (R^2 = 0.5905, $p < 0.001$) and cyanobacteria (R^2 = 0.2305, $p < 0.001$) decrease concomitantly with the increasing Ni/P ratios, when the Ni availability increases (Figure 3.2 and Table 3.3). The

coccolithophores showed the opposite, i.e., increasing Fe/P ratios with increasing Ni/P ratios (R^2 = 0.9868, $p < 0.001$), when the Ni availability increases. For cyanobacteria, the Fe/P ratio decreases from 78 mmol/mol to 41mmol/mol when [Ni'] increases from 0.014 to 3.917 pM, slightly bouncing back to 57 mmol/mol when [Ni'] further increases to 7.821 pM. Decreasing Zn/P and Mn/P ratios can be observed in all species with their increasing Ni/P ratios, when [Ni'] increases (all with $p < 0.01$, Figure 3.2D, 3.2E and Table 3.3). Slight increases of Zn/P and Mn/P are seen in cyanobacteria when [Ni'] increases further from 3.917 nM to 7.821 pM. Slightly decreasing Co/P ratios with increasing [Ni'] are observed in dinoflagellate (R^2 = 0.461, $p = 0.056$) and coccolithophore (R^2 = 0.960, $p = 0.059$). The Cu/P ratios decrease with increasing Ni/P ratios in coccolithophore (R^2 = 0.886, $p < 0.05$), while they slightly increase with the increasing Ni/P ratios in cyanobacteria (R^2 = 0.5957, $p < 0.001$) (Figure 3.2C). Subtle increases of Co/P and Cu/P ratios are observed in cyanobacteria when Ni increases from 3.917 pM to 7.821 pM.

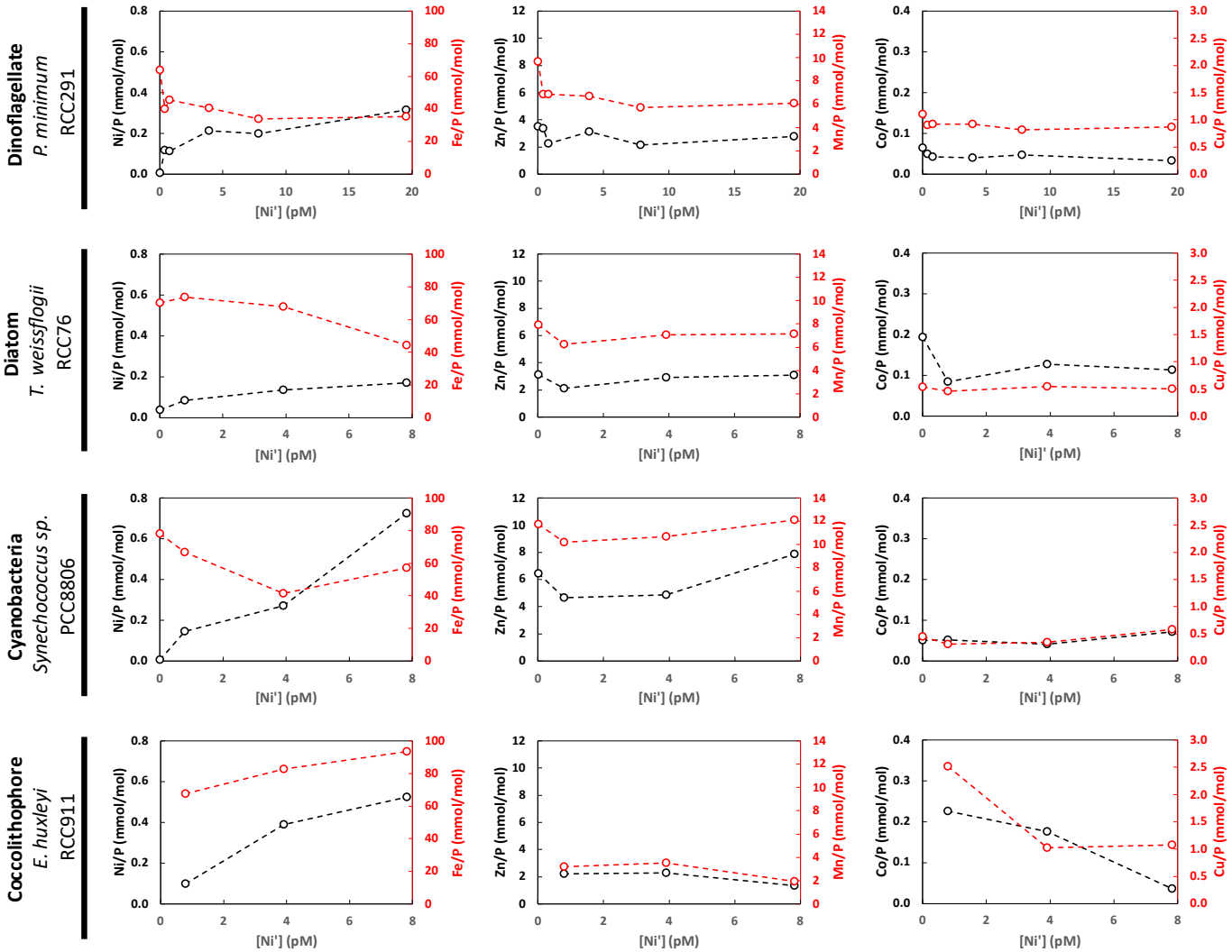


Figure 3.1 Metal quotas (Ni/P, Fe/P, Zn/P, Mn/P, Cu/P and Co/P) of four species of phytoplankton under varying Ni availability. Phytoplankton cultured in 2L flasks are compared here to keep all experimental settings consistent.

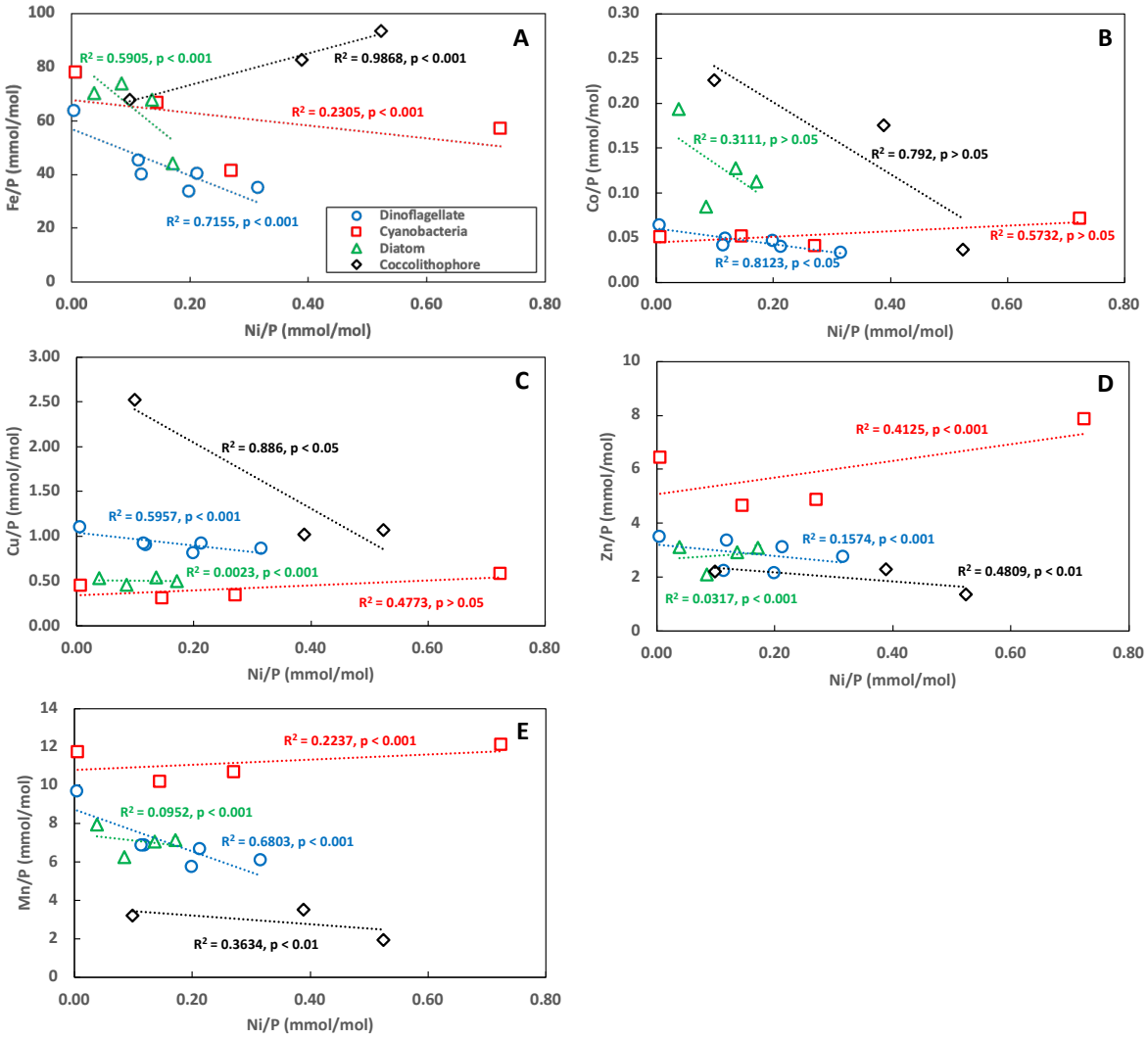


Figure 3.2. Covariations between Ni/P ratios and other metal/P ratios in four species of phytoplankton under varying Ni availability. The Ni/P ratios of four species of phytoplankton are plotted with (A) Fe/P, (B) Co/P, (C) Cu/P, (D) Zn/P and (E) Mn/P. The coefficient of determination and statistical significance of each trend are given next to the slope.

Table 3.1. Compilation of growth rate, metal quotas and $\Delta^{60}Ni_{cell\text{-}medium}$ for four cosmopolitan phytoplankton cultured under varying Ni availability. The growth rates, Ni/P ratios and Ni isotope compositions for dinoflagellate, cyanobacteria and diatom are adapted from data in Chapter 2. *The numbers represent the 2SD (standard deviation) of different independent analyses when n≥2, while numbers represent the 2SE (standard error) of 40 analytic cycles of one analysis when n=1. **The numbers are excluded for further discussion as the low Ni contents may influence the quality of isotopic analysis.

Phytoplankton	Species	Strain	[Ni'] in medium(pM)	Volume (L)	Growth rate μ (d^{-1})	Ni/P (mmol/mol)	Fe/P (mmol/mol)	Zn/P (mmol/mol)	Mn/P (mmol/mol)	Co/P(mmol/mol)	Cu/P(mmol/mol)	Δ^{60}Ni (‰)	2SD*	n
Dinoflagellate	*Prorocentrum minimum*	RCC 291	0.014	0.05	0.73	0.043	17.616	2.156	2.844	0.083	0.773	-0.35 **	0.04	2
			0.014	2.00		0.005	63.745	3.500	9.680	0.064	1.106	-2.17 **	0.12	2
			0.405	2.00		0.118	39.948	3.362	6.862	0.050	0.903	-0.05	0.01	2
			0.795	0.60	0.75	0.411	64.671	6.640	10.567	0.133	1.011	1.97	0.52	5
			0.795	0.60		0.210	42.763	3.982	6.774	0.063	0.865	0.97	0.29	5
			0.795	0.60		0.266	38.388	3.941	6.360	0.056	0.834	2.08	0.26	6
			0.795	2.00		0.114	45.411	2.241	6.854	0.042	0.924	0.46	0.09	3
			3.917	0.60		0.296	29.713	2.660	4.945	0.050	0.898	3.50	0.34	6
			3.917	2.00		0.213	40.466	3.118	6.692	0.041	0.924	3.35	0.09	3
			7.821	0.60	0.64	0.643	54.998	5.491	9.590	0.083	0.987	4.26	0.56	5
			7.821	0.60		0.293	23.454	2.148	4.001	0.047	0.804	4.51	0.15	6
			7.821	0.60		0.493	32.410	2.814	5.609	0.040	0.921	4.81	0.22	6
			7.821	2.00		0.199	33.852	2.154	5.736	0.047	0.811	3.13	0.05	2
			19.530	0.60		0.541	27.922	2.668	5.112	0.033	0.850	5.55	0.32	5
			19.530	2.00		0.315	35.221	2.768	6.080	0.033	0.865	4.98	0.03	4
Cyanobacteria	*Synechococcus sp.*	PCC 8806	0.014	2.00	0.62	0.006	78.128	6.441	11.744	0.051	0.452	-0.73 **	0.09	1
			0.795	2.00	0.47	0.145	66.780	4.659	10.181	0.051	0.312	0.58	0.10	2
			3.917	2.00		0.270	41.441	4.870	10.698	0.041	0.345	2.53	0.03	4
			7.821	2.00	0.47	0.724	57.205	7.853	12.102	0.071	0.582	4.83	0.04	4
Diatom	*Thalassiosira weissfloggi*	RCC 76	0.014	2.00	0.75	0.038	70.219	3.120	7.933	0.194	0.534	-0.41	0.08	1
			0.795	2.00	0.80	0.085	73.850	2.097	6.259	0.084	0.456	0.89	0.03	1
			3.917	2.00		0.136	67.938	2.912	7.069	0.128	0.542	1.54	0.04	2
			7.821	2.00	0.76	0.171	44.275	3.081	7.141	0.113	0.498	1.87	0.12	3
Coccolithophore	*Emiliania huxleyi*	RCC 911	0.795	2.00		0.098	67.736	2.209	3.206	0.226	2.519	7.04	1.15	1
			3.917	2.00		0.389	82.747	2.283	3.524	0.176	1.023	2.27	0.24	1
			7.821	2.00		0.524	93.554	1.356	1.940	0.037	1.073	1.19	0.01	2

Table 3.2. Responses of metal quotas to increasing Ni availability in four species of phytoplankton. Numbers shown stand for R^2 value, with orange shades for positive correlations and blue for negative correlations.

	Cyanobacteria	**Dinoflagellate**	**Diatom**	**Coccolithophore**
	Synechococcus sp.	*Prorocentrum minimum*	*Thalassiosira weissfloggi*	*Emiliania huxleyi*
Ni/P	0.959	0.753	0.906	0.927
Co/P	0.405	0.461	0.122	0.960
Fe/P	0.366	0.330	0.851	0.975
Zn/P	0.361	0.092	0.162	0.743
Mn/P	0.225	0.298	0.004	0.633
Cu/P	0.435	0.278	0.002	0.665

Table 3.3. Coefficient of determination (R^2 value) and statistical significance (p value, t-test) of covariations between Ni/P ratios and other metal quotas for four cosmopolitan phytoplankton species.

	Cyanobacteria	**Dinoflagellate**	**Diatom**	**Coccolithophore**
	Synechococcus sp.	*Prorocentrum minimum*	*Thalassiosira weissfloggi*	*Emiliania huxleyi*
		versus Ni/P		
Co/P	R^2 = 0.5732	R^2 = 0.8123	R^2 = 0.3111	R^2 = 0.792
	p > 0.05	**p < 0.05**	p > 0.05	p > 0.05
Fe/P	R^2 = 0.2305	R^2 = 0.7155	R^2 = 0.5905	R^2 = 0.9868
	p < 0.001	**p < 0.001**	**p < 0.001**	**p < 0.001**
Zn/P	R^2 = 0.4125	R^2 = 0.1574	R^2 = 0.0317	R^2 = 0.4809
	p < 0.001	**p < 0.001**	**p < 0.001**	**p < 0.01**
Mn/P	R^2 = 0.2237	R^2 = 0.6803	R^2 = 0.0952	R^2 = 0.3634
	p < 0.001	**p < 0.001**	**p < 0.001**	**p < 0.01**
Cu/P	R^2 = 0.4773	R^2 = 0.5957	R^2 = 0.0023	R^2 = 0.886
	p > 0.05	**p < 0.001**	**p < 0.001**	**p < 0.05**

One characteristic difference among the metal quotas in these four phytoplankton is that a co-enhancement of Ni/P and Fe/P ratios is only shown in coccolithophore under increasing Ni availability. Another finding is that the Fe, Zn, Mn, Co and Cu quotas in cyanobacteria increase slightly when [Ni'] increase from 3.917 pM to 7.821 pM, following an initial decrease when [Ni'] increases from 0.014 nM to 3.917 pM. Another difference is that Co/P and Cu/P ratios decrease with the increasing Ni availability in coccolithophores, a relationship which is not seen in other species.

In terms of Ni isotope results, the coccolithophore *Emiliania huxleyi* (RCC911) enriches the heavy isotopes of Ni relative to the culture media under varying Ni availability which agrees with the majority of observations in dinoflagellate, cyanobacteria and diatom (Table 3.1 and Figure 3.3) (see Chapter 2). One contrasting pattern in coccolithophores is the reducing $\Delta^{60}Ni_{cell\text{-}medium}$ with the increasing Ni availability such that the $\Delta^{60}Ni_{cell\text{-}medium}$ decreases from ~7.0‰ at [Ni'] = 0.014 pM to ~1.2‰ at [Ni'] = 7.821 pM, compared with the increasing patterns of $\Delta^{60}Ni_{cell\text{-}medium}$ obtained in the other three species.

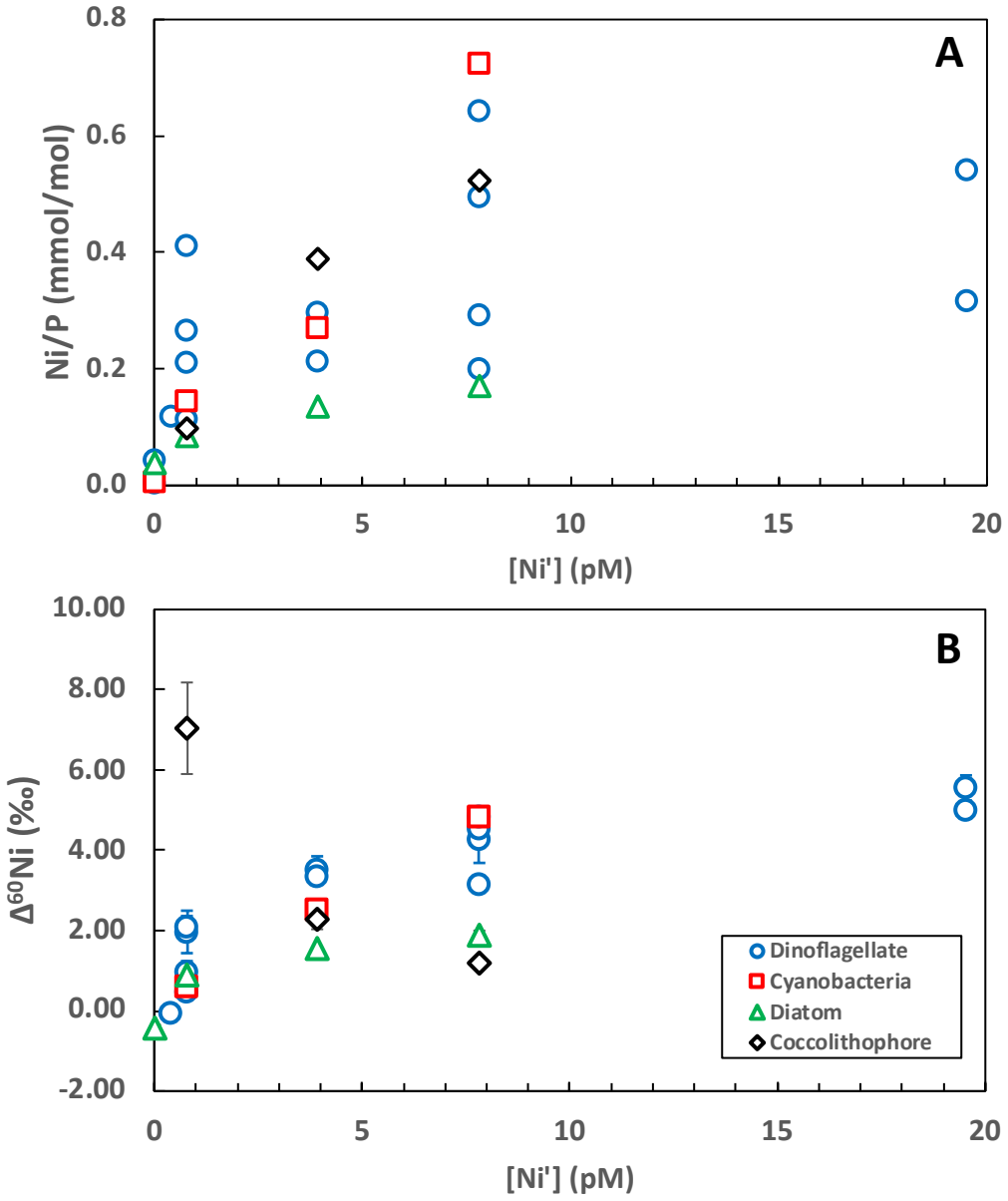


Figure 3.3. Physiological responses of four phytoplankton species under varying Ni availability. (A) cellular Ni/P ratios; (B) $\Delta^{60}Ni_{cell\text{-}medium}$. Dinoflagellate *Prorocentrum minimum* (RCC291), cyanobacteria *Synechococcus sp.* (PCC8806), diatom *Thalassiosira weissfloggi* (RCC76) and coccolithophore *Emiliania huxleyi* (RCC911) are compared. Data for dinoflagellate, cyanobacteria and diatom are replotted from Chapter 2. The error bars represent the standard deviations of duplicated analyses (2SD).

3.4 Discussion

This study provides the first Ni isotope data for coccolithophore *Emiliania huxleyi,* which is the ubiquitous and most abundant coccolithophore in the modern ocean. The new data are discussed in the context of dinoflagellate, cyanobacteria and diatom previously reported (see Chapter 2)

3.4.1 Variations of metal uptake characteristics among phytoplankton

The main characteristic differences between the coccolithophore and other three species in terms of the metal uptake patterns, are the synchronous increase of Fe and Ni quotas ($R^2 = 0.9868$, $p < 0.001$) as well as the significant decrease of Co ($R^2 = 0.960$, $p = 0.059$) and Cu ($R^2 = 0.886$, $p < 0.05$ with Ni/P ratios) quotas with the increasing Ni availability in the coccolithophore *Emilinania huexleyi* (RCC911), which are not seen in other three species. The results support the argument that the concentration of ambient dissolved metal is the primary factor controlling cellular metal quotas for the major bioactive trace metals (Twining and Baines, 2013). The cellular content of a metal can be influenced by the presence of other metal ions with similar charge and coordination chemistry via competitions between ions for transport through transmembrane channels and/or transporters (Twining and Baines, 2013). With the varying Ni availability, the initial contents of other metals remain constant and provide great baselines to see the covariations between Ni and other metals via competition and/or non-specific transport.

To evaluate the functions of Ni in different phytoplankton species, a comparative genomic analysis using genome-inferred proteomes for Ni-related proteins (e.g., ABC transporter, the high affinity Ni transporter family, superoxide dismutase and NiFe hydrogenase) in

different phytoplankton are performed (Zhang et al., 2022). Protein sequences used in this study are reference proteomes from the Universal Protein Resource (UniProt) (The UniProt Consortium, 2021), which are rigorously assembled and annotated by experts in the field, and adopted in proteome studies. To understand the usage of trace metals (mainly Ni) by phytoplankton as well as their strategies for transporting different metals, the metal-binding proteins are searched and identified by their functions, e.g., metal transporters or metalloproteins with other functions (Zhang et al., 2022).

The comparative genomic analysis shows the gene-referred proteins for Ni-SOD, high-affinity Ni transporter family and Ni/Co efflux system in the coccolithophore *Emiliania huxleyi* (Table 3.4). Proteins related to ATP-binding cassette (ABC-type) nickel transporter family, high-affinity Ni transporter family, Ni-SOD and NiFe hydrogenase are found in cyanobacteria *Synechococcus sp.*. As there is no whole genome sequence data for diatom *Thalassiosira weissfloggi* to allow the comparative genomic analysis, data of diatom *Thalassiosira oceanica* and *Thalassiosira pseudonana* are referred here. Both species are suggested to have encoded proteins of Ni-SOD, ABC transporter family, high-affinity Ni transporter family and NiFe hydrogenase in their genomes. Whole genome sequence data for dinoflagellate *Prorocentrum minimum* is currently unavailable.

Table 3.4. Protein analysis for Ni-related proteins in representative coccolithophore, diatom and cyanobacteria. Numbers shown represent the numbers of proteins found accounted for the functions.

	E. huxleyi	*T. oceanica*	*T. pseudonana*	*Synechococcus sp. (WH8102)*
Ubiquitin-domain-containing protein · Superoxide dismutase_ Nickel-type	30	23	2	0
ABC transporter · Nickel importer	0	1	1	15
High-affinity nickel-transport family protein	2	3	2	1
ABC transporter · Co/Ni transporter	0	0	0	1
ABC transporter · Co/Ni transporter	0	0	0	1
Putative nickel insertion protein	0	2	1	1
Nickel/cobalt efflux system	4	0	0	0
Putative nickel-containing superoxide dismutase	0	0	0	1
[NiFe]-hydrogenase/urease maturation factor_Ni2-binding GTPase	0	1	1	2

The distinct findings between the coccolithophore *Emilinania huexleyi* and other species suggest that the high-affinity Ni transporter family, the only gene-referred Ni-related transporter in the coccolithophore *Emilinania huexleyi*, may not inhibit the uptake of Fe but does so for Co and Cu, during Ni uptake (Figure 3.1–3.2 and Table 3.4). This discovery implies that Ni may compete with Co and Cu for binding sites at ABC-type transporter or Ni-specific permeases but not with Fe, as the radii of Co(II) (0.74 Å) and Cu(II) (0.72 Å) are much closer to the radius of Ni(II) (0.73 Å) as divalent ions, compared to Fe(II) (0.76 Å) (Irving and Williams, 1953). The synchronous increase of Ni and Fe indicates that there may be another uptake pathway for Fe in *Emilinania huexleyi* as the selectivity of ion sizes at the binding sites of Ni transporters may be restricted based on the competing uptake between metals with similar radii. Dinoflagellates, cyanobacteria and diatoms share similar patterns of metal quotas: when Ni availability increases, the increasing cellular Ni quotas in these three species are accompanied by decreasing Fe quotas ($p < 0.001$ for three species), and slightly decreasing or nearly constant Mn, Zn, Co and Cu quotas (Table 3.3). These patterns suggest a potential competition between Ni and Fe via the same transport system in these three species, which may also happen between Ni and other metals with likely less influence inferred from the magnitude of variations. These covariations with other divalent ions indicate the transport pathway in these three

species may be less Ni-specific. Compared with coccolithophore, these results further illustrate that the selectivity of ions via uptake pathways by phytoplankton may change between species.

Another characteristic pattern in metal quotas is the slight recovery of decreasing cellular Fe/P, Zn/P, Mn/P, Co/P and Cu/P ratios with increasing cellular Ni quotas observed in cyanobacteria *Synechococcus sp.* (PCC8806) when [Ni'] increases from 3.917 pM to 7.821 pM, which is not seen in the other three species (Table 3.1 and Figure 3.1). This finding suggests that the uptake of other metals may be inhibited by high-affinity Ni transport pathway under low Ni availability but may not be inhibited by low-affinity Ni transport pathway when Ni availability reaches certain level. One potential explanation is that, when Ni availability is low ([Ni'] = 0.014~3.917 pM), a more Ni-specific transport mechanism takes place for Ni acquisition, which inhibits the transport of other metals like Fe, Zn and Mn. Once the Ni availability is high, a relatively non-selective/less Ni-specific transport mechanism occurs, which simultaneously enhances the quotas of other metals during the uptake of Ni. This finding may suggest a transition of the uptake pathway in *Synechococcus sp.* from a high Ni selectivity to a low Ni selectivity when Ni availability increases.

The highest Ni quotas are observed in cyanobacteria *Synechococcus sp.* (PCC8806) among four species of phytoplankton under a similar range of Ni availability, followed by the range of dinoflagellate, coccolithophore and diatom. This observation agrees with various Ni-doping incubation experiments carried out on natural marine planktonic assemblages that the regions of surface ocean dominated by cyanobacteria are likely to be Ni-limiting as they may have a higher Ni requirement for growth and thus a higher proportion of

high-affinity Ni transporters (Dupont et al., 2010; Ho, 2013). To date, three Ni-containing enzymes have been found in marine cyanobacteria, including urease, Ni superoxide dismutase and NiFe hydrogenase, which may account for their high Ni requirements (Dupont et al., 2010, 2008; Ho, 2013; Li et al., 2022). A compilation has shown that there is a gradually decreasing optimal total dissolved Ni concentration for the optimal growth among diverse microbial taxa. This growth optimum peaks at Euryarchaeota, followed by Cyanobacteria, Proteobacteria and marine microalgae, suggesting that the biological need and function of Ni is the evolutionary relicts of the high Ni concentrations in the anoxic Archean when there was a higher Ni input from submarine volcanic eruption rich in komatiitic lavas (Arndt, 1991; Kamber, 2010; Zamble et al., 2017). The lack of elemental quotas in monotypic field-collected cells of these four cosmopolitan phytoplankton species currently hinders the direct extrapolations from culture studies to the modern ocean. The metal quota determination studies on phytoplankton are currently sparse for Ni, which the data are sometimes measured by different analytical methods (e.g., ICP-MS, SXRF) (Ho, 2013; Twining et al., 2012).

From the metal quotas, a bioaccumulation of Ni is observed in all species with increasing Ni availability. The uptake systems in dinoflagellates, diatoms and cyanobacteria share similar patterns and functions under increasing Ni availability: an inhibition of Fe uptake and a negligible influence on other metal quotas. A potential switch of the uptake pathway under varying Ni availability may be expected in cyanobacteria, which is supported by its complement of two types of transporter proteins. While in coccolithophores, a co-enhancement of Fe quotas and an inhibited uptake of Cu and Co are seen under increasing Ni availability, which suggests that coccolithophores may share a general/not Ni-specific uptake pathway with Cu and Co which have closer ionic radii to Ni, and have an individual

uptake pathway for Fe. These discoveries imply that the metal acquisition and regulating systems in phytoplankton can be species-dependent.

3.4.2 Factors influencing Ni isotope fractionation among phytoplankton

Ni isotope fractionation between cells and medium during phytoplankton growth varies with both phytoplankton species and ambient Ni availability (Figure 3.3B). Previous evaluation suggested that the replenishing rate of Ni from EDTA is on timescales equivalent to that of the biological uptake, which maintains a constant Ni isotope composition of bioavailable Ni pool in the medium (see Chapter 2). This constant bioavailable Ni pool suggests that:

$$\delta = \delta_0 + 1000(\propto_{cell-medium} - 1)$$

While δ and δ_0 represent the δ^{60}Ni of the final collected cells and the initial cells put into the medium. As the Ni contents in the initial cells are negligible with the absence of Ni addition and the cells were cultured in the set medium for at least three generation before experiments, the δ^{60}Ni of $NiCl_2$ (0.28 ± 0.06‰, n=5) was used for δ_0. As δ-δ_0 equals to $\Delta^{60}Ni_{cell\text{-}medium}$, the formula can be simplified as below.

$$\Delta^{60}Ni_{cell-medium} = 1000(\propto_{cell-medium} - 1)$$

The coccolithophore *Emiliania huxleyi* (RCC911) cultured in this study shows a decreasing $\Delta^{60}Ni_{cell\text{-}medium}$ with increasing Ni availability, which contrasts with the

increasing $\Delta^{60}Ni_{cell\text{-}medium}$ patterns reported in dinoflagellates, cyanobacteria and diatoms under identical culturing conditions (Figure 3.3B) (see Chapter 2). Although the competition between Ni-EDTA binding and coccolithophore acquisition system has to be considered for the final $\Delta^{60}Ni_{cell\text{-}medium}$, the distinctively decreasing trend of $\Delta^{60}Ni_{cell\text{-}medium}$ should remain the same, as the competition under varying Ni availability should be identical with the presence of the same EDTA concentration (~0.1 mM).

Based on the comparative genomic analysis (Table 3.4), representative coccolithophores, diatoms and cyanobacteria all have Ni-SOD and high-affinity Ni transporter families, which therefore cannot be the controlling factor for the two contrasting $\Delta^{60}Ni_{cell\text{-}medium}$ patterns. The remaining differences are the absence of an ABC-type Ni transporter, and the NiFe hydrogenase in coccolithophores, or the presence of a Ni/Co efflux system in coccolithophores only.

It has been proposed that cellular Ni isotope compositions can be influenced by uptake and transport processes inside the cells (Chapter 2). For instance, in the subcellular Ni isotope analysis conducted in dinoflagellates, the uptake process may be a combination of an equilibrium fractionation which preferentially takes up heavy isotopes of Ni via protein binding at the cellular surface ($\Delta^{60}Ni_{cell\text{-}medium}$ = 4.97 ± 0.21‰, n=3) after the competition of relative binding strengths with ambient ligands, followed by a cross-membrane transport process that may be associated with a kinetic fractionation, preferentially transporting light isotopes of Ni from the protein-bound Ni pool to the cytosol ($\Delta^{60}Ni_{cell\text{-}medium}$ = 4.37 ± 0.22‰, n=3) for enzymatic activities and/or further to periplasm ($\Delta^{60}Ni_{cell\text{-}medium}$ = 3.76 ± 0.40‰, n=3) for storage of excess metals (see Chapter 2). A similar process involving protein binding and transport for metal acquisition has

also been proposed for a high-affinity Cu transporter (Ctr1) (Walke et al., 2022). With the assumption that ABC-type Ni transporters may have lower Ni affinity than the high-affinity Ni transporter family, ABC-type Ni transporters may preferentially enrich isotopically light Ni compared with the high-affinity ones. This hypothesis agrees with Zn isotope data in cultured diatoms which show a higher $\Delta^{66}Zn_{cell\text{-}medium}$ of –0.2‰ for high-affinity Zn uptake at low Zn concentration and a lower $\Delta^{66}Zn_{cell\text{-}medium}$ of –0.8‰ for low-affinity Zn uptake at high Zn concentration (John et al., 2007). With the potential isotope fractionation ($\Delta^{66}Zn_{bioavailable\text{-}medium}$ = –0.16 ~ –0.33‰) between Zn-EDTA and Zn^{2+} prior to biological uptake considered (Köbberich and Vance, 2019), Zn isotope data in John et al. (2007) show a likely positive $\Delta^{66}Zn_{cell\text{-}medium}$ (–0.04 ~ +0.13‰) for high-affinity Zn uptake and a negative $\Delta^{66}Zn_{cell\text{-}medium}$ (–0.47 ~ –0.64‰) for low-affinity Zn uptake. As for coccolithophores, with their overall enrichment of heavy Ni isotopes shown, the absence of ABC-type Ni transporters (i.e., low-affinity Ni uptake pathway) which likely enrich isotopically light Ni may not be the controlling factor for the distinctive $\Delta^{60}Ni_{cell\text{-}medium}$ trend compared with the other three species. The absent enzymatic activity of NiFe hydrogenase is also unlikely to cause the difference as this would be an internal fractionation process within the cells and the bulk cellular Ni isotope compositions should stay the same. These deductions leave the Ni/Co efflux system encoded only in the genes of the coccolithophore *Emiliania huxleyi* to be the controlling factor for its distinctive decreasing $\Delta^{60}Ni_{cell\text{-}medium}$ trend with the increasing Ni availability.

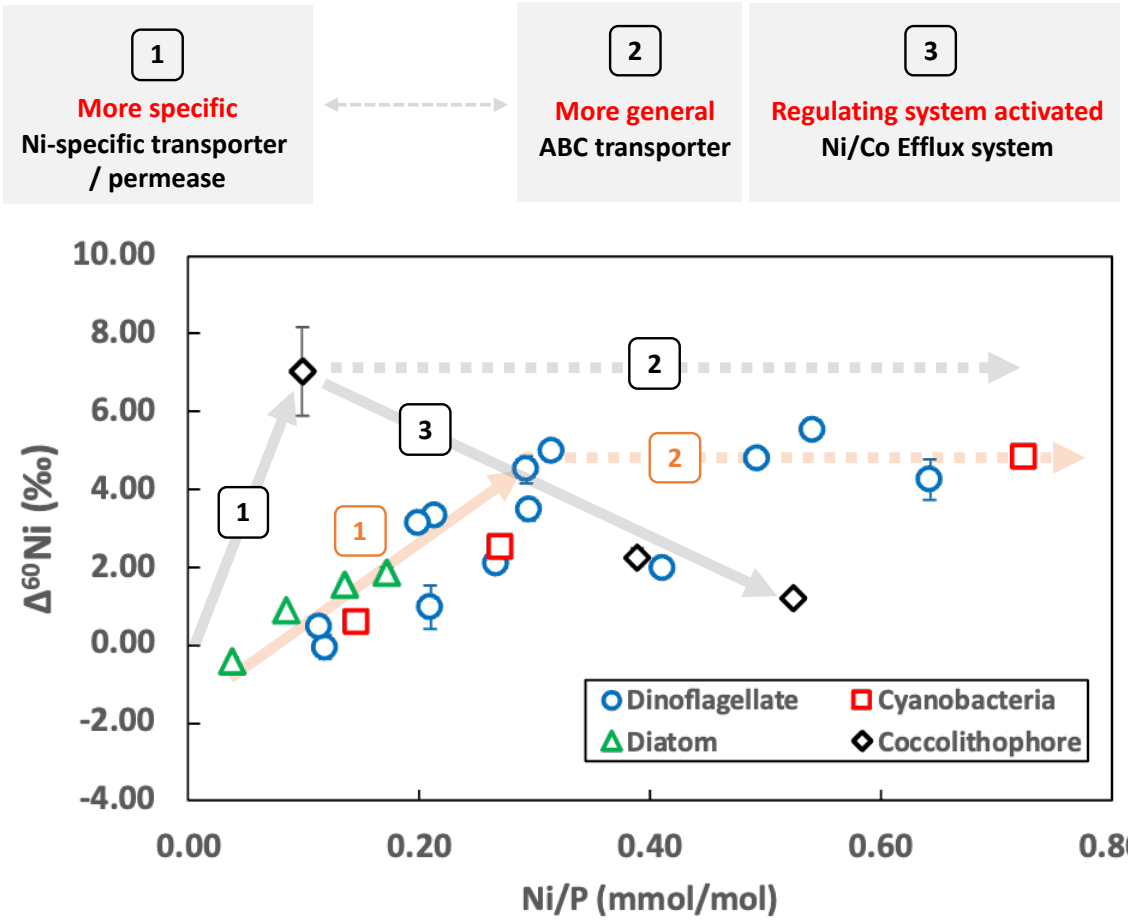


Figure 3.4. $\Delta^{60}Ni_{cell\text{-}medium}$ versus Ni/P ratios for four species of phytoplankton with potential physiological mechanisms. The error bars represent the standard deviations (2SD) for Ni isotope compositions. Mechanisms in grey are potential mechanisms for coccolithophore, while the mechanisms in orange are for other three species. Dinoflagellate *Prorocentrum minimum* (RCC291), cyanobacteria *Synechococcus sp.* (PCC8806), diatom *Thalassiosira weissfloggi* (RCC76) and coccolithophore *Emiliania huxleyi* (RCC911) are compared. Data for dinoflagellate, cyanobacteria and diatom are replotted from Chapter 2.

Overload of Ni ions may induce toxicity in microbial cells through mismetallation of metalloenzymes, spurious binding to enzymes and indirect oxidative stress, thus microorganisms use Ni efflux systems to balance the excess Ni in the cytoplasm (Macomber and Hausinger, 2011; Sydor and Zamble, 2013). The metalloregulator of Ni is most studied in bacteria because of their experimental tractability and relatively sparsely understood for phytoplankton. Nickel exporters involved in the efflux of a subset of

substrates have been reported to be cation diffusion facilitator (CDF), major facilitator protein superfamily (MFS), resistance nodulation cell-division (RND) and P-type ATPases in bacterial studies, which are all capable of mediating excess Ni, Co and several other metals (Zamble et al., 2017). Given the lack of further characterization of these regulators in this study, it is challenging to propose a definitive export pathway accounted for the patterns seen in the coccolithophores.

There are two potential explanations for the decreasing $\Delta^{60}Ni_{cell\text{-}medium}$ with increasing Ni availability observed in the coccolithophores, in combination with the gene-referred protein groups considered: (1) The isotope fractionation during biological uptake under each Ni availability is varying. This isotope fractionation can be more positive ($\Delta^{60}Ni_{cell\text{-}medium}$ ~7‰) when Ni availability is low, and it can be less positive ($\Delta^{60}Ni_{cell\text{-}medium}$ ~1‰) when Ni availability is high. The varying isotope fractionation may be controlled by switches between different uptake mechanisms with varying Ni availability, for instance more Ni-specific uptake pathways with stronger binding strength and larger isotope fractionation factor under low Ni availability and less-selective uptake pathways with lower strong binding strength and smaller isotope fractionation factor under high Ni availability. (2) The decreasing $\Delta^{60}Ni_{cell\text{-}medium}$ trend is due to an additional isotope fractionation exerted by an activated efflux system when the Ni availability increases and causes excess Ni accumulated in the cells. The presence of a Ni/Co efflux supports the later suggestion, which preferentially removes heavy isotopes of Ni out of the cellular pool, potentially via the binding with Ni efflux protein family, resulting in net-negative changes to the cellular $\Delta^{60}Ni_{cell\text{-}medium}$. This further implies that the efflux system in coccolithophores may be essentially different than the ones in dinoflagellate, diatom and cyanobacteria, based on the completely different $\Delta^{60}Ni_{cell\text{-}medium}$ trends under same

culturing conditions. The efflux system in *E. huxleyi* may function via protein-binding pathway and preferentially remove isotopically heavy Ni from the cells, resulting lighter isotope compositions in cells. On the other hand, the efflux systems in dinoflagellate, diatom and cyanobacteria may function via some low-affinity pathways such as diffusion, which preferentially effluxes isotopically light Ni and results in heavier isotope compositions in cells.

Based on the results of genomic analysis and the observations that each phytoplankton species without Ni/Co efflux protein family shown in their genes has its characteristic isotope fractionation factor during its growth following Rayleigh distillation isotope fractionation process, the latter explanation may be more plausible at this stage. Current evidence does not fully exclude the possibility that there is a switch between high-affinity Ni uptake (Ni-specific) at low Ni concentration to low-affinity Ni uptake at high Ni concentration, as dinoflagellate, diatom and cyanobacteria all seem to follow the trend increasing to $\Delta^{60}Ni_{cell\text{-}medium}$ of ~5‰ when Ni/P ratios are ~0.3 mmol/mol and staying constant with the increasing Ni/P quotas (Figure 3.4). Here we provide a schematic diagram compiling processes which may cause isotope fractionations in the coccolithophores *E. huxleyi* (Figure 3.5).

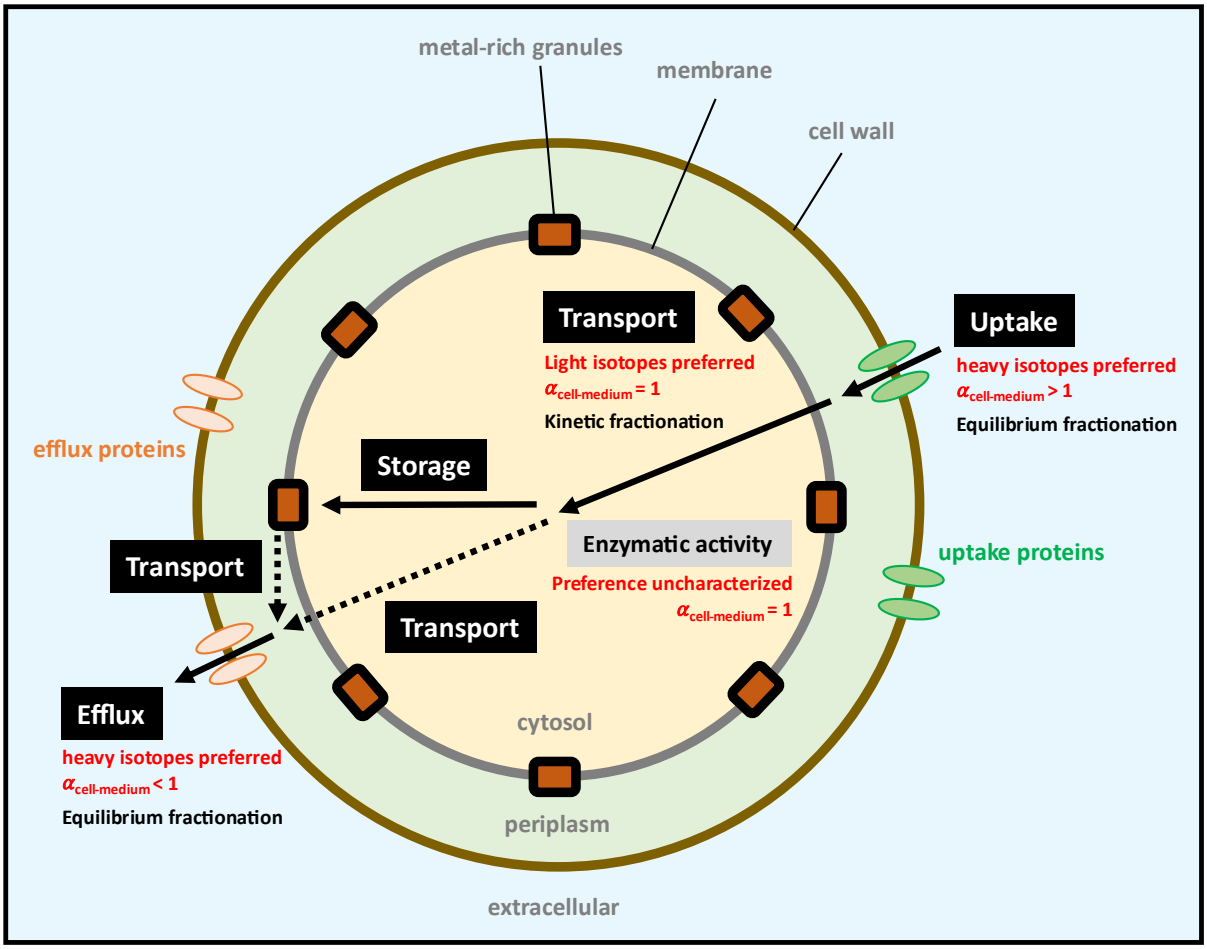


Figure 3.5. Schematic diagram for processes causing Ni isotope fractionations in cultured coccolithophores *E. huxleyi*. Uptake and efflux systems favour isotopically heavy Ni by equilibrium fractionation via protein bindings and cause net $\Delta^{60}Ni_{cell\text{-}medium}$ changes with $\alpha_{cell\text{-}medium}$ >1 and <1 for uptake and efflux processes, respectively. Transport process may prefer isotopically light Ni by kinetic fractionation via ion diffusion but will not cause net $\Delta^{60}Ni_{cell\text{-}medium}$ change as an internal mechanism. Ni isotope fractionations during enzymatic activity and metal storage have not been characterised yet, but they will not cause net $\Delta^{60}Ni_{cell\text{-}medium}$ changes as internal metabolic mechanisms.

In terms of the bulk cellular $\Delta^{60}Ni_{cell\text{-}medium}$, the processes involved in the exchanges with extracellular environments may change the bulk composition, e.g., uptake and efflux system at the cellular surface. As the Ni quotas in coccolithophore are in comparable or lower level to dinoflagellate and cyanobacteria (Figure 3.3A), it suggests that the distinctive presence of Ni/Co efflux system in the coccolithophore *E. huxleyi* is likely due to its lower tolerance for cellular Ni content. While the other internal biological processes

like transport, storage and enzymatic activity may cause isotope fractionation between various subcellular fractions (e.g., cell wall, membrane, cytosol) but no net changes in terms of the bulk $\Delta^{60}Ni_{cell\text{-}medium}$. Transport processes are likely to enrich isotopically light Ni via kinetic fractionation based on subcellular analysis (see Chapter 2). For storage processes, increasing amounts of histidine-rich proteins (HRPs) with strong binding to Ni have been reported in prokaryotic proteomes and bacteria, which suggests an enrichment of heavy Ni isotopes may be expected in the storage pool compared to the ambient cellular composition (Cheng et al., 2013). There is no study characterizing Ni isotope fractionation during enzymatic activity thus far. A similar framework may also be applicable for dinoflagellates, diatoms and cyanobacteria without considering the effects from efflux system (Figure 3.5).

Our finding here indicates the accumulation of Ni and other metals induced by the increasing Ni availability higher than [Ni'] = 0.795 pM may exert a biological toxicity on the cultured coccolithophores and activate the Ni-regulating metalloenzymes. Despite the presence of the Ni/Co efflux system, the bulk cellular Ni/P ratios still increase with the increasing ambient Ni concentration (Figure 3.3A), which suggests that the Ni efflux is lower than the uptake Ni flux and results in the overall accumulated Ni quotas. With the decreasing $\Delta^{60}Ni_{cell\text{-}medium}$ and increasing Ni quotas in coccolithophores considered, it indicates that the isotope fractionation factor during the efflux of Ni should have a larger magnitude of $\Delta^{60}Ni_{cell\text{-}medium}$ change to cause a net decrease of cellular isotope compositions when Ni uptake and efflux system both take place.

This study may provide the first Ni isotope evidence for Ni-regulating processes in marine phytoplankton. The coccolithophore *Emiliania huxleyi* shows distinct

physiological responses under similar culturing conditions to other cosmopolitan phytoplankton species, suggesting that either its environment-sensing/Ni-regulating ability is more active/sensitive or it has lower resilience for high cellular Ni content, with the gene-referred protein responsible for effluxing Ni. Although the resistance to the toxicity caused by Ni accumulated in cells may vary with phytoplankton species and whether every type of Ni efflux processes causes isotope fractionation is not clearly understood, the finding here indicates that Ni isotopes may be a powerful tracer for physiological responses in phytoplankton as their characteristic signals may provide a new way to study potential environmental pressures exerted on marine phytoplankton.

3.4.3 Biological isotope fractionations in Ni, Cu and Zn systems

As micro-nutrients, Cu, Ni and Zn have the top three highest complex stability in order based on the Irving-Williams series and similar ionic diameters with their doubly-charged ions (Irving and Williams, 1953). They may compete for binding sites with each other in aqueous solution due to the similar ionic radii and share similar biological isotope fractionation patterns because of their shared high complex stability (Figure 3.6).

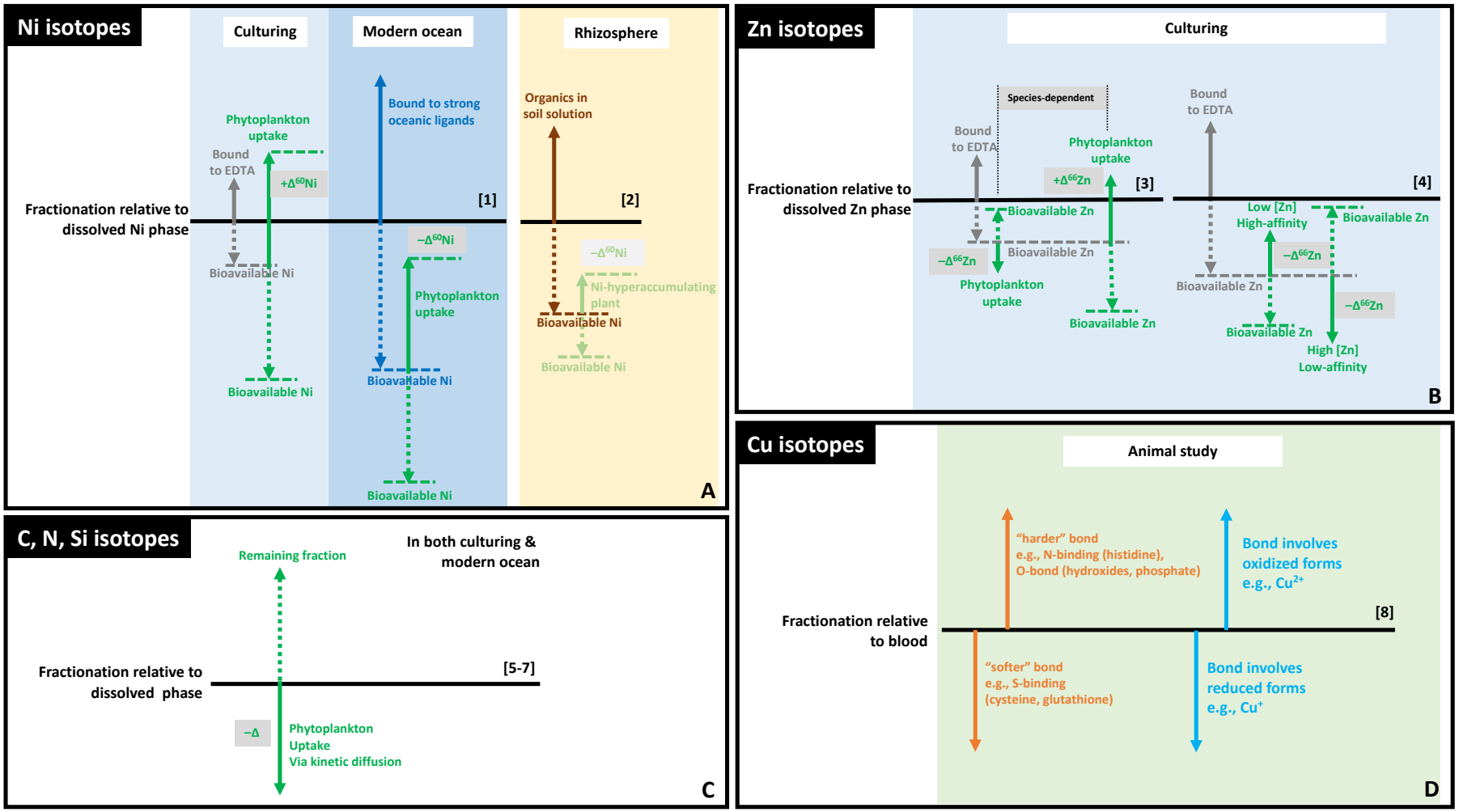


Figure 3.6. Schematic comparison of biological isotope fractionations in multiple isotope systems. (A) Ni, (B) Zn, (C) C, N, Si and (D) Cu isotope systems. Solid lines represent drivers for isotope fractionations, while dotted lines stand for the remaining reservoir/bioavailable pool. References: [1] Chapter 2; [2] Deng et al. (2014); [3] Köbberich and Vance (2019); [4] John et al. (2007); [5] Cardinal et al. (2007); [6] Fogel and Cifuentes (1993); [7] Sutton et al. (2013); [8] Balter et al. (2013).

In the Ni isotope system, it has been proposed that both under culturing conditions and in the modern ocean, the relative binding strengths between phytoplanktonic acquisition system and ambient ligands control the isotope compositions of each component (Figure 3.6A). This mechanism suggests an enrichment of isotopically heavy Ni in phytoplankton cells after the competition with organic chelators EDTA under culturing condition, and an enrichment of isotopically light Ni in phytoplankton cells after the competition with strong ligands in the modern ocean. The Zn isotope system has also been applied to investigate marine phytoplankton uptake. Köbberich and Vance (2017) reported Zn isotope signatures in two open-ocean diatom species, showing nearly unfractionated signals in *T. oceanica* and an enrichment of heavy Zn isotopes ($\Delta^{66}Zn_{cell\text{-}medium}$ up to +0.85‰) in *Chaetoceros sp.* at low Fe conditions, compared to bioavailable Zn pool in the medium. Later, another study suggested that only one cyanobacteria strain out of twelve phytoplankton species including cyanobacteria, diatom and coccolithophore enriched heavy isotopes of Zn from the culturing media and the rest strains all enriched light isotopes of Zn (Figure 3.6B) (Köbberich and Vance, 2019). This preferential uptake of light isotopes agrees with many isotope systems of biologically active elements like C, N and Si – that phytoplankton favor light isotopes relative to culturing media and seawater via kinetic diffusion process (Figure 3.6C) (Cardinal et al., 2007; Fogel and Cifuentes, 1993; Sutton et al., 2013). The dominant transport pathways control the isotope ratios in cultured marine diatom *T. oceanica*: a shift of $\Delta^{66}Zn_{cell\text{-}medium}$ from -0.2‰ at low Zn availability dominated by high-affinity Zn transporters to -0.8‰ at high Zn availability dominated by low-affinity Zn transporters (Figure 3.6B) (John et al., 2007).

Nickel isotope fractionations during the growth of higher plants under high and low Zn treatments have been characterised and reported that both Ni-hyperaccumulating and non-Ni-accumulating plants enrich isotopically light Ni from the media (Deng et al., 2014; Estrade et al., 2015). It was reported that under low Zn treatment, the Ni isotope fractionation between plant and medium ($\Delta^{60}Ni_{plant\text{-}medium}$) was greater in the Ni-hyperaccumulating plants *Alyssum murale* and *Noccaea caerulescens* ($\Delta^{60}Ni_{plant\text{-}medium}$ = –0.9 ~ –0.63‰) than non-Ni-accumulating plant *Thlaspi arvense* ($\Delta^{60}Ni_{plant\text{-}medium}$ = –0.21‰), suggesting a great permeability of the low-affinity Ni transport system in these hyperaccumulators (Deng et al., 2014). In the same study, under high Zn treatment, the reduced magnitudes of Ni isotope fractionation ($\Delta^{60}Ni_{plant\text{-}medium}$ = -0.11 ~ -0.07‰) were observed in these Ni-hyperaccumulating plants, which suggests that Ni may compete with Zn and go through low-affinity transport system of Zn, as no high-affinity Ni transporter has been identified in higher plants (Deng et al., 2014). An enrichment of light isotopes of Zn has also been observed in most plants but with smaller magnitudes of fractionation, potential via low-affinity transporter or ion diffusion (Deng et al., 2014). It has further been proved that there is an equilibrium fractionation between soil solutions and soil, with soil solution enriched in heavy isotopes of Ni, and these higher plants preferentially take up light isotopes from the bioavailable soil solution pool (Figure 3.6A) (Estrade et al., 2015; Zelano et al., 2018). An alternative view was provided that Ni accumulating plants enrich isotopically heavy Ni compared to soil ($\Delta^{60}Ni_{leaves\text{-}soil}$ = 0.09 ~ 1.06‰) and Ni hyperaccumulating plants cause no significant isotope fractionation during uptake and translocation, the heavy isotope signals were explained by the release of heavy Ni chelated by organics into bioavailable Ni pool during the restitution and decomposition of these organics (Ratié et al., 2019). These studies suggest that the

competitions between biological uptake and ambient ligands for Ni are ubiquitous in nature.

The scarcity of transition metals has brought the evolution of protein systems in organisms to specifically acquire these metals from the ambient environment and utilize them efficiently (da Silva and Williams, 1991; Williams and da Silva, 1996). If the biological acquisition for Ni is a combination of low- and high-affinity Ni transport systems, the proportion of high-affinity transporter is expected to increase and result in a higher cellular δ^{60}Ni when Ni is limiting to the organism. The absence of high-affinity Ni transporter in higher plants suggests that its requirement for Ni may not be as high as the requirement in marine phytoplankton, which is in agreement that the utilization of Ni in organisms is the relic of ancient ocean with higher Ni content (Konhauser et al., 2009). This observation points out that Ni may be sufficient in soils for higher plants to obtain via only by low-affinity Ni transport system or ion diffusion, but Ni is more likely to be limiting for bacteria and phytoplankton in the modern ocean as the high-affinity Ni transport systems presented.

The species-dependent Ni isotope fractionation factors among phytoplankton species may be controlled by the relative proportion of common Ni-binding amino acids, which suggests that higher proportion of amino acids with stronger bonds (oxygen > nitrogen > sulfur) may preferentially concentrate heavy isotopes of Ni in cells (see Chapter 2). Such enrichments of heavy isotopes in stronger bonds are also seen in Zn and Cu isotopic patterns in organs and body fluids from mice and sheep experiments (Figure 3.6D), though the physiological mechanisms influencing isotopic signals in mammalian cells may be more complicated compared with marine phytoplankton (Balter et al., 2013).

The aforementioned comparisons show that the evolution of metal acquisition system depends on the requirements of organisms and the bioavailable metal pools in the environments, which vary with oceanic or continental environments and adapt with the changes throughout the Earth history, for instance the appearance of life, the sources and types of ligands, beginning of oxidative weathering, and so on. Overall, organisms develop to acquire biologically sufficient nutrients and utilize them efficiently with least energy consumption to cope with the environment at that time.

3.5 Concluding remarks

This study provides the first Ni isotope evidence for a Ni-regulating process in cultured coccolithophores, which suggests isotopically heavy Ni is preferentially removed from the cells when Ni availability increases. The findings suggest that coccolithophore *E. huxleyi* (RCC911) may be more susceptible to increasing ambient Ni concentrations, with its unique metalloregulator Ni/Co efflux system to keep cellular homeostasis, which is not seen in dinoflagellate *P. minimum* (RCC291), cyanobacteria *Synechococcus sp.* (PCC8806) and diatom *T. weissfloggi* (RCC76). With metal quotas, comparative genomic analysis and Ni isotope analysis, the physiological responses of four cosmopolitan phytoplankton species are revealed to have characteristic patterns under varying Ni availability. It suggests that Ni isotopes in phytoplankton can potentially be an indicator for their physiological response to environments, but more data are required for systematic applications. The biological isotope fractionations in Ni, Cu and Zn systems show similar competitions for metal ions between biological metal acquisition system and other environmental components like ligands, suggesting a similar framework emphasizing the relative binding strengths at the molecular scale may be applicable for

these metal isotope systems, regardless of the perspectives from oceanic, continental or cellular environment.

3.6 References

Albarède, F., 2015. Metal Stable Isotopes in the Human Body: A Tribute of Geochemistry to Medicine, Elements Magazine.

Archer, C., Vance, D., Milne, A., Lohan, M.C., 2020. The oceanic biogeochemistry of nickel and its isotopes : New data from the South Atlantic and the Southern Ocean biogeochemical divide. Earth Planet. Sci. Lett. 535, 116118. https://doi.org/10.1016/j.epsl.2020.116118

Arndt, N.T., 1991. High Ni in Archean tholeiites. Tectonophysics 187, 411–419. https://doi.org/10.1016/0040-1951(91)90479-C

Balter, V., Lamboux, A., Zazzo, A., Télouk, P., Leverrier, Y., Marvel, J., Moloney, A.P., Monahan, F.J., Schmidt, O., Albarède, F., 2013. Contrasting Cu, Fe, and Zn isotopic patterns in organs and body fluids of mice and sheep, with emphasis on cellular fractionation. Metallomics 5, 1470–1482. https://doi.org/10.1039/c3mt00151b

Boiteau, R.M., Till, C.P., Ruacho, A., Bundy, R.M., Hawco, N.J., McKenna, A.M., Barbeau, K.A., Bruland, K.W., Saito, M.A., Repeta, D.J., 2016. Structural characterization of natural nickel and copper binding ligands along the US GEOTRACES eastern Pacific zonal transect. Front. Mar. Sci. 3, 1–16. https://doi.org/10.3389/fmars.2016.00243

Bottini, C., Dapiaggi, M., Erba, E., Faucher, G., Rotiroti, N., 2020. High resolution spatial analyses of trace elements in coccoliths reveal new insights into element incorporation in coccolithophore calcite. Sci. Rep. 10, 1–13. https://doi.org/10.1038/s41598-020-66503-x

Bruland, K.W., 1980. Oceanographic distributions of cadmium, zinc, nickel, and copper in the North Pacific. Earth Planet. Sci. Lett. 47, 176–198. https://doi.org/10.1016/0012-821X(80)90035-7

Cameron, V., Vance, D., 2014. Heavy nickel isotope compositions in rivers and the oceans. Geochim. Cosmochim. Acta 128, 195–211. https://doi.org/10.1016/j.gca.2013.12.007

Cardinal, D., Savoye, N., Trull, T.W., Dehairs, F., Kopczynska, E.E., Fripiat, F., Tison, J.L., André, L., 2007. Silicon isotopes in spring Southern Ocean diatoms: Large zonal changes despite homogeneity among size fractions. Mar. Chem. 106, 46–62. https://doi.org/10.1016/j.marchem.2006.04.006

Cheng, T., Xia, W., Wang, P., Huang, F., Wang, J., Sun, H., 2013. Histidine-rich proteins in prokaryotes: Metal homeostasis and environmental habitat-related occurrence. Metallomics 5, 1423–1429. https://doi.org/10.1039/c3mt00059a

Deng, T., Cloquet, C., Tang, Y.T., Sterckeman, T., Echevarria, G., Estrade, N., Morel, J.L., Qiu, R.-L., 2014. Nickel and Zinc Isotope Fractionation in Hyperaccumulating and Nonaccumulating Plants. Environ. Sci. Technol. 48, 11926–11933. https://doi.org/dx.doi.org/10.1021/es5020955

Dupont, C.L., Barbeau, K., Palenik, B., 2008. Ni uptake and limitation in marine Synechococcus strains. Appl. Environ. Microbiol. 74, 23–31. https://doi.org/10.1128/AEM.01007-07

Dupont, C.L., Buck, K.N., Palenik, B., Barbeau, K., 2010. Nickel utilization in phytoplankton assemblages from contrasting oceanic regimes. Deep. Res. Part I Oceanogr. Res. Pap. 57, 553–566. https://doi.org/10.1016/j.dsr.2009.12.014

Egleston, E.S., Morel, F.M.M., 2008. Nickel limitation and zinc toxicity in a urea-grown diatom. Limnol. Oceanogr. 53, 2462–2471. https://doi.org/10.4319/lo.2008.53.6.2462

Estrade, N., Cloquet, C., Echevarria, G., Sterckeman, T., Deng, T., Tang, Y.T., Morel, J.L., 2015. Weathering and vegetation controls on nickel isotope fractionation in surface ultramafic environments (Albania). Earth Planet. Sci. Lett. 423, 24–35. https://doi.org/10.1016/j.epsl.2015.04.018

Fogel, M.L., Cifuentes, L.A., 1993. Isotope fractionation during primary production. Org. geochemistry Princ. Appl. 73–98. https://doi.org/10.1007/978-1-4615-2890-6_3

Gall, L., Williams, H., Siebert, C., Halliday, A., 2012. Determination of mass-dependent variations in nickel isotope compositions using double spiking and MC-ICPMS. J. Anal. At. Spectrom. 27, 137–145. https://doi.org/10.1039/c1ja10209e

Gallon, J.R., 1981. The oxygen sensitivity of nitrogenase: a problem for biochemists and micro-organisms. Trends Biochem. Sci. 6, 19–23. https://doi.org/10.1016/0968-0004(81)90008-6

Gueguen, B., Rouxel, O., Ponzevera, E., Bekker, A., Fouquet, Y., 2013. Nickel Isotope Variations in Terrestrial Silicate Rocks and Geological Reference Materials Measured by MC-ICP-MS. https://doi.org/10.1111/j.1751-908X.2013.00209.x

Gueguen, B., Rouxel, O., Rouget, M.L., Bollinger, C., Ponzevera, E., Germain, Y., Fouquet, Y., 2016. Comparative geochemistry of four ferromanganese crusts from the Pacific Ocean and significance for the use of Ni isotopes as paleoceanographic tracers. Geochim. Cosmochim. Acta 189, 214–235. https://doi.org/10.1016/j.gca.2016.06.005

Gueguen, B., Sorensen, J. V., Lalonde, S. V., Peña, J., Toner, B.M., Rouxel, O., 2018. Variable

Ni isotope fractionation between Fe-oxyhydroxides and implications for the use of Ni isotopes as geochemical tracers. Chem. Geol. 481, 38–52. https://doi.org/10.1016/j.chemgeo.2018.01.023

Ho, T.Y., 2013. Nickel limitation of nitrogen fixation in Trichodesmium. Limnol. Oceanogr. 58, 112–120. https://doi.org/10.4319/lo.2013.58.1.0112

Ho, T.Y., Quigg, A., Finkel, Z. V., Milligan, A.J., Wyman, K., Falkowski, P.G., Morel, F.M.M., 2003. The elemental composition of some marine phytoplankton. J. Phycol. 39, 1145–1159. https://doi.org/10.1111/j.0022-3646.2003.03-090.x

Irving, B.H., Williams, R.J.P., 1953. The stability of transition-metal complexes. J. Chem. Soc.

John, S.G., Geis, R.W., Saito, M.A., Boyle, E.A., 2007. Zinc isotope fractionation during high-affinity and low-affinity zinc transport by the marine diatom Thalassiosira oceanica. Limnol. Oceanogr. 52, 2710–2714. https://doi.org/10.4319/lo.2007.52.6.2710

Kamber, B.S., 2010. Archean mafic-ultramafic volcanic landmasses and their effect on ocean-atmosphere chemistry. Chem. Geol. 274, 19–28. https://doi.org/10.1016/j.chemgeo.2010.03.009

Köbberich, M., Vance, D., 2017. Kinetic control on Zn isotope signatures recorded in marine diatoms. Geochim. Cosmochim. Acta 210, 97–113. https://doi.org/10.1016/j.gca.2017.04.014

Köbberich, M., Vance, D., 2019. Zn isotope fractionation during uptake into marine phytoplankton: Implications for oceanic zinc isotopes. Chem. Geol. 523, 154–161. https://doi.org/10.1016/j.chemgeo.2019.04.004

Konhauser, K.O., Pecoits, E., Lalonde, S. V., Papineau, D., Nisbet, E.G., Barley, M.E., Arndt, N.T., Zahnle, K., Kamber, B.S., 2009. Oceanic nickel depletion and a methanogen famine before the Great Oxidation Event. Nature 458, 750–753. https://doi.org/10.1038/nature07858

Lemaitre, N., Du, J., de Souza, G.F., Archer, C., Vance, D., 2022. The essential bioactive role of nickel in the oceans: Evidence from nickel isotopes. Earth Planet. Sci. Lett. 584, 117513. https://doi.org/10.1016/j.epsl.2022.117513

Li, H.T., Tuo, S. how, Lu, M.C., Ho, T.Y., 2022. The effects of Ni availability on H2 production and N2 fixation in a model unicellular diazotroph: The expression of hydrogenase and nitrogenase. Limnol. Oceanogr. 1–11. https://doi.org/10.1002/lno.12151

Mackey, D.J., O'Sullivan, J.E., Watson, R.J., Pont, G.D., 2002. Trace metals in the Western Pacific: Temporal and spatial variability in the concentrations of Cd, Cu, Mn and Ni. Deep. Res. Part I Oceanogr. Res. Pap. 49, 2241–2259. https://doi.org/10.1016/S0967-0637(02)00124-3

Macomber, L., Hausinger, R.P., 2011. Mechanisms of nickel toxicity in microorganisms.

Metallomics 3, 1153–1162. https://doi.org/10.1039/c1mt00063b

Middag, R., Baar, H.J.W. De, Bruland, K.W., 2020. The Distribution of Nickel in the West-Atlantic Ocean , Its Relationship With Phosphate and a Comparison to Cadmium and Zinc 7, 1–17. https://doi.org/10.3389/fmars.2020.00105

Morel, F.M.M., Hudson, R.J.M., Price, N.M., 1991. Limitation of productivity by trace metals in the sea. Limnol. Oceanogr. 36, 1742–1755. https://doi.org/10.4319/lo.1991.36.8.1742

Morel, F.M.M., Milligan, A.J., Saito, M.A., 2014. Marine Bioinorganic Chemistry: The Role of Trace Metals in the Oceanic Cycles of Major Nutrients, 2nd ed, Treatise on Geochemistry: Second Edition. Elsevier Ltd. https://doi.org/10.1016/B978-0-08-095975-7.00605-7

Morel, F.M.M., Rueter, J.G., Anderson, D.M., Guillard, R.R.L., 1979. Aquil: a chemically definied phytoplankton culture medium for trace metal studies.pdf. J. Phycol. 15, 135–141.

Morse, J.W., Luther, G.W., 1999. Chemical influences on trace metal-sulfide interactions in anoxic sediments. Geochim. Cosmochim. Acta 63, 3373–3378.

Poulton, A.J., Adey, T.R., Balch, W.M., Holligan, P.M., 2007. Relating coccolithophore calcification rates to phytoplankton community dynamics: Regional differences and implications for carbon export. Deep. Res. Part II Top. Stud. Oceanogr. 54, 538–557. https://doi.org/10.1016/j.dsr2.2006.12.003

Price, N.M., Harrison, G.I., Hering, J.G., Hudson, R.J., Nirel, P.M. V., Palenik, B., Morel, F.M.M., 1989. Preparation and Chemistry of the Artificial Algal Culture Medium Aquil. Biol. Oceanogr. 6, 443–461. https://doi.org/10.1080/01965581.1988.10749544

Price, N.M., Morel, F.M.M., 1991. Colimitation of phytoplankton nickel and nitrogen. Limnol. Oceanogr. 36, 1071–1077.

Ragsdale, S.W., 2009. Nickel-based enzyme systems. J. Biol. Chem. 284, 18571–18575. https://doi.org/10.1074/jbc.R900020200

Ratié, G., Jouvin, D., Garnier, J., Rouxel, O., Miska, S., Guimarães, E., Cruz Vieira, L., Sivry, Y., Zelano, I., Montarges-Pelletier, E., Thil, F., Quantin, C., 2015. Nickel isotope fractionation during tropical weathering of ultramafic rocks. Chem. Geol. 402, 68–76. https://doi.org/10.1016/j.chemgeo.2015.02.039

Ratié, G., Quantin, C., Maia De Freitas, A., Echevarria, G., Ponzevera, E., Garnier, J., 2019. The behavior of nickel isotopes at the biogeochemical interface between ultramafic soils and Ni accumulator species. J. Geochemical Explor. 196, 182–191. https://doi.org/10.1016/j.gexplo.2018.10.008

Sclater, F.R., Boyle, E., Edmond, J.M., 1976. On the marine geochemistry of nickel. Earth Planet. Sci. Lett. 31, 119–128. https://doi.org/10.1038/263042a0

Sunda, W.G., Price, N.M., Morel, F.M.M., 2005. Trace Metal Ion Buffers and Their Use in Culture Studies. Algal Cult. Tech. 7, 35–63.

Sutton, J.N., Varela, D.E., Brzezinski, M.A., Beucher, C.P., 2013. Species-dependent silicon isotope fractionation by marine diatoms. Geochim. Cosmochim. Acta 104, 300–309. https://doi.org/10.1016/j.gca.2012.10.057

Sydor, A.M., Zamble, D.B., 2013. Nickel metallomics: General themes guiding nickel homeostasis, Metal Ions in Life Sciences. https://doi.org/10.1007/978-94-007-5561-1_11

Takano, S., Liao, W., Tian, H., Huang, K., Ho, T., 2020. Sources of particulate Ni and Cu in the water column of the northern South China Sea : Evidence from elemental and isotope ratios in aerosols and sinking particles. Mar. Chem. 219, 103751. https://doi.org/10.1016/j.marchem.2020.103751

Takano, S., Tanimizu, M., Hirata, T., Shin, K.C., Fukami, Y., Suzuki, K., Sohrin, Y., 2017. A simple and rapid method for isotopic analysis of nickel, copper, and zinc in seawater using chelating extraction and anion exchange. Anal. Chim. Acta 967, 1–11. https://doi.org/10.1016/j.aca.2017.03.010

The UniProt Consortium, 2021. UniProt: the universal protein knowledgebase in 2021. Nucleic Acids Res. 49, D480–D489. https://doi.org/10.1093/nar/gkaa1100

Twining, B.S., Baines, S.B., 2013. The trace metal composition of marine phytoplankton. Ann. Rev. Mar. Sci. 5, 191–215. https://doi.org/10.1146/annurev-marine-121211-172322

Twining, B.S., Baines, S.B., Vogt, S., Nelson, D.M., 2012. Role of diatoms in nickel biogeochemistry in the ocean. Global Biogeochem. Cycles 26, GB4001.

Volbeda, A., Charon, M.-H., Piras, C., Hatchikian, E.C., Frey, M., Fontecilla-Camps, J.C., 1995. ARTICLES TABLE 1 X-ray structure determination Data and MIR phasing statistics Data set Crystals Measured hkls Unique hkls Resolution (A)t Completeness (%) Rmecge (%)t R de , (%) § Binding sites Phasing power II. Nature 373, 580.

Walke, G., Aupič, J., Kashoua, H., Janoš, P., Meron, S., Shenberger, Y., Qasem, Z., Gevorkyan-Airapetov, L., Magistrato, A., Ruthstein, S., 2022. Dynamical interplay between the human high-affinity copper transporter hCtr1 and its cognate metal ion. Biophys. J. 121, 1194–1204. https://doi.org/10.1016/j.bpj.2022.02.033

Wang, R.M., Archer, C., Bowie, A.R., Vance, D., 2019. Zinc and nickel isotopes in seawater from the Indian Sector of the Southern Ocean: The impact of natural iron fertilization versus Southern Ocean hydrography and biogeochemistry. Chem. Geol. 511, 452–464. https://doi.org/10.1016/j.chemgeo.2018.09.010

Winter, A., Henderiks, J., Beaufort, L.U.C., Rickaby, R.E.M., Brown, C.W., 2014. Poleward expansion of the coccolithophore Emiliania huxleyi 36, 316–325.

https://doi.org/10.1093/plankt/fbt110

Wu, G., Zhu, J.M., Wang, X., Han, G., Tan, D., Wang, S.J., 2019. A novel purification method for high precision measurement of Ni isotopes by double spike MC-ICP-MS. J. Anal. At. Spectrom. 34, 1639–1651. https://doi.org/10.1039/c9ja00077a

Yang, S., Hawco, N.J., Pinedo-gonzález, P., Bian, X., Huang, K., Zhang, R., John, S.G., 2020. A new purification method for Ni and Cu stable isotopes in seawater provides evidence for widespread Ni isotope fractionation by phytoplankton in the North Pacific. Chem. Geol. 547, 119662. https://doi.org/10.1016/j.chemgeo.2020.119662

Yang, S.C., Kelly, R.L., Bian, X., Conway, T.M., Huang, K.F., Ho, T.Y., Neibauer, J.A., Keil, R.G., Moffett, J.W., John, S.G., 2021. Lack of redox cycling for nickel in the water column of the Eastern tropical north pacific oxygen deficient zone: Insight from dissolved and particulate nickel isotopes. Geochim. Cosmochim. Acta 309, 235–250. https://doi.org/10.1016/j.gca.2021.07.004

Zamble, D., Rowinska-Zyrek, M., Kozlowski, H., 2017. The Biological Chemistry of Nickel. Royal Society of Chemistry. https://doi.org/10.1039/9781788010580-FP007

Zelano, I.O., Cloquet, C., Fraysse, F., Dong, S., Janot, N., Echevarria, G., Montargès-Pelletier, E., 2018. The influence of organic complexation on Ni isotopic fractionation and Ni recycling in the upper soil layers. Chem. Geol. 483, 47–55. https://doi.org/10.1016/j.chemgeo.2018.02.023

Zhang, Q., Bendif, E.M., Zhou, Y., Nevado, B., Shafiee, R., Rickaby, R.E.M., 2022. Declining metal availability in the Mesozoic seawater reflected in phytoplankton succession. Nat. Geosci. 15, 932–941. https://doi.org/10.1038/s41561-022-01053-7

Zhang, Q., Snow, J.T., Holdship, P., Price, D., Watson, P., Rickaby, R.E.M., 2018. Direct measurement of multi-elements in high matrix samples with a flow injection ICP-MS: Application to the extended: Emiliania huxleyi Redfield ratio. J. Anal. At. Spectrom. 33, 1196–1208. https://doi.org/10.1039/c8ja00031j

CHAPTER 4
Ni isotope fractionation during the formation of amorphous nickel sulfides

(This chapter is submitted as:
Ni isotope fractionation during the formation of amorphous nickel sulfides.
T.H. Wang, Y.T. Hsieh, J. Cosmidis, G.M. Henderson. In review)

4 Ni isotope fractionation during the formation of amorphous nickel sulfides

4.1 Introduction

Nickel (Ni) is a bioactive and essential trace metal for various enzymatic activities in organisms. Ni-containing enzymes (e.g., urea, Ni-Fe hydrogenase, Ni superoxide dismutase, and methy-coenzyme M reductase) are involved in the production and utilization of gases including CO, CO_2, H_2, O_2, CH_4 and NH_3, and therefore influence the global carbon, nitrogen and oxygen cycles (Ragsdale, 2009). The concentration of dissolved Ni in the modern ocean ranges from 2 to 12 nM, showing a nutrient-like pattern with depth, with depletion in the photic zone due to enzymatic utilization by biology (Bruland et al., 2014; Sclater et al., 1976).

In oxygen-rich oceanic settings, dissolved Ni is initially scavenged by Fe-Mn oxides and organic matter, and subsequently transported to sediments (Gall et al., 2013; Sclater et al., 1976). In anoxic environments below the sediment-seawater interface, the re-dissolution of Fe-Mn oxides and the oxidation of organic matter lead to the release of Ni back to the water column (Hindersmann and Mansfeldt, 2014; Tribovillard et al., 2006). In euxinic (anoxic and sulfidic) settings generated by the activity of sulfate reducing bacteria (SRB), the released Ni can be re-sequestered by precipitation as Ni-sulfides or co-precipitation with Fe-sulfides (Abraitis et al., 2004; Houben et al., 2017; Huerta-Diaz and Morse, 1992). Sulfides can be an important output of oceanic dissolved Ni under anoxic environments (e.g., Black Sea) either by scavenging of particle reactive sulfidized species or sulfide precipitation; Ni has a high affiliation for sulfide (Vance et al., 2016). As

the solubilities and reactivities of Ni are different among Ni-sulfide forms (Mansor et al., 2019; Wilkin and Rogers, 2010), the way that Ni is hosted leads to varying bioavailability of Ni and sedimentary Ni output in the environment.

Understanding of the formation mechanism of Ni-sulfides in low-temperature environments has significantly improved in recent decades. Precipitation experiments have reported the formation of a variety of Ni-sulfide phases (e.g., hydrated NiS, α-NiS, millerite (β-NiS), polydymite (Ni_3S_4), heazlewoodite (Ni_3S_2) and vaesite (NiS_2); (Huang et al., 2009; Jeong and Manthiram, 2001; Wang et al., 1997; Wilkin and Rogers, 2010), which have mostly been studied in a nanocrystalline state. It was suggested that Ni is likely incorporated into Fe-sulfides, as Fe has a higher reaction kinetic then Ni and thus can precipitate faster as Fe-sulfides when Ni and Fe are present with hydrogen sulfide, leaving Ni to adsorb on or co-precipitate with Fe-sulfides (Morse and Luther, 1999). Recently, however, it has been argued that under the experimental condition of $[Ni]_{aq}/[Fe]_{aq}$ = 1:1, the kinetics of Ni-sulfide precipitation is comparable or higher than Fe-sulfides (Mansor et al., 2019).

Ni isotopes have been applied as a tracer in environmental studies such as vegetation, weathering, adsorption and the formation of secondary minerals (Castillo Alvarez et al., 2020; Estrade et al., 2015; Gueguen et al., 2018; Parigi et al., 2022b, 2022a; Ratié et al., 2019, 2018, 2015; Sorensen et al., 2020; Spivak-Birndorf et al., 2018; Wang and Wasylenki, 2017; Wasylenki et al., 2015). Nickel isotope fractionation during the precipitation of a mixture of millerite (β-NiS) and polydymite (Ni_3S_4) has been characterized to be ($\varepsilon_{S\text{-}L}$ = –0.73‰) (Parigi et al., 2022a), which suggests an enrichment of lighter Ni isotopes in the solid phase. This fractionation is similar to other Ni-

containing minerals during adsorption or formation (e.g., calcite, birnessite) (Castillo Alvarez et al., 2020; Sorensen et al., 2020). However, the formation mechanism of Ni-sulfide is complex and characterization of Ni isotope fractionation in crystalline Ni-sulfides alone (a mixture of millerite and polydymite; Parigi et al., 2022a) is insufficient to unravel the formation of Ni-sulfides.

This study aims to characterize the isotope fractionation during the formation of amorphous nickel sulfides, which serve as essential precursors for crystalline Ni-sulfides and provide important insights for the development of Ni-sulfides. With the comparison between the isotope signals in amorphous and crystalline Ni-sulfide phases, we assess the potential of applying Ni isotopes as a geochemical proxy for environmental studies, especially under euxinic conditions.

4.2 Previous work on Ni-sulfide precipitation experiments

The precipitation of amorphous spherical Ni-sulfide particles with a 10-nm diameter was first reported using nickel sulfate and sodium sulfide solution via a controlled double-jet precipitation technique (CDJP) at room temperature (Wang et al., 1997). These amorphous Ni-sulfide particles transformed into cubic crystalline particles with a ~200-nm diameter when the aging condition was at 80°C and low pH (3–3.5) (Wang et al., 1997).

The initial nickel sulfide phase precipitated in Earth surface aqueous environments has been suggested to be a nanoparticulate material with a crystalline millerite (β-NiS) core and a hydrated amorphous shell, yielding a general formula $NiS \cdot 1.5H_2O$, which is invisible in X-ray powder diffraction analysis (XRD) (Huang et al., 2009). The chemical

formula was later revised to be $Ni_{1.1}S \cdot 1.5H_2O$ (Huang et al., 2010). This hydrated NiS was reported to reform into polydymite (Ni_3S_4) or heazlewoodite (Ni_3S_2) under acidic conditions (pH = 3~5) but not in neutral or basic conditions (pH >7) (Huang et al., 2009).

In another experimental study, crystalline α-NiS was reported to be the initial precipitate with residual Ni-O coordination revealed, by reacting $NiSO_4 \cdot 6H_2O$ solution with NaOH solution purged with 10% H_2S gas in an anoxic glovebox (Wilkin and Rogers, 2010). This α-NiS was reported to transform into polydymite (Ni_3S_4) and vaesite (NiS_2) in the presence of elemental sulfur (Wilkin and Rogers, 2010). Later, an experimental study referred to the initial XRD-amorphous Ni-sulfides as polyphasic Ni-sulfides, reporting that this amorphous phase aged to hexagonal α-NiS phase within a few days to weeks (Mansor et al., 2019). In the presence of sulfate-reducing bacteria (SRB) *Desulfovibrio vulgaris*, α-NiS transformed into polydymite (Ni_3S_4) and vaesite (NiS_2), while under abiotic precipitation only polydymite was obtained (Mansor et al., 2019).

Recently, a mixture of millerite (β-NiS) and polydymite (Ni_3S_4) was obtained during abiotic precipitation experiments by using $NiSO_4$ and Na_2S solution in an anoxic glovebox after 72 hours (Parigi et al., 2022a). While a mixture of α-NiS, polydymite (Ni_3S_4) and vaesite (NiS_2) was obtained in biotic precipitation experiments after 1 day in the presence of SRB by adding sulfate and $NiCl_2$ solutions (Parigi et al., 2022b).

The observations for the development of Ni-sulfides in low-temperature conditions generally come to a consensus that amorphous phases precipitate first and age to crystalline phases with time, though the reported mineral phases are not fully consistent

between studies. The enhancement of crystallinity is generally favored at low pH, and in the presence of elemental sulfur and microbial activity.

4.3 Materials and Methods

4.3.1 Nickel sulfide precipitation experiments

Nickel sulfide precipitation experiments were conducted under both oxic and anoxic conditions to compare the sulfide phases precipitated and their isotopic fractionations under oceanic conditions with varying oxygen levels. The sulfide precipitations in oxic conditions (O_2 ~21%) were carried out and collected in laminar flow hoods in metal-free clean labs at the Department of Earth Sciences, University of Oxford. While the sulfide precipitations in anoxic conditions (O_2 < 2ppmv) were performed in a glovebox laboratory at the same department. The glovebox was ventilated with pure N_2, equipped with heated Pb catalysts to further remove O_2 and was monitored for oxygen level by using an anaerobic monitor CAM-12 (COY Lab Products).

Two main types of experiments were designed to understand the nature of Ni-sulfide formation: (1) "Time-series" experiments: for understanding the kinetic precipitation of Ni-sulfides with time under three different ionic strengths, i.e., Milli-Q (MQ, Merck Millipore), 1:1 mixture of Milli-Q and synthetic seawater (0.5 SW) and synthetic seawater (SW), at room temperature, carried out under both oxic and anoxic conditions; (2) " Ni/S ratio" experiments: precipitation experiments with varying Ni/sulfide ratios, for understanding the Ni isotope signals of both precipitates and solutions, and the fractionation pattern.

In the "time-series" experiments, Ni-sulfide precipitation experiments were carried out with three ionic strengths (MQ, 0.5SW and SW) separately, under both oxic (O_2 ~21%) and anoxic (O_2 < 2ppmv) conditions (thus six experimental conditions in total). The concentrations of Ni (~340 **μ**mol/L) and sulfide (~450 **μ**mol/L) in the solution were fixed under all conditions, by adding same amount of aliquots from a high-purity nickel solution (Alfra-Aesar, plasma standard solution, Specpure®) and a $Na_2S \cdot 9H_2O$ solution made from crystalline $Na_2S \cdot 9H_2O$ powders (Sigma-Aldrich, purity ≥ 99.99%, trace metals basis). The precipitation experiments were carried out in 50 mL polypropylene (PP) centrifuge tubes. The dominant matrix including MQ, 0.5SW and SW were well mixed with Ni aliquots first and then $Na_2S \cdot 9H_2O$ aliquots were added to initiate the reaction. The initial pH was set ~8. The precipitation experiments were monitored for 48 h, with more frequent collections in the first hour. The solutions were collected at each interval by filtering 1 mL of solution through 0.22 μm filters to polytetrafluoroethylene (PTFE) vials, evaporated completely and dissolved in 2% HNO_3 for concentration measurements.

In the "Ni/S ratio" experiments, one batch was conducted in MQ under both oxic (O_2 ~21%) and anoxic (O_2 < 2ppmv) conditions for 10 min and another batch was conducted in MQ under anoxic condition (O_2 < 2ppmv) for 6 h. The precipitation experiments were carried out adding different volumes of Ni solution and a fixed volume of $Na_2S \cdot 9H_2O$ solution into 50 mL PP centrifuge tubes with Milli-Q water (MQ), which yields a range of Ni concentrations of 260~7800 **μ**mol/L and a constant $Na_2S \cdot 9H_2O$ concentration of ~450 **μ**mol/L. The MQ matrix was well mixed with Ni aliquots first and added with $Na_2S \cdot 9H_2O$ aliquots to initiate the reaction. The precipitates (Ni-sulfides, solid phase) were

centrifuged and separated from the supernatant (dissolved Ni, liquid phase). The collected precipitates were digested with 7 mL 6M HCl in PTFE vials at 120°C overnight (Guinoiseau et al., 2018), then evaporated to dryness and dissolved in 2% HNO_3 for concentration analysis.

4.3.2 X-ray diffraction (XRD) analysis

A portion of the final Ni precipitates from the time-series precipitation experiments were centrifuged, rinsed with deoxygenated Milli-Q water and dried in an anoxic glove box for mineral phase characterization. The collected precipitates were crushed by hand with a mortar and pestle to finer grains (<30 μm, ideally ~10 μm) and passed through a sieve. The powders for each sample were then placed on a zero-background silicon plate and mixed with acetone to create a slurry which adheres to the holder.

Mineral phases within collected precipitates were determined by powder X-ray diffraction analysis using a PANalytical Empyrean Series 2 powder diffractometer in the Department of Earth Sciences, University of Oxford. The instrument was operated with an accelerating voltage of 40 kV, a generator setting of 40 mA, a divergence slit of 1° and a beam mask of 10 mm. The XRD patterns were collected from 5.01 to 79.97° 2θ angle with a step size of 0.026° using CoKα radiation source (Kα_1: λ = 1.78901Å; Kα_2: λ = 1.79290Å; K_β: λ = 1.62083Å) under continuous scan type. Semi-quantitative results were calculated by HighScore Panalytical software using referenced scale factor and Reference Intensity Ratio (RIR) from the International Centre of Diffraction Data (ICDD) mineral database (Chung, 1975, 1974a, 1974b). Mineral phase identification was carried out by searching and matching with the Powder Diffraction File PDF–4+ mineral database accessed by license through the ICDD.

4.3.3 Ni concentration and isotope analysis

The collected precipitates were digested in 6M HCl, evaporated completely and re-dissolved in 2% HNO_3 for further Ni chemistry and analyses.

The measurement for Ni concentration was carried out using a PerkinElmer NexION 350D quadrupole inductively coupled plasma mass spectrometer (ICP-MS) at the Department of Earth Sciences, University of Oxford. The precision and accuracy of elemental analysis were monitored with low-Ni-content river water standard SLRS-6 from National Research Council Canada, which yielded a reproducibility of 0.627 ± 0.028 μg/L (n = 13) and a RSD <4.5% for Ni, in agreement with the certified value 0.616 ± 0.008 μg/L (Yang et al., 2015). After the acquisition of Ni contents, samples were subsampled and double-spiked at a sample-to-spike ratio of 0.4 with a mixture of ^{61}Ni-^{62}Ni with a ratio of 25:75 for Ni isotope analysis (Gall et al., 2012; see Appendix A).

Prior to Ni isotope analysis, the chemical separation for Ni from the solution matrix was carried out using a three-stage ion exchange chromatography, in a Class 100 laminar flow hood in the metal-free clean laboratory at the Department of Earth Sciences, University of Oxford (following the approach of Gall et al. (2012) and Saunders et al. (2020, as described in Appendix A). The first and second cation column exploit the ability of Ni to form strong complexes with ammonia and dimethylglyoxime (DMG), respectively. The third anion column was applied to separate any remaining Fe from Ni. The total procedural blanks for chemical treatment including sample digestion and Ni purification were assessed along with every batch of column chemistry and were usually less than 4.2 ng.

Ni isotope compositions were determined using a Nu Plasma high resolution multi-collector inductively coupled plasma mass spectrometer (MC-ICP-MS) at the Department of Earth Sciences, University of Oxford (as described in Appendix A). All isotope analyses were conducted with working concentration of 200 ng/g total Ni in 2% HNO_3 at low resolution mode. Sample solutions were introduced into the plasma using a PFA nebulizer (ESI scientific, 50μLmin^{-1}) coupled with an Aridus II desolvating nebulizer system (Teledyne CETAC Technologies) which can enhance the sensitivity and minimize oxide formation during ionization. Sample solutions were diluted to give ion beam intensities of total Ni in standards and samples of ~15V. Each isotope measurement consists of 40 cycles which include 10s integration time for acquiring ion beam intensity. The potential interference of ^{58}Fe on ^{58}Ni was corrected by simultaneous measurement of ^{57}Fe (Gall et al., 2012). A normalized argon index (NAI) was applied to monitor the thermal condition of plasma and minimize potential interferences on Ni isotopes (Fietzke and Frische, 2016). The data reduction method for the deconvolution of the double-spike was performed online (Siebert et al., 2006).

All Ni isotope compositions reported in this study are represented as delta notation (δ) in per mil deviation (‰) relative to Ni isotope standard SRM 986 (high-purity Ni metal).

$$\delta^{60}Ni = \left[\frac{(^{60}Ni/^{58}Ni)_{sample}}{(^{60}Ni/^{58}Ni)_{SRM986}} - 1\right] \times 1000\ (‰)$$

The long-term average values and reproducibilities of two in-house sulfide standards (Kam and Sud), and the USGS Mn nodule standard (Nod-P-1) over a 30-month period

were -0.88 ± 0.06‰ (n=43), 0.79 ± 0.06‰ (n=43) and 0.37 ± 0.07‰ (n=36), respectively. The δ^{60}Ni value of Nod-P-1 is in agreement with the range (δ^{60}Ni = 0.328~0.41‰) of previously published values (Gueguen et al., 2018, 2016, 2013; Ratié et al., 2015; Wu et al., 2019).

4.4 Results

4.4.1 Ni-sulfide mineral characterization

In all precipitation experiments conducted in this study, black or dark brownish precipitates readily formed right after the mixing of Ni and $Na_2S \cdot 9H_2O$ solutions, which agrees with the description for polyphasic Ni-sulfide precursors seen in previous studies (Mansor et al., 2019). The crystalline mineral phases are determined to be mainly halite (NaCl) and oldhamite (CaS) in the experiment conducted in both 0.5SW and SW, in the final precipitates collected after 48-h "time-series" experiments (Figure 4.1). There is no detectable peak in medium dominated with MQ. These results suggest that the black Ni precipitates during precipitation experiments in all conditions are largely dominated by amorphous Ni-sulfides, given the high concentrations of Ni and sulfide in the media and the precipitated Ni fractions calculated from the remaining solutions (Tables 4.1–4.2).

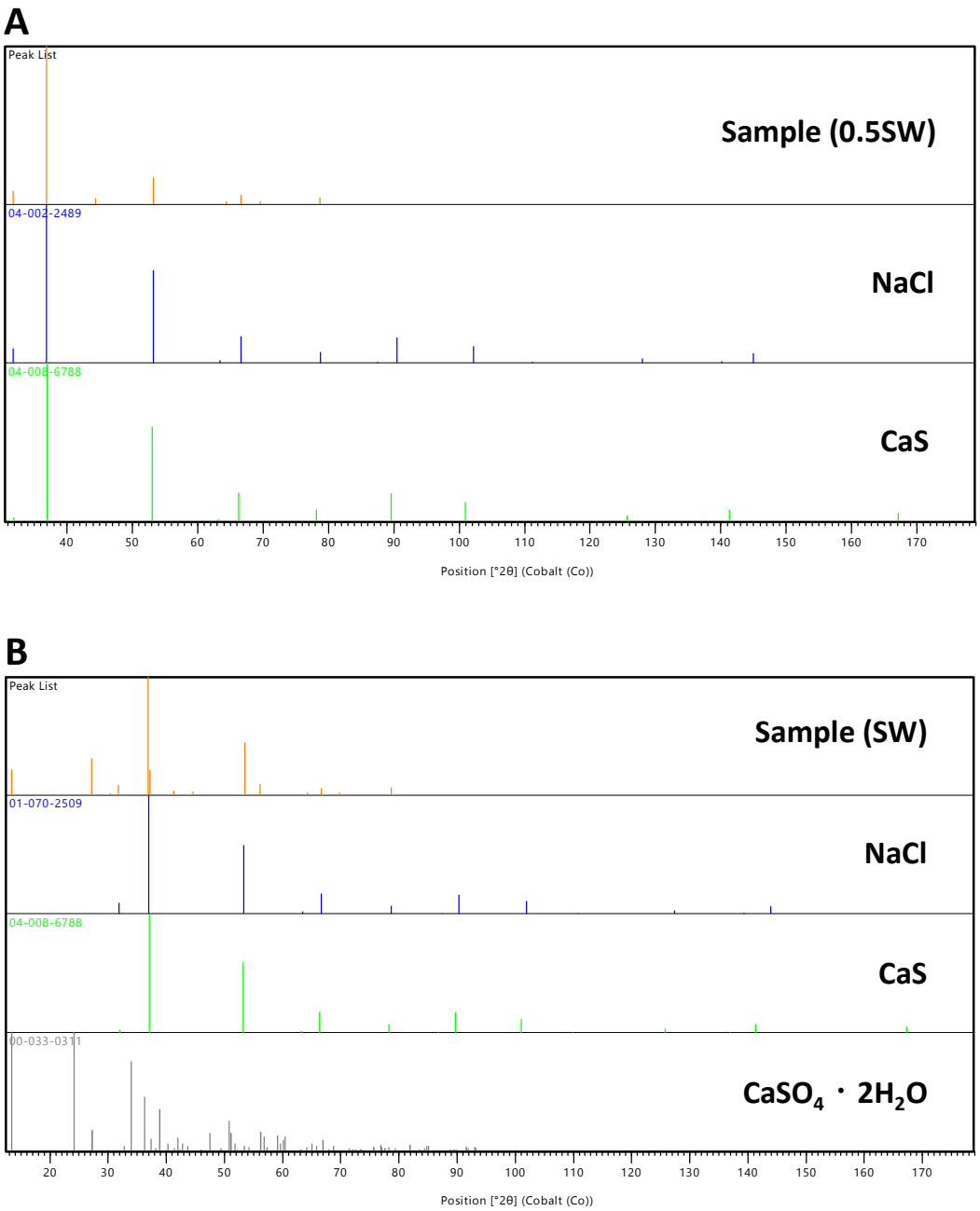


Figure 4.1. X-ray diffraction patterns of Ni precipitates from "time-series" experiments in media (A) 0.5SW and (B) SW under anoxic condition for 48 h. The numbers (left side) stated for the suggested minerals (right side) represent the reference code.

Table 4.1. Compilation of Ni precipitated fractions and Ni isotope compositions under varying ionic strengths in oxic condition (O_2~21‰, laminar flow hood) for oxic "time-series" experiments.

Experimental condition	Sample ID	Time (s)	Ni precipitated (%)	$\delta^{60}Ni_L$ (‰)	2SD (‰)	n
NiS precipitation in Milli-Q $[Ni]_{ini}$ = ~340μmolL^{-1} pH = ~8	MQ_0	1	0.00	-0.10	0.03	4
	MQ_1min	60	88.45	0.66	0.02	4
	MQ_5min	300	86.02	0.27	0.01	4
	MQ_10min	600	86.69	0.16	0.04	4
	MQ_30min	1800	85.88	0.09	0.05	4
	MQ_1H	3600	80.04	0.08	0.04	4
	MQ_6H	21600	75.35	0.30	0.02	4
	MQ_24H	86400	68.88	0.26	0.06	4
	MQ_48H	172800	64.45	0.27	0.04	4
NiS precipitation in 0.5SW (MQ:SW=1:1) $[Ni]_{ini}$ = ~340μmolL^{-1} pH = ~8	1/2SW_0	1	0.00			
	1/2SW_1min	60	27.09			
	1/2SW_5min	300	39.93			
	1/2SW_10min	600	36.21			
	1/2SW_30min	1800	41.65			
	1/2SW_1H	3600	43.02			
	1/2SW_6H	21600	42.90			
	1/2SW_24H	86400	42.38			
	1/2SW_48H	172800	37.53			
NiS precipitation in SW $[Ni]_{ini}$ = ~340μmolL^{-1} pH = ~8	SW_0	1	0.00			
	SW_1min	60	13.62			
	SW_5min	300	14.39			
	SW_10min	600	19.33			
	SW_30min	1800	11.75			
	SW_1H	3600	12.70			
	SW_6H	21600	7.48			
	SW_24H	86400	2.29			
	SW_48H	172800	0.31			

Table 4.2. Compilation of Ni precipitated fractions and Ni isotope compositions under varying ionic strengths in anoxic condition (O_2 <2ppmv, glovebox) for anoxic "time-series" experiments.

Experimental condition	Sample ID	Time (s)	Ni precipitated (%)	$\delta^{60}Ni_L$ (‰)	2SD (‰)	n
NiS precipitation in Milli-Q $[Ni]_{ini}$ = ~340μmolL^{-1} pH = ~8	MQ_0	1	0.00	-0.02	0.05	4
	MQ_1min	60	94.39	2.57	0.06	4
	MQ_5min	300	94.93	1.94	0.03	4
	MQ_10min	600	94.21	1.32	0.08	4
	MQ_30min	1800	92.82	0.99	0.08	4
	MQ_1H	3600	90.57	0.70	0.13	4
	MQ_6H	21600	87.62	0.60	0.09	4
	MQ_24H	86400	85.57	0.70	0.20	4
	MQ_48H	172800	81.53	0.83	0.27	4
NiS precipitation in 0.5SW (MQ:SW=1:1) $[Ni]_{ini}$ = ~340μmolL^{-1} pH = ~8	1/2SW_0	1	0.00			
	1/2SW_1min	60	57.60			
	1/2SW_5min	300	69.93			
	1/2SW_10min	600	70.91			
	1/2SW_30min	1800	63.45			
	1/2SW_1H	3600	64.82			
	1/2SW_6H	21600	60.34			
	1/2SW_24H	86400	64.79			
	1/2SW_48H	172800	63.97			
NiS precipitation in SW $[Ni]_{ini}$ = ~340μmolL^{-1} pH = ~8	SW_0	1	0.00	-0.07	0.04	4
	SW_1min	60	38.83	0.76	0.05	4
	SW_5min	300	50.20	1.08	0.02	3
	SW_10min	600	58.05	1.16	0.03	3
	SW_30min	1800	54.81	1.05	0.04	3
	SW_1H	3600	42.44	0.88	0.06	4
	SW_6H	21600	31.67	0.38	0.05	4
	SW_24H	86400	19.94	0.32	0.06	4
	SW_48H	172800	29.75	0.26	0.06	4

4.4.2 Isotope fractionation during "time-series" Ni-sulfide precipitation

In general, the precipitated fractions of Ni are higher in anoxic condition (19.9~94.9%) (Figure 4.2A) than oxic condition (0.3~88.4%) (Figure 4.2C), regardless of the ionic strengths (MQ, 0.5SW and SW). In both high and low oxygen level, the precipitated fractions of Ni decrease with the increasing ionic strength, highest in MQ and lowest in

SW. Nickel precipitated fractions decrease along with the reaction time in MQ and SW but remain relatively constant in 0.5SW, under both oxic and anoxic condition.

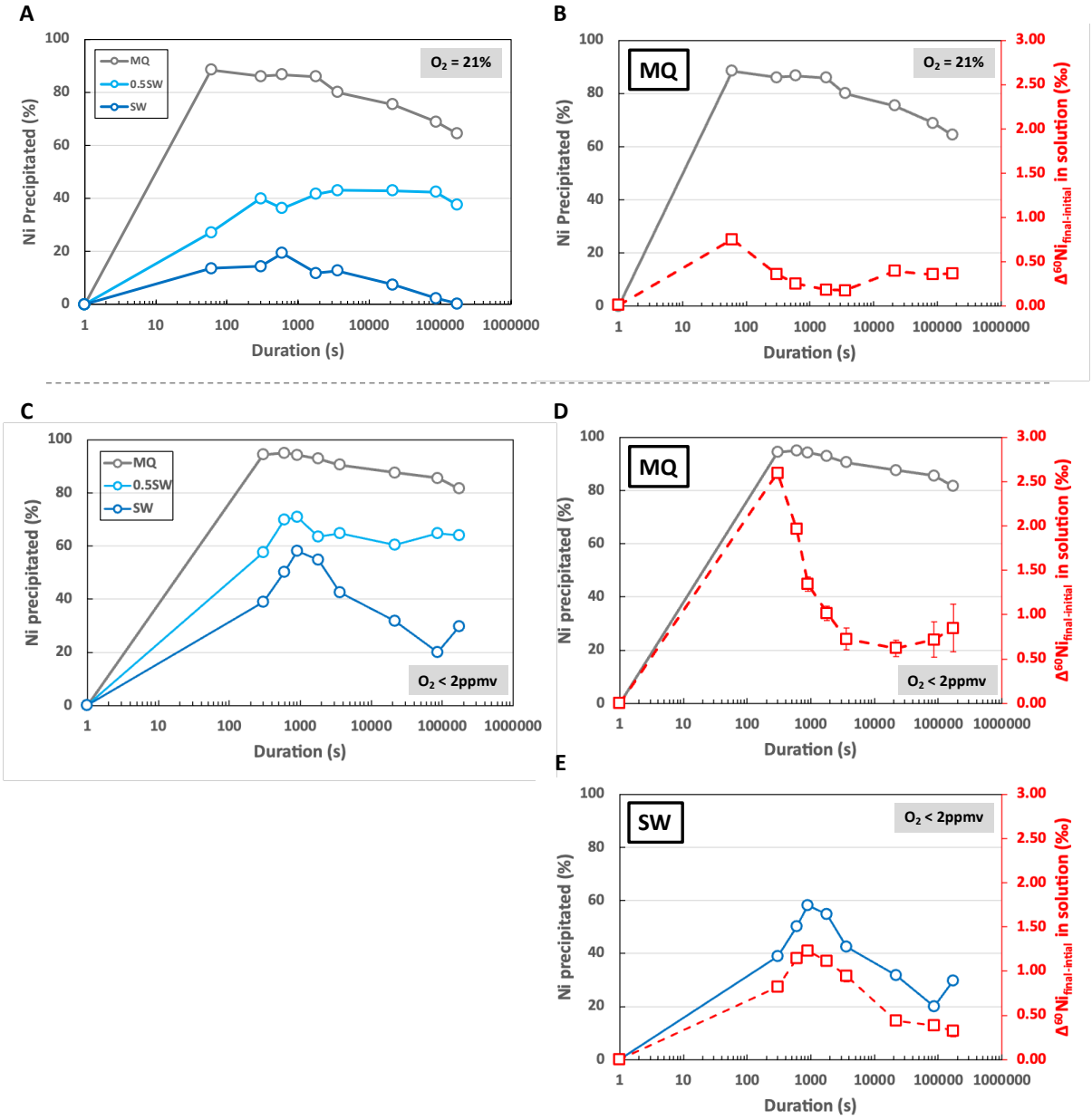


Figure 4.2. "Time-series" experiments – Ni-sulfide precipitation from media with different ionic strengths under oxic (A) and anoxic (C) conditions, and precipitated Ni fraction and $\Delta^{60}Ni_{final-initial}$ in the solution during Ni-sulfide precipitations in MQ under oxic condition (B), in MQ (D) and SW (E) under anoxic conditions. In time-series experiments (A) and (C), the concentrations of Ni (~340μM) and sulfide (~442.4 μM) are fixed. Media with different ionic strengths including Milli-Q water (MQ), 1:1 mixed Milli-Q water and seawater (SW) and seawater (SW) are applied. Oxic condition stands for O_2 ~21% of in laminar flow hood, while anoxic condition stands for O_2 <2ppmv in glove box. For Ni isotope data in (B), (D) and (E), the error bars represent the standard deviations (2SD) of the isotope compositions in solutions.

Compared to the $\delta^{60}Ni$ of initial solution ($\delta^{60}Ni$ = -0.09 ± 0.03 ‰, n=4), an enrichment of heavier Ni isotopes ($\Delta^{60}Ni_{final\text{-}initial}$ = 0.18~2.59‰ in solution) is observed in all collected solutions (MQ and SW) with time, which suggests that the Ni precipitates preferentially take up lighter Ni isotopes and leave the remaining solutions with higher $\delta^{60}Ni$ values (Figures 4.2B, 4.2D and 4.2E). This observation is in agreement with the direction of Ni isotope fractionations reported during the formation of crystalline Ni-sulfides, in both biotic ($\Delta^{60}Ni_{solid\text{-}aq}$ = –1.99‰; Parigi et al., 2022b) and abiotic fashions ($\Delta^{60}Ni_{solid\text{-}aq}$ = –0.73 ± 0.08‰; Parigi et al., 2022a).

In MQ solution under oxic condition, the Ni isotope composition in solution reaches equilibrium after 6 h, with an equilibrated $\Delta^{60}Ni_{final\text{-}initial}$ of ~0.4‰ (Figure 4.2B). In both MQ and SW solutions under anoxic condition, the Ni isotope compositions reach equilibrium similarly after 6 h, with an equilibrated $\Delta^{60}Ni_{final\text{-}initial}$ of ~0.6‰ in MQ (Figure 4.2D) and an equilibrated $\Delta^{60}Ni_{final\text{-}initial}$ of ~0.45‰ in SW (Figure 4.2E). The isotopic variation during the kinetic evolution is larger under anoxic condition ($\Delta^{60}Ni_{final\text{-}initial}$ = 0.62~2.59‰) than oxic condition ($\Delta^{60}Ni_{final\text{-}initial}$ = 0.19~0.76‰) with respect to MQ matrix. In SW matrix under anoxic condition, the $\Delta^{60}Ni_{final\text{-}initial}$ varies from 0.33 to 1.23‰.

4.4.3 Ni-sulfide precipitation under varying Ni/S ratios

In general, the Ni precipitates are enriched in light isotopes of Ni compared to the remaining solutions (Table 4.3). The lighter $\delta^{60}Ni$ values measured in solution under anoxic condition when the NiS precipitation is close to completion ($f \sim 1$) may be caused by either the contamination from the trace Ni-sulfide particles remaining in the solution or the low Ni contents left in solution after >96% of Ni is precipitated. While the heavier $\delta^{60}Ni$ values measured in the precipitates when Ni precipitation rates are low may be

caused by the contamination from the residual solution after centrifugation and separation. Similar patterns influenced by contamination have also been reported in CdS precipitation experiments (Guinoiseau et al., 2018).

Table 4.3. Compilation of Ni precipitated fractions and Ni isotope compositions of liquid ($\delta^{60}Ni_L$) and solid ($\delta^{60}Ni_S$) phases for "Ni/S ratio" experiments under both oxic and anoxic settings. 2SD represent the standard deviation of the values with number of the analysis (n).

Experimental condition	$[Ni]_{ini}$ (μM)	Ni precipitated (%)	$\delta^{60}Ni_L$ (‰)	2SD (‰)	n	$\delta^{60}Ni_S$ (‰)	2SD (‰)	n
NiS precipitation in Milli-Q Oxic $[Na_2S \cdot 9H_2O]$ = 442.4 μM pH = ~8 Reaction time = 10 min	340μM	88.40	0.66	0.02	4			
	420μM	60.27	0.05	0.02	4	-0.16	0.04	4
	520μM	49.34	0.10	0.04	4	-0.25	0.03	4
	680μM	0.07	-0.09	0.03	4	-0.38	0.07	4
	860μM	0.14	0.00	0.03	4	-0.38	0.02	4
	1040μM	24.55	-0.03	0.07	4	-0.25	0.07	4
	1720μM	6.46	-0.04	0.05	4	-0.22	0.03	4
	3460μM	2.24	-0.10	0.04	4	-0.13	0.11	4
	5200μM	2.81	-0.08	0.02	4	-0.13	0.03	4
	7800μM	2.78	-0.07	0.03	4	-0.11	0.02	4
NiS precipitation in Milli-Q Anoxic $[Na_2S \cdot 9H_2O]$ = 472 μM pH = ~8 Reaction time = 10 min	260μM	96.21	-0.56	0.12	3	-0.07	0.03	3
	340μM	88.75	0.02	0.07	3	-0.09	0.06	3
	420μM	74.01	0.17	0.07	3	-0.13	0.01	3
	520μM	62.17	0.23	0.04	3	-0.22	0.03	3
	1040μM	23.62	0.05	0.04	3	-0.29	0.08	3
	3460μM	2.82	-0.07	0.03	3	-0.34	0.09	3
NiS precipitation in Milli-Q Anoxic $[Na_2S \cdot 9H_2O]$ = 491.6 μM pH = ~8 Reaction time = 6 h	260μM	99.97	-0.44	0.01	3	0.02	0.18	4
	340μM	96.22	0.41	0.09	3	-0.08	0.05	4
	420μM	79.13	0.38	0.14	4	-0.13	0.07	4
	520μM	66.67	0.38	0.11	4	-0.28	0.07	4
	1040μM	29.07	0.12	0.07	4	-0.42	0.18	4
	3460μM	0.36	0.00	0.08	4	0.23	0.04	4

4.5 Discussion

4.5.1 Ni isotope fractionation during amorphous nickel sulfide precipitation

Although black or dark brownish precipitates were observed during precipitation experiments, no clear crystalline patterns for Ni-related sulfides were obtained in the mineral phase identification using X-ray diffraction analysis, for experiments conducted

in 0.5SW and SW matrix under anoxic condition (Figure 4.1). Whereas there was no clear peak obtained in MQ matrix under anoxic conditions for any crystalline mineral. These results suggest that the precipitates are likely to be amorphous in the experimental settings in this study, given the set concentrations of Ni and sulfide, oxygen levels and reaction times. The results agree with previous observations that XRD-invisible Ni sulfides, so-called polyphasic Ni sulfide precursors, are the first to be precipitated from solution with dissolved Ni and sulfide at 25°C (Jeong and Manthiram, 2001; Mansor et al., 2019; Wang et al., 1997; Wilkin and Rogers, 2010). This XRD-invisible phase has been characterized to be a hydrated nanocrystalline NiS with a core-shell structure, which includes a 1-3 nm core composed of crystalline millerite (β-NiS, rhombohedral) and a 3-5 nm shell composed of Ni-rich materials with structural H_2O in an amorphous configuration, resulting in an approximate chemical composition of $Ni_{1.1}S \cdot 1.5H_2O$ (Huang et al., 2009, 2010).

The isotope data with varying Ni/S^{2-} ratios display similar trends in all conditions: increasing $\delta^{60}Ni_{solution}$ and $\delta^{60}Ni_{solid}$ with decreasing Ni/S^{2-} ratios and increasing precipitation percentages. These data are fitted to both the Rayleigh fractionation model and an equilibrium fractionation model. The Rayleigh fractionation model is stated as:

$$\frac{R_R}{R_{R_0}} = f^{(\alpha-1)} \quad (4.1)$$

R_R is the $^{60}Ni/^{58}Ni$ ratio of the residual reactant, while R_{R0} is the $^{60}Ni/^{58}Ni$ ratio of the initial solution. α represents the fractionation factor and f represents the fraction of Ni remaining in solution.

The formula can be expressed in δ notation as below, where δ and δ_0 denote the final and initial Ni isotope compositions.

$$\delta = \delta_0 + 1000(\alpha - 1)lnf \quad (4.2)$$

The extent of fractionation is expressed as a fractionation factor (epsilon, ε) in parts per 1000 as below, where $\alpha_{S\text{-}L}$ is the isotope fractionation factor between precipitates and solution.

$$\varepsilon_{S\text{-}L} = (\alpha_{S\text{-}L} - 1) \times 1000\ (‰) \quad (4.3)$$

While in the equilibrium fractionation mode, the $\alpha_{S\text{-}L}$ is defined following:

$$\propto_{S-L} = \frac{\delta^{60}Ni_S + 1000}{\delta^{60}Ni_L + 1000} \approx 1 + \frac{(\delta^{60}Ni_S - \delta^{60}Ni_L)}{1000} \quad (4.4)$$

In previous studies, Ni isotope fractionation between solid and solution ($\varepsilon_{S\text{-}L}$) during precipitation of polydymite (Ni_3S_4) and millerite (β-NiS) has been characterized to be -0.73 ± 0.08‰ following the Rayleigh fractionation model, which suggests that sulfide mineral precipitates preferentially enrich isotopically light Ni and shift the remaining solution toward heavy δ^{60}Ni (Parigi et al., 2022a).

In this study, Ni isotope data of both precipitates and solutions best fit to the Rayleigh fractionation model when the reaction time is 10 min under both oxic and anoxic conditions (Figure 4.3 and Figure 4.4A). The estimated isotope fractionation $\varepsilon_{S\text{-}L}$ between precipitates and solution is slightly larger ($\varepsilon_{S\text{-}L} = -0.26$‰) in oxic condition compared to

anoxic condition (ε_{S-L} = –0.22‰), but they are nearly identical and suggest that similar mineral phases are present. With longer reaction time (6h), the isotope data of precipitates and solutions fit better to the equilibrium fractionation model with a fractionation factor ε_{S-L} = –0.5‰, suggesting the extended duration allows the system to reach equilibrium adequately (Figure 4.4B).

The Ni isotope fractionation (ε_{S-L}) of amorphous hydrated NiS precipitated in this study is estimated to be –0.22 ~ –0.26‰ under both oxic (Figure 4.3) and anoxic (Figure 4.4) conditions which suggests the ambient oxygen may not have significant influence on the sulfide precipitation, given the high concentrations of dissolved Ni and sulfide and the short equilibrium time. With 6 h reaction time, a more negative ε_{S-L} of –0.5‰ for the process is obtained, which suggests that the precipitates enrich more isotopically light Ni compared to the precipitates obtained with 10 min reaction time. There is no detectable peak in precipitates obtained with 48h reaction time, which suggests the mineral phases obtained with time shorter than this are also likely to be amorphous.

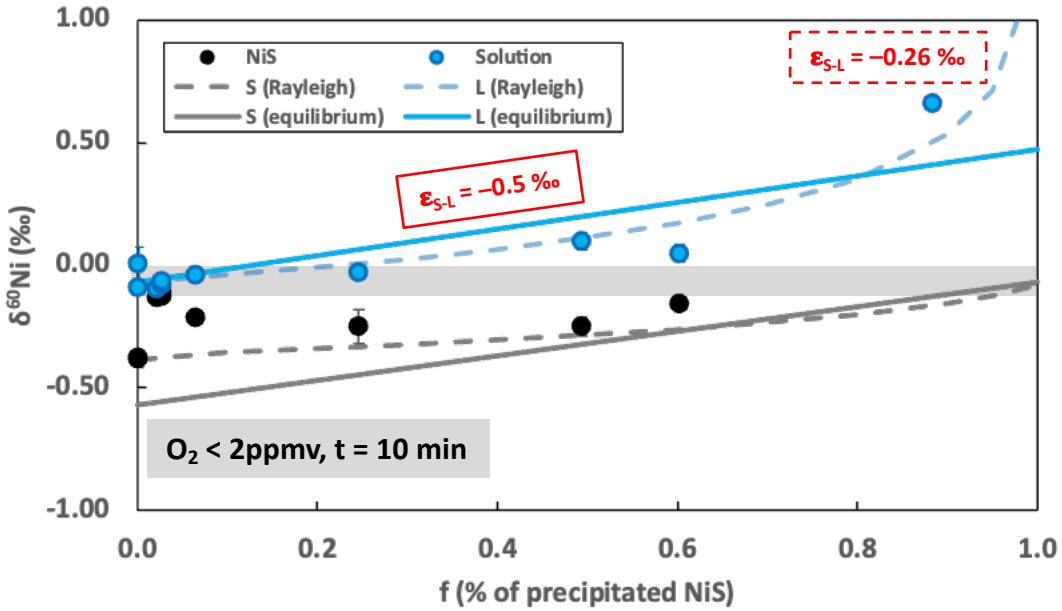


Figure 4.3. Oxic "Ni/S ratio" experiments – Ni-sulfide precipitation in MQ under oxic condition with 10 min equilibrium time. The grey shade represents the initial δ^{60}Ni of the media. The $\varepsilon_{S\text{-}L}$ value is determined by fitting the Ni isotope data with both the Rayleigh fractionation model (dotted line) and the equilibrium model (solid line). The initial $\delta^{60}Ni_L$ is -0.07‰. The error bars represent the standard deviations (2SD) of the isotope compositions, and are inside symbol size where not shown.

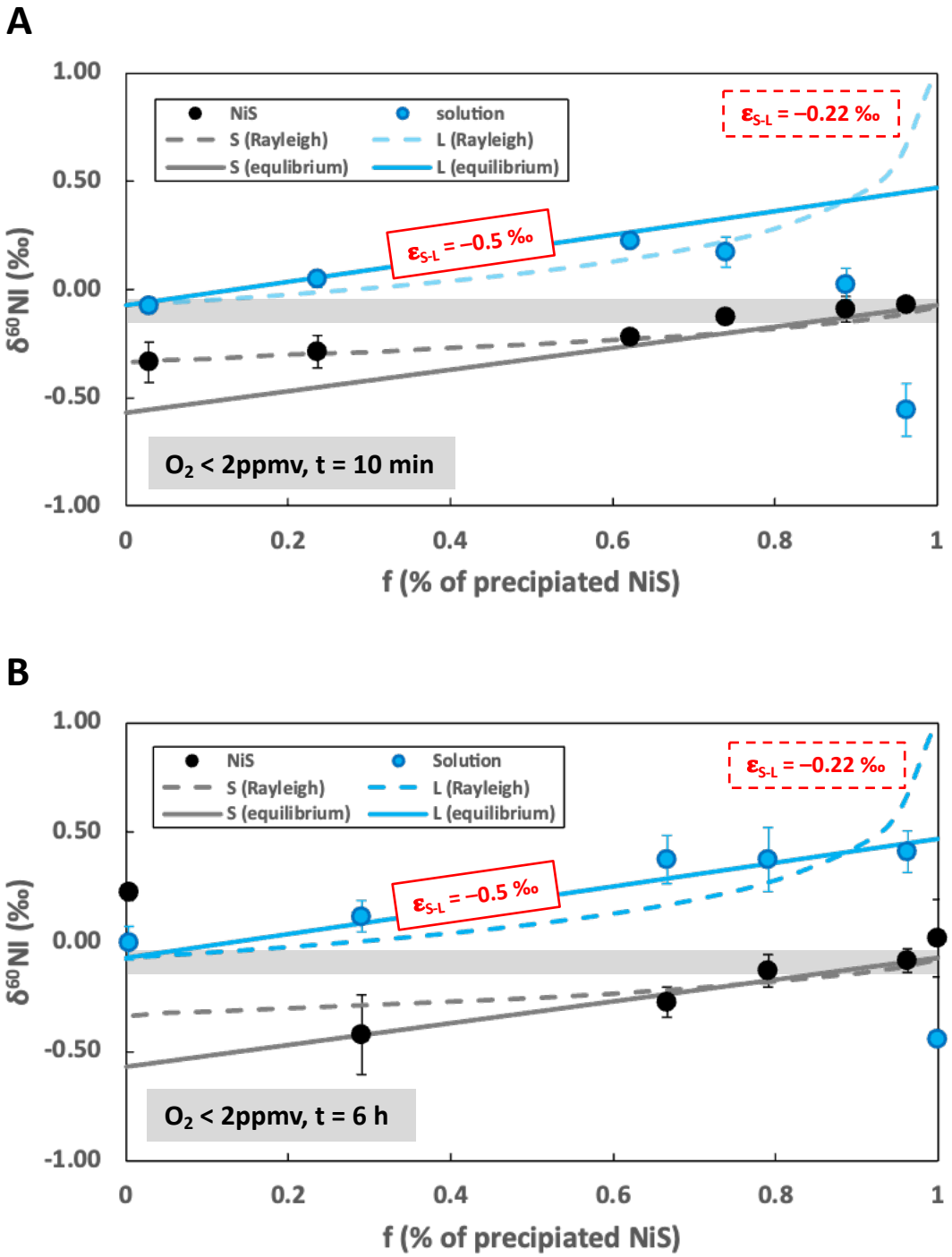


Figure 4.4. Anoxic "Ni/S ratio" experiments – Ni-sulfide precipitation in MQ under anoxic condition with (A) 10 min and (B) 6 h equilibrium time. The grey shade represents the initial δ^{60}Ni of the media. The $\varepsilon_{S\text{-}L}$ (NiS-solution) value is determined by fitting the Ni isotope data with both the Rayleigh fractionation model (dotted line) and the equilibrium model (solid line). The initial $\delta^{60}Ni_L$ is -0.074‰. The error bars represent the standard deviations (2SD) of the isotope compositions.

This study provides the first characterization of Ni isotope fractionation during the formation of amorphous hydrated NiS, showing an overall enrichment of lighter Ni isotopes in the precipitates and a lower magnitude of isotope fractionation compared to the precipitated mineral phases of Parigi et al. (2022a). The isotopic compositions of solid and solutions under varying Ni/S ratios follow the Rayleigh fractionation process with 10 min reaction time and the equilibrium fractionation process with 6 h reaction time (Figures 4.3 and 4.4), which suggests that 6 h allows the precipitated sulfides isotopically exchange with the solution adequately (Beard and Johnson, 2004; Parigi et al., 2022a; Wiederhold, 2015; Wiesli et al., 2004). Rayleigh fractionation can reflect an equilibrium isotope signal if the precipitation rate is adequately slow allowing each increment of precipitates in isotopic equilibrium with solution during precipitation (Beard and Johnson, 2004; Parigi et al., 2022a; Wiesli et al., 2004). On the other hand, Rayleigh fractionation can also reflect a kinetic isotope signal if the precipitation rate is fast and results in a non-equilibrium solid-solution system.

The preferential enrichment of lighter Ni isotopes in the amorphous phase precipitated in 10 min reaction time can be explained as a result of kinetic isotope effects, coupled with the inefficiency of exchange between Ni precipitated and Ni in the solution (Beard and Johnson, 2004; Wiederhold, 2015). Isotope signals in precipitates likely reflect both the early kinetic effect and the possible equilibrium fractionations at later stage (Parigi et al., 2022a). The later equilibrium fractionation may play the main role in the precipitates acquired with 6 h reaction time (Figure 4.4B). The equilibrium isotope fractionation may influence the superficial layer of the precipitated minerals but not significant on the isotope compositions of bulk precipitates and solution (Parigi et al.,

2022a). Furthermore, diffusion in solid-state has been argued to be extremely low or negligible at low temperature, and the redissolution-reprecipitation (recrystallization) reaction of minerals may be the only way to shift the isotope composition of a solid phase towards equilibrated values at low temperature (Beard and Johnson, 2004; Poulson et al., 2005; Wiesli et al., 2004). Therefore, the different $\varepsilon_{S\text{-}L}$ in amorphous Ni-sulfides with different reaction durations obtained from our Rayleigh and equilibrium fractionation model implies that recrystallization of precipitated amorphous Ni-sulfides occurred and changed bulk isotope compositions of precipitates between 10 min and 6 h.

The characteristic difference between the isotope fractionation factors estimated for amorphous hydrate NiS ($\varepsilon_{S\text{-}L} = -0.22 \sim -0.26‰$ after 10 min; –0.5‰ after 6 h) in this study and crystalline phases ($\varepsilon_{S\text{-}L} = -0.73‰$; Parigi et al., 2022a) may be interpreted by the varying coordination and the associated chemical bonds. It has been proposed that the preferential enrichment of lighter isotopes of Ni in Fe oxyhydroxides (Gueguen et al., 2018; Wang and Wasylenki, 2017; Wasylenki et al., 2015) and calcites (Castillo Alvarez et al., 2021) during co-precipitation experiments are not controlled by the kinetics of the reaction but the changing coordination and bonding environments. Wang and Wasylenki (2017) reported that ferrihydrite co-precipitation experiments reflect an equilibrium isotope fractionation between three pools of Ni, with their δ^{60}Ni in an order of incorporated > dissolved > adsorbed. After phase transformation, the preferential incorporation of isotopically light Ni relative to the surface-adsorbed Ni during hematite formation is related to the distortion of Ni-O octahedra in the hematite structure, which yields weaker Ni-O bond strength on average (Wang and Wasylenki, 2017). Similar enrichments of lighter isotopes into the solid phase have also been reported to be related to the distorted Ni-O octahedron in the $Ni(OH)_2$ during Ni hydroxide precipitation,

instead of the different bond-lengths (Parigi et al., 2022a). Another example of enrichment of lighter isotopes caused by structural distortion has been found that lighter Mg isotopes are preferentially enriched in Mg hydroxycarbonate due to the distortion of MgO_6 octahedra in the structure (Mavromatis et al., 2012).

Parigi et al. (2022a) attributed the Ni isotope fractionation ($\varepsilon_{S\text{-}L} = -0.73‰$) during the formation of crystalline Ni-sulfides to a change in coordination environment from Ni-O to Ni-S, suggesting that there is no significant isotope fractionation during the transformation of millerite (β-NiS) to polydymite (Ni_3S_4) which are both composed of Ni-S bonds, despite the changes in the structure and coordination environment. The Ni isotope fractionation ($\varepsilon_{S\text{-}L} = -0.22 \sim -0.26‰$ after 5min; $-0.5‰$ after 6 h) in this study during the formation of amorphous hydrated NiS shows less enrichment of isotopically light Ni than into crystalline phases, which may be explained by the different coordination in amorphous hydrated NiS resulting in a relatively stronger binding strength compared to crystalline phases (which may be distorted), as an equilibrium for isotope signals is seen after 6 h reaction time (Figure 4.4B).

4.5.2 Implications for Ni-sulfide formation mechanism

Our findings suggest that Ni isotopic signals during the formation of amorphous Ni-sulfides may reflect a kinetic fractionation process with short reaction duration (10 min), while isotope signals closer to equilibrium develops with longer reaction duration (6 h). Following this, the isotope signals in later crystalline phases may reflect the structures, bond lengths and coordination environment. For precursors of Ni sulfides (i.e., XRD-amorphous and hydrated NiS), the isotopic compositions reflect the first Ni taken up by the phase and there is insufficient time to subsequently achieve isotopic equilibrium. As

amorphous Ni-sulfides mature and crystalline Ni-sulfides develope (e.g., α-NiS, millerite (β-NiS), polydymite (Ni_3S_4), vaesite (NiS_2), godlevskite (Ni_9S_8), heazlewoodite (Ni_3S_2), Ni-rich mackinawite (Ni_xFe_{1-x} ; x≤0.56), pentlandite ($(Ni,Fe)_9S_8$), violarite ($(Ni,Fe)_3S_4$) and bravoite ($(Ni,Fe)S_2$) depending on the settings of Ni/S ratios, the presence of Fe and biological processes), recrystallization and chemical exchange allow equilibrium isotope signals to be developed between the precipitated Ni sulfides and the remaining solution (Mansor et al., 2019).

The early-stage polyphasic Ni-sulfide precursors were observed to develop into more crystalline nanoparticles up to α-NiS within a few days to weeks (Figure 4.5) (Mansor et al., 2019). The formation of α-NiS was reported to be at similar timescales at room temperature, while it was accelerated to less than a day at 60°C (Wilkin and Rogers, 2010). The presence of stacking faults and twinning structures observed during α-NiS formation indicate the crystal growth mechanism through particle attachment of nanoparticles or soluble nanoclusters, which may be followed by atomic rearrangements to form higher stability structures (De Yoreo et al., 2015; Mansor et al., 2019). It has been suggested that the degree of supersaturation during sulfide precipitation is extremely high since most metal sulfides have low solubilities (Rickard and Luther, 2006). Thus, the early stage of sulfide formation is likely dominated by nucleation events, while the additional/later mineral growth can only proceed through particle attachment or re-assembly of previously formed particles. These observations are in agreement with our findings; that Ni isotope signals in amorphous Ni-sulfides likely reflect the reaction kinetics of early nucleation events, while the Ni isotope signals in later amorphous Ni-sulfides and crystalline Ni-sulfides likely reflect the equilibrium processes including crystallization by particle attachment or re-assembly of mineral particles.

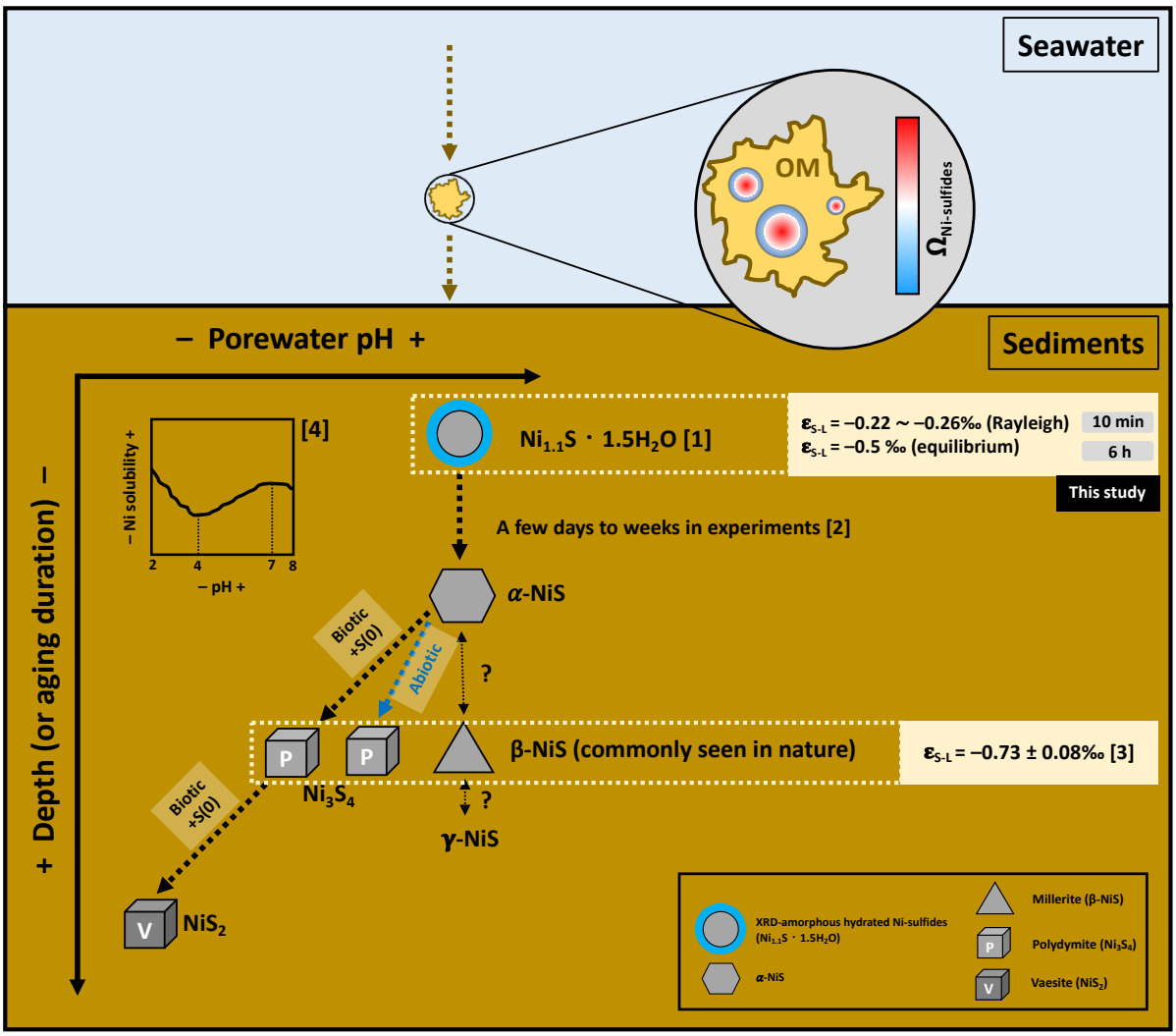


Figure 4.5. Schematic diagram of the development of Ni-sulfides and related reported Ni isotope fractionations under euxinic ocean settings. In euxinic water column, microbial respiration within aggregates of decaying organic matters (OM) leads to microenvironments supersaturated with respect to Ni-sulfides and precipitation of Ni-sulfides (Guinoiseau et al., 2018; Horner et al., 2017). The initial Ni-sulfide is XRD-amorphous hydrated Ni-sulfide, in both euxinic seawater columns and sediments. With aging duration or depth, amorphous Ni-sulfides transform into α-NiS within few days or weeks. Subsequently, α-NiS transforms into polydymite via either biotic or abiotic pathways, which the final pH in biotic precipitation experiments was reported to be slightly lower than the abiotic pathway (Mansor et al., 2019). The formation of polydymite has been reported in abiogenic precipitation but not for vaesite (Wilkin and Rogers, 2010). The formation of α-NiS, β-NiS and **γ**-NiS were mentioned in the previous work (Thiel and Gessner, 1914), but the detailed mechanism in nature remains to be confirmed. The Ni isotope fractionation factor ($\boldsymbol{\varepsilon}_{S\text{-}L}$) between solid and liquid phases during the formation of XRD-amorphous Ni-sulfides changes from –0.22~–0.26‰ with 10 min reaction time to –0.5‰ with 6 h reaction time. While the $\boldsymbol{\varepsilon}_{S\text{-}L}$ of a mixture of millerite and polydymite is determined to be –0.73 ± 0.08‰ (Parigi et al., 2022a),

respectively. References: [1] Huang et al. (2009); [2] Mansor et al. (2019); [3] Parigi et al. (2022a); [4] Wilkin and Rogers (2010).

Hexagonal α-NiS is generally regarded as a metastable phase, its stability with time appears to vary with conditions. It was reported to stay stable for over 6 months in aqueous solution at room temperature (Wang et al., 2006; Wilkin and Rogers, 2010). Alternatively, a study has shown that α-NiS is rapidly transformed to polydymite (Ni_3S_4) and then vaesite (NiS_2) with the presence of elemental sulfur during precipitation experiments (Figure 4.5) (Wilkin and Rogers, 2010). The added elemental sulfur partially oxidizes Ni from Ni^{2+} in α-NiS to Ni^{3+} in polydymite and produce polysulfides (e.g., S_2^{2-} in vaesite) by reacting with H_2S (Mansor et al., 2019). The oxidation of amorphous hydrated NiS to polydymite has also been shown to occur under anoxic condition (< 2 ppm O_2) (Huang et al., 2009). A pathway of Ni-sulfide formation (reaction 1) has been reported to share comparable processes as Fe-sulfide system (reaction 2) (Benning et al., 2000; Hunger and Benning, 2007; Mansor et al., 2019; Wang and Morse, 1996) .

Amorphous hydrated NiS → α-NiS → polydymite (Ni_3S_4) → vaesite (NiS_2) (reaction 1)

Amorphous FeS → mackinawite (FeS) → greigite (Fe_3S_4) → pyrite (FeS_2) (reaction 2)

The formation of polydymite and vaesite have been reported to mainly happen under acidic pH (Huang et al., 2009; Wang et al., 1997), which was interpreted by referring to Fe-sulfide system that (1) protons act as oxidants for the transformation of MeS to Me_3S_4 (Bourdoiseau et al., 2011) and (2) higher rate of dissolution-reprecipitation (recrystallization) rates to form MeS_2 from either MeS or Me_3S_4 (Schoonen and Barnes,

1991; Wang and Morse, 1996). The latter agrees with our findings that Ni isotope signals recorded in Ni-sulfides may reflect the kinetic effects in early-stage amorphous products as their relatively lower recrystallization rate, and the equilibrium effects in later crystalline products due to the relatively higher recrystallization rate with the development of minerals. The less negative $\varepsilon_{S\text{-}L}$ in amorphous Ni-sulfidfes (–0.22 ~ –0.26‰ after 10 min; –0.5‰ after 6 h) than the reported mixture of polydymite and millerite ($\varepsilon_{S\text{-}L} = -0.73$‰) suggests that the controlling factor of Ni isotope fractionation in Ni-sulfides may change through mineral development. Future studies looking into the Ni isotope signals during the formation of α-NiS, which is currently lacking as an intermediate product during the transformation between amorphous hydrate Ni-sulfides to crystalline polydymite or vaesite, would be beneficial for an integrated understanding of Ni-sulfide formation and the switching point between kinetic and equilibrium signals.

The presence of sulfate-reducing bacteria (SRB) has been reported to enhance the crystallinity and size of precipitated Ni-sulfides by facilitating the transformation of polyphasic precursors to more crystalline structures through both bacterial metabolites and localized precipitation within low pH micro-environments around cell walls, also with faster growth and transformation rate (Mansor et al., 2019). The Ni isotope fractionation during the formation of microbially mediated Ni-sulfides has been characterized with a fractionation factor of $\Delta^{60}Ni_{solid\text{-}aq} = -1.99$‰, consistent with a closed-system equilibrium isotope fractionation process, which shows a distinct difference between kinetic and equilibrium processes in Ni-sulfide system and a strong preference of lighter Ni isotopes with biological processes involved (Parigi et al., 2022b). Bacterial activity can be influenced by changes of environmental parameters, for instance, pH, nutrient availability and oxygen level (Singh et al., 2006), which may also exert effects

on respective Ni isotopic signals. Future investigations on Ni isotope fractionation during Ni utilization by SRB under varying conditions will be important for interpreting the differences between biogenic and non-biogenic Ni-sulfides in nature.

This study provides the first Ni isotopic signatures during the abiotic formation of amorphous hydrated Ni-sulfides and suggests clearly different natures of nickel sulfide formation during different stages, which have not been measured or considered before. These characteristic patterns indicate the potential of Ni isotopes as a tracer probing into the formation mechanism of Ni-sulfides and their foreseeable applications in environmental studies.

4.5.3 Link to modern sediment settings

Nickel isotope composition of dissolved Ni in the ocean (δ^{60}Ni = 1.44 ± 0.15‰) is significantly heavier than its main input from rivers (δ^{60}Ni = 0.8‰), which suggests either that the sedimentary outputs remove isotopically light Ni from seawater to drive the high δ^{60}Ni in the ocean, or that there are other, as yet characterized, isotopically heavy Ni inputs to the ocean (Cameron and Vance, 2014).

In oxic condition, sorption to particulate Fe-Mn oxides are regarded as an important output for Ni (Gall et al., 2013; Peacock and Sherman, 2007; Shaw et al., 1990). The organic-rich sediments at Peruvian upwelling region with low oxygen level show slightly lower δ^{60}Ni values (δ^{60}Ni = 0.94~1.33‰) compared to the average deep ocean (δ^{60}Ni = 1.33 ± 0.13‰; Lemaitre et al., 2022) but not sufficient to balance the oceanic Ni budget (Ciscato et al., 2018). Light Ni isotope compositions (δ^{60}Ni = –0.2 ~ –0.8‰) have been reported in Mn-rich sediments from the eastern Pacific, which suggests a diagenetic

remobilization of isotopically heavy Ni from Mn-rich sediments into the ocean, as an important benthic Ni flux balancing oceanic Ni budget (Little et al., 2020).

In euxinic (i.e., anoxic and sulfidic) environments, dissolved Ni can be sequestered either by co-precipitation with Fe-sulfides such as mackinawite (FeS) and pyrite (FeS_2) (Abraitis et al., 2004; Algeo and Maynard, 2004; Houben et al., 2017; Huerta-Diaz and Morse, 1992; Ikogou et al., 2017; Noël et al., 2015) or precipitation as discrete Ni-sulfides (Ferris et al., 1987). Lighter Ni isotope compositions at the surface seawater in the Black Sea were explained by the fractionation between dissolved Ni pool and Ni sulfidized species ($\Delta^{60}Ni_{Ni2+ - Ni(HS)+}$ = +0.66‰ at 25℃) (Fujii et al., 2011; Vance et al., 2016). Also, the difference of δ^{60}Ni between seawater and sediments ($\Delta^{60}Ni_{sediment\text{-}seawater}$ = −0.70‰) in euxinic Black Sea was explained by the potential removal pathway via sulfide formation (Vance et al., 2016).

The enrichment of lighter Ni isotopes during the formation of amorphous Ni-sulfides provided here ($\varepsilon_{S\text{-}L}$ = (−0.22 ~ −0.26‰ after 10 min; −0.5‰ after 6 h) and the formation of crystalline phases ($\varepsilon_{S\text{-}L}$ = −0.73‰; Parigi et al., 2022a) indicates that precipitation of Ni into sulfides is an isotopically light Ni output compared to the ocean reservoir, in euxinic settings. It was thought that the co-precipitation with Fe-sulfides is more important in terms of Ni removal under euxinic conditions due to the higher abundance of Fe (~5 wt%) compared to Ni (~0.005 wt%) in Earth's upper crust (Rudnick and Gao, 2013) and the slower reaction kinetics of Ni compared to Fe, which results in the preferential incorporation of Ni into the faster-precipitating Fe-sulfides (Morse and Luther, 1999). Subsequent observations indicated that Ni removal is decoupled from Fe-

sulfides under sulfidic and weakly acidic (pH 4~6) porewaters, suggesting the formation of discrete Ni-sulfides (Frohne et al., 2011; Huerta-Diaz et al., 1998).

Ni-sulfides have been reported in the anoxic sediments of the Black Sea (Kiratli and Ergin, 1996) and in the Baltic Sea sediments associated with pyrite nodules (Huang et al., 2010). Ni-sulfides such as millerite (NiS) are found to occur mostly in organic-rich sediments including coals (Belkin and Luo, 2008), associated with the participation of Ni during diagenetic mineralizing processes. Thus far, amorphous Ni-sulfides have not been reported in natural settings, which is likely due to its short existence time (few days to weeks) before transforming into crystalline Ni-sulfides such as α-NiS (Mansor et al., 2019). Amorphous Ni-sulfides are likely to appear in both surface sediments (Kiratli and Ergin, 1996; Vance et al., 2016) and the overlying water column (Kiratli and Ergin, 1996) in euxinic ocean settings (Figure 4.5), where the O_2 concentration decreases to essentially zero and sulfides start to form. While its subsequent transformation into crystalline Ni-sulfides likely occurs in surface sediments where for instance millerite (β-NiS) has been found (Kiratli and Ergin, 1996), the distribution of its further developed phases like polydymite (Ni_3S_4) and vaesite (NiS_2) is poorly constrained and limited by sparse data. Nevertheless, the changing solubilities and Ni isotope compositions along the development of Ni-sulfides play important roles controlling the bioavailability of Ni and its isotopes in euxinic ocean settings.

4.5.4 Implications for global oceanic Ni mass balance

The decreasing pH induced by the microbial activity of SRB may change the solubility of Ni-sulfides and their Ni isotope compositions during Ni-sulfide development, further influencing the global ocean mass balance of Ni. With the presence of SRB, it has been

suggested that the micro-environments around the cell walls of bacteria are chemically distinct from the bulk solution due to the limited diffusion at small scales, which indicates that sulfide concentration as well as the protons and organics (e.g., acetate) generated from microbial sulfate reduction reaction (reaction 3) will be concentrated in these micro-environments (Mansor et al., 2019; Purcell, 1977).

$2\ C_2H_4OHCOO^- + SO_4^{2-} \rightarrow 2\ CH_3COO^- + 2\ HCO_3^- + HS^- + H^+$ (reaction 3)

In previous bacterial cultures and natural biofilms studies, the pH of these micro-environments has been shown to reach as low as 3.5 compared to nearly neutral bulk solution (De Los Ríos et al., 2003; Hidalgo et al., 2009; Hunter and Beveridge, 2005). The combination of low pH in micro-environments and presence of elemental sulfur is likely the reason for the characteristics of biogenic Ni-sulfides (Mansor et al., 2019). The micro-environments with low pH (pH ≤ 5) around the surface of SRB are likely suitable to facilitate the formation of polydymite and vaesite (Mansor et al., 2019). The precipitation in acidic micro-environments may encounter a decrease in the degree of supersaturation as metal solubility increases with decreasing pH, which may result in slower nucleation rates and faster growth rates compared to higher pH settings (Lewis, 2010). Similar observations have been reported during the formation of Fe-sulfides (mackinawite and pyrite) which tend to grow larger when precipitated under acidic condition (Schoonen and Barnes, 1991; Wang and Morse, 1996).

As the formation of polydymite and vaesite is favored under low pH condition and metal solubility tends to increase with decreasing pH (Huang et al., 2009; Wang et al., 1997), the decrease of pH in the micro-environments induced by the released protons from

microbial sulfate reduction reaction is likely to trigger partial releases of Ni to the micro-environments during the development of Ni-sulfides from amorphous to crystalline phase (Mansor et al., 2019; Pankhania et al., 1986; Voordouw, 2002). The solubility of Ni mainly increases in two pH intervals: when the pH decreases from modern seawater ocean level (~8.1) to ~7 and when pH decreases below 4 (Figure 4.5). This calculation is based on a Ni speciation model taking Ni^{2+}, $NiHS^{+}$ and $Ni(HS)_3^{-}$ into account as a function of pH, with total dissolved sulfide assumed to be 1 mM (Wilkin and Rogers, 2010), which remains to be confirmed in natural settings. Based on Ni isotope signals, it suggests a remobilization of isotopically heavy Ni to the ambient solution during the phase transformations from amorphous to crystalline Ni-sulfides under both abiotic and biotic formation processes, with likely larger magnitude of changes on pH and solubility in the biotic process. Depending on the pH reduction during Ni-sulfide development, via abiotic or abiotic pathway, the solubility of Ni can increase by an order of magnitude when pH decreases from 8 to 7, decrease by two orders of magnitude when pH decreases from 7 to 4 and increase again when pH is below 4 (Wilkin and Rogers, 2010).

The $\delta^{60}Ni$ of euxinic Black Sea sediments is around 0.3 to 0.6‰, which has been explained by the Ni removal as sulfidized species ($\Delta^{60}Ni_{Ni2+ - Ni(HS)+}$ = 0.66‰ at 25°C; Fujii et al., 2014) from seawaters into sediments, given the $\delta^{60}Ni$ of potential Ni input from River Danube and open ocean feeding the deep Black Sea through the Bosphorous are around 1.25‰ and 1.44‰, respectively (Vance et al., 2016). Considering a Ni output flux of 0.15 × 10^8 mol Ni/yr into euxinic sediments (Ciscato et al., 2018; Vance et al., 2016) and that the pH ranges at the 75m depth and in the deep-water part are 8.35~8.41 and 7.88~8.30, respectively (Polonsky and Grebneva, 2019), the porewater pH in the Black Sea sediments ranging from 7.3~7.6 at the surface to 6.5~7.0 at the ~300 cm depth (Aloisi et

al., 2004) indicates an increase of Ni solubility from ~1 × 10^{-5} M at pH ~8 in the bottom seawaters to ~2 × 10^{-5} M at pH ~7.5 in the core-top sediments (Wilkin and Rogers, 2010). With depth in sediments, Ni solubility increases to ~3 × 10^{-5} M at pH ~7.0 and decreases slightly back to ~2 × 10^{-5} M at pH ~6.5, suggesting that Ni solubility and Ni-sulfide formation under euxinic conditions can be largely controlled by the pH which is likely the result of sulfate reducing microbial activity. Although more data are needed to assess this potential Ni outflux from euxinic sediments in oceanic Ni budget, the changing solubility suggests that 1~2 times of 0.15 × 10^{8} mol Ni/yr may outflux from euxinic sediments at the Black Sea after early diagenesis (aging and equilibrium), given that Ni isotope fractionations between Ni inputs (δ^{60}Ni = 1.25~1.44‰; Vance et al., 2016) and sediments (δ^{60}Ni = 0.3~0.6‰; Vance et al., 2016) in the Black Sea are consistent with a local Ni removal as crystalline sulfides ($\Delta^{60}Ni_{Ni2+ - Ni(HS)+}$ = 0.66‰, Fujii et al., 2014; ε_{S-L} = −0.73 ± 0.08‰, Parigi et al., 2022a).

Experimental results show that the timescale of this benthic Ni flux from mineral transformation may be a few days to months, depending on the mineral phases and environmental conditions (e.g., pH and elemental S) (Huang et al., 2009; Mansor et al., 2019; Wang et al., 2006; Wilkin and Rogers, 2010). This study proposes a diagenetic remobilization of heavy Ni isotopes to the ocean likely at the surface of euxinic sediments, via Ni-sulfide transformation from amorphous to crystalline phases, which can contribute to balance marine Ni budget.

4.6 Conclusions

This study provides constraints on Ni isotope fractionation during the formation of amorphous hydrated Ni-sulfides under conditions with varying oxygen levels and ionic

strengths. No significant differences on the precipitated mineral phases and estimated isotope fractionations were observed between settings of high and low oxygen level within the short reaction time of this study (~48 h). The precipitated amorphous Ni-sulfides show enrichments of isotopically light Ni from the media, and the precipitation broadly follows the Rayleigh fractionation process with a fractionation factor $\varepsilon_{S\text{-}L}$ of –0.22 ~ –0.26‰ with 10 min reaction time and fits to the equilibrium fractionation process with a fractionation factor $\varepsilon_{S\text{-}L}$ of –0.5‰ after 6 h. This work suggests that the Ni isotope signals recorded in Ni-sulfides evolves with mineral development, with more crystalline phases becoming increasingly isotopically light. This may reflect a kinetic isotope effect during nucleation events in the early-stage amorphous Ni-sulfides, compared to an isotope fractionation closer to equilibrium during crystallization. In natural settings, the decreased pH generated by the activity of sulfate reducing bacteria may facilitate the phase transformation of Ni-sulfides from amorphous to crystalline phases, increase the solubility of Ni, and trigger a remobilization of isotopically heavy Ni back to the ocean, at the surface of euxinic sediments. The new constraints on Ni isotope fractionation during sulfide formation will help in the use of Ni isotopes in sulfides and sediments as a tracer to understand present and past environmental processes.

4.7 References

Abraitis, P.K., Pattrick, R.A.D., Vaughan, D.J., 2004. Variations in the compositional, textural and electrical properties of natural pyrite: A review. Int. J. Miner. Process. 74, 41–59. https://doi.org/10.1016/j.minpro.2003.09.002

Algeo, T.J., Maynard, J.B., 2004. Trace-element behavior and redox facies in core shales of Upper Pennsylvanian Kansas-type cyclothems. Chem. Geol. 206, 289–318. https://doi.org/10.1016/j.chemgeo.2003.12.009

Aloisi, G., Wallmann, K., Drews, M., Bohrmann, G., 2004. Evidence for the submarine weathering of silicate minerals in Black Sea sediments: Possible implications for the marine Li and B cycles. Geochemistry, Geophys. Geosystems 5. https://doi.org/10.1029/2003GC000639

Beard, B.L., Johnson, C.M., 2004. Fe Isotope Variations in the Modern and Ancient Earth and Other Planetary Bodies. Rev. Mineral. Geochemistry 55, 319–357.

Belkin, H.E., Luo, K., 2008. Late-stage sulfides and sulfarsenides in Lower Cambrian black shale (stone coal) from the Huangjiawan mine, Guizhou Province, People's Republic of China. Mineral. Petrol. 92, 321–340. https://doi.org/10.1007/s00710-007-0201-9

Benning, L.G., Wilkin, R.T., Barnes, H.L., 2000. Reaction pathways in the Fe-S system below 100°C. Chem. Geol. 167, 25–51. https://doi.org/10.1016/S0009-2541(99)00198-9

Bourdoiseau, J.A., Jeannin, M., Rémazeilles, C., Sabot, R., Refait, P., 2011. The transformation of mackinawite into greigite studied by Raman spectroscopy. J. Raman Spectrosc. 42, 496–504. https://doi.org/10.1002/jrs.2729

Bruland, K.W., Middag, R., Lohan, M.C., 2014. Controls of Trace Metals in Seawater, 2nd ed, Treatise on Geochemistry: Second Edition. Elsevier Ltd. https://doi.org/10.1016/B978-0-08-095975-7.00602-1

Cameron, V., Vance, D., 2014. Heavy nickel isotope compositions in rivers and the oceans. Geochim. Cosmochim. Acta 128, 195–211. https://doi.org/10.1016/j.gca.2013.12.007

Castillo Alvarez, C., Quitte, G., Schott, J., Oelkers, E.H., 2021. Nickel isotope fractionation as a function of carbonate growth rate during Ni coprecipitation with calcite. Geochim. Cosmochim. Acta 299, 184–198. https://doi.org/10.1016/j.gca.2021.02.019

Castillo Alvarez, C., Quitté, G., Schott, J., Oelkers, E.H., 2020. Experimental determination of Ni isotope fractionation during Ni adsorption from an aqueous fluid onto calcite surfaces. Geochim. Cosmochim. Acta 273, 26–36. https://doi.org/10.1016/j.gca.2020.01.010

Chung, F.H., 1975. Quantitative interpretation of X-ray diffraction patterns of mixtures.

III. Simultaneous determination of a set of reference intensities. J. Appl. Crystallogr. 8, 17–19. https://doi.org/10.1107/s0021889875009454

Chung, F.H., 1974a. Quantitative interpretation of X-ray diffraction patterns of mixtures. I. Matrix-flushing method for quantitative multicomponent analysis. J. Appl. Crystallogr. 7, 519–525. https://doi.org/10.1107/s0021889874010375

Chung, F.H., 1974b. Quantitative interpretation of X-ray diffraction patterns of mixtures. II. Adiabatic principle of X-ray diffraction analysis of mixtures. J. Appl. Crystallogr. 7, 526–531. https://doi.org/10.1107/s0021889874010387

Ciscato, E.R., Bontognali, T.R.R., Vance, D., 2018. Nickel and its isotopes in organic-rich sediments: implications for oceanic budgets and a potential record of ancient seawater. Earth Planet. Sci. Lett. 494, 239–250. https://doi.org/10.1016/j.epsl.2018.04.061

De Los Ríos, A., Wierzchos, J., Sancho, L.G., Ascaso, C., 2003. Acid microenvironments in microbial biofilms of antarctic endolithic microecosystems. Environ. Microbiol. 5, 231–237. https://doi.org/10.1046/j.1462-2920.2003.00417.x

De Yoreo, J.J., Gilbert, P.U.P.A., Sommerdijk, N.A.J.M., Penn, R.L., Whitelam, S., Joester, D., Zhang, H., Rimer, J.D., Navrotsky, A., Banfield, J.F., Wallace, A.F., Michel, F.M., Meldrum, F.C., Cölfen, H., Dove, P.M., 2015. Crystallization by particle attachment in synthetic, biogenic, and geologic environments. Science (80-.). 349. https://doi.org/10.1126/science.aaa6760

Estrade, N., Cloquet, C., Echevarria, G., Sterckeman, T., Deng, T., Tang, Y.T., Morel, J.L., 2015. Weathering and vegetation controls on nickel isotope fractionation in surface ultramafic environments (Albania). Earth Planet. Sci. Lett. 423, 24–35. https://doi.org/10.1016/j.epsl.2015.04.018

Ferris, F.G., Fyfe, W.S., Beveridge, T.J., 1987. Bacteria as nucleation sites for authigenic minerals in a metal-contaminated lake sediment. Chem. Geol. 63, 225–232. https://doi.org/10.1016/0009-2541(87)90165-3

Fietzke, J., Frische, M., 2016. Experimental evaluation of elemental behavior during LA-ICP-MS: Influences of plasma conditions and limits of plasma robustness. J. Anal. At. Spectrom. 31, 234–244. https://doi.org/10.1039/c5ja00253b

Frohne, T., Rinklebe, J., Diaz-Bone, R.A., Du Laing, G., 2011. Controlled variation of redox conditions in a floodplain soil: Impact on metal mobilization and biomethylation of arsenic and antimony. Geoderma 160, 414–424. https://doi.org/10.1016/j.geoderma.2010.10.012

Fujii, T., Moynier, F., Blichert-Toft, J., Albarède, F., 2014. Density functional theory estimation of isotope fractionation of Fe, Ni, Cu, and Zn among species relevant to geochemical and biological environments. Geochim. Cosmochim. Acta 140, 553–576. https://doi.org/10.1016/j.gca.2014.05.051

Fujii, T., Moynier, F., Dauphas, N., Abe, M., 2011. Theoretical and experimental investigation of nickel isotopic fractionation in species relevant to modern and ancient oceans. Geochim. Cosmochim. Acta 75, 469–482. https://doi.org/10.1016/j.gca.2010.11.003

Gall, L., Williams, H., Siebert, C., Halliday, A., 2012. Determination of mass-dependent variations in nickel isotope compositions using double spiking and MC-ICPMS. J. Anal. At. Spectrom. 27, 137–145. https://doi.org/10.1039/c1ja10209e

Gall, L., Williams, H.M., Siebert, C., Halliday, A.N., Herrington, R.J., Hein, J.R., 2013. Nickel isotopic compositions of ferromanganese crusts and the constancy of deep ocean inputs and continental weathering effects over the Cenozoic. Earth Planet. Sci. Lett. 375, 148–155. https://doi.org/10.1016/j.epsl.2013.05.019

Gueguen, B., Rouxel, O., Ponzevera, E., Bekker, A., Fouquet, Y., 2013. Nickel Isotope Variations in Terrestrial Silicate Rocks and Geological Reference Materials Measured by MC-ICP-MS. https://doi.org/10.1111/j.1751-908X.2013.00209.x

Gueguen, B., Rouxel, O., Rouget, M.L., Bollinger, C., Ponzevera, E., Germain, Y., Fouquet, Y., 2016. Comparative geochemistry of four ferromanganese crusts from the Pacific Ocean and significance for the use of Ni isotopes as paleoceanographic tracers. Geochim. Cosmochim. Acta 189, 214–235. https://doi.org/10.1016/j.gca.2016.06.005

Gueguen, B., Sorensen, J. V., Lalonde, S. V., Peña, J., Toner, B.M., Rouxel, O., 2018. Variable Ni isotope fractionation between Fe-oxyhydroxides and implications for the use of Ni isotopes as geochemical tracers. Chem. Geol. 481, 38–52. https://doi.org/10.1016/j.chemgeo.2018.01.023

Guinoiseau, D., Galer, S.J.G., Abouchami, W., 2018. Effect of cadmium sulphide precipitation on the partitioning of Cd isotopes: Implications for the oceanic Cd cycle. Earth Planet. Sci. Lett. 498, 300–308. https://doi.org/10.1016/j.epsl.2018.06.039

Hidalgo, G., Burns, A., Herz, E., Hay, A.G., Houston, P.L., Wiesner, U., Lion, L.W., 2009. Functional tomographic fluorescence imaging of pH microenvironments in microbial biofilms by use of silica nanoparticle sensors. Appl. Environ. Microbiol. 75, 7426–7435. https://doi.org/10.1128/AEM.01220-09

Hindersmann, I., Mansfeldt, T., 2014. Trace element solubility in a multimetal-contaminated soil as affected by redox conditions. Water. Air. Soil Pollut. 225. https://doi.org/10.1007/s11270-014-2158-8

Horner, T.J., Pryer, H. V., Nielsen, S.G., Crockford, P.W., Gauglitz, J.M., Wing, B.A., Ricketts, R.D., 2017. Pelagic barite precipitation at micromolar ambient sulfate. Nat. Commun. 8, 1–11. https://doi.org/10.1038/s41467-017-01229-5

Houben, G.J., Sitnikova, M.A., Post, V.E.A., 2017. Terrestrial sedimentary pyrites as a potential source of trace metal release to groundwater – A case study from the Emsland, Germany. Appl. Geochemistry 76, 99–111.

https://doi.org/10.1016/j.apgeochem.2016.11.019

Huang, S., Harris, K.D.M., Lopez-Capel, E., Manning, D.A.C., Rickard, D., 2009. 'Amorphous nickel sulfide' is hydrated nanocrystalline NiS with a core-shell structure. Inorg. Chem. 48, 11486–11488. https://doi.org/10.1021/ic901512z

Huang, S., Lopez-Capel, E., Manning, D.A.C., Rickard, D., 2010. The composition of nanoparticulate nickel sulfide. Chem. Geol. 277, 207–213. https://doi.org/10.1016/j.chemgeo.2010.08.001

Huerta-Diaz, M.A., Morse, J.W., 1992. Pyritization of trace metals in anoxic marine sediments: RN - Geochim. Cosmochim. Acta, v. 56, p. 2681-2702. Geochim. Cosmochim. Acta 56, 2681–2702.

Huerta-Diaz, M.A., Tessier, A., Carignan, R., 1998. Geochemistry of trace metals associated with reduced sulfur in freshwater sediments. Appl. Geochemistry 13, 213–233. https://doi.org/10.1016/S0883-2927(97)00060-7

Hunger, S., Benning, L.G., 2007. Greigite: A true intermediate on the polysulfide pathway to pyrite. Geochem. Trans. 8, 1–20. https://doi.org/10.1186/1467-4866-8-1

Hunter, R.C., Beveridge, T.J., 2005. Application of a pH-sensitive fluoroprobe (C-SNARF-4) for pH microenvironment analysis in Pseudomonas aeruginosa biofilms. Appl. Environ. Microbiol. 71, 2501–2510. https://doi.org/10.1128/AEM.71.5.2501-2510.2005

Ikogou, M., Ona-Nguema, G., Juillot, F., Le Pape, P., Menguy, N., Richeux, N., Guigner, J.M., Noël, V., Brest, J., Baptiste, B., Morin, G., 2017. Long-term sequestration of nickel in mackinawite formed by Desulfovibrio capillatus upon Fe(III)-citrate reduction in the presence of thiosulfate. Appl. Geochemistry 80, 143–154. https://doi.org/10.1016/j.apgeochem.2017.02.019

Jeong, Y.U., Manthiram, A., 2001. Synthesis of nickel sulfides in aqueous solutions using sodium dithionite. Inorg. Chem. 40, 73–77. https://doi.org/10.1021/ic000819d

Kiratli, N., Ergin, M., 1996. Partitioning of heavy metals in surface Black Sea sediments. Appl. Geochemistry 11, 775–788. https://doi.org/10.1016/S0883-2927(96)00037-6

Lemaitre, N., Du, J., de Souza, G.F., Archer, C., Vance, D., 2022. The essential bioactive role of nickel in the oceans: Evidence from nickel isotopes. Earth Planet. Sci. Lett. 584, 117513. https://doi.org/10.1016/j.epsl.2022.117513

Lewis, A.E., 2010. Review of metal sulphide precipitation. Hydrometallurgy 104, 222–234. https://doi.org/10.1016/j.hydromet.2010.06.010

Little, S.H., Archer, C., Mcmanus, J., Najorka, J., Wegorzewski, A. V, Vance, D., 2020. Towards balancing the oceanic Ni budget. Earth Planet. Sci. Lett. 547, 116461. https://doi.org/10.1016/j.epsl.2020.116461

Mansor, M., Winkler, C., Hochella, M.F., Xu, J., 2019. Nanoparticulate nickel-hosting phases in sulfidic environments: Effects of ferrous iron and bacterial presence on mineral formation mechanism and solid-phase nickel distribution. Front. Earth Sci. 7, 1–15. https://doi.org/10.3389/feart.2019.00151

Mavromatis, V., Pearce, C.R., Shirokova, L.S., Bundeleva, I.A., Pokrovsky, O.S., Benezeth, P., Oelkers, E.H., 2012. Magnesium isotope fractionation during hydrous magnesium carbonate precipitation with and without cyanobacteria. Geochim. Cosmochim. Acta 76, 161–174. https://doi.org/10.1016/j.gca.2011.10.019

Morse, J.W., Luther, G.W., 1999. Chemical influences on trace metal-sulfide interactions in anoxic sediments. Geochim. Cosmochim. Acta 63, 3373–3378.

Noël, V., Morin, G., Juillot, F., Marchand, C., Brest, J., Bargar, J.R., Muñoz, M., Marakovic, G., Ardo, S., Brown, G.E., 2015. Ni cycling in mangrove sediments from New Caledonia. Geochim. Cosmochim. Acta 169, 82–98. https://doi.org/10.1016/j.gca.2015.07.024

Pankhania, I.P., Gow, L.A., Hamilton, W.A., 1986. The effect of hydrogen on the growth of Desulfovibrio vulgaris (Hildenborough) on lactate. J. Gen. Microbiol. 132, 3349–3356. https://doi.org/10.1099/00221287-132-12-3349

Parigi, R., Chen, N., Reid, J.W., Ptacek, C.J., Blowes, D.W., 2022a. Nickel isotope fractionation during precipitation of Ni secondary minerals and synchrotron-based analysis of the precipitates. Geochim. Cosmochim. Acta 317, 91–105. https://doi.org/10.1016/j.gca.2021.10.027

Parigi, R., Pakostova, E., Reid, J.W., Saurette, E.M., McBeth, J.M., Ptacek, C.J., Blowes, D.W., 2022b. Nickel Isotope Fractionation As an Indicator of Ni Sulfide Precipitation Associated with Microbially Mediated Sulfate Reduction. Environ. Sci. Technol. 56, 7954–7962. https://doi.org/10.1021/acs.est.2c00523

Peacock, C.L., Sherman, D.M., 2007. Sorption of Ni by birnessite: Equilibrium controls on Ni in seawater. Chem. Geol. 238, 94–106. https://doi.org/10.1016/j.chemgeo.2006.10.019

Polonsky, A.B., Grebneva, E.A., 2019. The Spatiotemporal Variability of pH in Waters of the Black Sea. Dokl. Earth Sci. 486, 669–674. https://doi.org/10.1134/S1028334X19060072

Poulson, R.L., Johnson, C.M., Beard, B.L., 2005. Iron isotope exchange kinetics at the nanoparticulate ferrihydrite surface. Am. Mineral. 90, 758–763. https://doi.org/10.2138/am.2005.1802

Purcell, E.M., 1977. Life at low Reynolds number. Am. J. Phys. 45, 3–11. https://doi.org/10.1119/1.10903

Ragsdale, S.W., 2009. Nickel-based enzyme systems. J. Biol. Chem. 284, 18571–18575. https://doi.org/10.1074/jbc.R900020200

Ratié, G., Garnier, J., Calmels, D., Vantelon, D., Guimarães, E., Monvoisin, G., Nouet, J., Ponzevera, E., Quantin, C., 2018. Nickel distribution and isotopic fractionation in a Brazilian lateritic regolith: Coupling Ni isotopes and Ni K-edge XANES. Geochim. Cosmochim. Acta 230, 137–154. https://doi.org/10.1016/j.gca.2018.03.026

Ratié, G., Jouvin, D., Garnier, J., Rouxel, O., Miska, S., Guimarães, E., Cruz Vieira, L., Sivry, Y., Zelano, I., Montarges-Pelletier, E., Thil, F., Quantin, C., 2015. Nickel isotope fractionation during tropical weathering of ultramafic rocks. Chem. Geol. 402, 68–76. https://doi.org/10.1016/j.chemgeo.2015.02.039

Ratié, G., Quantin, C., Maia De Freitas, A., Echevarria, G., Ponzevera, E., Garnier, J., 2019. The behavior of nickel isotopes at the biogeochemical interface between ultramafic soils and Ni accumulator species. J. Geochemical Explor. 196, 182–191. https://doi.org/10.1016/j.gexplo.2018.10.008

Rickard, D., Luther, G.W., 2006. Metal sulfide complexes and clusters. Rev. Mineral. Geochemistry 61, 421–504. https://doi.org/10.2138/rmg.2006.61.8

Rudnick, R.L., Gao, S., 2013. Composition of the Continental Crust, 2nd ed, Treatise on Geochemistry: Second Edition. Elsevier Ltd. https://doi.org/10.1016/B978-0-08-095975-7.00301-6

Saunders, N.J., Barling, J., Harvey, J., Halliday, A.N., Saunders, N.J., Barling, J., Harvey, J., Halliday, A.N., 2020. Heterogeneous nickel isotopic compositions in the terrestrial mantle - Part 1. Geochim. Cosmochim. Acta. https://doi.org/10.1016/j.gca.2020.06.029

Schoonen, M.A.A., Barnes, H.L., 1991. Reactions forming pyrite and marcasite from solution: II. Via FeS precursors below 100°C. Geochim. Cosmochim. Acta 55, 1505–1514.

Sclater, F.R., Boyle, E., Edmond, J.M., 1976. On the marine geochemistry of nickel. Earth Planet. Sci. Lett. 31, 119–128. https://doi.org/10.1038/263042a0

Shaw, T.J., Gieskes, J.M., Jahnke, R.A., 1990. Early diagenesis in differing depositional environments: The response of transition metals in pore water. Geochim. Cosmochim. Acta 54, 1233–1246. https://doi.org/10.1016/0016-7037(90)90149-F

Siebert, C., McManus, J., Bice, A., Poulson, R., Berelson, W.M., 2006. Molybdenum isotope signatures in continental margin marine sediments. Earth Planet. Sci. Lett. 241, 723–733. https://doi.org/10.1016/j.epsl.2005.11.010

Singh, R., Paul, D., Jain, R.K., 2006. Biofilms: implications in bioremediation. Trends Microbiol. 14, 389–397. https://doi.org/10.1016/j.tim.2006.07.001

Sorensen, V., Gueguen, B., Stewart, B.D., Peña, J., Rouxel, O., Toner, B.M., 2020. Large nickel isotope fractionation caused by surface complexation reactions with hexagonal birnessite 537. https://doi.org/10.1016/j.chemgeo.2020.119481

Spivak-Birndorf, L.J., Wang, S.J., Bish, D.L., Wasylenki, L.E., 2018. Nickel isotope fractionation during continental weathering. Chem. Geol. 476, 316–326. https://doi.org/10.1016/j.chemgeo.2017.11.028

Thiel, A., Gessner, H., 1914. Über Nickelsulfid und Kobaltsulfid. I. Die scheinbare Anomalie im Verhalten des Nickelsulfids gegen Säure, in: Zeitschrift Für Anorganische Chemie. John Wiley & Sons, Ltd, pp. 1–57.

Tribovillard, N., Algeo, T.J., Lyons, T., Riboulleau, A., 2006. Trace metals as paleoredox and paleoproductivity proxies: An update. Chem. Geol. 232, 12–32. https://doi.org/10.1016/j.chemgeo.2006.02.012

Vance, D., Little, S.H., Archer, C., Cameron, V., Andersen, M.B., Rijkenberg, M.J.A., Lyons, T.W., 2016. The oceanic budgets of nickel and zinc isotopes: The importance of sulfdic environments as illustrated by the Black Sea. Philos. Trans. R. Soc. A Math. Phys. Eng. Sci. 374. https://doi.org/10.1098/rsta.2015.0294

Voordouw, G., 2002. Carbon monoxide cycling by Desulfovibrio vulgaris Hildenborough. J. Bacteriol. 184, 5903–5911. https://doi.org/10.1128/JB.184.21.5903-5911.2002

Wang, H., Pring, A., Ngothai, Y., O'Neill, B., 2006. The kinetics of the α → β transition in synthetic nickel monosulfide. Am. Mineral. 91, 171–181. https://doi.org/10.2138/am.2006.1962

Wang, L., Schultz, M., Matijević, E., 1997. Preparation and properties of uniform amorphous and crystalline colloidal nickel sulfide. Colloid Polym. Sci. 275, 593–598. https://doi.org/10.1007/s003960050123

Wang, Q., Morse, J.W., 1996. Pyrite formation under conditions approximating those in anoxic sediments: I. Pathway and morphology. Mar. Chem. 52, 99–121. https://doi.org/10.1016/0304-4203(95)00082-8

Wang, S., Wasylenki, L.E., 2017. ScienceDirect Experimental constraints on reconstruction of Archean seawater Ni isotopic composition from banded iron formations. Geochim. Cosmochim. Acta 206, 137–150. https://doi.org/10.1016/j.gca.2017.02.023

Wasylenki, L.E., Howe, H.D., Spivak-birndorf, L.J., Bish, D.L., 2015. Ni isotope fractionation during sorption to ferrihydrite : Implications for Ni in banded iron formations. Chem. Geol. 400, 56–64. https://doi.org/10.1016/j.chemgeo.2015.02.007

Wiederhold, J.G., 2015. Metal stable isotope signatures as tracers in environmental geochemistry. Environ. Sci. Technol. 49, 2606–2624. https://doi.org/10.1021/es504683e

Wiesli, R.A., Beard, B.L., Johnson, C.M., 2004. Experimental determination of Fe isotope fractionation between aqueous Fe(II), siderite and 'green rust' in abiotic systems. Chem. Geol. 211, 343–362. https://doi.org/10.1016/j.chemgeo.2004.07.002

Wilkin, R.T., Rogers, D.A., 2010. Nickel sulfide formation at low temperature: Initial precipitates, solubility and transformation products. Environ. Chem. 7, 514–523. https://doi.org/10.1071/EN10076

Wu, G., Zhu, J.M., Wang, X., Han, G., Tan, D., Wang, S.J., 2019. A novel purification method for high precision measurement of Ni isotopes by double spike MC-ICP-MS. J. Anal. At. Spectrom. 34, 1639–1651. https://doi.org/10.1039/c9ja00077a

Yang, L., Nadeau, K., P., G., Brophy, C., Gedara, I.P., Meija, J., Mester, Z., 2015. SLRS-6 River Water Certified Reference Material for Trace Metals and other Constituents. Natl. Res. Counc. Canada 6. https://doi.org/doi.org/10.4224/crm.2015.slrs-6

CHAPTER 5

Controls on Ni isotope compositions of organic-rich sediments from Namibian margin

5 Controls on Ni isotope compositions of organic-rich sediments from Namibian margin

5.1. Introduction

Nickel (Ni) is biologically essential for various enzyme activities which control the global carbon, oxygen and nitrogen cycles via production and utilization of ubiquitous gases (e.g., O_2, H_2, CO, CO_2, CH_4, NH_3) (Mulrooney and Hausinger, 2003; Ragsdale, 2009). In the ocean, Ni is characterized by a nutrient-type seawater profile which is controlled by biological utilization in the photic zone and regeneration at depth, with strong correlations with phosphate in the upper water column and with silicate in the deep ocean (Bruland, 1980; Sclater et al., 1976). As an important component for many biological processes, Ni oceanic cycling involving various sources and sinks via distinct processes has been of interest in the community. The Ni isotope system (δ^{60}Ni) has been applied as a tracer for deciphering and quantifying these processes in oceanic Ni cycling

The δ^{60}Ni of the modern ocean is estimated to be 1.39‰ (Cameron and Vance, 2014; Ciscato et al., 2018; Takano et al., 2017), while the average δ^{60}Ni of deep ocean is around 1.33 ± 0.13‰ (Lemaitre et al., 2022). The inputs of Ni into the ocean, including river runoffs (δ^{60}Ni = 0.8‰; Cameron and Vance, 2014; Gueguen and Rouxel, 2021; Vance et al., 2016) , atmospheric deposition (δ^{60}Ni = 0.14‰; Cameron et al., 2009; Ciscato et al., 2018; Desboeufs et al., 2005; Gueguen and Rouxel, 2021; Vance et al., 2016) and hydrothermal inputs (estimated to be δ^{60}Ni = 0.1‰; Gueguen and Rouxel, 2021) are generally isotopically lighter than seawater. While δ^{60}Ni in most of the Ni outputs from the ocean, including oxic sediments (δ^{60}Ni = 1.62 ± 0.37‰; Gall et al., 2013; Gueguen and Rouxel, 2021; Little et al., 2020), carbonate sediments (δ^{60}Ni = 1.10~1.64‰; Ciscato et

al., 2018), organic-rich sediments (δ^{60}Ni = 1.12 ± 0.08‰; Ciscato et al., 2018) and ferromanganese crusts (δ^{60}Ni = 1.50‰; Gall et al., 2013), are generally similar to seawater. Therefore, the steady-state oceanic Ni budget requires isotopically heavy Ni inputs and/or isotopically light outputs.

A benthic flux of isotopically heavy Ni (δ^{60}Ni = 3.03‰) has recently been proposed from isotopically light (δ^{60}Ni = –0.2 ~ –0.8‰) Mn-rich sediments, during the diagenetic remobilization of Ni via either associated Ni sorption and desorption along cycles of Mn-oxide dissolution and precipitation or mineral transformation from birnessite to todorokite, which may help to balance oceanic Ni budget (Little et al., 2020). This mineral transformation from birnessite to todorokite has been observed to lose ~50% of sorbed Ni in experimental studies (Atkins et al., 2016). The isotopically light Ni retained in Fe oxyhydroxides and/or Fe-rich authigenic clays has also been suggested to induce remobilization of isotopically heavy Ni from sediments under reductive conditions (Little et al., 2020). The δ^{60}Ni of proposed diagenetic input flux to the ocean has subsequently been refined to about 2.85‰, given the new pelagic clay sediments measured and considered (Gueguen and Rouxel, 2021). These observations agree an isotopically heavy Ni input to the ocean under oxic to suboxic conditions, while the magnitude of flux and the representative Ni isotope composition remain to be justified with more data for natural samples.

In anoxic/euxinic ocean settings, sulfidation of dissolved Ni, scavenging of particle reactive sulfidised species or sulfide precipitation can also remove Ni from the ocean as an output flux (Vance et al., 2016). In euxinic sediments, the activity of sulfate-reducing bacteria ($2C_2H_4OHCOO^- + SO_4^{2-} \rightarrow 2CH_3COO^- + 2HCO_3^- + HS^- + H^+$; Mansor et al., 2019;

Purcell, 1977) can generate protons and organics (e.g., acetate), induce the decreasing pH in ambient micro-environments and can facilitate the transformation of Ni-sulfides from amorphous ($Ni_{1.1}S \cdot 1.5H_2O$) to crystalline phases (e.g., polydymite (Ni_3S_4) and vaesite (NiS_2)), via dissolution of formed crystals and recrystallization (Mansor et al., 2019; Wilkin and Rogers, 2010; Wang et al., submitted). This decreasing pH may increase the solubility of Ni-sulfide and lead to a partial remobilization of precipitated Ni into the ocean during Ni-sulfide development (Mansor et al., 2019). From an experimental study, the magnitude of Ni isotope fractionation during the formation of amorphous Ni-sulfides ($\varepsilon_{S\text{-}L}$ = −0.22 ~ −0.26‰) (see Chapter 4) has been proposed to be smaller than the fractionation during the formation of a mixed crystalline polydymite and vaesite ($\varepsilon_{S\text{-}L}$ = −0.73‰) (Parigi et al., 2022), which further suggests a potential release of isotopically heavy Ni during the transformation of Ni-containing sulfides (see Chapter 4). However, these experimental observations have not been verified yet with sulfide-containing marine sediments. The magnitude of isotope fractionation during diagenetic remobilization of Ni in euxinic sediments and its contribution to the oceanic Ni budget remain unknown.

In this study, we address the knowledge gap by measuring Ni isotope compositions in dysoxic (2.0~0.2 mL/L of O_2, equals to 87~8.7 μmol/kg of O_2; Tyson and Pearson, 1991) to euxinic (anoxic and sulfidic) sediments from the Namibian margin, coupled with complementary trace metal inventories in ambient seawaters, particulates and porewaters. We show distinct δ^{60}Ni and trace metal profiles in sediment cores, which suggest a benthic flux of isotopically heavy Ni from these euxinic sediments. We revisit the oceanic Ni budget and refine representative δ^{60}Ni values for both organic-rich sediment deposition and benthic Ni flux from sediments.

5.2 Materials and methods

5.2.1 Study area

Samples investigated in this study were collected from the northern Benguela upwelling system (BUS) at ~23°S transect off Namibian margin, from nearshore stations to offshore stations, up to 70 nautical miles (NM) from the coast, during a cruise of R/V Mirabilis in May 2019 (Figure 5.1). Seawater and particulate samples were collected at stations 23005 and 23070, 5 NM and 70 NM away from the coast, respectively. The water column at station 23005 is about 66.3 m deep, with a bottom water oxygen (BWO) level of 1.3 μmol/kg. While the water column at station 23070 is about 301.5 m deep, with a BWO level of 55.4 μmol/kg. Sediment cores and porewater samples within were recovered at stations 23010 and 23060 on the 23°S transect, 10 NM and 60 NM away from the coast, respectively. Station 23010 is about 100.5 m water depth, characterized to have a BWO level of 2.7 μmol/kg and a total organic carbon (TOC) content ranging from 5.0% to 10.8%. Station 23060 is about 352.5 m water depth, characterized to have a BWO level of 67.3 μmol/kg and a TOC content ranging from 2.6% to 3.8%.

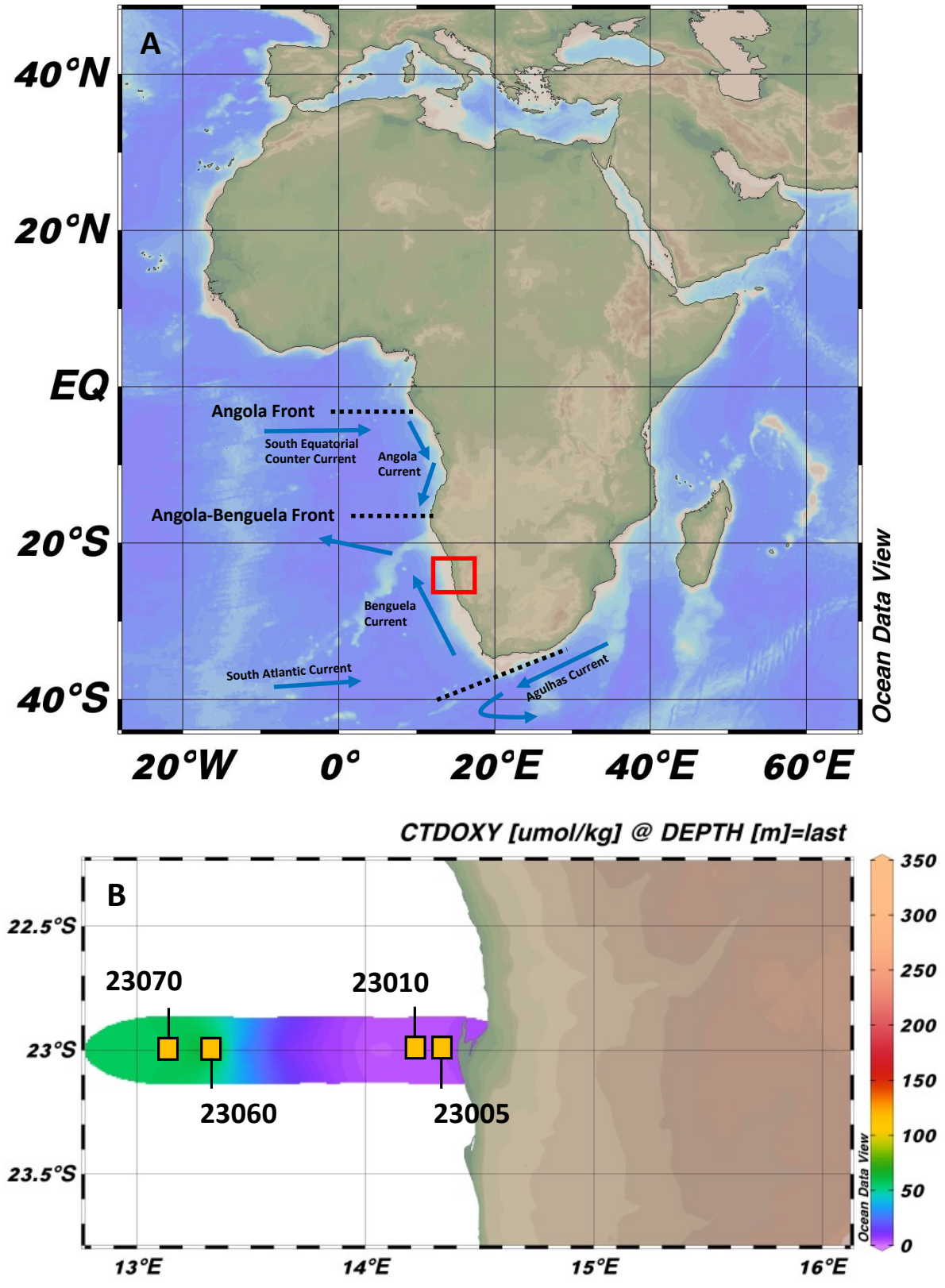


Figure 5.1. (A) Sampling area (red square) plotted with regional ocean currents impacting Benguela upwelling system (BUS). (B) Sampling sites (yellow) with bottom water oxygen concentrations along the sampling transect (23°S).

The BUS off-shore southwestern Africa is one of the most productive upwelling regions in the global ocean, providing an opportunity to study organic-rich sediments deposited with a range of BWO levels displaying various sedimentary redox states (Chavez and Messié, 2009; Inthorn et al., 2006; Mohrholz et al., 2008). It starts from the northern boundary at around 15~17°S where the poleward Angola Current and the equatorward Benguela Current converge, to the southern boundary at the tip of Africa around 35°S (Figure 5.1A). The Benguela Current originates from both the South Atlantic Current flowing eastward as part of the South Atlantic subtropical gyre and the part of the Agulhas Current flowing equatorward (Garzoli and Gordon, 1996; Mercier et al., 2003).

The coastal upwelling in BUS is driven by the alongshore equatorward winds which drive offshore Ekman transport of the surface waters and lead to the upwelling of cool and macronutrient-rich central water masses to the surface (Bordbar et al., 2021; Duncombe Rae, 2005). These upwelled water masses consist of the macronutrient-rich and oxygen-depleted South Atlantic Central Water (SACW) and the well-oxygenated Eastern SACW (200~300 μmol/kg of O_2) (Duncombe Rae, 2005; Liu and Tanhua, 2021). The current in the northern Benguela has seasonal variability, with nutrient-rich and oxygen-depleted SACW transported from the Angola Gyre in austral summer, and oxygen-rich Eastern SACW transported equatorward, based on an oceanographic mooring data 20 nautical miles (NM) off Namibian margin at 23°S transect (Mohrholz et al., 2008). The mixing between both water masses has been reported in the northern Benguela from Angola-Benguela frontal zone (ABFZ) to the Lüderitz upwelling cell (~27°S) (Mohrholz et al., 2008). The upwelling has been reported to be perennial in the northern Benguela (17~29°S) (Hutchings et al., 2009). The oxygen minimum zones (OMZ) off Namibian margin are caused by a combination of oxygen consumption by remineralization and

poleward advection of oxygen-depleted tropical waters (Mohrholz et al., 2008; Monteiro and van der Plas, 2006).

As one of the strongest upwelling regions in the ocean, the BUS drives a hotspot of primary production (~976 g C m^{-2} yr^{-1}) annually (Chavez and Messié, 2009). The BUS is characterized with high organic carbon concentration and a widespread OMZ from the shelf to upper continental margin, serving as a major sink for atmospheric CO_2 (Mollenhauer et al., 2002). The seawater in the shelf region off Namibian margin experience seasonal anoxia during the austral summer, coupled with the appearance of H_2S in bottom waters caused by bacterial sulfate reduction and episodic methane releases (Brüchert et al., 2003; Emeis et al., 2004; Mohrholz et al., 2008). The presence of H_2S in the water column indicates that more energetically favorable terminal electron acceptors, including manganese and iron oxide minerals, would have been reduced and released to porewaters as soluble products (Noble et al., 2012).

Our sampling area is located in the BUS region with high primary production and varying BWO levels, which offers a suitable setting for understanding the impact of varying BWO levels on Ni isotopes in nearshore and offshore sediments. According to the sedimentary ^{14}C ages and the corresponding sedimentation rates on the inner shelf between 20.6°S and 25.5°S in the Benguela upwelling region, the sedimentation rate has been reported to be the highest of 112 cm·ky^{-1} on the uppermost slope at ~646 m depth and decrease downslope to about 22 cm·ky^{-1} at ~ 2289 m depth (Inthorn et al., 2006). As the sampling sites in this study are closer to the coast, compared to the sites reported in Inthorn et al. (2006), these sites may have similar or higher sedimentation rates than 112 cm·ky^{-1}.

5.2.2 Sample collection

Background information of temperature, salinity and oxygen level at the stations investigated in this study were measured by CTD Sea-Bird SBE 9 rosettes.

Seawater samples at different depths for Ni concentration analysis were subsampled from CTD Sea-Bird SBE 9 rosettes, filtered with in-line acid-cleaned 0.2 μm Acropak™ 500 polyethersulfone membrane filter capsules with Supor® membrane into acid-cleaned high-density polyethylene (HDPE) bottles. Seawater samples were also collected by pumping waters from ~10 m depth at stations with portable pumping kit including Masterflex® L/S® pump drive, L/S® Easy-Load pump head and L/S® C-Flex tubing (inner diameter 6.4 mm). Results from these two methods are compared to assess potential contamination from the steel frame and wire of the CTD rosette. Collected seawater samples were acidified to pH $<$ 2 with sub-boiled concentrated hydrochloric acid (HCl).

Particulate samples were collected from the surface seawaters pumped up from ~10 m depth at stations into acid-cleaned 20L high-density polyethylene (LDPE) cubic containers (Thermo Scientific™), by using the same portable pumping kit for seawaters. Collected surface seawaters were filtered through polyethersulfone (PES) filters (47 mm diameter, 0.8 μm pore size) to collect particulate samples, by using portable filtering kit connected to vacuum pump (Cole-Parmer®). All filters and filter holders were acid-leached with 1.2M HCl before use adopting the recommended methods in the GEOTRACES cookbook for sampling and sample-handling protocols (Cutter et al., 2017). The filtering unit was rinsed with Milli-Q water three times and the seawater sample of interest once between each sample. The cassette blanks for trace elements of filters were

also assessed (~1.6 ng for Ni; see Appendix A). After the filtration, the PES filters were detached and sealed in acid-cleaned plastic sample bags for storage.

Sediment cores were collected using MC-400 Multi-Corer equipped with 4 polycarbonate sample tubes (10 cm diameter × 58 cm high). All sample tubes have pre-drilled holes at 2-cm intervals to facilitate porewater extraction. After porewater sample collection, sediment cores were subsampled with 1-cm intervals with a plastic core liner using a piston to avoid core distortion and shortening and sealed in acid-cleaned plastic sample bags for storage.

Porewater samples were collected by inserting acid-cleaned Rhizons with pore size 0.6 μm into these pre-drilled holes on sealed core liners on deck, at constant intervals (2~3 cm). These Rhizon samplers were attached to syringes for extracting porewaters immediately. All extractions were done within 1 hour after core retrieval. The extracted porewaters were transferred to acid-cleaned HDPE bottles for storage and acidified to pH $<$ 2 with sub-boiled concentrated HCl. As the handling was not done in an anoxic condition (e.g., glovebox filled with N_2), potential impact on redox sensitive species (e.g., H_2S, Fe^{2+}) in sediments or porewaters might be expected.

All samples collected during the cruise were stored in a cold room at 4°C onboard the research vessel until further processing in the lab.

5.2.3 Sample digestion

Approximately 0.1g of freeze-dried sediment powders were digested with concentrated HF and concentrated HNO_3 with a volumetric ratio of 1:3, ultrasonicated for 30 min and refluxed at 85°C on hotplate for 24 h. The sample solutions were fully dried down at 85°C, added with 4 mL of 6M HCl, ultrasonicated for 30 min and refluxed at 120°C for 24 h. The aliquots were further added with 6 mL of concentrated HNO_3 to form reverse aqua regia, ultrasonicated for 30 min and refluxed at 120°C for 24 h. The solutions were evaporated to dryness at 120°C, then treated with 3 mL of 30% H_2O_2 with 0.5 mL added each time to let it react at room temperature until the reaction smoothed, and left at room temperature to react for 24 h. If there were any residues, the 30% H_2O_2 treatment was repeated until they were fully dissolved. The aliquots were then dried down and dissolved in 2% HNO_3 for analysis. Two reference materials SDO-1 and SGR-1b were processed along the digestion to assess the treatment (see Appendix D, Table D.5–D.6.).

For particulate samples, the total digestion method provided in the GEOTRACES cookbook was adapted in this study (Cullen and Sherrell, 1999; Cutter et al., 2017; Ohnemus et al., 2014). Polyethersulfone (PES, Supor®, 47 mm) filters were placed against the wall of the vial, close to the top edge to avoid submerging any part of the filter in the digestion medium, and refluxed with 1 mL of 50% HNO_3/ 10% HF at 130°C for 4 h. After cooling to room temperature, the aliquots were collected, dried down fully at 85°C and dissolved in 2% HNO_3 for analysis. The reference material BCR-414 was processed along with the digestion to assess the treatment (recovery 101.1% for Ni; see Appendix D, Table D.3).

5.2.4 Elemental concentration measurement

The concentrations of major and trace elements were measured using a PerkinElmer NexION 350D quadrupole inductively coupled plasma mass spectrometer (ICP-MS) at the Department of Earth Sciences, University of Oxford. Three operating modes including standard mode, kinetic energy discrimination (KED) mode and dynamic reaction cell (DRC) mode were applied to optimize the signals and minimize the potential interferences on measured masses, and were adjusted with elements of interest. Details of the potential interferences, operating mode and cell gas flow for each element can be found in Zhang et al. (2018). The precision and accuracy for the elemental analyses were monitored daily with SLRS-6 (river water standard) or NASS-7 (seawater certified reference material for trace metals). For SLRS-6 measured by quadrupole ICP-MS with normal introduction system, the measured values of most elements agreed with the certified values within 5%, and the precision (RSD) for most elements were better than 5% (see Appendix D, Table D.1).

The quadrupole ICP-MS was connected to an automated preconcentration system seaFAST (Elemental Scientific) for measuring Ni in seawater samples, and Ni and Mn in porewater samples, which enhances concentrations of interested elements and improve the analytical precision by extracting transition metals from major elemental matrix (e.g., Na and Ca). The same quadrupole ICP-MS was also connected to Prep-FAST M5 autosampler system to enable a flow injection automation system (FIAS) to inject micro-volume of samples directly to mass spectrometer for measuring Ba and Fe in porewater samples. The injections were measured by the fast-scanning quadrupole and the average intensity data (cps) were taken from three injections per replicate (Zhang et al., 2018).

For NASS-7 measured with quadrupole ICP-MS coupled with seaFAST, the precisions (RSD) of most elements were better than 5% (see Appendix D, Table D.2).

The total organic carbon in freeze-dried sediment powders was measured by Rock-Eval® analyzer. The concentration of sulfate (SO_4^{2-}) in unacidified porewater samples was determined using an Ion Chromatography (DIONEX instrument) at the Department of Geography, University of Oxford.

5.2.5 Ni isotope analysis

After the acquisition of Ni contents, sediment sample digest solutions were subsampled and double-spiked at a sample-to-spike ratio of 0.4 with a spike mixture of ^{61}Ni-^{62}Ni with a ratio of 25:75 prior to Ni purification procedure and isotope analysis (Gall et al., 2012; Saunders et al., 2020; see Appendix A).

The digested and double-spiked sediment solutions were treated with a three-stage ion exchange chromatography (Gall et al., 2012; Saunders et al., 2020; see Appendix A) to chemically separated Ni from matrix, in a Class 100 laminar flow hood in a metal-free laboratory at the Department of Earth Sciences, University of Oxford. The first and second column with cation resin AG50W-X4 (chloride form, 200-400 mesh) exploit the ability of Ni to form strong complexes with ammonia and dimethyglyoxime (DMG), respectively. The third column with anion resin AG1-X8 (chloride form, 200-400 mesh) separates any remaining Fe from Ni. With respect to sediment samples, the total procedural blanks for chemical processing including sample digestion and Ni purification were assessed in every batch of column chemistry and were stably less than 4.7 ng (n=5), which were

negligible compared to the content of Ni (~1400 ng of total Ni) processed through the procedure at a time.

Ni isotope compositions in sediment samples were determined using a Nu Plasma high resolution multi-collector inductively coupled plasma mass spectrometer (MC-ICP-MS) at the Department of Earth Sciences, University of Oxford. All isotope analyses were performed in low resolution mode. Sample aliquots were introduced into the plasma via a PFA nebulizer (Elemental Scientific, 50 μLmin^{-1}) coupled with an Aridus II desolvating system (CETAC Technologies). Each isotope measurement consists of 40 cycles with 10 s integration time for acquiring ion beam intensity. The potential interference of ^{58}Fe on ^{58}Ni was corrected by the simultaneous measurement of ^{57}Fe during the determination (Gall et al., 2012; Saunders et al., 2020). A normalized argon index (NAI) was exploited to monitor thermal condition of plasma and minimize potential interferences on Ni isotopes, during the tuning on a daily basis (Fietzke and Frische, 2016; Yu et al., 2020; see Appendix A.6).

All Ni isotope compositions are expressed in delta notation (δ) in per mil deviation (‰), relative to Ni isotopic standard SRM986 (high-purity Ni metal).

$$\delta^{60}Ni = \left[\frac{(^{60}Ni/^{58}Ni)_{sample}}{(^{60}Ni/^{58}Ni)_{SRM986}} - 1\right] \times 1000\ (‰) \quad (5.1)$$

Long term reproducibility of Ni isotope analysis was assessed by repeated measurement of two in-house sulfide standard Kam and Sud, and the Mn nodule standard Nod-P-1 (USGS) over 30 months, which yields -0.88 ± 0.06‰ (n=43), 0.79 ± 0.06‰ (n=43) and

0.37 ± 0.07‰ (n=36), respectively. The measured δ^{60}Ni values of Nod-P-1 are in agreement with the range (δ^{60}Ni = 0.328 ~ 0.41‰) reported in previous studies (Gueguen et al., 2018, 2016, 2013; Ratié et al., 2015; Wu et al., 2019).

5.3 Results

5.3.1 Seawaters and particulates

The oxygen (O_2) concentrations in the water columns are the highest at the surface and decrease with depths at both station 23005 and 23070 (Figure 5.2 and Table 5.1), which the bottom water oxygen (BWO) is ~2 μmol/kg at station 23005 and ~55 μmol/kg at station 23070. Supplementary hydrographic data (i.e., oxygen level, temperature and salinity) along the transect 23°S suggest that the low oxygen level inshore is caused by the combination of advection of oxygen-poor South Atlantic Central Water (SACW) poleward from Angola Gyre into the north Benguela and local oxygen consumption during remineralization of sinking particles on the inner shelf (Figure 5.3–5.5). The BWO levels are low at both stations which are likely caused by oxygen-poor source waters (SACW). The lower BWO level at inshore station 23005 is likely further decreased by local consumption via remineralization, with similar temperature and salinity compared to the offshore station 23070.

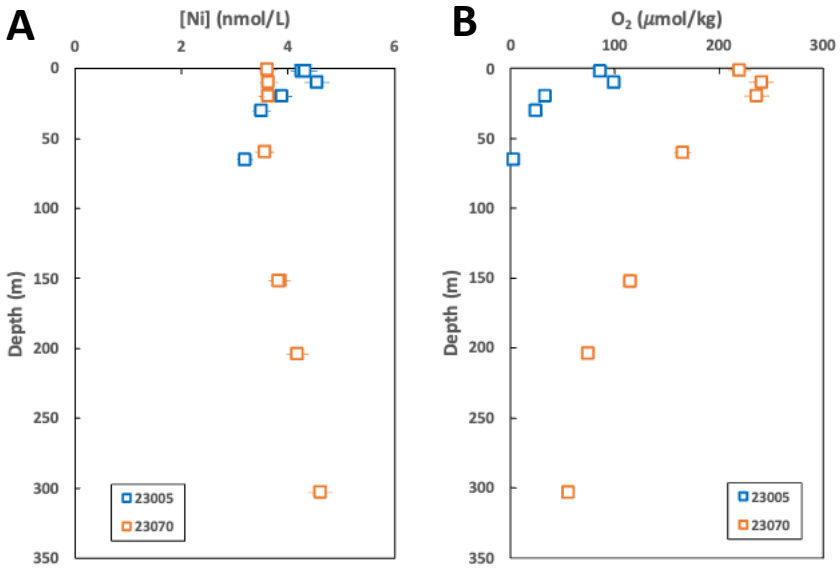


Figure 5.2. Depth profiles of dissolved Ni and oxygen level for seawaters collected at stations 23005 (blue squares) and 23070 (orange squares). Depth represents meters below sea level (mbsl).

Table 5.1. Seawater profiles of O_2 concentration, temperature, salinity and Ni concentration at stations 23005 and 23070. Samples noted with "dup" were measured as duplications during Ni concentration measurements.

Sample ID	Depth (m)	O_2 (μmol/kg)	Temp (℃)	Salinity (‰)	Ni (nM)
Station 23005 (14.318°E, 23.001°S)					
23005_2m	2	85.8	13.11	35.21	4.3
23005_2m_dup	2	85.8	13.11	35.21	4.3
23005_10m	10	98.9	13.12	35.18	4.5
23005_20m	20	33.3	12.84	35.17	3.9
23005_30m	30	24.4	12.82	35.16	3.5
23005_65m	65	2.3	12.60	35.17	3.2
Station 23070 (13.133°E, 23.001°S)					
23070_1m	1	220	15.70	35.24	3.6
23070_10m	10	241	15.65	35.25	3.6
23070_20m	20	236	15.32	35.24	3.6
23070_60m	60	165	14.36	35.23	3.6
23070_152m	152	115	12.02	35.08	3.9
23070_152m_dup	152	115	12.02	35.08	3.8
23070_204m	204	74.3	10.87	34.97	4.2
23070_303m	303	55.4	9.69	34.85	4.6

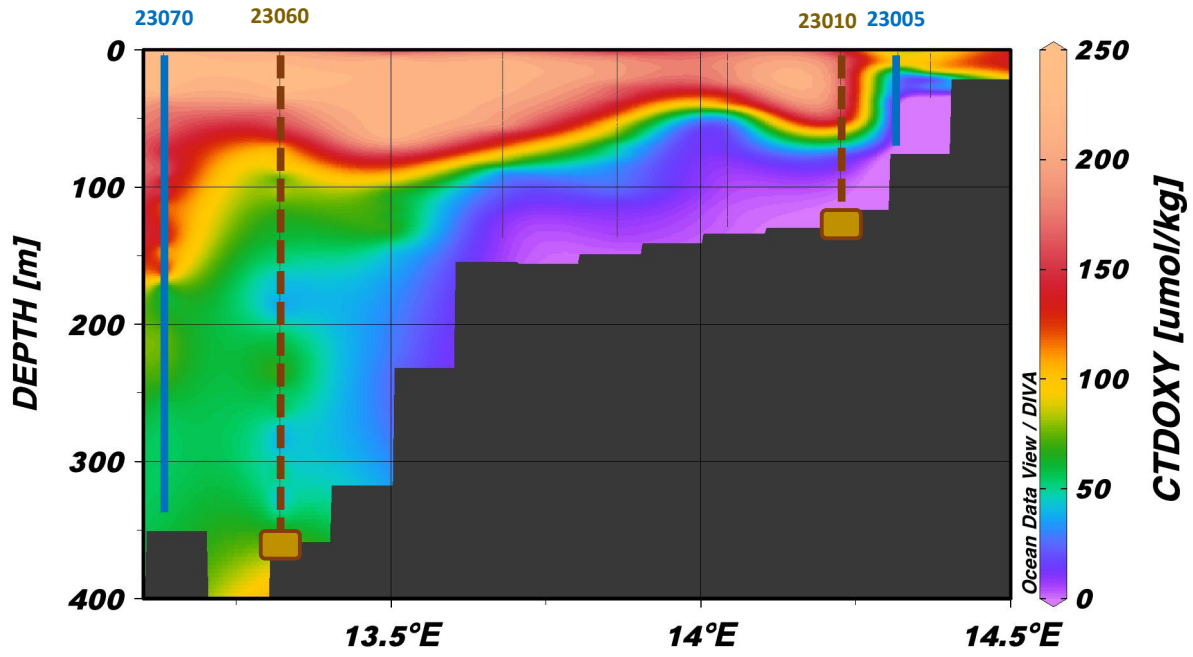


Figure 5.3. Seawater profiles of oxygen concentration (μmol/kg) along the 23°S transect with the stations where the sediment (brown) and seawater (blue) samples were sampled.

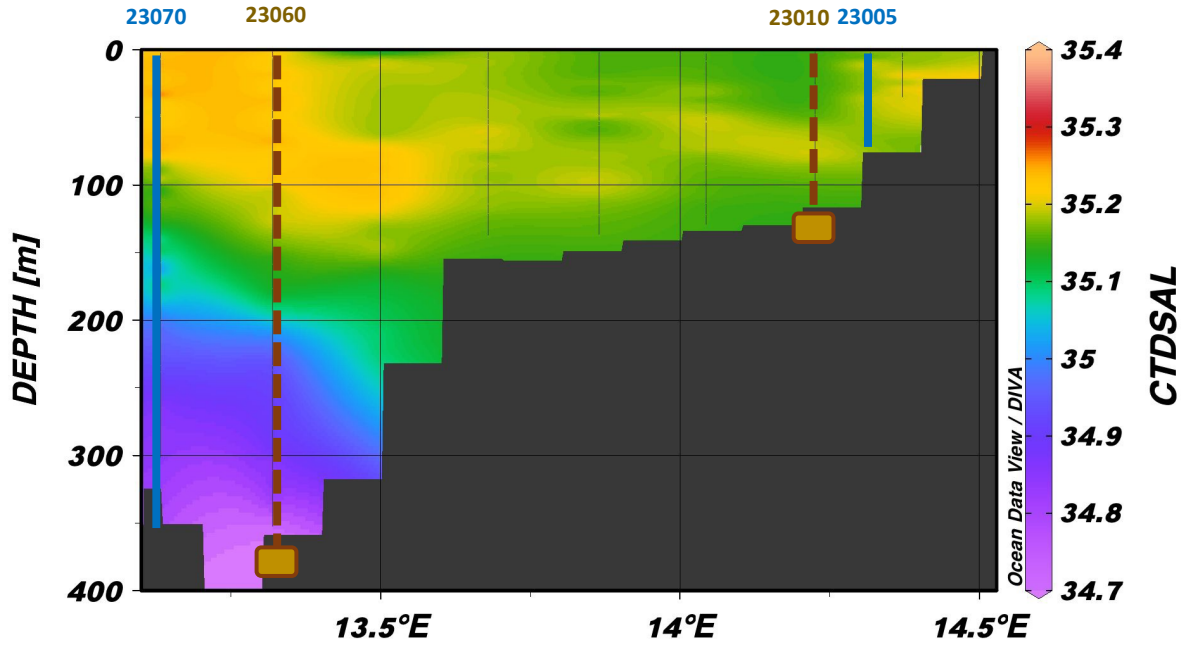


Figure 5.4. Seawater profiles of salinity (‰) along the 23°S transect with the stations where the sediment (brown) and seawater (blue) samples were sampled.

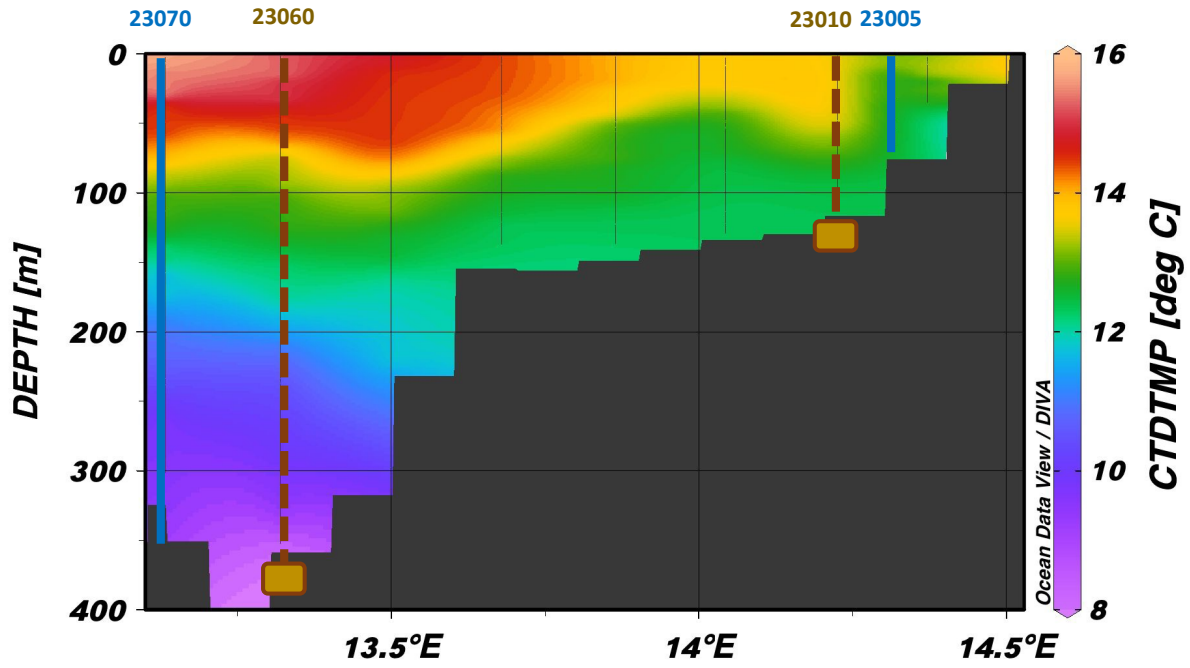


Figure 5.5. Seawater profiles of temperature (℃) along the 23°S transect with the stations where the sediment (brown) and seawater (blue) samples were sampled.
.

The potential contamination from steel frame and wire of CTD Sea-Bird SBE 9 rosettes is assessed to be negligible, which suggests that the waters collected should have original signals from seawaters (Figure 5.6 and Table 5.2). The seawater profile of dissolved Ni generally decreases with depth at inshore station 23005, from ~4.3 nM at 2 m depth to ~3.2 nM at 65 m depth, with a slight increase to 4.5 nM around 10 m depth (Figure 5.2). While the dissolved Ni increases with depth at offshore station 23070, from ~3.6 nM at the surface to 4.6 nM at ~300 m depth.

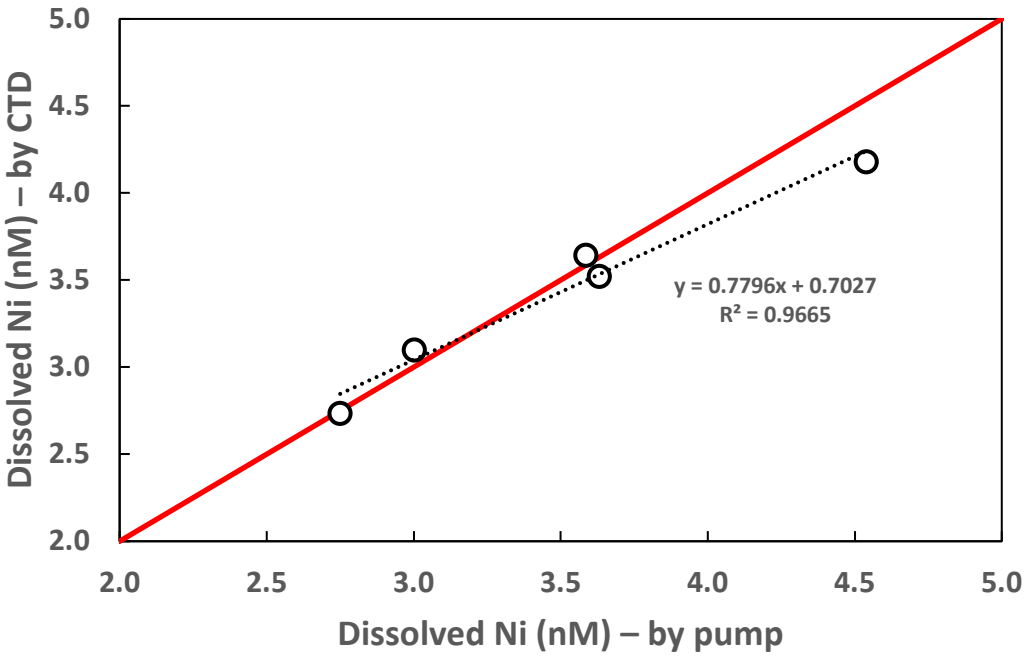


Figure 5.6. Comparison of Ni concentrations in 10m-depth seawaters collected by pump and CTD at various stations off Namibian margin. The red line denotes the 1:1 line.

Table 5.2. Ni concentrations in 10m-depth seawaters collected by pump and CTD at various station off Namibian margin.

Station	[Ni] (nM) by pump	[Ni] (nM) by CTD
20005	3.6	3.6
20040	3.0	3.1
20070	2.8	2.7
23005	4.5	4.2
23070	3.6	3.5

For particulate samples, the concentrations of Ni, Ba, Fe, Mn and P are higher at the inshore station 23005 relative to that at the offshore station 23070, while Fe is only above the detection limit or procedural blank at the inshore station 23005 (Figure 5.7 and Table 5.3). The concentration of Ca is higher at the offshore station 23070 than the inshore station 23070.

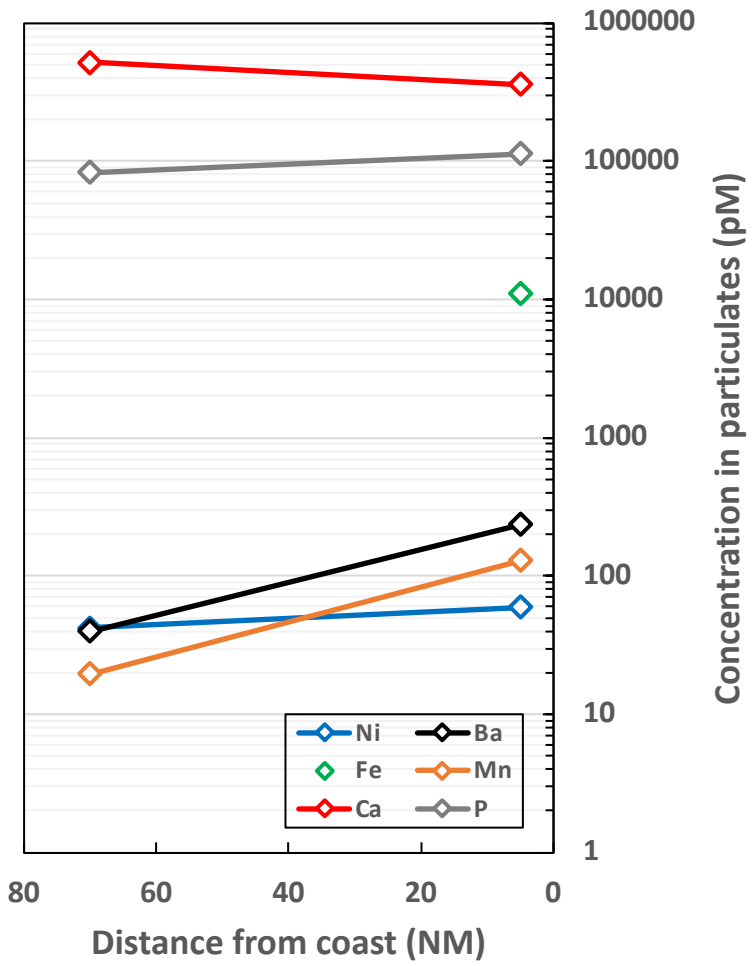


Figure 5.7. Elemental concentrations in particulate samples filtered from surface seawaters (~10 m depth) at stations 23005 and 23070.

Table 5.3. Major and trace element concentration in particulate samples filtered from surface seawaters at stations 23005 and 23070. "n.a." suggests the number is either below the detection limit of that element or below the procedural blank.

Station	Depth (m)	Volume (L)	P (pM)	Ca (pM)	Ni (pM)	Fe (pM)	Mn (pM)	Ba (pM)
23005	10	3.15	113405	357852	59.2	11022	129	236
23070	10	2.75	82707	516742	42.3	n.a.	19.6	39.8

5.3.2 Sediments and porewaters

Both sediment cores are enriched in total organic carbon (TOC), where the nearshore core 23010 is relatively more enriched (5.0~10.8%) than the offshore core 23060 (2.6~3.8%) (Figure 5.8 and Table 5.4). The ranges of TOC contents at both stations are within the range (2~15‰) for a reported mudbelt off southwest Africa (Inthorn et al., 2006). The TOC content at station 23010 agrees with the average TOC content of 9% reported for the diatom belt (Calvert and Price, 1970). However, the range of TOC contents at both stations is narrower than the range (1.7~22.3%) reported for Namibian shelf sediments (Calvert and Price, 1983). The strong smell of H_2S was found during the sediment core retrieval at the inshore station 23010, but not at the offshore station 23060. Though the content of H_2S was not measured directly during this cruise.

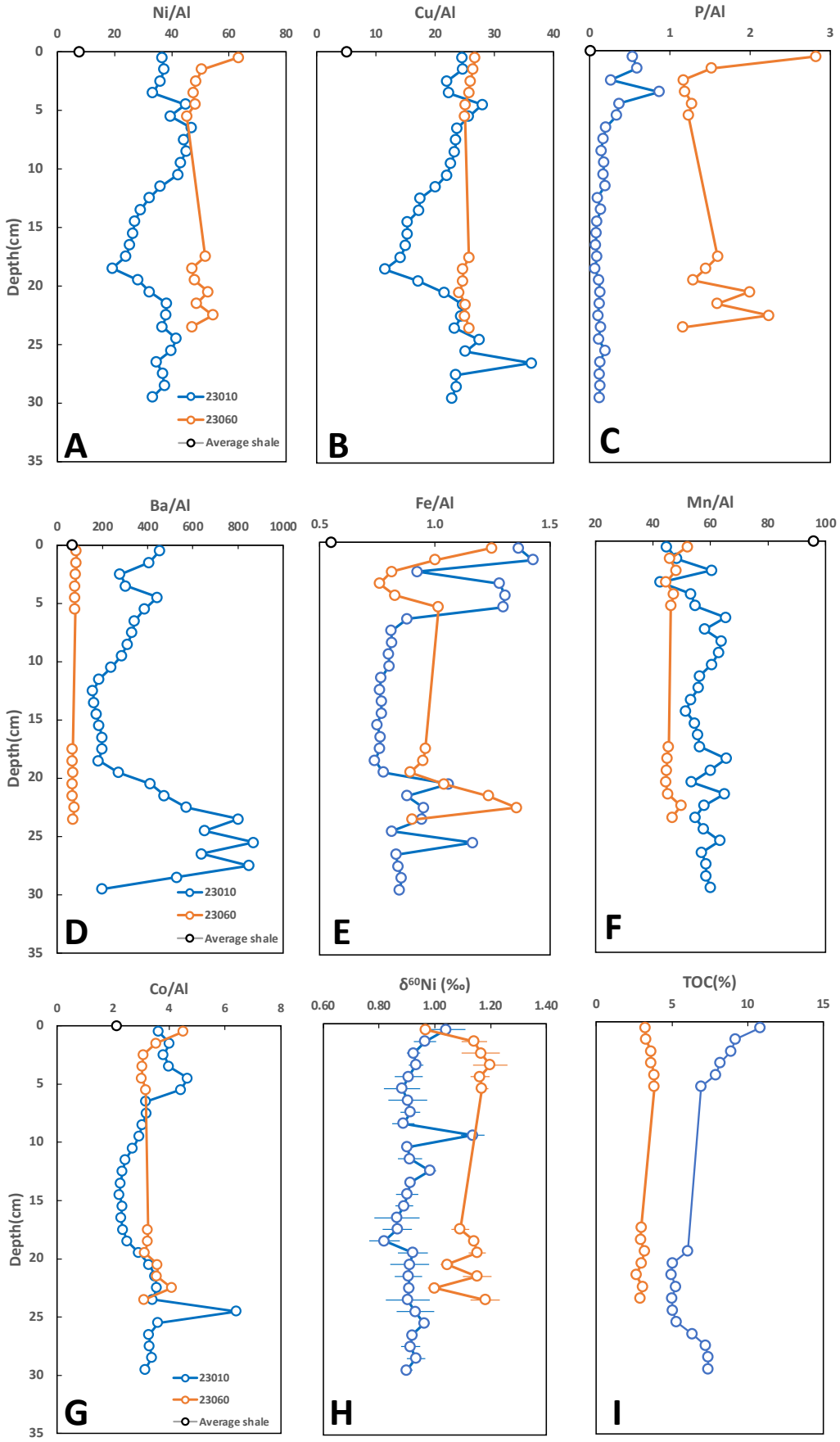

Ni/Al
Cu/Al
P/Al
Depth(cm)
23010
23060
Average shale
A
B
C
Ba/Al
Fe/Al
Mn/Al
D
E
F
Co/Al
δ⁶⁰Ni (‰)
TOC(%)
G
H
I

Figure 5.8. Depth profiles of element/Al ratios, TOC and Ni isotope compositions in sediment samples collected at stations 23010 (blue) and 23060 (orange). Depth represents centimeters below seafloor (cmbsf). Elemental ratios are compared to average shale values (black circles) (Borchers et al., 2005; Heinrichs et al., 1980). Error bars noted in δ^{60}Ni values represent the standard deviation (2SD).

Table 5.4. Geochemical profiles of sediment cores 23010 and 23060, including bottom water oxygen (BWO) concentrations, TOC contents, element/Al ratios and Ni isotope compositions. Depth represents centimeters below seafloor (cmbsf). 2SD stands for the analytical error of δ^{60}Ni value with duplications (n).

Sample ID	Depth (cm)	BWO (μmol/kg)	TOC (%)	Ni/Al ($\times10^{-4}$)	Cu/Al ($\times10^{-4}$)	Co/Al ($\times10^{-4}$)	Fe/Al ($\times10^{-4}$)	Mn/Al ($\times10^{-4}$)	Ba/Al ($\times10^{-4}$)	P/Al ($\times10^{-4}$)	δ^{60}Ni (‰)	2SD (‰)	n
R/V Mirabilis, core 23010 (14.226°E, 23.001°S), 102 m water depth													
23010_0-1	0-1	2.7	10.8	36.6	24.5	3.62	1.36	44.9	454	0.54	1.04	0.07	4
23010_1-2	1-2	2.7	9.2	37.4	24.6	4.03	1.43	48.2	407	0.59	0.97	0.04	4
23010_2-3	2-3	2.7	8.9	35.9	22.0	3.81	0.93	60.4	278	0.26	0.92	0.02	4
23010_3-4	3-4	2.7	8.2	33.4	22.3	4.00	1.28	42.6	304	0.86	0.93	0.03	4
23010_4-5	4-5	2.7	7.9	44.8	27.9	4.67	1.30	53.2	444	0.37	0.91	0.05	4
23010_5-6	5-6	2.7	6.9	39.5	25.6	4.42	1.30	54.7	387	0.34	0.88	0.06	3
23010_6-7	6-7	2.7		46.9	23.7	3.17	0.88	65.3	342	0.20	0.90	0.07	3
23010_7-8	7-8	2.7		44.3	23.5	3.20	0.81	58.0	332	0.17	0.91	0.04	3
23010_8-9	8-9	2.7		45.1	23.3	3.04	0.81	63.9	310	0.14	0.89	0.04	3
23010_9-10	9-10	2.7		43.1	22.6	2.93	0.80	62.9	286	0.17	1.14	0.04	4
23010_10-11	10-11	2.7		42.1	21.9	2.71	0.80	60.4	239	0.17	0.90	0.02	4
23010_11-12	11-12	2.7		36.0	20.1	2.44	0.77	56.2	186	0.19	0.91	0.04	4
23010_12-13	12-13	2.7		32.1	17.4	2.34	0.76	55.9	158	0.10	0.98	0.02	4
23010_13-14	13-14	2.7		29.2	17.2	2.26	0.77	53.1	162	0.14	0.91	0.01	4
23010_14-15	14-15	2.7		27.1	15.2	2.23	0.77	51.4	173	0.09	0.90	0.04	4
23010_15-16	15-16	2.7		26.5	15.3	2.33	0.75	54.5	186	0.08	0.89	0.03	4
23010_16-17	16-17	2.7		25.3	15.0	2.29	0.76	55.6	199	0.08	0.86	0.08	4
23010_17-18	17-18	2.7		23.9	14.1	2.36	0.76	56.3	199	0.09	0.87	0.05	4
23010_18-19	18-19	2.7		19.2	11.5	2.52	0.74	65.5	183	0.06	0.82	0.05	4
23010_19-20	19-20	2.7	6.0	28.3	17.1	2.92	0.78	59.9	271	0.11	0.92	0.05	4
23010_20-21	20-21	2.7	5.0	32.3	21.5	3.29	1.06	53.5	413	0.13	0.91	0.07	3
23010_21-22	21-22	2.7	5.0	38.2	24.6	3.51	0.88	65.0	475	0.12	0.91	0.05	3
23010_22-23	22-23	2.7	5.2	38.1	24.4	3.56	0.95	57.8	571	0.10	0.91	0.02	4
23010_23-24	23-24	2.7	5.0	36.7	23.3	3.43	0.94	54.6	803	0.13	0.90	0.08	3
23010_24-25	24-25	2.7	5.1	41.6	27.4	6.42	0.81	57.6	653	0.11	0.93	0.07	3
23010_25-26	25-26	2.7	5.3	39.8	25.1	3.62	1.17	63.3	871	0.19	0.96	0.02	4
23010_26-27	26-27	2.7	6.3	34.7	36.2	3.29	0.83	57.0	639	0.13	0.92	0.02	3
23010_27-28	27-28	2.7	7.2	36.8	23.5	3.31	0.84	58.5	849	0.12	0.91	0.03	3
23010_28-29	28-29	2.7	7.4	37.5	23.5	3.39	0.85	58.6	530	0.13	0.93	0.03	4
23010_29-30	29-30	2.7	7.4	33.3	22.8	3.15	0.85	60.0	199	0.12	0.90	0.02	3
R/V Mirabilis, core 23060 (13.32°E, 23.000°S), 352.5 m water depth													
23060_0-1	0-1	67.299	3.2	63.3	26.7	4.51	1.25	52.0	85.3	2.83	0.97	0.02	3
23060_1-2	1-2	67.299	3.3	50.5	26.4	3.54	1.00	46.0	84.2	1.52	1.14	0.05	4
23060_2-3	2-3	67.299	3.6	48.5	25.9	3.09	0.81	48.0	82.7	1.17	1.16	0.07	3
23060_3-4	3-4	67.299	3.6	47.5	25.7	3.04	0.76	44.6	79.3	1.19	1.20	0.06	3
23060_4-5	4-5	67.299	3.8	48.1	25.1	3.03	0.83	47.2	78.0	1.28	1.16	0.03	4
23060_5-6	5-6	67.299	3.8	45.3	25.0	3.17	1.02	46.3	79.3	1.23	1.17	0.02	3
23060_17-18	17-18	67.299	3.0	51.7	25.7	3.24	0.96	45.4	67.8	1.60	1.09	0.03	3
23060_18-19	18-19	67.299	2.9	47.0	24.7	3.24	0.95	44.9	68.6	1.45	1.14	0.01	4
23060_19-20	19-20	67.299	3.2	47.9	24.7	3.13	0.89	44.9	69.4	1.29	1.15	0.03	3
23060_20-21	20-21	67.299	3.0	52.7	24.0	3.59	1.04	44.5	66.9	1.99	1.04	0.02	3
23060_21-22	21-22	67.299	2.6	48.7	25.1	3.57	1.23	45.1	67.7	1.59	1.15	0.05	4
23060_22-23	22-23	67.299	3.1	54.4	25.0	4.10	1.35	49.7	77.1	2.24	1.00	0.02	3
23060_23-24	23-24	67.299	2.9	47.0	25.7	3.12	0.90	46.7	70.1	1.16	1.18	0.05	4

The element/Al ratios in both cores are all significantly higher than the ratios of average shale (Borchers et al., 2005; Heinrichs et al., 1980), except for Mn/Al ratios, which are significantly lower than that of average shale in both cores. The Ni/Al, Cu/Al and P/Al ratios are generally higher in core 23060 than core 23010, while the Mn/Al and Ba/Al

ratios are higher in core 23010 than core 23060. Compared to core 23060, the Fe/Al ratios are higher in core 23010 in the upper 6 cm and are lower in core 23010 for the section below 6 cm. The Ni/Al and Cu/Al ratios generally show a good synchronicity with depths in both cores. The Ba/Al ratios in core 23010 decrease from the surface to around 18~19 cm depth, display a significant positive excursion around at 25-26 cm depth and decrease again further down the core. The Ni isotope compositions are generally lighter in core 23010 (0.82~1.14‰) compared to core 23060 (0.97~1.20‰), with similar compositions in both cores towards the surface of the seafloor (Figure. 5.8H).

For porewater samples, the concentrations of dissolved Fe, Mn and Ni are generally higher than the mean ocean value in both cores (Figure 5.9 and Table 5.5) (Nozaki, 2001). Between these two cores, the concentrations of dissolved Fe and Mn are higher in core 23060, while the concentrations of dissolved Ni are higher in core 23010. Dissolved Fe in core 23060 displays a significant enrichment at the upper ~13 cm, while the concentration drops below this depth, to a comparable range relative to the concentration in core 23010. The concentrations of dissolved Mn and Ni decrease with depths in both cores. The sulfate concentrations in the porewaters extracted from core 23060 generally agree with the average in the ocean (~28 mM; Canfield and Farquhar, 2009), while the sulfate concentrations in porewaters extracted from core 23010 (9.5~22.9 mM) are notably lower than mean ocean (~28 mM) with a significant drop starting from ~17 cm depth.

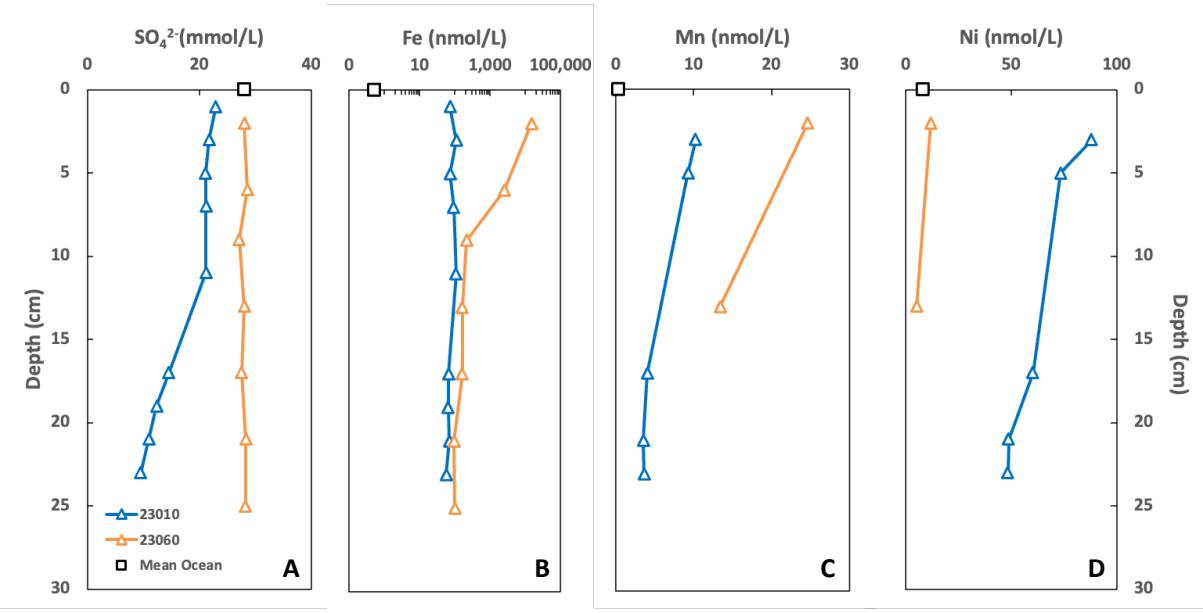


Figure 5.9. Depth profiles of sulfate and trace metal (Fe, Mn and Ni) concentration in porewater samples extracted from sediment cores 23010 (blue) and 23060 (orange). Depth represents centimeters below seafloor (cmbsf). Mean ocean values are noted as black squares (Nozaki, 2001).

Table 5.5. Depth profiles of sulfate and trace metal concentrations in porewater samples extracted from sediment cores 23010 and 23060.

Depth (cm)	$SO4^{2-}$ (mM)	Fe (nM)	Mn (nM)	Ni (nM)
Core 23010 (14.226°E, 23.001°S)				
1	22.9	73		
3	21.8	110	10.3	88
5	21.1	74	9.3	73
7	21.2	94		
11	21.2	109		
17	14.6	67	4.1	60
19	12.4	64		
21	11.0	70	3.5	49
23	9.5	57	3.7	48
Core 23060 (13.32°E, 23.000°S)				
2	28.0	14909	24.6	11.9
6	28.6	2505		
9	27.1	217		
13	28.0	164	13.4	5.2
17	27.5	161		
21	28.3	94		
25	28.2	101		

5.4 Discussion

5.4.1 Regional water mass mixing versus local redox changes

The Ni concentrations and oxygen levels in the seawater profiles along the 23°S transect show distinct patterns between inshore and offshore stations which have varying oxygen concentrations (Figure 5.2). The concentration of dissolved Ni decreases with depth at the inshore station 23005, while it increases with depth at the offshore station 23070 (Figure 5.2A).

The hydrographic data (temperature and O_2 level) of seawater along 23°S transect suggest that the dissolved Ni concentration at the offshore station 23070 likely reflects the upwelling of the micro-nutrient rich, oxygen poor South Atlantic Central Water (SACW) (Figure 5.10A) and the signals exerted by the primary production at the surface which increases O_2 level and decreases dissolved Ni concentration (Figure 5.10B). The dissolved Ni pattern at the inshore station 23005 is likely governed by local redox changes which may cause remineralization of formed minerals from sediments as lateral benthic input.

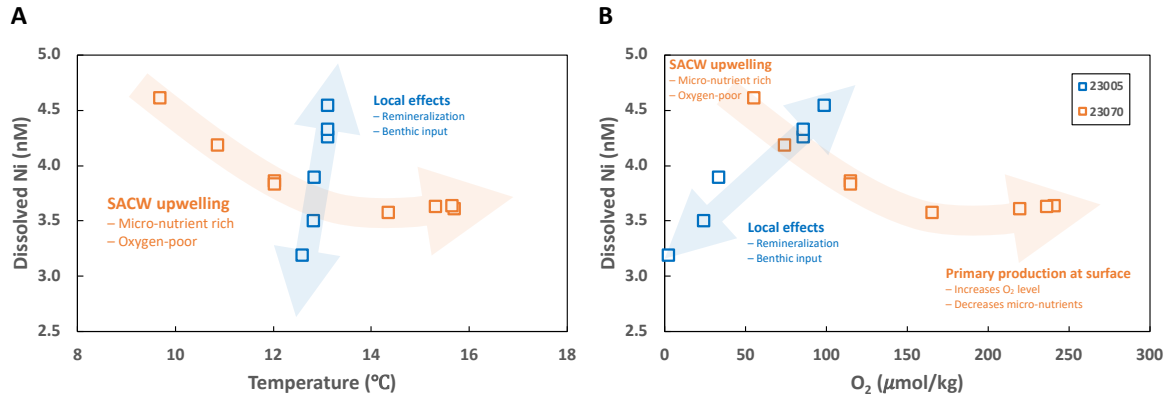


Figure 5.10. Local effect versus water mass mixing for seawaters collected at stations 23005 and 23070. Dissolved Ni values are plotted with temperature and oxygen level.

As a biologically essential micro-nutrient, dissolved Ni profile in the ocean is influenced by the biological uptake at the surface and the subsequent remineralization at depths, which the patterns can be seen at the offshore station 23070. While the patterns at the inshore station 23005 suggest that the lateral transport from Namibian coasts may play a more important role controlling the seawater profiles of dissolved Ni. These enhancements can be caused by the release from sediments interacting with oxygen-depleted waters, which has commonly been found in the Benguela upwelling region and Peruvian margin (Bruland et al., 2005; Liu et al., 2022; Noble et al., 2012; Plass et al., 2021). These anoxic bottom waters can facilitate metal fluxes from sediments by the reductive dissolution of metal-oxides (Heggie and Lewis, 1984; Johnson et al., 1988; Lohan and Bruland, 2008).

Particulate Ni concentration is higher at the inshore station 23005, compared to the offshore station 23070 (Figure 5.7), which suggests that more particulate Ni can originate from the re-suspended organic-rich sediments inshore, further implying that local effects may play a role on coastal seawater. In addition to Ni, enrichment of Fe, Ba, Mn and P in particulates at the inshore station 23005 can also been observed. While the offshore particulates enrich more Ca, which suggests that its composition may be mainly calcareous and biogenic, for instance coccoliths. At the inshore station 23005, the concentration of particulate Fe (~11 nM) is higher than the concentration of dissolved Fe (~8.3 nM) at ~10 m depth, which supports the observations that advected particulate Fe is an important component in oceanic iron inventory (Lam et al., 2006; Lohan and Bruland, 2008; Moore and Braucher, 2008). The fractions in particulates also contribute to the oceanic inventory for other metals, for instance at station 23005, ~1.3% of

dissolved Ni and ~2.9% of dissolved Mn, but the contributions are less significant than particulate Fe.

Overall, the patterns from dissolved and particulate Ni suggests the controlling factors are different at stations 23005 and 23070; the inshore signals reflect mainly about local redox changes, while the offshore signals records more about regional water mass mixing of SACW.

5.4.2 Evidence for a benthic input of Ni from sulfidic sediments

The sediments collected along the 23°S transect in the shelf region off Namibian, are generally enriched in trace metals (Ni, Cu, Co, Fe, Ba), total organic carbon and phosphorus (P) (Figure 5.8), compared to the composition of average shale (Borchers et al., 2005; Heinrichs et al., 1980). The Ni in the sediments is more enriched at the offshore station 23060, compared to the inshore station 23010 (Figure 5.8A).

These observations between these two cores may be explained by their redox status. With the low BWO level (~2 μmol/kg), TOC content (5.0~10.8%) and the presence of H_2S at the inshore station, it suggests an euxinic (anoxic and sulfidic) setting for the sediment core 23010. While the BWO level (~55 μmol/kg), TOC content (2.6~3.8%) and the absence of H_2S at the offshore station, it suggests a dysoxic (2.0~0.2 mL/L of O_2, equals to 87~8.7 μmol/kg of O_2; Tyson and Pearson, 1991) setting for the sediment core 23060.

The results of sulfate, Fe and Mn concentration in porewaters provide supplementary evidence for the redox conditions at both cores. The porewater profiles of sulfate show a significant consumption of sulfate in core 23010 ($[SO_4^{2-}]$ = 9.5~22.9 mM) and a relatively

slight consumption in core 23060 ($[SO_4^{2-}]$ = 27.1~28.6 mM) (Figure 5.9A), compared to its mean concentration of ~28.4 mM in the modern ocean (Kah et al., 2004). These consumptions of sulfate suggest that it has been used as an electron acceptor for the degradation of organic matters via dissimilatory sulfate reduction, indicating further that manganese and iron oxides in the sediments should have been reduced (Jorgensen and Kasten, 2006). The most common dissimilatory sulfate reductions are carried out by sulfate-reducing bacteria (SRB) which conserve energy and release H_2S to the environment (Jorgensen and Kasten, 2006). This dissimilatory sulfate reduction is supported by the lower Fe and Mn concentrations in porewaters within core 23010 where the sulfate has been markedly consumed, compared to core 23060 (Figure 5.9B and 5.9C). These porewater profiles suggest that the nearshore core 23010 is in a more oxygen-depleted biogeochemical settings with the presence of H_2S, while core 23060 is less reduced in terms of biogeochemical zonation as its sulfate concentration just starts to be utilized. The less reduced condition in core 23060 is also supported by the significant (approximately two-order) drop of Fe concentration in the porewater profile in core 23060 from ~14909 nM to ~93 nM (Figure 5.9B), which reflects the reduction of iron, as a favored electron acceptor prior to sulfate reduction in the porewater biogeochemical sequence (Jorgensen and Kasten, 2006).

Due to the more reduced status of sediment core 23010, metal fluxes (e.g., Ni, Cu, Co, Fe) from sediments induced by reductive dissolution of metallic oxides can be expected inshore, which has been observed to be relatively depleted in sediments (Figure 5.8). This is also evidenced by the higher Ni concentration in the porewaters in core 23010, which suggests a reductive remobilization of Ni from oxides in sediments into porewaters (Figure 5.9D). However, the mechanism controlling sedimentary Mn may be different,

which is markedly depleted in both cores (average Mn/Al at 23010 = ~57 ($\times10^{-4}$); at 23060 = ~47 ($\times10^{-4}$)) relative to the composition of average shale (Mn/Al = 96($\times10^{-4}$)) (Borchers et al., 2005; Heinrichs et al., 1980). This depletion can be explained by the interaction between sediments and oxygen-depleted bottom waters in the Namibian shelf region, that Mn is remobilized from Mn oxyhydroxides into porewaters either via chemical reduction or microbial catalysis (Thamdrup et al., 1994b, 1994a). This is supported by the enrichment of Mn in porewaters observed in both cores, while the porewater Mn is higher in the offshore core 23060 (Figure 5.9C), as it is relatively depleted in sediments (Figure 5.8F).

The contrasting difference between the depletion of Mn and the enrichments of sulfide-forming elements like Ni, Cu, Co and Fe suggests that sulfide formation may play an important role controlling the metal inventories in Namibian sediments, with the presence of H_2S, as Mn is not fixed as sulfides but the others are (Heggie and Lewis, 1984). This negatively-correlated relationship between Mn and other trace metals is not seen in other upwelling regions such as the Gulf of California (Brumsack, 1989) and Peruvian margin (Böning et al., 2004), where Co is depleted synchronously with Mn. As the appearance of hydrogen sulfide has been confirmed in both Namibian (Borchers et al., 2005) and Peruvian margin (Xie et al., 2019; Plass et al., 2020; Plass et al., 2021), one possible explanation is the differences in the characteristics of local bedrocks as detrital sources, between Namibian and Peruvian regions.

5.4.3 Detrital versus authigenic controls on Ni in the sediments

The Ni isotope compositions (δ^{60}Ni) in the two sediment cores show a systematic difference; the δ^{60}Ni of 0.82~1.14‰ in the inshore core 23010, which has lower Ni/Al

ratios, higher TOC contents and euxinic porewater chemistry, are generally ~0.2‰ lower than the δ^{60}Ni of 0.97~1.20‰ in the offshore core 23060, which has higher Ni/Al ratios, lower TOC contents and dysoxic porewater chemistry (Figure 5.8).

It has been reported that the δ^{60}Ni of authigenic Ni in organic-rich sediments likely record the isotope composition of deep ocean with limited isotope fractionations, but which has only been verified in Peruvian sediments (Ciscato et al., 2018). As one of most productive upwelling regions, Namibian sediments provide another great opportunity to test the argument. To obtain the precise amount and isotope composition of authigenic Ni in the sediments, a correction for removing the detrital Ni fraction is implemented here.

$$[Ni]_{authigenic} = [Ni]_{bulk} - [Al]_{bulk} \times (Ni/Al)_{detrital} \quad (5.2)$$

For the expression, $[Ni]_{authigenic}$ and $[Ni]_{bulk}$ stand for the Ni concentration in the authigenic fraction and the bulk sediments, respectively. While $(Ni/Al)_{detrital}$ represents the Ni/Al for the detrital source of Ni. A Ni/Al ratio of 9.18×10^{-4} for the detrital fraction is applied for the Namibian sediments collected in this study, which is adapted from the Ni/Al ratio in the suspended load of Orange River, in the south of the sampling sites (28~29°S), the main sedimentary source for Namib Erg (23~27°S) and Skeleton Erg (17~22°S) via the equatorward Benguela Current (Garzanti et al., 2014, 2012). The Ni/Al ratio of 3.3×10^{-4} is applied in other literature data for organic-rich sediments from other upwelling regions (Böning et al., 2012; Ciscato et al., 2018). The Ni isotope composition of the authigenic Ni fraction in sediments can then be calculated as below.

$$\delta^{60}Ni_{authigenic} = \frac{\delta^{60}Ni_{bulk} - f_{detrital} \times \delta^{60}Ni_{detrital}}{f_{authigenic}} \quad (5.3)$$

In the expression, $\delta^{60}Ni_{authigenic}$, $\delta^{60}Ni_{detrital}$ and $\delta^{60}Ni_{bulk}$ represent the Ni isotope compositions for authigenic fraction, detrital fraction and bulk sediments, respectively. While $f_{detrital}$ and $f_{authigenic}$ are the proportion of detrital and authigenic fraction in a sample, respectively. The $\delta^{60}Ni_{detrital}$ of 0.115 ± 0.011‰, the average of bulk silicate earth, is applied in this study (Klaver et al., 2020). This calculation yields authigenic fractions as 52~80% and 80~85% of the bulk Ni in sediment core 23010 and 23060, respectively (Figure 5.11 and Table 5.6).

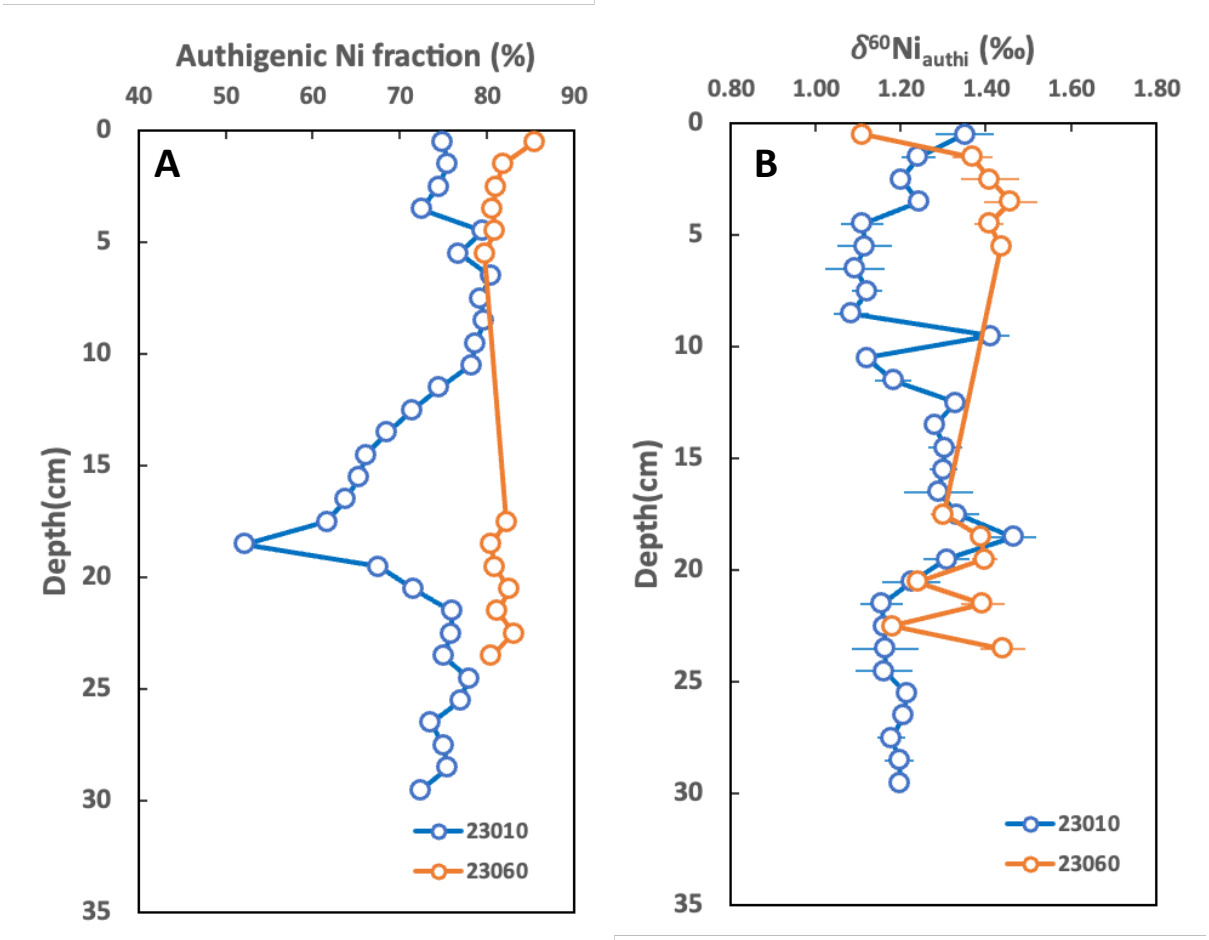
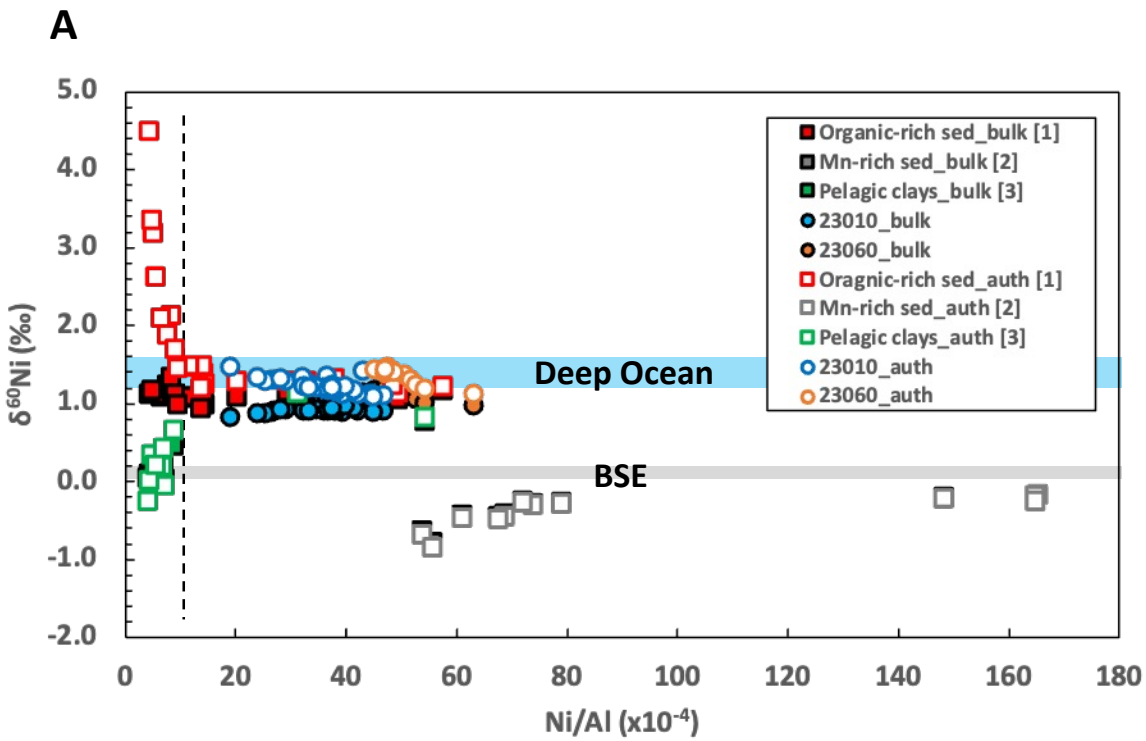


Figure 5.11. Depth profiles of calculated authigenic Ni fraction and Ni isotope composition in Namibian sediment cores 23010 and 23060. Error bars noted in δ^{60}Ni values represent the standard deviation (2SD) of duplicated measurements.

Table 5.6. Estimated authigenic Ni fraction and Ni isotope composition in Namibian sediment cores 23010 and 23060. A Ni/Al ratio of 9.18×10^{-4} for the detrital fraction is applied.

Sample ID	Depth (cm)	Ni_{total} (µg/g)	Ni_{authi} (µg/g)	Ni_{authi} (%)	$\delta^{60}Ni_{authi}$ (‰)
R/V Mirabilis, core 23010 (14.226°E, 23.001°S), 102 m water depth, BWO = 2.7 µmol/kg					
23010_0-1	0-1	10.5	7.8	74.9	1.35
23010_1-2	1-2	9.4	7.1	75.5	1.24
23010_2-3	2-3	15.6	11.6	74.5	1.20
23010_3-4	3-4	8.5	6.2	72.5	1.24
23010_4-5	4-5	10.5	8.3	79.5	1.11
23010_5-6	5-6	10.4	8.0	76.7	1.12
23010_6-7	6-7	19.4	15.6	80.4	1.09
23010_7-8	7-8	24.1	19.1	79.3	1.12
23010_8-9	8-9	24.3	19.4	79.6	1.08
23010_9-10	9-10	11.4	9.0	78.7	1.41
23010_10-11	10-11	27.1	21.2	78.2	1.12
23010_11-12	11-12	28.8	21.5	74.5	1.18
23010_12-13	12-13	32.9	23.5	71.4	1.33
23010_13-14	13-14	28.0	19.2	68.5	1.28
23010_14-15	14-15	27.7	18.3	66.1	1.30
23010_15-16	15-16	31.5	20.6	65.4	1.30
23010_16-17	16-17	29.6	18.9	63.8	1.29
23010_17-18	17-18	26.8	16.5	61.6	1.33
23010_18-19	18-19	25.6	13.4	52.2	1.46
23010_19-20	19-20	19.9	13.4	67.5	1.31
23010_20-21	20-21	14.4	10.3	71.6	1.23
23010_21-22	21-22	21.0	15.9	76.0	1.16
23010_22-23	22-23	20.2	15.3	75.9	1.16
23010_23-24	23-24	18.8	14.1	75.0	1.16
23010_24-25	24-25	23.3	18.1	77.9	1.16
23010_25-26	25-26	16.5	12.7	77.0	1.21
23010_26-27	26-27	19.7	14.5	73.6	1.21
23010_27-28	27-28	24.3	18.2	75.0	1.18
23010_28-29	28-29	27.1	20.4	75.5	1.20
23010_29-30	29-30	25.2	18.3	72.4	1.20
R/V Mirabilis, core 23060 (13.32°E, 23.000°S), 352.5 m water depth, BWO = 67.3 µmol/kg					
23060_0-1	0-1	33.8	28.9	85.5	1.11
23060_1-2	1-2	20.8	17.0	81.8	1.37
23060_2-3	2-3	28.2	22.8	81.1	1.41
23060_3-4	3-4	27.1	21.8	80.7	1.46
23060_4-5	4-5	30.8	25.0	80.9	1.41
23060_5-6	5-6	18.2	14.5	79.7	1.44
23060_17-18	17-18	32.0	26.3	82.2	1.30
23060_18-19	18-19	24.7	19.8	80.5	1.39
23060_19-20	19-20	23.6	19.1	80.8	1.40
23060_20-21	20-21	34.1	28.2	82.6	1.24
23060_21-22	21-22	17.1	13.9	81.2	1.39
23060_22-23	22-23	21.0	17.4	83.1	1.18
23060_23-24	23-24	23.5	18.9	80.5	1.44

The results suggest that the δ^{60}Ni values of the authigenic Ni fractions in the Namibian sediments collected in this study generally agree with the mean δ^{60}Ni of deep ocean (1.33 ± 0.13‰) (Lemaitre et al., 2022), as well as the organic-rich sediments from Peruvian regions (Ciscato et al., 2018) and the pelagic clay sediments from the Western Pacific (Gueguen and Rouxel, 2021), when the Ni/Al ratios are higher than ~10 × 10^{-4} in the sediment samples (Ciscato et al., 2018) (Figure 5.12). When the initial Ni/Al ratios are lower than ~10 × 10^{-4}, the calculated δ^{60}Ni values of authigenic Ni fraction scatter significantly, in agreement with previous observations (Ciscato et al., 2018). The δ^{60}Ni of authigenic Ni fraction ranges from 1.02 to 1.46‰ in core 23010, and it ranges from 1.11‰ to 1.46‰ in core 23060 (Figure 5.12B), which are generally within the range of deep ocean δ^{60}Ni (1.33 ± 0.13‰) (Lemaitre et al., 2022). While the Ni/Al ratios are generally higher in core 23060 (45–65 × 10^{-4}) than core 23010 (20-50 × 10^{-4}) (Figure 5.12B).



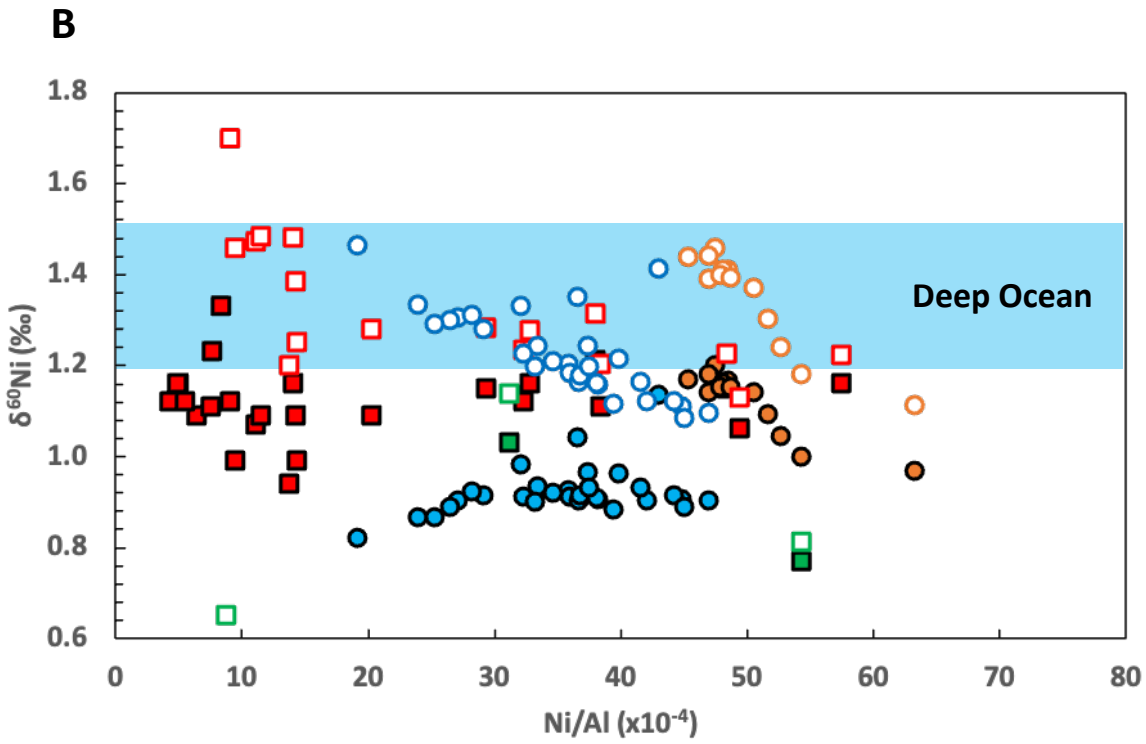


Figure 5.12. δ^{60}Ni values of bulk sediments and authigenic phase plotted with Ni/Al ratios for sediment samples in this study and previously reported sediments under varying environmental settings. Comparison (A) at full scale and (B) with more focus on Namibian sediments cores 23010 and 23060. Colored filled symbols represent bulk sediments, while colored open symbols represent authigenic phases with corrections for detrital phases. The Ni/Al ratio of 9.18 from the suspended phase of Ni in Orange River is applied for sediment samples in this study (Garzanti et al., 2012), while the Ni/Al ratio of 3.3 ($\times10^{-4}$) is applied for others as previously suggested (Böning et al., 2012). The blue shade denotes the global deep ocean δ^{60}Ni value (1.33 ± 0.13‰) (Lemaitre et al., 2022) and the grey shade denotes the δ^{60}Ni value (0.115 ± 0.11‰) of bulk silicate earth (Klaver et al., 2020). The dotted line denotes the convergence of δ^{60}Ni values when Ni/Al is higher than $\sim10\times10^{-4}$, in agreement with Ciscato et al. (2018). The framework of the figure is adapted from Ciscato et al. (2018). Data source: [1] Ciscato et al. (2018), [2] Little et al. (2020) and [3] Gueguen and Rouxel (2021).

An observable difference in Ni/Al ratios can be found in Namibian sediments collected in this study, which may be induced by post-depositional diagenesis. While a limited difference in δ^{60}Ni of authigenic fraction can be observed between the two cores, which demonstrates a great potential of Ni isotopes in authigenic fraction of organic-rich sediments as a proxy for seawater chemistry under dysoxic to euxinic settings.

5.4.4 Sulfide formation dominates the diagenetic cycling of Ni in BUS sediments

It has been suggested that the decreasing pH generated by the activity of sulfate reducing bacteria and the presence of elemental sulfur can facilitate the development of Ni-related sulfides from amorphous (hydrated NiS) to crystalline phases (polydymite (Ni_3S_4) and vaesite (NiS_2)) (Mansor et al., 2019; see Chapter 4). Ni isotope fractionation during the formation of amorphous Ni-sulfides has been reported to follow Rayleigh fractionation with a fractionation factor ($\varepsilon_{S\text{-}L} = (\alpha_{S\text{-}L} - 1) \times 1000$ (‰), where $\alpha_{S\text{-}L}$ is the isotope fractionation factor between precipitates and solution) of -0.22 ~ -0.26‰ after 10 min and reach an equilibrium fractionation with a $\varepsilon_{S\text{-}L}$ of –0.50‰ after 6 h (see Chapter 4). For crystalline Ni-sulfides, $\varepsilon_{S\text{-}L}$ has been determined to be -0.73 ± 0.08‰ for the formation of mixed polydymite and vaesite (Parigi et al., 2022; see Chapter 4). During the mineral transformation under low pH, the solubility of Ni in porewaters increases and may facilitate a remobilization of isotopically heavy Ni from minerals into the porewaters. This remobilization is supported by the lower δ^{60}Ni values and Ni/Al ratios observed in core 23010, compared to core 23060 (Figure 5.8). The presence of H_2S produced by SRB nearshore suggests that such an environment requires more electron acceptors for the degradation of TOC, thus consuming Fe and Mn quantitatively, and sulfate significantly in porewaters (Figure 5.9). This finding suggests that the characteristic appearance of H_2S nearshore off Namibian margin can play an important role in controlling the δ^{60}Ni values in the sediments, as a threshold, which triggers the formation of sulfides, and the subsequent remobilization of Ni and its isotopes, reflected in the coupled sediment and porewater samples here.

The δ^{60}Ni values of authigenic Ni fraction in the sediment core 23060 correlate negatively with Ni/Al, P/Al, Fe/Al, Mn/Al, Co/Al and the proportions of authigenic Ni, which are not seen in core 23010 (Figure 5.13). These correlations suggest that more Ni-containing authigenic phases in the sediments can enrich these elements (Ni, P, Fe, Mn, Co) and lighter Ni isotopes, indicating that the formation of authigenic phases controls Ni and its isotopes in core 23060. While in core 23010 nearshore, the presence of H_2S, sulfide formation and development may influence the signals recorded in the sediments for both trace metals and Ni isotope compositions.

The decreasing pH in the micro-environments surrounding SRB has been reported to lead to the decreasing solubility of Fe-sulfides (when pH is below 6) and Ni-sulfides (when pH decreases from 8.1 to 7, and when pH is below 4) (Mansor et al., 2019; Wilkin and Rogers, 2010). The decreasing solubility of Fe- and Ni-sulfides may similarly influence the solubilities of other trace metals (e.g., Mn, Cu, Co) co-precipitated (Morse and Luther, 1999). This changing solubility suggests the development of Fe- and Ni-sulfides may incorporate and release trace metals back and forth repeatedly, indicating that the authigenic signals reflected in core 23060 may be disrupted in core 23010 with the appearance of sulfide minerals (Figure 5.13).

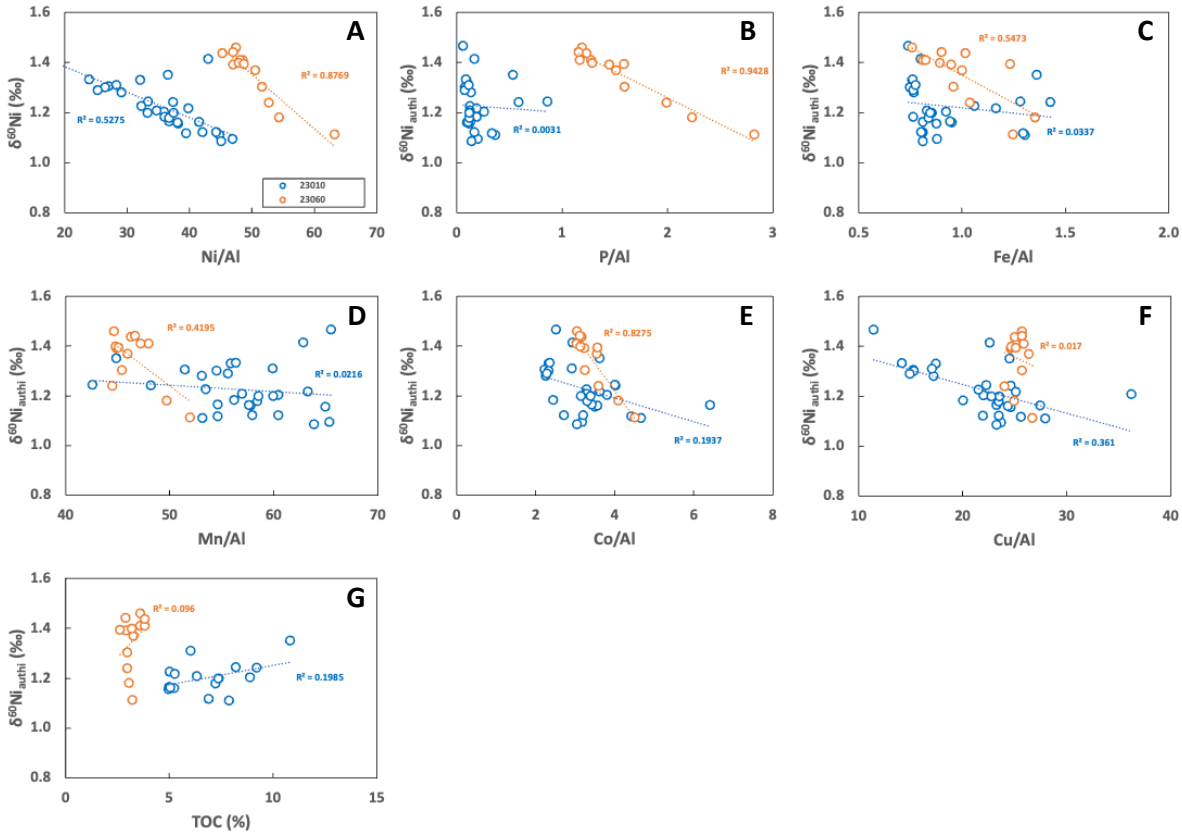


Figure 5.13. Relationship between Ni isotope compositions of authigenic Ni fraction, metal/Al ratios and TOC contents in Namibian sediment cores 23010 and 23060. Data points are shown in blue for core 23010 and orange for core 23060. Dotted lines represent the regression lines, which are colored by sediment cores.

Interestingly, in the upper 6 cm of sediment core 23010, the δ^{60}Ni values of authigenic Ni fraction show a positive correlation (R^2 = 0.83) with TOC content (Figure 5.14), which is not seen in other sections. These results suggest that the organic matter may preferentially enrich heavy Ni isotopes, compared to Ni-containing detrital and authigenic phases, but the δ^{60}Ni values of organic matter may be similar or slightly lighter than seawater (δ^{60}Ni = 1.44 ± 0.15‰) (Cameron and Vance, 2014; Ciscato et al., 2018; Takano et al., 2017), which is likely due to the competition between sinking organic matters and other strong oceanic ligands for Ni (see Chapter 2). This correlation is only seen in the core-top sediments nearshore likely due to the faster sedimentation rate here, compared to the sedimentation rate offshore (Inthorn et al., 2006). While in the bottom

section of core 23010 or core 23060, the signals from organic matter may be overprinted by subsequent diagenesis, for instance the degradation of organic matter and the reductive dissolution of oxide minerals. In this case, fast sedimentation rate may enable the primitive signals from organic matter to be preserved in these "fresh" core-top sediments, on relatively short geological timescales.

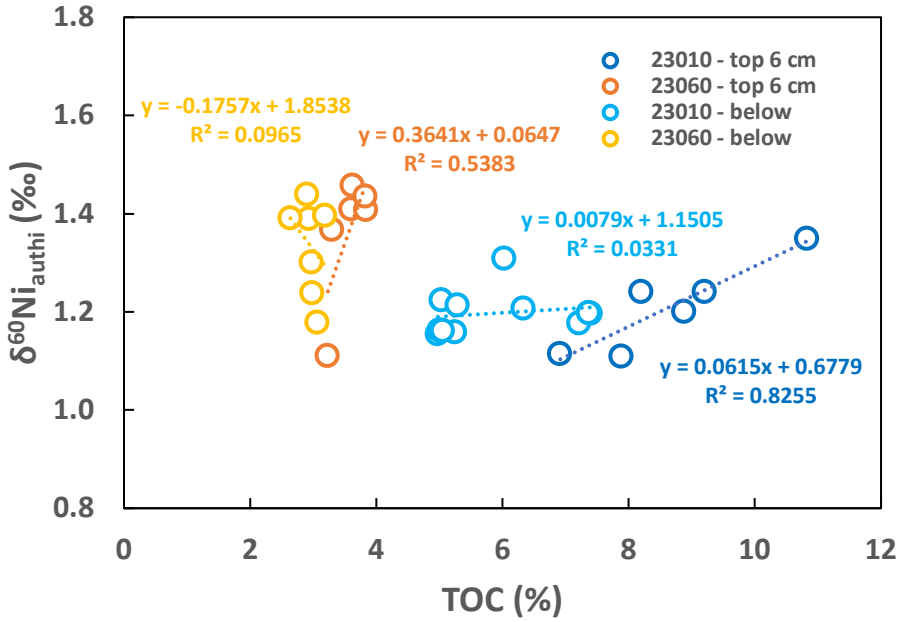


Figure 5.14. δ^{60}Ni of authigenic Ni fraction in sediment samples plotted with TOC contents. Each sediment core is separated into the "top 6 cm" section and the "below" section. Colored dotted lines represent the regression lines for sections.

As a key oceanic output of Ni, processes related to Fe-Mn oxides, including dissolution and precipitation of Mn-oxides, mineral transformation from birnessite to todorokite and scavenging by Fe oxyhydroxides or authigenic clays, haven been proposed to closely control the δ^{60}Ni values in oceanic Ni cycling (Little et al., 2020). Experimental studies have suggested a large isotope fractionation towards light isotopes ($\Delta^{60}Ni_{MnO2\text{-}aqueous}$ = –2.8 ~ –3.4‰) during the sorption of Ni onto birnessite (Sorensen et al., 2020). During

diagenesis, birnessites can undergo mineral transformation to the tectomanganate todorokites, which may cause less incorporation of Ni in the crystal structure, a potential release of isotopically heavy Ni back to porewaters and a fractionation towards light isotopes in the todorokites (Atkins et al., 2016, 2014; Chen et al., 2022; Little et al., 2020; Wegorzewski et al., 2020). The Ni isotope fractionation has been characterized to be $\Delta^{60}Ni_{mineral\text{-}medium}$ = −0.23∼ −0.77‰ during adsorption onto Fe oxyhydroxides (Gueguen et al., 2018; Wasylenki et al., 2015) and −0.11 ± 0.09‰ during onto smectites (Spivak-Birndorf et al., 2018).

In comparison to these processes associated with Fe-Mn oxides, the Namibian sediments investigated here show a relatively narrow variation of Mn/Ni ratios and a negative correlation (R^2 ∼0.7) between the δ^{60}Ni values and Mn/Ni ratios (Figure 5.14). This trend is in contrast to the ones proposed for related Mn cycling and Fe oxyhydroxides/clays scavenging showing positive correlations between δ^{60}Ni and Mn/Ni ratios, which suggest that neither Mn cycling or Fe oxyhydroxides/clays might be the main mechanism controlling the δ^{60}Ni values in Namibian sediments.

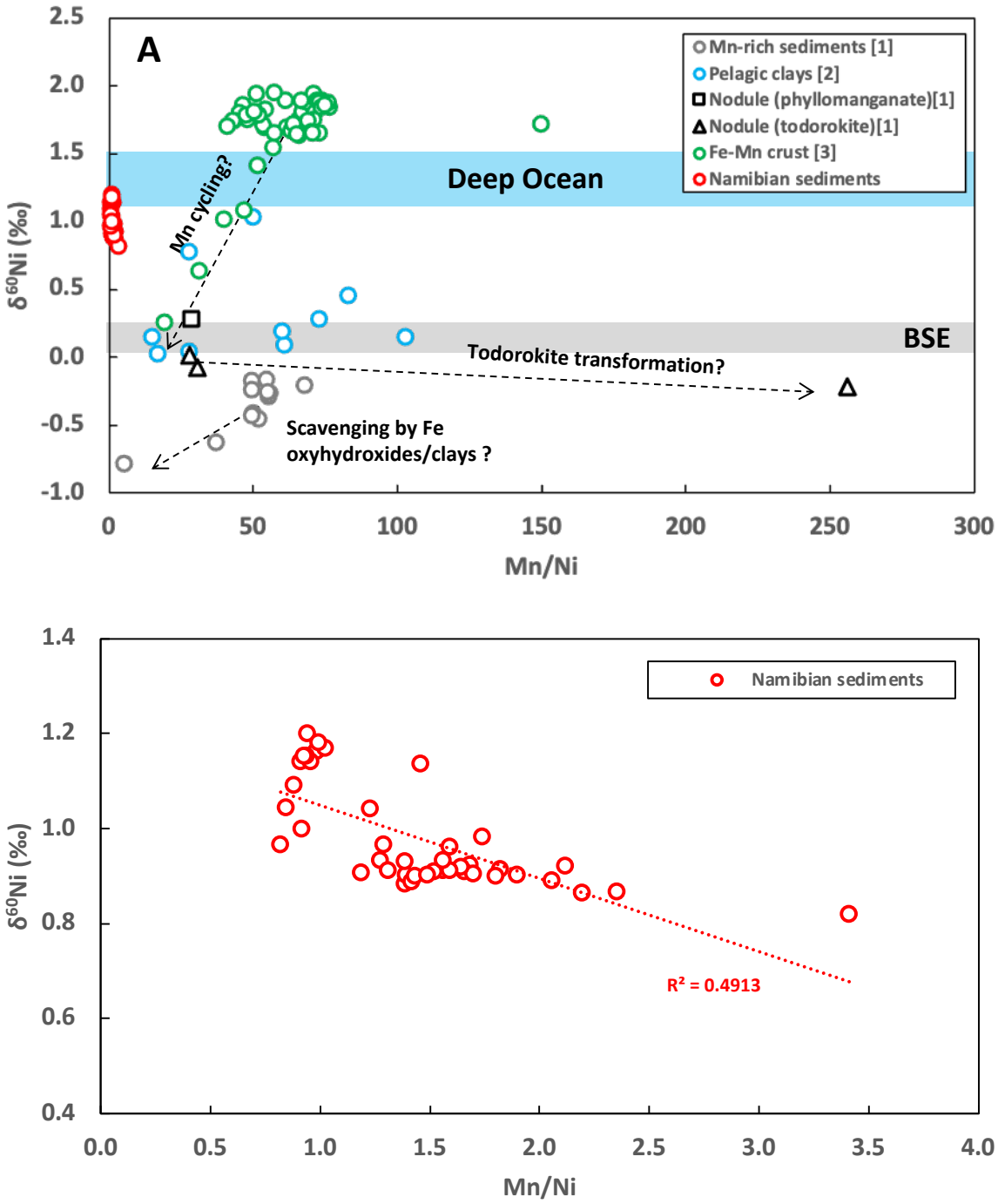


Figure 5.15. δ^{60}Ni values plotted with Mn/Ni ratios for sediment samples in this study and Mn-/Fe-related processes in the ocean reported in previous studies. (A) displays the full ranges and (B) shows the data in this study (red circles). The framework of (A) is adapted from Little et al. (2020). The blue shade denotes the global deep ocean δ^{60}Ni value (1.33 ± 0.13‰) (Lemaitre et al., 2022) and the grey shade denotes the δ^{60}Ni value (0.115 ± 0.11‰) of bulk silicate earth (Klaver et al., 2020). Data source: [1] Little et al. (2020), [2] Gueguen and Rouxel (2021) and [3] Gueguen et al. (2016).

A consistent relationship between Ni and TOC has been reported in sediments collected in various upwelling regions (e.g., Peru, Chile, Namibia), which implies Ni a clear indicator for organic sinking fluxes (Böning et al., 2015, 2009, 2004; Calvert and Price, 1983; Ciscato et al., 2018). In contrast to this strong positive correlation, the nearshore sediments collected in this study show a negative trend between Ni and TOC, in that sediments with higher TOC contents have lower Ni concentrations (Figure 5.15). The offshore sediment core 23060, with dysoxic redox condition, generally falls in the positive Ni-TOC trend with other organic-rich sediments reported in Peruvian, Chilean and Namibian margin (Böning et al., 2015, 2009, 2004; Calvert and Price, 1983; Ciscato et al., 2018), while sediment core 23010 deviates from the trend (Figure 5.15). The potential explanation is the combined effect of the euxinic setting (presence of H_2S), the formation of Ni-containing sulfides and the subsequent development of sulfide minerals with potential Ni remobilization (diagenetic transformation).

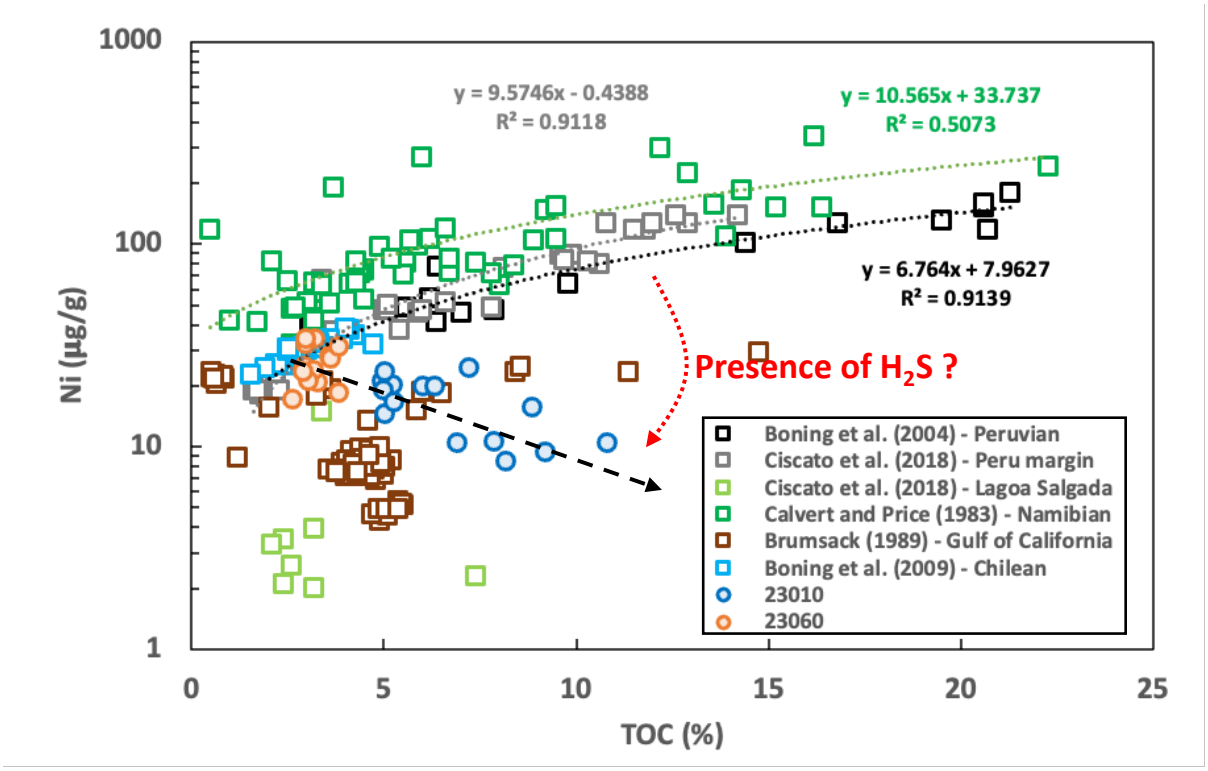


Figure 5.16. Ni abundances plotted with TOC contents in Namibian sediments (this study) and other organic-rich sediments. Total Ni and TOC data in Brumsack (1989), Calvert and Price (1983), Böning et al. (2004), Böning et al. (2005), Böning et al. (2009) and Ciscato et al. (2018) are compared. Colored dotted lines represent the regression lines for each dataset. The black dotted arrow represents the trend between these two parameters in our sediment samples.

Our findings show evidence that sulfide formation and cycling may dominate Ni and its isotopes in BUS sediments, especially in euxinic sediments. It is different to the Mn oxide cycling thought to control Ni cycling in oxic ocean settings. The Ni–TOC relationship suggests that the Namibian region with the presence of H_2S, may undergo different Ni cycling processes, compared to other upwelling regions (e.g., Peru and Chile).

5.4.5 Implications for the oceanic budget of Ni and its isotopes

An imbalance on the budget of Ni fluxes and isotopes in the oceanic Ni cycle has been raised, actively discussed and continuously refined with the emerging of new data since the recent decade (Cameron and Vance, 2014; Ciscato et al., 2018; Gueguen and Rouxel, 2021; Little et al., 2020). Given the new Namibian sample set measured and early diagenesis effect on dysoxic/euxinic sediments observed in this study, we revisit this imbalance problem and provide a refined budget (Table 5.7).

Table 5.7. Budget for Ni and its isotopes in the modern ocean. It is based on a mass balance calculation of best estimated Ni fluxes and their δ^{60}Ni values. Values in bold font denote numbers proposed in this study. Values with stars represents numbers determined by mass balance calculation.

	Flux ($\times10^8$mol/yr)		δ^{60}Ni (‰)	
	Range	Best guess	Mean + SD or range	Best guess
Reservoir				
Global Ocean[a,b,c]		108000	1.44 ± 0.08	1.44
Input Fluxes				
Rivers[b,d,e]	3.6–5.11	3.6	–	0.80
Dust[a,d,e,f,g]	–	0.076	–0.09 to 0.37	0.14
Benthic[h,e,i]	0.6–3.7	1.44	3.17 ± 1.08	**3.23***
Hydrothermal[e]	–	0.14		0.10
Output fluxes				
Pelagic clay sediments[e,h,j]	1.5–5.9	3.08	1.62 ± 0.37	1.62
Carbonate sediments[a]	0.031 to 0.44	0.14	1.10 to 1.64	1.29
Organic-rich sediments[a,e,i]	1.1–2.4	1.6	**1.45 ± 0.57***	**1.45***
Euxinic sediments-Black Sea[a,d,i]	0.093 to 0.25	0.15	0.3 to 0.6	0.45
Total input	4.42–9.03	5.26		**1.44***
Total output	2.72–9.00	4.97		**1.52**
Residence time (yr)	11960–39706	20548–21730		

Reference: (a) Ciscato et al. (2018); (b) Cameron and Vance (2014); (c)Takano et al. (2017); (d) Vance et al. (2016); (e) Gueguen and Rouxel (2021); (f) Desboeufs et al. (2005); (g) Cameron et al. (2009); (h) Little et al. (2020); (i) This study; (j) Gall et al. (2013).

The main Ni input into the ocean is delivered by rivers with a flux of 3.6×10^8 mol/yr and a concentration-weighted δ^{60}Ni value of 0.8‰ (Cameron and Vance, 2014; Gueguen and Rouxel, 2021; Vance et al., 2016). Other identified inputs are atmospheric dust and hydrothermal with fluxes of 0.076×10^8 mol/yr (Cameron et al., 2009; Ciscato et al., 2018; Desboeufs et al., 2005; Gueguen and Rouxel, 2021; Vance et al., 2016) and 0.14×10^8 mol/yr (Gueguen and Rouxel, 2021), respectively. The δ^{60}Ni values for dust and hydrothermal inputs are 0.14‰ (Ciscato et al., 2018; Vance et al., 2016) and 0.10‰(Gueguen and Rouxel, 2021) , respectively, close to the δ^{60}Ni value of bulk silicate earth (δ^{60}Ni = 0.115 ± 0.11‰) (Klaver et al., 2020). It has been recently proposed that a benthic flux from oxic sediments can occur, during the diagenetic transformation from birnessite to todorokite in oxic/suboxic settings and the subsequent release of Ni due to the decreased incorporation of Ni in the mineral structure , or via cycles of redox-driven Mn-oxide dissolution and precipitation (Atkins et al., 2016; Little et al., 2020). This benthic flux was first modelled to be 1.44×10^8 mol/yr with a δ^{60}Ni value of 3.03‰, based on mass balance calculation assuming a steady state (Little et al., 2020), which was later refined to a flux of 3.7×10^8 mol/yr with a δ^{60}Ni value of 2.85‰ (Gueguen and Rouxel, 2021).

The main sink of Ni in the ocean has been reported to be pelagic clay sediments, or called authigenic oxic sediments, with a flux of 3.08×10^8 mol/yr and a mean δ^{60}Ni of 1.62‰ (Gall et al., 2013; Gueguen and Rouxel, 2021; Little et al., 2020). Other output fluxes are organic-rich sediments, euxinic sediments and carbonate sediments, with fluxes of 1.6×10^8 mol/yr (Ciscato et al., 2018; Gueguen and Rouxel, 2021), 0.15×10^8 mol/yr (Ciscato et al., 2018; Vance et al., 2016) and 0.14×10^8 mol/yr (Ciscato et al., 2018), respectively;

and the estimated δ^{60}Ni values of 1.12‰, 0.45‰ and 1.29‰ (Ciscato et al., 2018), respectively.

Here, a refined δ^{60}Ni of 1.45‰ representative for organic-rich sediments is proposed by calculating an average δ^{60}Ni (n = 79) for authigenic Ni fraction in organic-rich sediments from Namibian (this study) and Peruvian regions (Ciscato et al., 2018). Using the assumption that steady state conditions prevail in the modern ocean, a mass balance model can be applied to calculate Ni isotope compositions and magnitudes of the input and output fluxes:

$$\Sigma F_i^{in} \times \delta^{60}Ni_i^{in} = \Sigma F_i^{out} \times \delta^{60}Ni_i^{out} \quad (5.4)$$

where F_i^{in} and F_i^{out} represent the Ni input and output fluxes, respectively, and $\delta^{60}Ni_i^{in}$ and $\delta^{60}Ni_i^{out}$ are the representative Ni isotope compositions. Using equation (5.4), the magnitudes and weighted δ^{60}Ni values are calculated as 5.26×10^8 mol/yr with a δ^{60}Ni value of 1.44‰ for the total Ni input flux, given the total flux of 4.97×10^8 mol/yr with a δ^{60}Ni of 1.52‰ for the total output flux based on the refined Ni isotope composition (δ^{60}Ni = 1.45‰) representative for organic-rich sediments.

Given that the best-estimated range of net input and output flux is 4.97~5.26 × 10^8 mol/yr, with the assumption of a global ocean volume of 1.35×10^{21} kg and a mean Ni concentration of 8 nM which yields to 1.08×10^{13} moles Ni in the modern ocean (Little et al., 2020), the residence time is calculated to be 21~22 kyr, in agreement with previous estimates (10~21 kyr) (Little et al., 2020; Sclater et al., 1976). While the full range of

residence time can be 12∼40 kyr based on all the variations of input and output reported previously.

Using equation (5.4) for further calculation for each flux, with fluxes provided previously, the Ni isotope composition of diagenetic benthic flux would be 3.23‰, given a flux of 1.44×10^8 mol/yr (Little et al., 2020) and the assumption that the mass balance at steady-state conditions is preserved. It suggests a remobilization of isotopically heavy Ni from the sediments, with a magnitude of isotope fractionation (3.23‰) slightly larger than the previous estimates (∼3‰ by Little et al., 2020; ∼2.85‰ by Gueguen and Rouxel, 2021). This benthic flux includes the remobilization of Ni in both oxic and anoxic sediments, with the relative contribution remaining to be determined. Such a diagenetic effect in euxinic marine sediments, via mineral transformation under decreasing pH from amorphous (ε_{S-L} = −0.22 ∼ −0.50‰) to crystalline sulfides (ε_{S-L} = −0.73 ± 0.08‰) with resulted increasing solubility, may release isotopically heavy Ni and contribute to balance the oceanic Ni budget (see Chapter 4), which has not been considered before. With the remobilization of Ni and its isotopes during diagenetic transformation of minerals observed in both oxic and anoxic ocean settings, it indicates that early diagenesis can play an important role governing the cycling and inventory of Ni and its isotopes in the ocean.

5.5. Conclusions

We report Ni isotope compositions in organic-rich sediments and the complementary profiles of trace metals in ambient porewaters, seawaters and particulates off Namibian margin in the north BUS. The inshore sediments generally have ∼0.2‰ lighter δ^{60}Ni values and lower Ni/Al ratios, compared to the sediments offshore, which can be explained by the diagenetic transformation of sulfide minerals and the resulted

remobilization of isotopically heavy Ni from the sediments under euxinic condition. This reduced redox status is supported by the significant consumption of SO_4^{2-} concentration recorded in the porewaters. Lateral transportations of Ni, Cu and Cd from the coast are clearly observed in the sediments inshore but not offshore. The δ^{60}Ni of authigenic Ni fraction in organic-rich sediments may reflect the isotope composition of deep ocean, with limited isotope fractionation and varying Ni/Al ratios, likely caused by post-depositional diagenesis. In general, offshore stations record more about regional water mass mixing and primitive authigenic phases, while inshore stations reflect more about local redox changes including sulfide formation.

We suggest that the diagenetic remobilization of Ni can occur in euxinic sediments and contribute to balance the oceanic Ni budget. With the δ^{60}Ni of 1.45‰ for organic-rich marine sediments refined here, a δ^{60}Ni value of 3.23‰ representative for the diagenetic benthic flux is proposed to balance the oceanic Ni budget, which is slightly higher than the previous models (2.85~3.00‰), given that the magnitudes and δ^{60}Ni values of other input and output fluxes remain similar to previous studies. With refined sources and sinks from recent literatures, we best-guess the residence time of Ni in the ocean is about 21-22 kyr, in parallel with previous estimates (10~21 kyr).

Our comprehensive sample set discloses an integrated Ni cycling in a strong upwelling region with high productivity, showing the potential of applying Ni isotopes in organic-rich marine sediments as an indicator for paleo-studies and prompting more future researches on the magnitudes and triggers of early diagenesis on Ni and its isotopes in the ocean.

5.6 References

Atkins, A.L., Shaw, S., Peacock, C.L., 2016. Release of Ni from birnessite during transformation of birnessite to todorokite: Implications for Ni cycling in marine sediments. Geochim. Cosmochim. Acta 189, 158–183. https://doi.org/10.1016/j.gca.2016.06.007

Atkins, A.L., Shaw, S., Peacock, C.L., 2014. Nucleation and growth of todorokite from birnessite: Implications for trace-metal cycling in marine sediments. Geochim. Cosmochim. Acta 144, 109–125. https://doi.org/10.1016/j.gca.2014.08.014

Böning, P., Brumsack, H.J., Böttcher, M.E., Schnetger, B., Kriete, C., Kallmeyer, J., Borchers, S.L., 2004. Geochemistry of Peruvian near-surface sediments. Geochim. Cosmochim. Acta 68, 4429–4451. https://doi.org/10.1016/j.gca.2004.04.027

Böning, P., Brumsack, H.J., Schnetger, B., Grunwald, M., 2009. Trace element signatures of Chilean upwelling sediments at ~ 36°S. Mar. Geol. 259, 112–121. https://doi.org/10.1016/j.margeo.2009.01.004

Böning, P., Cuypers, S., Grunwald, M., Schnetger, B., Brumsack, H.J., 2005. Geochemical characteristics of Chilean upwelling sediments at ~36°S. Mar. Geol. 220, 1–21. https://doi.org/10.1016/j.margeo.2005.07.005

Böning, P., Fröllje, H., Beck, M., Schnetger, B., Brumsack, H.J., 2012. Underestimation of the authigenic fraction of Cu and Ni in organic-rich sediments. Mar. Geol. 323–325, 24–28. https://doi.org/10.1016/j.margeo.2012.07.004

Böning, P., Shaw, T., Pahnke, K., Brumsack, H.J., 2015. Nickel as indicator of fresh organic matter in upwelling sediments. Geochim. Cosmochim. Acta 162, 99–108. https://doi.org/10.1016/j.gca.2015.04.027

Borchers, S.L., Schnetger, B., Böning, P., Brumsack, H.J., 2005. Geochemical signatures of the Namibian diatom belt: Perennial upwelling and intermittent anoxia. Geochemistry, Geophys. Geosystems 6. https://doi.org/10.1029/2004GC000886

Bordbar, M.H., Mohrholz, V., Schmidt, M., 2021. The Relation of Wind-Driven Coastal and Offshore Upwelling in the Benguela Upwelling System. J. Phys. Oceanogr. 51, 3117–3133. https://doi.org/10.1175/JPO-D-20-0297.1

Brüchert, V., Jørgensen, B.B., Neumann, K., Riechmann, D., Schlösser, M., Schulz, H., 2003. Regulation of bacterial sulfate reduction and hydrogen sulfide fluxes in the central Namibian coastal upwelling zone. Geochim. Cosmochim. Acta 67, 4505–4518. https://doi.org/10.1016/S0016-7037(03)00275-8

Bruland, K.W., 1980. Oceanographic distributions of cadmium, zinc, nickel, and copper in the North Pacific. Earth Planet. Sci. Lett. 47, 176–198. https://doi.org/10.1016/0012-821X(80)90035-7

Bruland, K.W., Rue, E.L., Smith, G.J., DiTullio, G.R., 2005. Iron, macronutrients and diatom

blooms in the Peru upwelling regime: Brown and blue waters of Peru. Mar. Chem. 93, 81–103. https://doi.org/10.1016/j.marchem.2004.06.011

Brumsack, H.J., 1989. Geochemistry of recent TOC-rich sediments from the Gulf of California and the Black Sea. Geol. Rundschau 78, 851–882. https://doi.org/10.1007/BF01829327

Burdige, D.J., 1993. The biogeochemistry of manganese and iron reduction in marine sediments. Earth Sci. Rev. 35, 249–284. https://doi.org/10.1016/0012-8252(93)90040-E

Calvert, S.E., Price, N.B., 1983. Geochemistry of Namibian Shelf Sediments. Coast. Upwelling Its Sediment Rec. 337–375. https://doi.org/10.1007/978-1-4615-6651-9_17

Calvert, S.E., Price, N.B., 1970. Minor metal contents of recent organic-rich sediments off South West Africa. Nature 227, 593–595. https://doi.org/10.1038/227593a0

Cameron, V., Vance, D., 2014. Heavy nickel isotope compositions in rivers and the oceans. Geochim. Cosmochim. Acta 128, 195–211. https://doi.org/10.1016/j.gca.2013.12.007

Cameron, V., Vance, D., Archer, C., House, C.H., 2009. A biomarker based on the stable isotopes of nickel. Proc. Natl. Acad. Sci. 106, 10944–10948. https://doi.org/10.1073/pnas.0900726106

Canfield, D.E., Farquhar, J., 2009. Animal evolution, bioturbation, and the sulfate concentration of the oceans. Proc. Natl. Acad. Sci. U. S. A. 106, 8123–8127. https://doi.org/10.1073/pnas.0902037106

Chavez, F.P., Messié, M., 2009. A comparison of Eastern Boundary Upwelling Ecosystems. Prog. Oceanogr. 83, 80–96. https://doi.org/10.1016/j.pocean.2009.07.032

Chen, L., Archer, C., Little, S.H., Peacock, C.L., 2022. An isotopically heavy source of nickel: Release of nickel during birnessite transformation into todorokite. Goldschmidt abstract.

Ciscato, E.R., Bontognali, T.R.R., Vance, D., 2018. Nickel and its isotopes in organic-rich sediments: implications for oceanic budgets and a potential record of ancient seawater. Earth Planet. Sci. Lett. 494, 239–250. https://doi.org/10.1016/j.epsl.2018.04.061

Cullen, J.T., Sherrell, R.M., 1999. Techniques for determination of trace metals in small samples of size-fractionated particulate matter: Phytoplankton metals off central California. Mar. Chem. 67, 233–247. https://doi.org/10.1016/S0304-4203(99)00060-2

Cutter, G.A., Andersson, P., Codispoti, L., Croot, P., Place, P., Hoe, T., Kingdom, U., Francois, R., Sciences, O., Lohan, M., Circus, D., Obata, H., 2017. Sampling and Sample-handling

Protocols for GEOTRACES Cruises. GEOTRACES.

Desboeufs, K. V., Sofikitis, A., Losno, R., Colin, J.L., Ausset, P., 2005. Dissolution and solubility of trace metals from natural and anthropogenic aerosol particulate matter. Chemosphere 58, 195–203. https://doi.org/10.1016/j.chemosphere.2004.02.025

Duncombe Rae, C.M., 2005. A demonstration of the hydrographic partition of the Benguela upwelling ecosystem at 26°40'S. African J. Mar. Sci. 27, 617–628. https://doi.org/10.2989/18142320509504122

Emeis, K.C., Brüchert, V., Currie, B., Endler, R., Ferdelman, T., Kiessling, A., Leipe, T., Noli-Peard, K., Struck, U., Vogt, T., 2004. Shallow gas in shelf sediments of the Namibian coastal upwelling ecosystem. Cont. Shelf Res. 24, 627–642. https://doi.org/10.1016/j.csr.2004.01.007

Fietzke, J., Frische, M., 2016. Experimental evaluation of elemental behavior during LA-ICP-MS: Influences of plasma conditions and limits of plasma robustness. J. Anal. At. Spectrom. 31, 234–244. https://doi.org/10.1039/c5ja00253b

Gall, L., Williams, H., Siebert, C., Halliday, A., 2012. Determination of mass-dependent variations in nickel isotope compositions using double spiking and MC-ICPMS. J. Anal. At. Spectrom. 27, 137–145. https://doi.org/10.1039/c1ja10209e

Gall, L., Williams, H.M., Siebert, C., Halliday, A.N., Herrington, R.J., Hein, J.R., 2013. Nickel isotopic compositions of ferromanganese crusts and the constancy of deep ocean inputs and continental weathering effects over the Cenozoic. Earth Planet. Sci. Lett. 375, 148–155. https://doi.org/10.1016/j.epsl.2013.05.019

Garzanti, E., Andò, S., Vezzoli, G., Lustrino, M., Boni, M., Vermeesch, P., 2012. Petrology of the Namib Sand Sea: Long-distance transport and compositional variability in the wind-displaced Orange Delta. Earth-Science Rev. 112, 173–189. https://doi.org/10.1016/j.earscirev.2012.02.008

Garzanti, E., Vermeesch, P., Andò, S., Lustrino, M., Padoan, M., Vezzoli, G., 2014. Ultra-long distance littoral transport of Orange sand and provenance of the Skeleton Coast Erg (Namibia). Mar. Geol. 357, 25–36. https://doi.org/10.1016/j.margeo.2014.07.005

Garzoli, S.L., Gordon, A.L., 1996. Origins and variability of the Benguela Current. J. Geophys. Res. 101, 897–906.

Gueguen, B., Rouxel, O., 2021. The Nickel isotope composition of the authigenic sink and the diagenetic flux in modern oceans. Chem. Geol. 563, 120050. https://doi.org/10.1016/j.chemgeo.2020.120050

Gueguen, B., Rouxel, O., Ponzevera, E., Bekker, A., Fouquet, Y., 2013. Nickel Isotope Variations in Terrestrial Silicate Rocks and Geological Reference Materials Measured by MC-ICP-MS. https://doi.org/10.1111/j.1751-908X.2013.00209.x

Gueguen, B., Rouxel, O., Rouget, M.L., Bollinger, C., Ponzevera, E., Germain, Y., Fouquet, Y.,

2016. Comparative geochemistry of four ferromanganese crusts from the Pacific Ocean and significance for the use of Ni isotopes as paleoceanographic tracers. Geochim. Cosmochim. Acta 189, 214–235. https://doi.org/10.1016/j.gca.2016.06.005

Gueguen, B., Sorensen, J. V., Lalonde, S. V., Peña, J., Toner, B.M., Rouxel, O., 2018. Variable Ni isotope fractionation between Fe-oxyhydroxides and implications for the use of Ni isotopes as geochemical tracers. Chem. Geol. 481, 38–52. https://doi.org/10.1016/j.chemgeo.2018.01.023

Heggie, D., Lewis, T., 1984. Cobalt in pore waters of marine sediments. Nature 311, 453–455. https://doi.org/10.1038/311453a0

Heinrichs, H., Schulz-Dobrick, B., Wedepohl, K.H., 1980. Terrestrial geochemistry of Cd, Bi, Tl, Pb, Zn and Rb. Geochim. Cosmochim. Acta 44, 1519–1533. https://doi.org/10.1016/0016-7037(80)90116-7

Hutchings, L., van der Lingen, C.D., Shannon, L.J., Crawford, R.J.M., Verheye, H.M.S., Bartholomae, C.H., van der Plas, A.K., Louw, D., Kreiner, A., Ostrowski, M., Fidel, Q., Barlow, R.G., Lamont, T., Coetzee, J., Shillington, F., Veitch, J., Currie, J.C., Monteiro, P.M.S., 2009. The Benguela Current: An ecosystem of four components. Prog. Oceanogr. 83, 15–32. https://doi.org/10.1016/j.pocean.2009.07.046

Inthorn, M., Wagner, T., Scheeder, G., Zabel, M., 2006. Lateral transport controls distribution, quality, and burial of organic matter along continental slopes in high-productivity areas. Geology 34, 205–208. https://doi.org/10.1130/G22153.1

Johnson, K.S., Stout, P.M., Berelson, W.M., Sakamoto-Arnold, C.M., 1988. Cobalt and copper distributions in the waters of Santa Monica Basin, California. Nature 332, 527–530. https://doi.org/10.1038/332527a0

Jorgensen, B.B., Kasten, S., 2006. Sulfur cycling and methane oxidation, in: Marine Geochemistry. pp. 271–309. https://doi.org/10.1007/3-540-32144-6_8

Kah, L.C., Lyons, T.W., Frank, T.D., 2004. Low marine sulphate and protracted oxygenation of the Proterozoic biosphere. Nature 431, 834–838. https://doi.org/10.1038/nature02974

Klaver, M., Ionov, D.A., Takazawa, E., Elliott, T., 2020. The non-chondritic Ni isotope composition of Earth's mantle. Geochim. Cosmochim. Acta 268, 405–421. https://doi.org/10.1016/j.gca.2019.10.017

Lam, P.J., Bishop, J.K.B., Henning, C.C., Marcus, M.A., Waychunas, G.A., Fung, I.Y., 2006. Wintertime phytoplankton bloom in the subarctic Pacific supported by continental margin iron. Global Biogeochem. Cycles 20, 1–12. https://doi.org/10.1029/2005GB002557

Lemaitre, N., Du, J., de Souza, G.F., Archer, C., Vance, D., 2022. The essential bioactive role of nickel in the oceans: Evidence from nickel isotopes. Earth Planet. Sci. Lett. 584,

117513. https://doi.org/10.1016/j.epsl.2022.117513

Little, S.H., Archer, C., Mcmanus, J., Najorka, J., Wegorzewski, A. V, Vance, D., 2020. Towards balancing the oceanic Ni budget. Earth Planet. Sci. Lett. 547, 116461. https://doi.org/10.1016/j.epsl.2020.116461

Liu, M., Tanhua, T., 2021. Water masses in the Atlantic Ocean: Characteristics and distributions. Ocean Sci. 17, 463–486. https://doi.org/10.5194/os-17-463-2021

Liu, T., Krisch, S., Xie, R.C., Hopwood, M.J., Dengler, M., 2022. Sediment Release in the Benguela Upwelling System Dominates Trace Metal Input to the Shelf and Eastern South Atlantic Ocean Global Biogeochemical Cycles. https://doi.org/10.1029/2022GB007466

Lohan, M.C., Bruland, K.W., 2008. Elevated Fe(II) and dissolved Fe in hypoxic shelf waters off Oregon and Washington: An enhanced source of iron to coastal upwelling regimes. Environ. Sci. Technol. 42, 6462–6468. https://doi.org/10.1021/es800144j

Mansor, M., Winkler, C., Hochella, M.F., Xu, J., 2019. Nanoparticulate nickel-hosting phases in sulfidic environments: Effects of ferrous iron and bacterial presence on mineral formation mechanism and solid-phase nickel distribution. Front. Earth Sci. 7, 1–15. https://doi.org/10.3389/feart.2019.00151

Mercier, H., Arhan, M., Lutjeharms, J.R.E., 2003. Upper-layer circulation in the eastern Equatorial and South Atlantic Ocean in January-March 1995. Deep. Res. Part I Oceanogr. Res. Pap. 50, 863–887. https://doi.org/10.1016/S0967-0637(03)00071-2

Mohrholz, V., Bartholomae, C.H., van der Plas, A.K., Lass, H.U., 2008. The seasonal variability of the northern Benguela undercurrent and its relation to the oxygen budget on the shelf. Cont. Shelf Res. 28, 424–441. https://doi.org/10.1016/j.csr.2007.10.001

Mollenhauer, G., Schneider, R.R., Müller, P.J., Spieß, V., Wefer, G., 2002. Glacial/interglacial variablity in the Benguela upwelling system: Spatial distribution and budgets of organic carbon accumulation. Global Biogeochem. Cycles 16, 81-1-81–15. https://doi.org/10.1029/2001gb001488

Monteiro, P.M.S., van der Plas, A.K., 2006. Low oxygen water (LOW) variability in the Benguela system: Key processes and forcing scales relevant to forecasting. Large Mar. Ecosyst. 14, 71–90. https://doi.org/10.1016/S1570-0461(06)80010-8

Moore, J.K., Braucher, O., 2008. Sedimentary and mineral dust sources of dissolved iron to the world ocean. Biogeosciences 5, 631–656. https://doi.org/10.5194/bg-5-631-2008

Morse, J.W., Luther, G.W., 1999. Chemical influences on trace metal-sulfide interactions in anoxic sediments. Geochim. Cosmochim. Acta 63, 3373–3378.

Mulrooney, S.B., Hausinger, R.P., 2003. Nickel uptake and utilization by microorganisms. FEMS Microbiol. Rev. 27, 239–261. https://doi.org/10.1016/S0168-6445(03)00042-1

Noble, A.E., Lamborg, C.H., Ohnemus, D.C., Lam, P.J., Goepfert, T.J., Measures, C.I., Frame, C.H., Casciotti, K.L., DiTullio, G.R., Jennings, J., Saito, M.A., 2012. Basin-scale inputs of cobalt, iron, and manganese from the Benguela-Angola front to the South Atlantic Ocean. Limnol. Oceanogr. 57, 989–1010. https://doi.org/10.4319/lo.2012.57.4.0989

Nozaki, Y., 2001. Elemental distribution: overview, in: Steele, J.H., Thorpe, S.A., Turekian, K.K. (Eds.), Marine Chemistry and Geochemistry. pp. 7–12.

Ohnemus, D.C., Auro, M.E., Sherrell, R.M., Lagerström, M., Morton, P.L., Twining, B.S., Rauschenberg, S., Lam, P.J., 2014. Laboratory intercomparison of marine particulate digestions including Piranha: A novel chemical method for dissolution of polyethersulfone filters. Limnol. Oceanogr. Methods 12, 530–547. https://doi.org/10.4319/lom.2014.12.530

Parigi, R., Chen, N., Reid, J.W., Ptacek, C.J., Blowes, D.W., 2022. Nickel isotope fractionation during precipitation of Ni secondary minerals and synchrotron-based analysis of the precipitates. Geochim. Cosmochim. Acta 317, 91–105. https://doi.org/10.1016/j.gca.2021.10.027

Plass, A., Schlosser, C., Sommer, S., Dale, A.W., Achterberg, E.P., Scholz, F., 2020. The control of hydrogen sulfide on benthic iron and cadmium fluxes in the oxygen minimum zone off Peru. Biogeosciences 17, 3685–3704. https://doi.org/10.5194/bg-17-3685-2020

Plass, A., Dale, A.W., Scholz, F., 2021. Sedimentary cycling and benthic fluxes of manganese, cobalt, nickel, copper, zinc and cadmium in the Peruvian oxygen minimum zone. Mar. Chem. 233, 103982. https://doi.org/10.1016/j.marchem.2021.103982

Purcell, E.M., 1977. Life at low Reynolds number. Am. J. Phys. 45, 3–11. https://doi.org/10.1119/1.10903

Ragsdale, S.W., 2009. Nickel-based enzyme systems. J. Biol. Chem. 284, 18571–18575. https://doi.org/10.1074/jbc.R900020200

Ratié, G., Jouvin, D., Garnier, J., Rouxel, O., Miska, S., Guimarães, E., Cruz Vieira, L., Sivry, Y., Zelano, I., Montarges-Pelletier, E., Thil, F., Quantin, C., 2015. Nickel isotope fractionation during tropical weathering of ultramafic rocks. Chem. Geol. 402, 68–76. https://doi.org/10.1016/j.chemgeo.2015.02.039

Saunders, N.J., Barling, J., Harvey, J., Halliday, A.N., Saunders, N.J., Barling, J., Harvey, J., Halliday, A.N., 2020. Heterogeneous nickel isotopic compositions in the terrestrial mantle - Part 1. Geochim. Cosmochim. Acta. https://doi.org/10.1016/j.gca.2020.06.029

Sclater, F.R., Boyle, E., Edmond, J.M., 1976. On the marine geochemistry of nickel. Earth Planet. Sci. Lett. 31, 119–128. https://doi.org/10.1038/263042a0

Sorensen, V., Gueguen, B., Stewart, B.D., Peña, J., Rouxel, O., Toner, B.M., 2020. Large nickel isotope fractionation caused by surface complexation reactions with hexagonal birnessite 537. https://doi.org/10.1016/j.chemgeo.2020.119481

Spivak-Birndorf, L.J., Wang, S.J., Bish, D.L., Wasylenki, L.E., 2018. Nickel isotope fractionation during continental weathering. Chem. Geol. 476, 316–326. https://doi.org/10.1016/j.chemgeo.2017.11.028

Takano, S., Tanimizu, M., Hirata, T., Shin, K.C., Fukami, Y., Suzuki, K., Sohrin, Y., 2017. A simple and rapid method for isotopic analysis of nickel, copper, and zinc in seawater using chelating extraction and anion exchange. Anal. Chim. Acta 967, 1–11. https://doi.org/10.1016/j.aca.2017.03.010

Thamdrup, B., Fossing, H., Jorgensen, B.B., 1994a. Manganese, iron, and sulfur cycling in a coastal marine sediment, Aarhus Bay, Denmark. Geochim. Cosmochim. Acta 58, 5115–29.

Thamdrup, B., Glud, R.N., Hansen, J.W., 1994b. Manganese oxidation and in situ manganese fluxes from a coastal sediment. Geochim. Cosmochim. Acta 58, 2563–2570. https://doi.org/10.1016/0016-7037(94)90032-9

Tyson, R. V., Pearson, T.H., 1991. Modern and ancient continental shelf anoxia: an overview. Geol. Soc. Spec. Publ. 1–24. https://doi.org/10.2307/3515153

Vance, D., Little, S.H., Archer, C., Cameron, V., Andersen, M.B., Rijkenberg, M.J.A., Lyons, T.W., 2016. The oceanic budgets of nickel and zinc isotopes: The importance of sulfdic environments as illustrated by the Black Sea. Philos. Trans. R. Soc. A Math. Phys. Eng. Sci. 374. https://doi.org/10.1098/rsta.2015.0294

Wasylenki, L.E., Howe, H.D., Spivak-Birndorf, L.J., Bish, D.L., 2015. Ni isotope fractionation during sorption to ferrihydrite: Implications for Ni in banded iron formations. Chem. Geol. 400, 56–64. https://doi.org/10.1016/j.chemgeo.2015.02.007

Wegorzewski, A. V., Grangeon, S., Webb, S.M., Heller, C., Kuhn, T., 2020. Mineralogical transformations in polymetallic nodules and the change of Ni, Cu and Co crystal-chemistry upon burial in sediments. Geochim. Cosmochim. Acta 282, 19–37. https://doi.org/10.1016/j.gca.2020.04.012

Wilkin, R.T., Rogers, D.A., 2010. Nickel sulfide formation at low temperature: Initial precipitates, solubility and transformation products. Environ. Chem. 7, 514–523. https://doi.org/10.1071/EN10076

Wu, G., Zhu, J.-M., Wang, X., Han, G., Tan, D., Wang, S.-J., 2019. A novel purification method for high precision measurement of Ni isotopes by double spike MC-ICP-MS. J. Anal. At. Spectrom. 17–19. https://doi.org/10.1039/c9ja00077a

Xie, R.C., Rehkämper, M., Grasse, P., van de Flierdt, T., Frank, M., Xue, Z., 2019. Isotopic evidence for complex biogeochemical cycling of Cd in the eastern tropical South Pacific. Earth Planet. Sci. Lett. 512, 134–146. https://doi.org/10.1016/j.epsl.2019.02.001

Yu, Y., Siebert, C., Fietzke, J., Goepfert, T., Hathorne, E., Cao, Z., Frank, M., 2020. The impact of MC-ICP-MS plasma conditions on the accuracy and precision of stable isotope measurements evaluated for barium isotopes. Chem. Geol. 549, 119697. https://doi.org/10.1016/j.chemgeo.2020.119697

Zhang, Q., Snow, J.T., Holdship, P., Price, D., Watson, P., Rickaby, R.E.M., 2018. Direct measurement of multi-elements in high matrix samples with a flow injection ICP-MS: Application to the extended: Emiliania huxleyi Redfield ratio. J. Anal. At. Spectrom. 33, 1196–1208. https://doi.org/10.1039/c8ja00031j

CHAPTER 6
Outlook

6 Outlook

6.1 Potential application of Ni isotopes

Can Ni isotopes in BIFs be applied as an indicator for early photosynthesis?

The cause of the Great Oxidation Event (GOE) has been actively debated. The rise of atmospheric partial pressure of oxygen from ~10^{-5} present atmospheric level (PAL) to approximately 0.02~0.04 PAL happened around 2.4 billion years ago (Ga)(Holland, 2006; Lyons et al., 2014). Several "whiffs", transient pulses of oxygenation, have been suggested to happen slightly earlier than the GOE (2.9-2.5 Ga) but not sufficient to hold the persistence of free O_2 in the atmosphere (Anbar et al., 2007; Crowe et al., 2013; Reinhard et al., 2009). The evolution of oxygenic photosynthesis are thought to occur long before the GOE by various evidence including biomarkers, redox-sensitive metals, stromatolites, microfossils, kerogeneous shales and isotopes (C and U-Th-Pb system) (Buick, 2008; Fiantis, 1967; Lalonde and Konhauser, 2015; Planavsky et al., 2014; Rosing and Frei, 2004). An alternative view has also been raised that oxygenic photosynthesis only occurred shortly before Makganyene snowball Earth event around 2.3-2.2 Ga as it could have destroyed a methane greenhouse and triggered a snowball Earth event at the time (Kopp et al., 2005).

As an archive for oceanic chemistry, banded iron formations (BIFs) can preserve histories of many Archean and Proterozoic processes and provide insights into understanding of early microbial life and its impacts on the evolution of Earth system e.g., the GOE around 2.4 billion years ago (Ga). It has been reported that a significant and continuous decline of the oceanic Ni concentration recorded in BIFs started around 2.7 Ga, reaching a twofold

decrease around 2.7-2.4 Ga and a fivefold decrease by 2.2 Ga, may have reduced the activity of methanogens in the ancient ocean and disrupted the supply of biogenic methane because Ni is a key metal cofactor in methane-producing enzymes (Konhauser et al., 2009; Ragsdale, 2009; Thauer, 1998). An alternative view is that the weathering of Ni-containing sulfides at the time may have supplied small but biologically crucial Ni to the ocean, sustaining sufficient methane to prevent Earth from entering a long-lasting icehouse while allowing O_2 to accumulate in the atmosphere (Wang et al., 2019).

Nickel and its isotopes in BIFs have been applied to understand early oceanic history. Currently, one Ni isotope composition in a BIF has been reported with $\delta^{60}Ni = 0.46 \pm 0.03‰$ for a 3.75 Ga BIF sample (Gueguen et al., 2013). The Ni isotope composition for Eoarchean BIFs was subsequently suggested to be homogeneous by the measurements on several more 3.75 Ga BIFs (Wasylenki and Wang, 2016). With the observed isotope fractionations ($\Delta^{60}Ni_{solution\text{-}solid} = 0.08 \sim 0.24‰$ when $f_{solid} < 70\%$; $\Delta^{60}Ni_{solution\text{-}solid} = 0.34 \sim 0.50‰$ when $f_{solid} > 70\%$) during the sorption between synthetic ferrihydrites (precursor of BIFs) (S. J. Wang and Wasylenki, 2017) and the potential proportions of Ni incorporated into iron oxides during BIF deposition referred from Cu isotope study both taken into consideration (Chi Fru et al., 2016), the $\delta^{60}Ni$ of 3.75 Ga seawater has been reconstructed to be 0.54~0.70‰. The difference (0.74~0.90‰) between Ni isotope composition in 3.75 Ga seawater ($\delta^{60}Ni = 0.54 \sim 0.70‰$) and modern seawater ($\delta^{60}Ni = 1.44 \pm 0.15‰$) was explained by the lack of oxidative weathering at the time which retains the isotopically lighter Ni in weathering products and therefore adds heavier Ni into the oceans (S. J. Wang and Wasylenki, 2017).

As discussed in Chapter 2, Ni isotope fractionations during the growth of cyanobacteria *Synechococcus sp.* under Ni concentration of 6~3400 nM including the concentration range of both estimated Archean ocean (up to 400 nM) and modern ocean (2~12 nM) have been constrained by laboratory culturing experiments. The difference between isotopic compositions of collected cells and the medium ($\Delta^{60}Ni_{cell\text{-}medium}$) increases with the increasing Ni concentration and reaches +0.86‰ when the total Ni concentration is about 340 nM (Figure 6.1), which is in line with the difference (0.74~0.90‰) between estimated Archean seawater δ^{60}Ni and the modern ocean. The trend observed imply that the decreasing Ni concentration in seawater through the geological history may lead to a decreasing biogeochemical fractionation at the surface ocean.

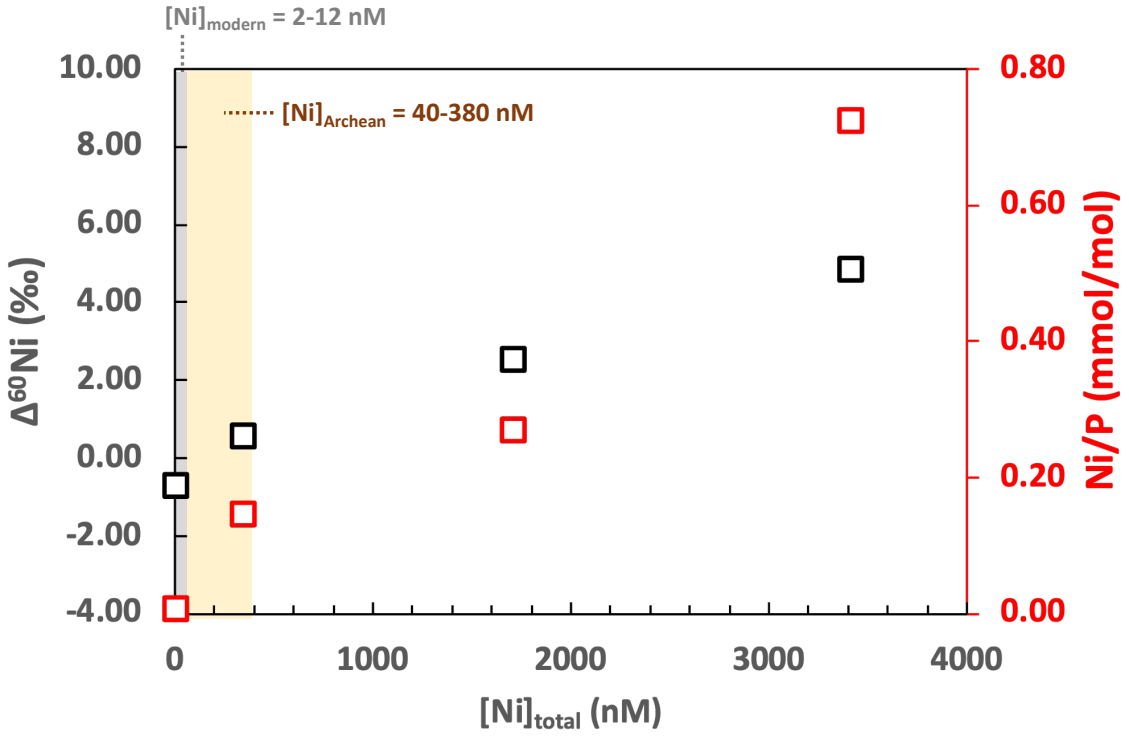


Figure 6.1. Cellular Ni/P ratios and Δ^{60}Ni of cultured cyanobacteria Synechococcus sp. under varying Ni availability. The grey and yellow band represent the Ni concentration in modern ocean and estimated Archean ocean (Konhauser et al., 2009), respectively.

This hypothesis suggests that the δ^{60}Ni signals captured in ferrihydrite particles, the precursors of BIFs, may potentially be an indicator for early cyanobacterial photosynthesis at the surface of ancient ocean, as another explanation for the difference of δ^{60}Ni between Archean ocean and modern ocean (Figure 6.2).

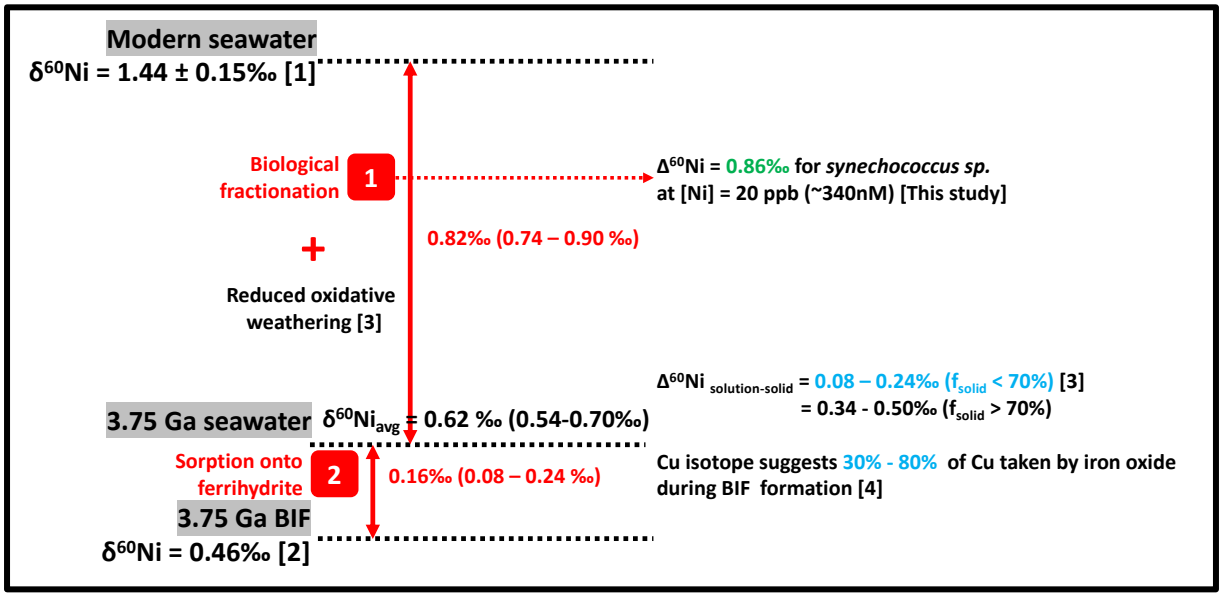


Figure 6.2. Compilation of processes potentially influencing the signals recorded in BIFs around 3.75 Ga. The fractionation ($\Delta^{60}Ni_{cell\text{-}meidum}$) observed during cyanobacteria growth under Archean-like condition is within the range of estimated gap between the δ^{60}Ni of modern and 3.75 Ga seawater. [1]Cameron et al. (2009); [2]Gueguen et al. (2013); [3]Wang and Wasylenki (2017); [4]Chi Fru et al. (2016).

The schematic mechanism of how Ni isotope signals of Archean ocean is influenced by the biological activity of cyanobacteria and recorded in BIFs is shown in Figure 6.3. Under Archean-like Ni concentration, the growth of cyanobacteria enriches isotopically heavy Ni and leaves the ambient seawater isotopically light. When the oxygen is generated and released by the cyanobacteria, the oxygen will trigger the formation of ferrihydrite particles which is the precursor of BIFs. The ferrihydrite particles may record the chemistry of its ambient seawater at the surface ocean. Although the isotope

fractionation during both the transformation from ferrihydrite particles to BIFs and the subsequent diagenesis have not been evaluated yet.

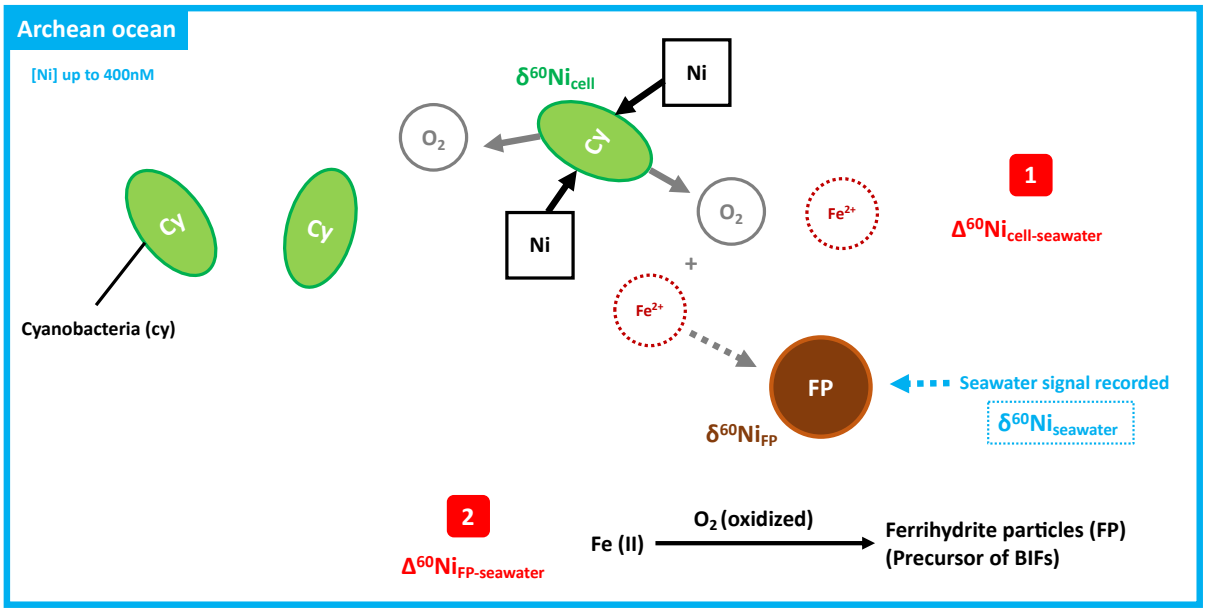


Figure 6.3. Conceptual mechanism linking the δ^{60}Ni signals recorded in ferrihydrite particles (precursor of BIF) and cyanobacterial photosynthesis. The sparce oxygen generated by cyanobacteria leads to the formation of ferrihydrite particles which record the chemistry of ambient seawater.

As mentioned in Chapter 2, the direction of Ni isotope fractionation compared to Ni reservoir likely depends on the relative binding energy between processes happening in the reservoir of interest. For instance, in the modern ocean, the binding strengths of phytoplankton acquisition system and Ni-ligands binding have to be considered, which ultimately results in the enrichment of light isotopes in phytoplankton cells and enrichment of heavy isotopes in ligands with strong binding compared to the δ^{60}Ni of dissolved Ni in the seawater. Though in lab-based experiments, biological uptake and ligand-binding both have been shown to take up heavy isotopes from the Ni pool (Nomura et al., 2013). The ligands in the Archean ocean may have had less influence than in the modern ocean. It has been suggested that the phytoplankton community is the

major source and control of Cu-binding organic ligands. The source of ligands may be less and/or less organic in Archean ocean when the evolution of life was still in its infancy. With the less or absent of organic ligands at the time which may have stronger binding strength and compete with biological uptake, it suggests that the isotope fractionation during growth of cyanobacteria may be closer to the observation under laboratory experiments.

With the observed cyanobacterial isotope fractionation under Archean-like condition, the Ni isotope signals recorded in the 3.75 Ga BIF may serve as a new evidence of oxygenic photosynthesis well before the GOE. It supports the argument that the production of O_2 might be sparce, local (at the surface ocean) and not sufficient to cause a permanent change to atmospheric composition and is in agreement that microorganisms were involved in the primary oxidation of dissolved Fe (II) to the ferrihydrite particles (Konhauser et al., 2007; Pecoits et al., 2015). Biological BIFs are modelled to form via abiotic oxidation by any available O_2 generated through oxygenic photosynthesis, for instance, by cyanobacteria in the surface ocean (Cloud, 1972; Klein and Beukes, 1989) and/or biotic oxidation by chemolithotrophic bacteria (microaerophilic Fe(II)-oxidizers), for instance, by genera *Gallionella* in hydrothermal settings (Holm, 1989). In lights of the bioessential role of Ni as a metal cofactor, it would also be plausible that the δ^{60}Ni signals recorded in BIFs reflect the activity of methanogens (Ragsdale, 2009). However, it has been reported that methanogens preferentially assimilate isotopically light Ni relative to the medium ($\Delta^{60}Ni_{cell\text{-}medium}$ = -0.4∼-1.5‰), this assimilation would leave the ambient environment isotopically heavy and disagree with the calculated δ^{60}Ni of 3.75 Ga BIF (Cameron et al., 2009; Gueguen et al., 2013). Overall, the cyanobacterial isotope data provided in Chapter 3 supports that cyanobacteria may be the driver of the low δ^{60}Ni in

the Archean ocean, as well as suggesting that a further investigation on Ni isotope fractionation during chemolithotrophic bacteria is required to constrain the compelling story in this critical geological period.

In terms of the low δ^{60}Ni estimated in the Archean Ocean compared to the modern ocean, an alternative explanation is the absence of both Mn-oxides in oxic sediments which enrich isotopically light Ni from the ocean ($\delta^{60}Ni_{MnO2\text{-}aqueous}$ = −2.8 ~ −3.4‰; Sorensen et al., 2020) and the subsequent benthic input of isotopically heavy Ni (δ^{60}Ni estimated to be 3.03‰; Little et al., 2020) during diagenetic remobilization of Ni via Mn-oxide dissolution and precipitation, and/or during the transformation from birnessite to todorokite. Without the presence of sufficient oxygen in the Archean Ocean, these two coupled processes may not take place at that time, which results in a lower δ^{60}Ni in the Archean ocean compared to the modern ocean. Based on the oceanic Ni budget (see Table 5.7, Chapter 5) and the steady-state condition of the ocean reservoir, the absence of both Mn-oxides in oxic sediments and the triggered diagenetic remobilization of Ni would lead to a δ^{60}Ni of 1.06‰ in anoxic Archean ocean, which leaves a gap towards estimated seawater composition (δ^{60}Ni = 0.54 – 0.70‰; Wang and Wasylenki, 2019) inferred from BIF records.

$$\delta_{sw} = \sum f_{input} \times \delta_{input} + \sum f_{output} \times \delta_{output}$$

6.2 Future work

In chapter 2 and Chapter 3, we present the first direct characterization of Ni isotope fractionation during marine phytoplankton growth. We propose a new of framework that considers the relative binding strengths between phytoplankton metal acquisition systems and ambient ligands, in terms of Ni isotope fractionation observed in both lab-based experiments and in the modern ocean. Following our work, it would be beneficial to characterize Ni isotope fractionation during Ni binding to organic ligands. The ligands encompass Ni-binding proteins in biology like histidine and cysteine, and Ni-ligands found in the ocean with pyrrole structure like cyclic peptides and porphyrins. This research will provide important insights into our hypothesis and contribute significantly to the understanding of oceanic Ni biogeochemistry and its cycling.

Additionally, expanding our understanding from cellular to molecular scale, it would be valuable to explore the influence of enzymatic activity (e.g., NiFe hydrogenase, urease, Ni-SOD) in marine phytoplankton on observed Ni isotope fractionation. By targeting one enzyme at a time, adjusting parameters such as Ni availability, Fe availability and nitrogen source, we can investigate the switch in functional enzymes and related proteins. This work will shed light on the detailed mechanisms by which different species of phytoplankton cause varying Ni isotope fractionation, contributing to our understanding of regionally-variable Ni isotope compositions found in the surface ocean.

In Chapter 4 and Chapter 5, we conduct a direct characterization of Ni isotope fraction during amorphous Ni-sulfide formation and apply Ni isotopes in a Namibian sample set as a case study. To further advance our understanding, it is critical to acquire and compile more data from natural samples to validate whether Ni isotopes in marine sediments can

serve as a promising geochemical tracer for seawater chemistry. Also, it is important to evaluate the role of early diagenesis in these natural climate archives. Observations have shown the diagenetic remobilization of Ni in sediments under both oxic and anoxic conditions, with remobilization occuring via Mn-oxides under oxic conditions and via sulfides under anoxic conditions. Therefore, it is essential to investigate whether other forms of early diagenesis (e.g., related to organics) may influence Ni isotope records and develop methods to differentiate these secondary signals from the primary records.

6.3 References

Anbar, A.D., Duan, Y., Lyons, T.W., Arnold, G.L., Kendall, B., Creaser, R.A., Kaufman, A.J., Gordon, G.W., Scott, C., Garvin, J., Buick, R., 2007. A whiff of oxygen before the great oxidation event? Science (80-.). 317, 1903–1906. https://doi.org/10.1126/science.1140325

Buick, R., 2008. When did oxygenic photosynthesis evolve? Philos. Trans. R. Soc. B Biol. Sci. 363, 2731–2743. https://doi.org/10.1098/rstb.2008.0041

Cameron, V., Vance, D., Archer, C., House, C.H., 2009. A biomarker based on the stable isotopes of nickel. Proc. Natl. Acad. Sci. 106, 10944–10948. https://doi.org/10.1073/pnas.0900726106

Cloud, P., 1972. A working model of the primitive Earth. Am. J. Sci. https://doi.org/10.2475/ajs.272.6.537

Crowe, S.A., Døssing, L.N., Beukes, N.J., Bau, M., Kruger, S.J., Frei, R., Canfield, D.E., 2013. Atmospheric oxygenation three billion years ago. Nature 501, 535–538. https://doi.org/10.1038/nature12426

Fru, E.C., RodrÃ-Guez, N.P., Partin, C.A., Lalonde, S. V., Andersson, P., Weiss, D.J., Albani, A. El, Rodushkin, I., Konhauser, K.O., 2016. Cu isotopes in marine black shales record the Great Oxidation Event. Proc. Natl. Acad. Sci. U. S. A. 113, 4941–4946. https://doi.org/10.1073/pnas.1523544113

Gueguen, B., Rouxel, O., Ponzevera, E., Bekker, A., Fouquet, Y., 2013. Nickel Isotope Variations in Terrestrial Silicate Rocks and Geological Reference Materials Measured by MC-ICP-MS. https://doi.org/10.1111/j.1751-908X.2013.00209.x

Holland, H.D., 2006. The oxygenation of the atmosphere and oceans. https://doi.org/10.1098/rstb.2006.1838

Holm, N.G., 1989. Modern Metalliferous Hydrothermal Sediment and Their Implications for Banded Iron Formations 77, 41–45.

Klein, C., Beukes, N.J., 1989. Geochemistry and sedimentology of a facies transition - from microbanded to granular iron-formation - in the early Proterozoic Transvaal Supergroup, South Africa. Precambrian Res. 47, 99–139. https://doi.org/10.1016/0301-9268(90)90033-M

Konhauser, K.O., Amskold, L., Lalonde, S. V., Posth, N.R., Kappler, A., Anbar, A., 2007. Decoupling photochemical Fe(II) oxidation from shallow-water BIF deposition. Earth Planet. Sci. Lett. 258, 87–100. https://doi.org/10.1016/j.epsl.2007.03.026

Konhauser, K.O., Pecoits, E., Lalonde, S. V., Papineau, D., Nisbet, E.G., Barley, M.E., Arndt, N.T., Zahnle, K., Kamber, B.S., 2009. Oceanic nickel depletion and a methanogen famine before the Great Oxidation Event. Nature 458, 750–753. https://doi.org/10.1038/nature07858

Kopp, R.E., Kirschvink, J.L., Hilburn, I.A., Nash, C.Z., 2005. The paleoproterozoic snowball Earth: A climate disaster triggered by the evolution of oxygenic photosynthesis. Proc. Natl. Acad. Sci. U. S. A. 102, 11131–11136. https://doi.org/10.1073/pnas.0504878102

Lalonde, S. V., Konhauser, K.O., 2015. Benthic perspective on Earth's oldest evidence for oxygenic photosynthesis. Proc. Natl. Acad. Sci. U. S. A. 112, 995–1000. https://doi.org/10.1073/pnas.1415718112

Little, S.H., Archer, C., Mcmanus, J., Najorka, J., Wegorzewski, A. V, Vance, D., 2020. Towards balancing the oceanic Ni budget. Earth Planet. Sci. Lett. 547, 116461. https://doi.org/10.1016/j.epsl.2020.116461

Lyons, T.W., Reinhard, C.T., Planavsky, N.J., 2014. The rise of oxygen in Earth's early ocean and atmosphere. Nature. https://doi.org/10.1038/nature13068

Nomura, M., Kudo, T., Adachi, A., Aida, M., Fujii, Y., 2013. fractionation of isotopes in Ni and Pb chelate complex formation reactions Mass-Dependent and -Independent Fractionation of Isotopes in Ni and Pb Chelate Complex Formation Reactions 2, 1–7. https://doi.org/10.1063/1.4833685

Pecoits, E., Smith, M.L., Catling, D.C., Philippot, P., Kappler, A., Konhauser, K.O., 2015. Atmospheric hydrogen peroxide and Eoarchean iron formations. Geobiology 13, 1–14. https://doi.org/10.1111/gbi.12116

Planavsky, N.J., Asael, D., Hofmann, A., Reinhard, C.T., Lalonde, S. V., Knudsen, A., Wang, X., Ossa Ossa, F., Pecoits, E., Smith, A.J.B., Beukes, N.J., Bekker, A., Johnson, T.M., Konhauser, K.O., Lyons, T.W., Rouxel, O.J., 2014. Evidence for oxygenic photosynthesis half a billion years before the Great Oxidation Event. Nat. Geosci. 7, 283–286. https://doi.org/10.1038/ngeo2122

Ragsdale, S.W., 2009. Nickel-based enzyme systems. J. Biol. Chem. 284, 18571–18575. https://doi.org/10.1074/jbc.R900020200

Reinhard, C.T., Raiswell, R., Scott, C., An Bar, A.D., Lyons, T.W., 2009. A late archean sulfidic sea stimulated by early oxidative weathering of the continents. Science (80-.). 326, 713–716. https://doi.org/10.1126/science.1176711

Rosing, M.T., Frei, R., 2004. U-rich Archaean sea-floor sediments from Greenland - indications of > 3700 Ma oxygenic photosynthesis. Earth Planet. Sci. Lett. 217, 237–244. https://doi.org/10.1016/S0012-821X(03)00609-5

Sorensen, V., Gueguen, B., Stewart, B.D., Peña, J., Rouxel, O., Toner, B.M., 2020. Large nickel isotope fractionation caused by surface complexation reactions with hexagonal birnessite 537. https://doi.org/10.1016/j.chemgeo.2020.119481

Thauer, R.K., 1998. Biochemistry of methanogenesis: a tribute to Marjory Stephenson:1998 Marjory Stephenson Prize Lecture. Microbiology 144, 2377–2406. https://doi.org/10.1099/00221287-144-9-2377

Wang, S., Wasylenki, L.E., 2017. ScienceDirect Experimental constraints on reconstruction of Archean seawater Ni isotopic composition from banded iron formations. Geochim. Cosmochim. Acta 206, 137–150. https://doi.org/10.1016/j.gca.2017.02.023

Wang, S.J., Rudnick, R.L., Gaschnig, R.M., Wang, H., Wasylenki, L.E., 2019. Methanogenesis sustained by sulfide weathering during the Great Oxidation Event. Nat. Geosci. https://doi.org/10.1038/s41561-019-0320-z

Wang, S.J., Wasylenki, L.E., 2017. Experimental constraints on reconstruction of Archean seawater Ni isotopic composition from banded iron formations. Geochim. Cosmochim. Acta 206, 137–150. https://doi.org/10.1016/j.gca.2017.02.023

Wasylenki, L.E., Wang, S.-J., 2016. Ni isotope signatures in banded iron formations before, during and after the Great Oxidation Event. American Geophysical Union, Fall meeting, 2016 AGUFM. V54A–06.

APPENDIX
Methodology and extended data

In light of the page limit, the methodology applied in this thesis is put in Appendix. Also, the data measured in this study but not included in the data chapters (manuscripts), the figures made for evaluation but not used at the end in the data chapters (manuscripts) for the clarity of the main stories, or any supplementary data are provided in this Appendix.

Appendix A. Methodology

A.1 Introduction

This chapter provides a general overview for all the methods involved in the thesis, including sample collection/digestion for various types of samples, Ni purification and instrumental analyses. The more specific and detailed information about the method will be in the chapter 2-6.

This work provides an opportunity to carry out analysis from both natural and lab-based samples to study Ni isotope fractionations in different angle of the Earth Sciences spectrum. A complete sample set including seawater, particulates, sediments and porewaters were collected from the Namibian margin, South Atlantic, whereas phytoplankton and sulfide samples were cultured/precipitated in the lab. For the collection of natural samples, the standard for metal-free processing was aimed to achieve, as samples might have low Ni content and could be easily contaminated (Cutter et al., 2017). The digestion methods varied with sample types and were designed or adapted from literatures specifically.

For precise determination of Ni isotope compositions, it is crucial and necessary to separate Ni from other elements which may cause polyatomic and/or isobaric interferences. The development of Ni purification technique and the protocols applied in this study are discussed. The method for extracting Ni from samples and subsequent isotope analysis was mainly adapted from Gall et al. (2012) and Saunders et al. (2020), which were both conducted in the Department of Earth Sciences, University of Oxford. The purification technique for Ni was developed by Gall et al. (2012) and modified by Saunders et al. (2020), which significantly reduced the amount of organic chelator dimethyglyoxime (DMG) to minimize the organics problem during the later breakdown, compared with others applying Ni-specific resin (Quitté and Oberli, 2006; Cameron et al., 2009). For Ni isotope analysis, the protocol for measuring samples with low Ni content (e.g., phytoplankton cells) was developed, and the normalized argon index (NAI) for monitoring thermal condition of plasma was adapted and firstly applied on Ni isotope measurement (Fietzke and Frische, 2016; Yu et al., 2020).

A.2 Sample collection

This study uses both lab-based samples (i.e., phytoplankton and sulfides) from culturing/precipitating experiments and natural sample from Namibian margin to improve the understanding of Ni isotope fractionation in natural processes and Ni cycle in the modern ocean.

The phytoplankton samples were cultured and collected in the OceanBug Laboratory at the Department of Earth Sciences, University of Oxford. The sulfide samples were precipitated and collected in the glovebox laboratory at the Department of Earth Sciences, University of Oxford.

A natural sample set including seawater, particulate matters filtered from seawater, sediments and porewater extracted from sediments were collected from eastern South Atlantic Ocean off Namibian margin during a cruise of R/V Mirabilis in May 2019 (Figure A.1). The sampling were taken place at nine stations along 20°S and 23°S transect, respectively (Table A.1). The week-long cruise was arranged by Regional Research Graduate Network in Oceanography (RGNO) which focuses on the biogeochemical oceanography in Benguela Upwelling System (BUS).

The detailed procedures for the collection and preparation for each kind of samples will be explained in the following sections (section A.2.1-A.2.6).

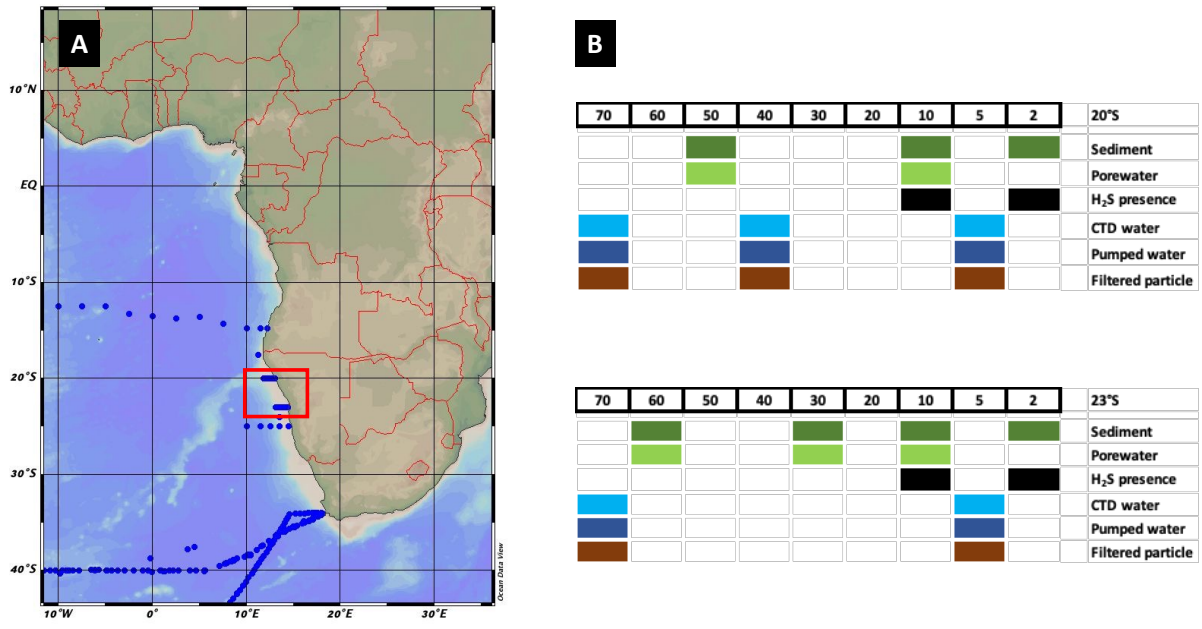


Figure A.1. (a) Map of sampling sites of this study off Namibian margin. In the red square are transect 20°S and 23°S. (b) Sampling strategy for a comprehensive set of samples including sediments, porewater extracted from sediments, seawater and particulate matters filtered from seawater. The numbers represent the distance to the coast in unit nautical mile (NM). 1 NM = 1.1508 miles.

Table A.1. Location of stations along 20°S and 23°S transect off Namibian margin. The distance noted in the table represents the distance between the station and the coast. NM: nautical miles (1 NM = 1.1508 miles); Lat: latitude; Long: longitude.

	Station/Distance (NM)	2	5	10	20	30	40	50	60	70
Transect 20°S	**Lat (°S)**	-20.0005	-20.0005	-19.999333	-19.999167	-19.999833	-20.000167	-19.999833	-19.9995	-20.000667
	Long(°E)	12.999	12.947333	12.858	12.68	12.504333	12.3255	12.147833	11.970833	11.792333
Transect 23°S	**Lat (°S)**	-23.000167	-23.001167	-23.000833	-22.999833	-23.0005	-23.0005	-23.0015	-23.000167	-23.000667
	Long(°E)	14.371333	14.317667	14.225833	14.043333	13.864333	13.679833	13.499333	13.32	13.132667

A.2.1 Seawater

Seawater samples were collected at three stations (20005, 20040 and 20070) and two stations (23005 and 23070) along transect 20°S and 23°S off Namibian margin, respectively (Figure A.1 and Table A.1).

Approximately 60 mL of seawater samples for major and trace element analysis were subsampled from CTD Sea-Bird SBE 9 rosettes and filtered with in-line acid-cleaned 0.2 μm AcroPak™ 500 capsule with Supor® membrane into acid-cleaned 60 mL high-density polyethylene (HDPE) bottles. Surface samples were collected by pumping water from ~10 m depth at the starboard side into both acid-cleaned 2L low density polyethylene (LDPE) cubic containers for Ni isotope analysis and acid-cleaned 40L LDPE cubic containers for further collection of particulate matters. Cole-Parmer peristaltic pump equipped with Masterflex tubing was used for pumping surface water.

Along with the use of CTD Sea-Bird SBE 9 rosettes, dissolved oxygen concentration, pressure, temperature and salinity at constant depth intervals were also measured.

Seawater samples were stored in a cold room at 4°C on board the research vessel until further processing. Samples were then transferred back to Department of Earth Sciences, University of Oxford and acidified to pH < 2 with sub-boiled concentrated HCl in the laminar flow hoods located in the metal-free clean lab.

A.2.2 Particulate matters

Particulate matters were collected at three stations (20005, 20040 and 20070) along the 20°S transect and two stations (23005 and 23070) along the 23°S transect off Namibian margin in the South Atlantic Ocean (Figure A.1 and Table A.1).

Collected seawater samples in cubic containers for particulate matters were filtered through both PES (polyethersulfone) filters (47 mm diameter, 0.8 **μ**m pore size) for further elemental analysis and quartz filters (Whatman QM-A Quartz Microfiber Filters, 47 mm diameter, 2.2 **μ**m pore size) for further organic carbon content analysis on board the R/V Mirabilis. A portable filtering kit connected to vacuum pump (Cole-Parmer) was used.

After the filtration, the filters were detached, sealed in pre-cleaned plastic bags and stored in a cold room at 4°C on board the research vessel until further processing onshore.

A.2.3 Sediment core

Sediments from Namibian margin were collected at three stations (20002, 20010 and 20050) along the 20°S transect and four stations (23002, 23010, 23030 and 23060) along the 23°S transect (Figure A.1 and Table A.1).

Samples were recovered using MC-400 Multi-corer equipped with 4 polycarbonate sample tubes (10 cm diameter × 58 cm height). All tubes have pre-drilled holes at 2-cm resolution for facilitating further porewater extraction. Sediment cores were then sub-sampled at 1-cm intervals with a plastic core liner using a piston to avoid core distortion

or shortening, sealed in acid-cleaned plastic bags and stored in a cold room at 4°C on board the research vessel before further processing.

A.2.4 Porewater

Porewater samples were collected at the stations where sediment cores were recovered at Namibian margin, i.e., three stations (20002, 20010 and 20050) along the 20°S transect and four stations (23002, 23010, 23030 and 23060) along the 23°S transect (Figure A.1 and Table A.1).

Pre-cleaned Rhizons with pore size 0.6 μm were all inserted into pre-drilled holes at constant intervals (2~3 cm) on sampler tubes of Multi-Corer to facilitate simultaneous extraction and minimize possible cross-contamination between intervals. The Rhizons samplers were then attached to syringes and used to extract porewaters immediately. The extracted porewater samples were transferred to pre-cleaned high-density polyethylene (HDPE) bottles and stored in a cold room at 4°C on board the research vessel before further processing.

Samples were then transferred back to Department of Earth Sciences, University of Oxford and acidified to pH < 2 with sub-boiled concentrated HCl in a laminar flow hood in a departmental metal-free clean lab.

A.2.5 Phytoplankton cells

The phytoplankton cultures for dinoflagellates, diatoms and coccolithophores were obtained from Roscoff Culture Collection (RCC). The cyanobacteria cultures were obtained from the Pasteur Culture Collection of Cyanobacteria (PCC).

Four kinds of phytoplankton species selected in this study are dinoflagellate *Prorocentrum minimum* (RCC291), diatom *Thalassiosira weissfloggi* (RCC76), coccolithophore *Emiliania huxleyi* (RCC911, calcifying; RCC174, non-calcifying) and cyanobateria *Synechococccus sp.* (PCC8806).

Th phytoplankton were cultured and collected at the Biogeochemistry and Algal Biology Laboratory in the Department of Earth Sciences, University of Oxford. The cells were cultured in Aquil* medium (NCMA) (Morel et al., 1979; Price et al., 1989), kept at 20°C, pH 8.1 and illuminated with 70-100 **μ**mol photons $m^{-2}s^{-1}$ on a day to night cycle of 12:12 hours.

The cells were harvested at the late exponential stage by centrifugation (4700 rpm for 25 min; 30 min for coccolithophores). For bulk cell analysis, the cells were rinsed 3 times with synthetic ocean water (Price et al., 1989) pre-cleaned by passing through Chelax-100 resin to remove weakly bound surface metals. Then the cells were kept frozen at -80°C before further digestion and analysis.

For three-component analysis designed to investigate different intracellular fractions and enzyme analysis, the collected cells were rinsed twice with synthetic ocean water and once with an extraction buffer (20 mmol L^{-1} Tris-Cl, pH 8.0). The cells were then

suspended in an extraction buffer (20 mmol L^{-1} Tris-Cl, pH 8.0) and sonicated 6 times for 20 s bursts (Hielscher UP200S ultrasonic processor, 70% amplitude, pulse frequency of 0.4 s s^{-1}) on ice with 20 s intervals between the bursts (adapted from Aharchaou et al., 2017; Zhang et al., 2018; Wilson et al., 2019). The addition of ice minimizes the increase of temperature of extraction buffer and prevents the denaturation of the proteins during the bursts. The cell lysate was centrifuged at 13200 rpm and 4℃ for 30 min. The supernatant containing protein fraction was collected for protein analysis and enzyme analysis (Protein fraction, P). 0.5 mL of Milli-Q water was added to the cell residues and the cells were boiled for 2 min. Then 0.5 mL of 1M NaOH was added to the residues and let react for 60 min at 70℃. The cell lysate was centrifuged again under the same setting and the supernatant was collected as cell debris fraction (CD). The residues were collected as metal-rich granules fraction (MRG).

A.2.6 Sulfides

The sulfides precipitated under oxic condition were carried out and collected in the metal-free clean labs at the Department of Earth Sciences, University of Oxford. Whereas the precipitation experiments under anoxic condition were performed in the glovebox laboratory at the same department. The glovebox was ventilated with pure N_2 and monitored using anaerobic monitor CAM-12 (COY Lab Products) for its oxygen level.

Nickel stock solution at 2.6 to 76.7 **μ**mol/L was reacted with a $Na_2S \cdot 9H_2O$ solution at 2.5 **μ**mol/L in three aqueous media with different ionic strengths: Milli-Q, 1:1 mixture of Milli-Q (Merck Millipore) and seawater (0.5 SW) and seawater (SW). The precipitates were collected by centrifuging the solution and then discarding the supernatant.

A.3 Reagents and laboratory equipment

All chemical works during sample preparation were carried out in Class 100 laminar flow hood in Class 10000 metal-free clean laboratories at the Department of Earth Sciences, University of Oxford.

Acids, i.e., HCl, HNO_3 and HF, used in this study were purified by in-house sub-boiling distillation system. All water (H_2O) used was 18.2MΩ-grade from a Merck Millipore water purification system. Solutions of dimethyglyoxime (DMG), ammonium citrate ($(NH_4)_2C_6H_6O_7$ and sodium hydroxide (NaOH) were prepared from crystalline commercial powders. Solution of sodium sulfide was prepared from Merck trace metal basis crystalline sodium sulfide nonahydrate ($Na_2S \cdot 9H_2O$) powder with ≥99.99% purity. Acetone and ethanol used were from reagent grade solution. Ammonia solution (NH_4OH, 25%) and hydrogen peroxide (H_2O_2) used in this study were commercial Merck suprapur® reagents.

A.4 Sample digestion

The digestion methods for samples reported in this study, including phytoplankton cells, particulates, sediments and sulfide precipitates, are stated in this section. All samples were digested applying conventional digestion methods (wet digestion) on hotplate which followed different recipes depending on each sample type. Microwave-assisted digestion was performed on two USGS shale standards SDO-1 and SGR-1b to assess the potential impact of different digestion methods on Ni isotope compositions.

A.4.1 Wet digestion

Bulk phytoplankton cell

The collected and rinsed cells were digested with concentrated HNO_3 with 30% H_2O_2 with a volumetric ratio of 3:2 on a hotplate at 110°C for 24 h, with the methods adapted from Zhang et al. (2018) and Wilson et al. (2019). The aliquots were then dried down and dissolved in 2% HNO_3 for analysis.

Organic-rich sediments

In general, 0.1g of freeze-dried sediment powders were added with concentrated HF and concentrated HNO_3 with a volumetric ratio of 1:3, ultrasonicated for 30 min, refluxed at 85°C for 24 h. The aliquots were dried down at 85°C, added 4 mL of 6M HCl, ultrasonicated for 30 min and refluxed at 120°C for 24 h. The aliquots were further added with 6 mL concentrated HNO_3 to form reverse aqua regia, ultrasonicated for 30 min and reflux at 120°C for 24 h. The solutions were dried down at 120°C, added 3 mL 30% H_2O_2 with 0.5 mL each time to let it react at room temperature until the reaction smoothed and left at room temperature to react for 24 h. The aliquots were dried down at 85°C as higher temperatures may cause strong fizzing. Then the residues were added with 1 mL of half-concentrated HNO_3 and refluxed at 120°C to check whether they were fully dissolved. If this was not the case, the cycles of H_2O_2 and half-concentrated HNO_3 were performed until the residues were fully dissolved. Finally, the aliquots were dried down and re-dissolved in 2 mL 2M HNO_3 for storage.

Particulates

For particulate samples, a total digestion method provided in the GEOTRACES cookbook was firstly applied (Cutter et al., 2017). The method is presented in Planquette and

Sherrell (2012) and Ohnemus et al. (2014), which are based on the development by Sherrell (1991) and Cullen and Sherrell (1999). As some residues could be seen in standard BCR-414 which was recommended in the cookbook, the treatment for organic-rich sediments was applied to get all samples and standards fully digested. The protocol mentioned here is adapted from the GROTREACES cookbook for particulate samples.

Polyethersulfone filters (PES, Supor®, 47mm) with particulates collected from Namibian margin were cut in half using a ceramic scissor (KYOCERA, Japan) to avoid contaminations. The halved PES filters were placed against the wall of the vial, close enough to the top edge to avoid submerging any part of the filter in the digestion medium. In this way, it allows refluxing whereby evaporated aliquot can slide down the side of the vial over the sampled face of the filter and continue refluxing. The other sides of filters without samples were dampened with residual seawater or the added acid, in order to let filters stick closely to the wall, preventing the refluxing acid to pass under the filters. The filters were refluxed with 1 mL of 50% HNO_3 / 10% HF at 130°C for 4 h. The filter material stayed intact in this acid mixture, but the potential of increasing organic matter matrix of digest solution has been raised for the hot immersion of filters (Cutter et al., 2017). After a cool down period, the droplets were collected from the cap and inside of the vials by either tapping the vials or rolling the solution around. The aliquots were dried down at 85°C, added 0.2 mL of concentrated HNO_3 to allow the matrix to be switched to nitric acid for analysis and dried down again at 130°C. The residues were dissolved in 2% HNO_3 for analysis.

Sulfide precipitates

The method for digesting sulfide precipitates was adapted from Guinoiseau et al. (2018). The collected sulfide precipitates from precipitation experiments were rinsed out and dissolved in 7 mL 6M HCl. It dissolved immediately after adding the acid. The solutions were then evaporated at 120°C and re-dissolved in 10 mL 2% HNO_3 for analysis.

A.4.2 Microwave-assisted digestion

In addition to normal wet digestion, organic-rich shale standards SDO-1 and SGR-1b were also digested by using microwave-assisted digestion method, in order to assess the potential influence on the Ni isotope compositions of samples during different sample treatments. The method was adapted from Gall (2011) which was developed at the Department of Earth Sciences, University of Oxford.

Weighed sample powders were pre-digested on hotplate at 85°C for at least 12 h, with a mixture of 4 mL concentrated HF, 2 mL concentrated HCl and 2 mL concentrated HNO_3, in order to break down the less resistant part before microwave digestion.

The solutions were then transferred to microwave vials and digested using a CEM MARS microwave. The temperature and pressure were programmed to increase stepwise to 210°C and 250 pounds per square inch (PSI) and held for 30 min at a maximum power of 1600 W. It took 4 min to ramp from ambient condition to 90°C and 50 PSI and hold it for 10 min before another ramp. Then another ramp increased the temperature and pressure to 120°C (30°C for each ramp) and 100 PSI (50 PSI for each ramp), and so on until it reached the working temperature and pressure.

After microwave digestion, the sample solutions were transferred back to clean Savillex beakers and evaporated to complete dryness. Then the residues were dissolved in 0.2 mL concentrated HNO_3 and dried down again to convert to HNO_3 form. The samples were re-dissolved in 2% HNO_3 for analysis.

It has been suggested any remaining organic materials after microwave digestion should be treated with repeated cycles of aqua regia (HNO_3 : HCl = 1 : 3) and a mixture of concentrated HNO_3– 30% H_2O_2 until the solution was clear (Gall, 2011). In this study, as the solutions were transparent after microwave-assisted digestion, the repeated cycles were skipped.

A.5 Purification of Ni in geological samples

It is important to purify Ni from samples of interest due to the influences on Ni isotopic signals from polyatomic and isobaric interferences formed during the ionization (section A.6.4.6), and the matrix effect from sample introduction with impurities. In this section, the development of Ni purification technique, method applied in this study, procedural blank and recovery assessment, and the efficiency of the method are discussed.

A.5.1 Development of Ni purification technique

The early purification methods for Ni isotopic analysis applied both ion exchange chromatography and liquid-liquid extraction, followed by analysis on TIMS (Brick and Lugmair, 1988; Morand and Allègre, 1983; Shimamura and Lugmair, 1983; Shukolyukov and Lugmair, 1993a, 1993b). The liquid-liquid extraction was reported to have low recovery of 70% (Quitté and Oberli, 2006). After the appearance of MC-ICP-MS, various

methods mainly using ion exchange chromatography were developed (Bizzarro et al., 2006; Cook et al., 2006; Quitté et al., 2006). The first purification of Ni for investigating stable Ni isotopes in geological materials was carried out by Tanimizu and Hirata (2006), which applied solvent extraction because of the potential isotope fractionation during ion exchange chromatography.

Most Ni purification methods applied di-methylglyoxime (DMG) as an organic chelator to bind Ni in neutral or ammoniacal solutions with its central square plane of nitrogen atoms (Nicholls, 1974). Methods developed at early stage using DMG, especially those using commercial Nickel Resin (Eichrom Technologies®), commonly resulted in a large quantity of DMG and related organic compounds in the purified Ni cut which was difficult to break down during further re-dissolution (Cameron et al., 2009; Quitté and Oberli, 2006). Due to the aforementioned problem in Ni chemistry, Gall et al. (2012) developed a method which significantly reduces the amount of DMG used in the chemistry. Saunders et al. (2020) further modified the method from Gall et al. (2012) to increase Ca and Mg removal in the first column and add additional HNO_3 steps to destroy column-related organics before the final dry down and dilution for analysis.

The purification method applied in this study was adapted from Gall et al. (2012) and Saunders et al. (2020), which were both developed in Department of Earth Sciences, University of Oxford.

A.5.2 Method applied in this study

All columns were made in-house with shrink-wrap Teflon and moulds. The dimensions of columns are listed in Table A.2.

A three-step ion exchange chromatography for Ni purification was applied in this study. The first step aims for the separation of the more electronegative divalent ions (e.g., Ni, Cu, Zn) by forming ammonia-complexes (e.g., $Ni(NH_3)_4^{2+}$) which are strongly bound to the resin, from either other non-divalent elements (e.g., Na, K, Al, Ti) or elements (e.g., Mg, Al, Fe) favoring the formation of citrate complexes which are not bound to the resin and eluted in this step. The second step aims to separate Ni from the remaining ammonium salts and divalent elements by firstly using oxalic acid-HCl solutions to separate elements (e.g., Fe, Al, Cr, Ti) with valences higher than +2 by forming oxalic complexes and secondly using HCl-acetone solutions to separate divalent elements (e.g., Mn, Cu, Zn, Cd, Sn). Ni is then eluted as a Ni-DMG complex in HCl-acetone media. The third and final step is to completely separate Fe from Ni using HCl-H_2O_2.

The full chemical procedure for the Ni purification technique applied in this study is described in detail below and summarized in Table A.3.

Column 1

Dissolved and spiked samples were evaporated and re-dissolved in 0.4 mL of 5M HCl, in order to convert samples to chloride form. Then 3.6 mL Milli-Q water (MQ), 0.6 mL 1M di-ammonium-hydrogen-citrate (dAHC, $C_6H_{14}N_2O_7$) and 1.4 mL 25% ammonia (NH_4OH) were added to make the solution a mixture of approximately 3M NH_4OH and 0.1M dAHC, which was ready for column 1. The sample solutions were subsequently loaded onto ion exchange columns filled with approximately 0.8 mL of cation resin (AG50W-X4, chloride form, 200-400 mesh), pre-cleaned by MQ, 6M HCl and 3M HCl, and pre-conditioned by 4 mL 3M NH_4OH–0.1M dAHC mixture. After sample loading, 1 mL of same 3M NH_4OH–0.1M

dAHC mixture and 1 mL 0.4M HCl were loaded onto columns to eluted remaining elements not of interest. The Ni-ammonium complex ($Ni_4(NH_3)_2$) was subsequently eluted in 2 mL 3M HCl. The collected Ni cuts were evaporated until almost dry at 130°C, added 0.3 mL of concentrated HNO_3 forming aqua regia to break the Ni-ammonium complex and refluxed at 150°C for 12 h.

Column 2

The Ni fractions from the first step were evaporated and re-dissolved in 0.1 mL 1M HCl. Then, 0.8 mL of MQ and 0.1 mL 0.5M oxalic acid were added to form a mixture of 0.1M HCl–0.05M oxalic acid. The sample aliquots were then loaded onto ion exchange columns filled with approximately 0.2 mL cation exchange resin (AG50W-X4, chloride form, 200-400 mesh), which were pre-cleaned by MQ, 6M HCl and 3M HCl, and pre-conditioned by 1 mL 0.1M HCl–0.05M oxalic acid. After sample loading, 3mL mixture of 0.1M HCl–0.05M oxalic acid and 3 mL mixture of 0.5M HCl–95% acetone were added to elute elements not of interest. The mixture of 0.5M HCl–95% acetone was also used to pre-condition the resin for the final Ni elution. The Ni-DMG complex was finally eluted in 1 mL mixture of 0.1M DMG–0.05M HCl–95% acetone. The eluted Ni cuts were evaporated at 90°C, added 0.1 mL concentrated HNO_3 to break down Ni-DMG complex and dried down again at 130°C. Then the fractions were dissolved in 0.1 mL concentrated HNO_3 and refluxed for 12 h.

Column 3

The Ni fractions from column 2 were evaporated and re-dissolved in 0.2 mL of 6M HCl–0.05% H_2O_2. The prepared solutions were then loaded onto columns filled with

approximately 0.1 mL anion exchange resin (AG1-X8, chloride form, 200-400 mesh), which were pre-cleaned by 6M HCl and MQ, and pre-conditioned by 0.5 mL 6M HCl–0.05% H_2O_2. Ni fractions were immediately eluted in 2 mL 6M HCl–0.05% H_2O_2 during loading and a further 0.2 mL of the same mixture, while Fe was retained on the resin under the condition of 6M HCl. The final Ni cuts were evaporated to dryness at 120°C, added 0.1 mL concentrated HNO_3 and dried down again. The residues were then re-dissolved in 2% HNO_3 for Ni isotope analysis.

Table A.2. Dimensions of column moulds used in this study for making Teflon columns.

	Volume of column (frit excluded) (µL)	Column diameter (mould) (mm)	Column length (mould) (mm)
Column 1	615	Tapered 4.4-3.5	50
Column 2	250	3.5	25
Column 3	120	3.5	12.5

Table A.3. Summary of chemical procedure for a three-step ion exchange chromatography separating Ni from biological and geological samples in this study.

	Reagents/Mixtures	Volume (mL)
Column 1 (AG50W-X4)		
Pre-cleaning	6M HCl	4
	MQ	4
	6M HCl	4
	MQ	4
	3M HCl	4
	MQ	4
Equilibration	(0.1M dAHC + 3M NH3)	4
Sample loading	sample in (0.1M dAHC + 3M NH3)	6
Rinse	(0.1M dAHC + 3M NH3)	1
	0.4M HCl	0.5
Ni Eluting	3M HCl	2
Column 2 (AG50W-X4)		
Pre-cleaning	6M HCl	1.5
	MQ	1.5
	6M HCl	1.5
	MQ	1.5
	3M HCl	1.5
	MQ	1.5
Equilibration	(0.1M HCl + 0.05M oxalic acid)	1
Sample loading	sample in (0.1M HCl + 0.05M oxalic acid)	1
Rinse	(0.1M HCl + 0.05M oxalic acid)	3
	(0.5M HCl + 95% acetone)	3
Ni Eluting	(0.1M DMG + 0.05M HCl + 95%acetone)	1
Column 3 (AG1-X8)		
Pre-cleaning	6M HCl	1
	MQ	1
	6M HCl	1
	MQ	1
Equilibration	(6M HCl + 0.05%H_2O_2)	0.5
Sample loading + Ni eluting	sample in (6M HCl + 0.05%H_2O_2)	0.2
Ni Eluting	(6M HCl + 0.05%H_2O_2)	0.2

A.5.3 Efficiency of Ni purification method in this study

In order to assess the efficiency of Ni purification method separating Ni from the elements in the matrix which may cause interferences on Ni isotope signals, the solutions of both in-house standards (Kam, Sud) and reference materials (Nod-P-1, BHVO-2, BIR-1, SDO-1) processed with Ni chemistry were measured for their elemental ratio relative to Ni (Table A.4).

The Fe/Ni ratios are all lower than 0.05, and mostly lower than 0.03 except for one of the Nod-P-1. Gall et al. (2012) suggested that there were significant isotope fractionations for Ni when the Fe/Ni ratios were higher than 0.04 as the interference of ^{58}Fe on ^{58}Ni, but the subsequent online correction by using ^{57}Fe to correct ^{58}Fe on ^{58}Ni allowed comparable $\delta^{60}Ni$ even when Fe/Ni ratios were higher than 2. Thus, the efficiency is sufficient to prevent potential inferences from Fe.

The metal/Ni ratios for Na, Mg, Cr and Zn ranging from 0.01 to 2 have been shown not to influence Ni isotope composition in the previous study (Gall et al., 2012), and these ratios are all lower than 2 in this study. The metal/Ni ratios for Ca and Ti have been reported to cause matrix effect on Ni isotope composition when the ratios were higher than 0.3 (Gall et al., 2012), but the ratios for both elements are all lower than 0.3 in this study. The Sc/Ni ratios are all lower than 0.004 in all processed standards in this study.

The K/Ni ratios range from ~0.03 to ~9 in all processed standards. Potassium is not likely to influence Ni isotopes for $^{23}Na^{39}K^{+}$ on ^{62}Ni which is naturally low in abundance (3.6345%) but double-spiked for Ni isotope analysis (section A.6.4.4). The Si/Ni ratios are mainly lower than 0.1, except for standards Kam, Sud and one of the Nod-P-1 where

Si/Ni ratios ranging 3~10 are observed. One potential interference from Si is the $^{29}Si_2^+$ on ^{58}Ni, but the isotope compositions of Kam, Sud and Nod-P-1 are measured consistently accurate through the entire project (see section A.6.4.8).

Table A.4. Elemental concentration for standards processed with Ni purification technique.

Sample	Fe/Ni (mol/mol)	Sc/Ni (mol/mol)	Ti/Ni (mol/mol)	Cr/Ni (mol/mol)	Zn/Ni (mol/mol)	K/Ni (mol/mol)	Mg/Ni (mol/mol)	Si/Ni (mol/mol)	Na/Ni (mol/mol)	Ca/Ni (mol/mol)
Nod-P1_202007	0.0482	0.0037	0.0070	0.0044	0.0009	1.4769	0.0202	10.3521	0.0135	0.2643
Kam_201911	0.0073	0.0011	0.0020	0.0010	0.0003	0.4353	0.0000	3.4357	0.0109	0.2705
Sud_201911	0.0137	0.0017	0.0033	0.0022	0.0037	0.0946	0.0113	6.2798	0.0220	0.1778
BHVO-2_201911	0.0141	0.0023	0.0064	0.0022	0.0057	1.0537	0.0166	0.0648	0.1571	0.2033
BIR-1_201911	0.0124	0.0019	0.0036	0.0018	0.0004	0.0782	0.0150	0.0218	0.1443	0.1583
Nod-P1_201911	0.0014	0.0002	0.0003	0.0002	0.0000	0.0299	0.0013	0.0011	0.0025	0.0159
SDO-L1_201911	0.0284	0.0021	0.0047	0.0057	0.0051	7.5685	0.0093	0.0000	0.0387	0.1776
SDO-L2_201911	0.0181	0.0016	0.0038	0.0021	0.0017	7.6048	0.0117	0.0408	0.0323	0.1616
SDO-A2_201911	0.0177	0.0026	0.0046	0.0025	0.0014	8.0200	0.0212	0.0403	0.0501	0.1885
SDO-A3_201911	0.0212	0.0033	0.0054	0.0035	0.0099	9.0011	0.0199	0.0000	0.0493	0.2485

A.5.4 Procedural blank

In order to quantify the contribution of Ni from the sample digestion and ion exchange chromatography, each batch of Ni chemistry for natural samples was carried out along with a blank sample. A summary for Ni procedural blank for different types of samples is shown in Table 2.5. It was usually around 3.7 to 4.7 ng, and it was slightly higher during the processing of sediment samples which was possibly caused by the digestion method with more steps and reagents added. In this study, Ni isotope measurements were usually carried out with lower sample sizes than other studies to cope with the low-Ni-content nature of biological samples, i.e., phytoplankton cells. The sample size of sediment and sulfide samples was usually around 400 ng, thus ~1.1% contribution of Ni from total procedural blank can be estimated. The sample size of biological samples was usually set as 200 ng, thus ~2.3% of blank contribution can be estimated.

Table A.5. Total Ni procedural blanks accumulated from the entire sample processing in sediments, biological and sulfide samples, with details of double-spikes applied for the calculation.

ID #	Date	Sample type	DS conc. (ppb)	DS amount (mL)	Blank (ng)
105566	2021.2.25	sediments	101190	0.01158	4.7
105633	2021.2.25	sediments	101190	0.01158	4.7
105706	2021.2.25	sediments	101190	0.01158	4.6
106141	2021.4.21	bio	1102.7	1.00787	4.1
106612	2021.6.10	bio	1102.7	1.01711	3.7
106766	2021.6.21	NiS	1102.7	1.01242	4.1
106804	2021.6.21	NiS	1102.7	1.01242	4.1
106842	2021.6.21	NiS	1102.7	1.01242	4.1

A.5.5 Yield of the Ni chemistry

The yields for Ni chemistry varied slightly with sample types but are generally around 97-102% based on the both the in-house standards (Kam and Sud) and geological standards (AGV-2 and Nod-P-1). The yields for AGV-2 are slightly lower as its relatively high matrix-to-Ni ratio compared with nodule (Nod-P-1) and nickel sulfide (Kam and Sud).

The yields shown in this study are comparable with other studies. Furthermore, with the addition of Ni spikes before chemistry and the subsequent double-spike calculation, any isotope fractionations related to incomplete Ni yields will be corrected. (section A.6.4.3.3).

A.6 Analysis

The general introduction of the analytical methods applied in this thesis are stated here, as the technical details and theoretical background may not be mentioned in each following chapter/paper. The cell number and pigment analysis are for the calculation of

phytoplankton growth rate. Major and trace element concentration measurements were carried out using ICP-MS, whereas Ni isotope analyses were carried out using MC-ICP-MS.

A.6.1 Measurement of cell number

The cell number of cultured phytoplankton was measured to estimate the population size and growth rate of the cultures. The measurements were carried out using an electronic particle counter Beckman Coulter® in OceanBug Laboratory at the Department of Earth Sciences, University of Oxford.

The cleaning program on Coulter Counter® was carried out on a daily basis before measurement. For the preparation, 1 mL of cultures from the culturing flasks were transferred to plastic vials and diluted with 9 mL of 3.5% NaCl solution right before the measurement. The diameters set for phytoplankton varied with species. General ranges for dinoflagellate, diatom, cyanobacteria and coccolithophore were 2-8 **µ**m, 5-15 **µ**m, 1.5-4 **µ**m and 2-8 **µ**m, respectively.

The growth rates based on the change of population sizes were calculated by the following equation:

$N_2 = N_1 e^{\mu t}$ (Equation A.1)

N_1 represents the initial population. N_2 represents the current population after a time t with a growth rate **µ**.

A.6.2 Pigments analysis

The pigments of phytoplankton were measured to provide supplementary information for phytoplankton growth. The measurements were carried out using TECAN Spark® multimode plate reader to analyze the abundance of chlorophyl, phycocyanin and optical density. The wavelengths set for chlorophyl phycocyanin and optical density were 485-680 nM, 595-680 nM and 750 nM, respectively.

Plates with capacity for 96 samples were used to measure multiple samples at one go. For the preparation, 200 **µ**L of cultures were pipetted to the plate right before the analysis.

A.6.3 Measurement of elemental concentration

All concentrations of major and trace elements reported in this study were measured using a PerkinElmer NexION 350D quadrupole inductively coupled plasma mass spectrometer (ICP-MS) at the Department of Earth Sciences, University of Oxford.

The following sections will discussion the basics of ICP-MS and current instrumental set-up for the analysis.

A.6.3.1 Introduction of ICP-MS

The mass spectrometer separates ions and charged molecules with different mass/charge (m/z) ratio by using the different behavior during acceleration through electric and magnetic fields. In general, parts of ICP-MS can be categorized into introduction system, plasma source, ion separator and detector.

A.6.3.1.1 Introduction system

There are various introduction systems currently available for ICP-MS. Two introduction systems applied in this thesis are discussed further here, i.e., direct injection system and desolvating system.

Direct injection system utilizes a micro-flow PFA nebulizer (Elemental Scientific Inc.) aspirating sample aliquot at a speed of 50**µ**Lmin^{-1} as small aerosols into a quartz cyclonic spray chamber. The structure of the spray chamber only allows fine aerosol droplets to pass through directly to plasma, whereas the rest of the sample aliquot condenses on the wall of spray chamber and is then discharged as waste. This introduction system can generate stable ion beam, but its low transfer efficiency requires relatively high concentration solution to carry out precise measurement. Another problem of direct injection system is the interference caused by the formation of isobaric molecules such as oxides, hydrides and nitrides from the acid solution (usually 2% HNO_3) aspirated into plasma together with the analyte.

Desolvating system (e.g., Aridus II in this study) aspirates sample aliquot into a heated chamber instead of spraying aerosols directly into plasma. The aerosols are evaporated in the chamber and transformed into a smaller droplet size. The heated droplets are then transferred into a heated hydrophobic PTFE membrane where the analyte is separated from the solvent by a hot flowing Ar gas. The dry analyte is then transferred directly into plasma for ionization. This process reduces up to 99% of solvent transferred into the plasma, which improves the sensitivity of a given analyte and minimizes the potential isobaric interferences derived from solvent molecules. The improved sensitivity enables the possibility of measuring samples with smaller sample sizes. However, a problem of

this introduction system is the potential mass fractionation of the sample in the membrane during the desolvating process.

A.6.3.1.2 Plasma source

The inductively coupled plasma uses Ar ionized by collisional motions in a high frequency electromagnetic field as the plasma source. The Ar sweep gas (~ 15 $Lmin^{-1}$) flows through a quartz torch which is surrounded by a copper load coil at the end. The high frequency is provided by a RF generator operating at a power of ~1300W, driving a current through the load coil which induces an electromagnetic field. The Ar gas flowing through this electromagnetic field is ignited by a high-voltage spark which produces free electrons stripped from Ar atoms. The electrons are then accelerated in the field and initiate a chain reaction by colliding with other Ar atoms to produce more electrons. The collisions can heat up the plasma to about 5000~8000K that provides sufficient energy to ionize most elements in the periodic table. The plasma sustains once the gas supply and energy supply are stable.

The ions created in the plasma are then extracted into the interface consisting of two nickel cones (sampler and skimmer cone) with holes of different sizes which allows a pressure difference to build up. The ions are transferred through the interface region by potential differences and guided by sets of optical lenses, in order to focus the ion beam to the detector. As all ions produced are positively charged, the repulsive force of charges favors heavier ions to pass through and rises an instrumental mass bias, which is also called “space-charge effect”.

A.6.3.1.3 Ion separator

In ICP-MS, the generated ions are separated by both their mass-to-charge ratio (m/z) and their kinetic energy. It occurs as the plasma source generated at the high voltage produces ion beams with large energy spread.

For quadrupole ICP-MS, such as PerkinElmer NexION 350D applied in this study, it separates ion beams using quadrupole. The quadrupole consists of four parallel metal rods. Each opposing rod pair is electrically connected. A radio frequency voltage with a DC offset is applied between one pair of rods and the other. Only ions with a certain mass-to-charge ratio (m/z) can reach the detector given certain ratio of voltages, whereas the other ions with unstable trajectories will collide with rods. This allows the mass spectrometer not only to select an ion with a particular m/z but also to screen through a range of m/z by continuously changing the applied voltage.

For MC-ICP-MS, such as Nu Plasma-HR applied in this study, it separates ion beams by using a double-focusing magnetic sector which consists of a magnetic field and an electric sector analyzer (ESA). The ions entering the ESA are separated with respect to their kinetic energy and focused into a beam of ions of sorted velocities which subsequently enter the magnetic field for actual mass separation procedure.

A.6.3.1.4 Detector

A number of different ion detection designs have been utilized since ICP-MS was first introduced in the early 1980s, two most commonly used ones are secondary electron multipliers (also called channel electron multipliers) for low counts and Faraday cups for high counts.

Secondary electron multipliers (SEM) operate with similar principles as photomultiplier tube used in inductively coupled plasma optical emission spectrometer (ICP-OES). Photomultiplier applies individual dynodes to convert photons to electrons, while SEM uses open glass cone coat with a semiconductor-type material to generate electrons when ions impinge on its surface. When a positively charged ion emerges from ion separator, it is then attracted to the high negative potential of the cone. When the ion hits the cone, one and more secondary electrons are emitted. This generating process for secondary electrons is repeated many times and results in a discrete pulse containing millions of electrons generated from the ion first hit the cone, which enlarges the abundance of original ions and their electric signals on detectors.

Faraday cups are applied to measure ion beams from ion separator when the ultratrace limits are not required. As there is no enhancement for the voltage, it can only be used for high ion currents. Their lower working range is in the order of 10^4 cps, which means the sensitivity of ICP-MS will be compromised if there is only one detector (Thomas, 2003).

For Perkin Elmer quadrupole ICP-MS NexION 350D, it is equipped with two SEM responsible for pulse and analog mode, respectively. These two modes provide ten orders of dynamic range and enable measurements for both high- and low-level analytes simultaneously. For signals lower than 2,000,000 counts per second (cps), the pulse mode is applied. Whereas for signals higher than 2,000,000 cps, it switches to analog mode to avoid saturating the detectors.

For Nu Plasma HR-MC-ICP-MS, it is equipped with 12 Faradays cups and a number of SEM with ion counting enabling a larger dynamic range of ion beam signals to be precisely measured. The detectors are configured in a fixed placement with a set of electronic lenses focusing the ion beams into individual detectors. The Ni isotopic analysis carried out in this study used only Faraday cups (see section A.6.4.5 for more details).

A.6.3.2 Instrumental set-up for ICP-MS

The PerkinElmer NexION 350D quadrupole ICP-MS used in this study is interfaced with an Elemental Scientific Inc. (ESI, USA) Prep-FAST M5 Auto-sampler system. This equipment provides the ability to dilute and inject micro-volume aliquots of blank, standard and sample directly into the mass spectrometer by using the flow injection automation system (FIAS) facility. The injections are measured by the fast-scanning quadrupole of the ICP-MS and the average data are calculated from three injections per replicate.

The determinations of elemental concentration were done using either direct injection, FIAS equipment, or seaFAST equipment depending on the sample type and elements of interest. The seaFAST is an automated preconcentration system for undiluted seawater. When the trace metals of interest were accompanied with the presence of high content of major elements, such as the trace metals in seawater and porewater samples, the seaFAST system was applied to enhance the concentration of the interested elements through preconcentration technique and optimize the analytical precision.

The NexION 350D has a collision/reaction cell to enhance the signal-to-background ratio and enable the measurement of many elements with spectral interference. Three modes,

i.e., standard mode, KED (Kinetic Energy Discrimination) mode and DRC (Dynamic Reaction Cell) mode, are available to be applied to optimize the signals and minimize the potential interferences on measured masses for various elements. Commercial grade helium gas (>99.999%) was used as a collision gas for KED mode, while electronic grade ammonia gas (>99.9995%) was used for reaction cell.

The instrument was optimized on a daily basis by monitoring the sensitivities of Li, Mg, In, Ce, Pb and U across the mass range and ensuring the CeO^+/Ce^+ ratio is maintained lower than 2.5%. The precision and accuracy of elemental analysis were monitored daily using river standard SLRS-6.

A.6.4 Determination of Ni isotopic composition

All the new Ni isotopic data provided in this thesis were measured using a Nu Plasma-HR multi-collector inductively coupled plasma mass spectrometry (MC-ICP-MS) at the Department of Earth Sciences, University of Oxford.

This section is a summary of the work conducted for developing a reliable and precise measurement protocol for Ni isotopic composition. This section demonstrates the basics of MC-ICP-MS, conventional expression of Ni isotopic composition, mass fractionations caused by instrument itself and different ways to correct them, different kinds of interferences during Ni isotope measurement, tests for developing a reliable protocol such as intensity test and normalized argon index test, the set-up applied in this study and the long-term reproducibility for various monitoring standards.

A.6.4.1 Introduction of MC-ICP-MS

The precise and accurate determination of isotopic ratios has been the interest of many researchers for decades as its important applications in many disciplines, such as earth and planetary sciences, environmental sciences, nuclear and forensic sciences, medical sciences, provenance studies for environmental and food samples, and archaeology (Mellon and Sandström, 1996; Laeter, 1998; Hoefs, 2004; Johnson et al., 2004; Faure and Mensing, 2005; Vanhaecke et al., 2009; Yang , 2009; Balcaen et al., 2010; Yang et al., 2018).

For many applications of isotopic ratios, the most important prerequisite is the high precision measurement as the variations of isotope composition can be subtle and only be identified and quantified by highly precise isotopic analysis. The precision of isotopic analysis using both quadrupole ICP-MS instruments and single-collector sector field units is limited to many studies as the interferences from ICP ion source and the presence of single collector only allows to monitor the signal from one nuclide at a given time. The precision of isotopic determination using traditional quadrupole-based instruments is limited to ≥ 0.1% RSD (Heumann et al., 1998). The precision for a sector field ICP-MS operated at low mass resolution is slightly better with ≤0.05% RSD (Vanhaecke et al., 1996). When the resolution in a sector field ICP-MS is increased from low (R = 300) to medium (R = 3000~4000), the internal isotope ratio precision is decreased back to about ≥0.1% RSD (Vanhaecke et al., 1997). The optimum precision of time-of-flight (TOF) ICP-MS is about ≤ 0.05% (Vanhaecke et al., 1999).

Due to the limited precisions for the above techniques, traditionally, thermal ionization mass spectrometry (TIMS) has been applied in acquiring the highest accuracy and precision of isotope ratios (Platzner, 1997). However, the time for sample preparation

and measurement using TIMS can be long. Subsequently, the development of multi-collector ICP-MS finally bridges the gap between the isotope ratio precision of ICP-MS and TIMS. As the signal intensities of the interested isotopes are monitored simultaneously, the signal drift with time and the instrumental stability should no longer affect the isotope ratios and the precisions (Walder et al., 1993; Halliday et al., 2000; Rehkämper et al., 2001). The appearance of MC-ICP-MS provides simple and robust sample introduction, high sample throughput, high mass resolution, flat-topped peaks, and accuracy and precision of isotope ratio determination comparable to TIMS (Albarède et al., 2004). Its precision can reach 0.002% under favorable condition at low mass resolution but is also dependent on interested elements (Wieser and Schwieters, 2005).

However, compared to TIMS, MC-ICP-MS has much larger instrumental mass fractionation, for instance by up to 25% for Li (1-2% observed for Li on TIMS) (Millot et al., 2004; Kasemann et al., 2005). The mechanisms of this mass bias within ICP-MS is not fully understood but is likely caused by the supersonic expansion of ions through the sampler cone and the space charge effect in the skimmer cone region. Both processes favor the transmission of the heavier isotope into the mass spectrometer and lead to different transmission efficiencies (sensitivities) for ions with different m/z ratios (Gillson et al., 1988; Platzner, 1997; Heumann et al., 1998). It is also found that the plasma conditions such as the sample gas flow rate and the geometry set-up for cones also influence the magnitude of isotope fractionation (Andrén et al., 2004). Furthermore, the instrumental mass fractionation drift along with the time as well.

Thus, proper correction method for instrumental mass fractionation on MC-ICP-MS is crucial for getting accurate isotope ratio (see section A.6.4.3).

A.6.4.2 Delta notation

The delta (δ) notation is a way to express the variations of isotopic ratios, which is reported in per mil (‰) deviation relative to a standard.

For Ni isotope system, the deviation of isotopic ratios ($^{n}Ni/^{58}Ni$, where n = 60, 61 or 62) are calculated relative to a pure Ni metal, i.e., Standard Reference Material (SRM) 986 from National Institute of Standards and Technologies (NIST) (Equation A.2). The isotopic ratios of standard SRM 986 were firstly determined by Gramlich et al. (1989a) using TIMS technique.

$$\delta\,^{n}Ni = \left[\frac{(^{n}Ni/^{58}Ni)_{sample}}{(^{n}Ni/^{58}Ni)_{SRM986}} - 1\right] \times 1000 \; (n = 60, 61 \; or \; 62) \quad \text{(Equation A.2)}$$

A.6.4.3 Instrumental mass fractionation correction

A mass bias is observed in mass spectrometer using ICP source, which enriches isotopically heavier ions compared to natural isotope ratios. It has been explained by the space-charge effect or so-called Coulomb repulsion which is the preferential deflection of lighter ions from the center of the ion beam in the expansion chamber (Becker, 2007).

The space-charge effect is a time-independent function of mass, which can be corrected by using various techniques, i.e., standard-sample-bracketing (SSB), element-doping and double-spiking.

The instrumental mass bias has been illustrated by various mathematical fractionation laws, e.g., linear, exponential, power, kinetic, etc., in order to calculate the instrumental

fractionation factor (*f*) (Russell et al., 1978; Hart and Zindler, 1989). As for ICP-MS analysis, the power law (Equation A.3) and the exponential law (Equation A.4) are the ones commonly used.

$$\frac{R_{true}}{R_{measured}} = (1+f)^{\Delta m} \quad \text{(Equation A.3)}$$

$$\frac{R_{true}}{R_{measured}} = \frac{n^1/n^2}{n_i^1/n_i^2} = \frac{n^1/n_i^1}{n^2/n_i^2} = \frac{\tau_1}{\tau_2} = (\frac{m_1}{m_2})^f \quad \text{(Equation A.4)}$$

The R_{true} and $R_{measured}$ represent the true (or corrected) and measured isotope ratio of interest, respectively. The f stands for the instrumental fractionation factor and Δm denotes the mass difference between the masses of two isotopes m_1 and m_2. Where n represents the number of ions and τ for the transmission of the mass spectrometer for a particular nuclide for most analytical data. Unsubscripted n denotes for a measured value and the "i" subscript is for the original solution.

The exponential fractionation law is first proposed by Russell et al. (1978) to explain that the fractionation factor *f* at high resolution studies is solely dependent on the absolute masses of the measured isotopes but not the difference of the masses between the isotopes as power fractionation law suggests. Albarède et al. (2004) argued that all these laws (linear, exponential, power, kinetic, etc.) only reflect particular ways of transmission in expanding chamber as a function of mass difference using different functional relationships. Maréchal et al. (1999) proposed a Generalized Fractionation Law (GFL) as a unified conceptual framework which covers most of the instrumental fractionation laws but with internal inconsistency. The exponential law has been demonstrated to account

for most of the measured mass bias (Albarède et al., 2015). However, the physics of mass fractionation remains elusive for the issue to be settled. Maréchal et al. (1999) reviewed and discussed that a value of $f \sim 2$ fits most of the elements across the mass range. This value implies that light isotopes are preferentially lost from the center of the beam, which has been interpreted variously including the notable space-charge effect. The continuously improved mass spectrometry with increasing transmission has suggested the change of f and raised new perspectives and demands a revisit to the physics of mass bias (Shirai and Humayun, 2011). For instance, Albarède et al. (2015) found the exponential fractionation factor f is about -0.24 ± 0.02 lnτ when τ (> 0.002) is higher than previously reported transmission with measurements on MC-ICP-MS Thermo Finnigan Neptune Plus with Jet cone, which is in contrast to $f \sim 2$ at lower transmission. The results suggest the transmission is needed to be considered when interpreting exponential fractionation factor in the future.

A.6.4.3.1 Standard-sample-bracketing

Among various ways to correct for instrumental mass bias, the standard-sample-bracketing technique is the most common and simplest one. This method interpolates the mass bias of an unknown sample between the bias inferred from two standard runs, one proceeding and one following the sample run (Figure A.2). Less stringent order of interpolations, e.g., standard-multiple samples-standard, are also used in studies. This interpolation scheme is the most general way to linearly interpolate the logarithms of the isotopic ratios, and it is easily adapted to procedures in which more than one sample is run between the bracketing standard (Albarède et al., 2004).

Standard-sample-bracketing technique is not applicable to TIMS measurements as each sample is on a different filament successively positioned by a rotating turret. The mass bias depends on the temperature, structure and composition of the sample film loaded on the filament (Albarède et al., 2004). Thus, the run condition for each sample can vary between samples and the mass bias cannot be accurately controlled. In contrast, ICP sources can work at steady state. With well-purified samples and standards which can be regarded as chemically equivalent, the condition of mass spectrometer can be ideally constant.

This technique requires the standard and sample to have exactly the same matrix or that all matrix elements are quantitatively removed during the chemical separation. If it is not the case, the correction may not be reliable. As fractionation during chemical separation can also happen, one way to compensate the fractionation is to process the bracketing standard the same way as sample of interest.

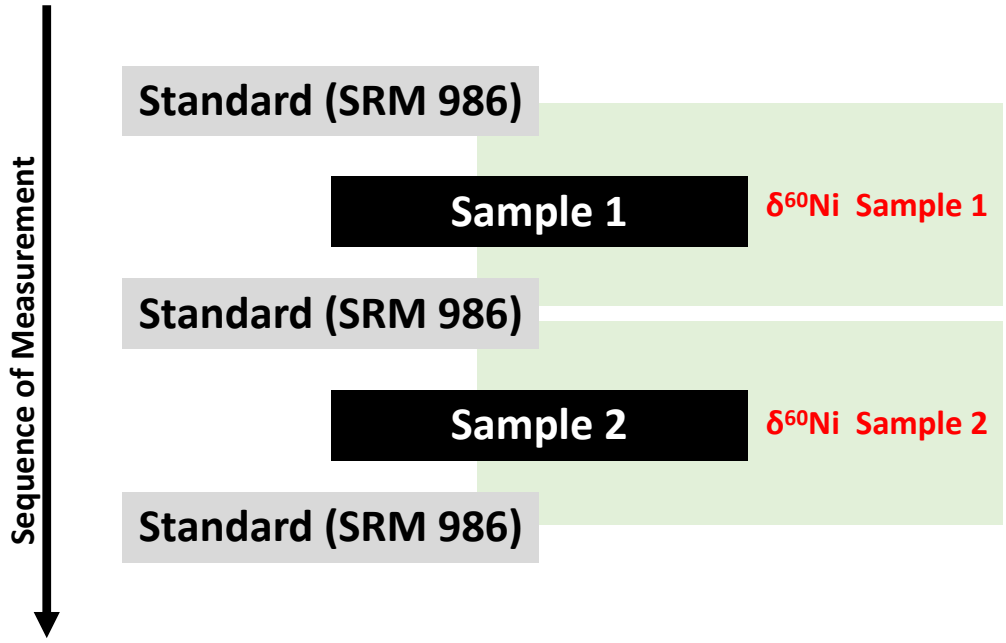


Figure A.2. Schematic diagram of standard-sample-bracketing technique used in this study during Ni isotopic analysis.

A.6.4.3.2 External correction by element-doping

The instrumental mass bias can also be externally corrected by adding a known amount of an element of similar mass to the interested element, with the assumption that elements of similar masses experience the same fractionation in the mass spectrometer.

As for Ni, Cu works theoretically the best as Cu has two naturally occurring isotopes, i.e., ^{65}Cu and ^{63}Cu, which have similar mass to Ni and do not interfere with Ni isotope masses (Chernonozhkin et al., 2015; Beunon et al., 2020). With the assumption that Ni and Cu have similar fractionation ($f_{Ni} \approx f_{Cu}$) and their fractionations both follow the exponential fractionation law, the instrumental mass bias of a measured Ni isotope ratio can be corrected for (Equation A.5 and A.6).

$$R_{Ni}^{corr} = R_{Ni}^{meas} \times \left(\frac{m_{60}}{m_{58}}\right)^{f_{Ni}} \text{ (Equation A.5)}$$

$$f_{Ni} \approx f_{Cu} = \frac{\ln(R_{Cu}^{true}/R_{Cu}^{meas})}{\ln(m_{65}/m_{63})} \text{ (Equation A.6)}$$

A.6.4.3.3 Internal correction by double-spike technique

A highly accurate and robust way to correct instrumental mass fractionation is the double-spike technique (Dodson, 1970; Galer, 1999; Johnson and Beard, 1999). The technique spikes the standard and sample with a solution containing two isotopes of the interested element with a known composition. It can be applied to any isotope system which the element of interest has at least four naturally occurring isotopes as the data reduction requires three isotope ratios. Furthermore, if the double-spike is added before

the chemical separation, any potential mass fractionation during the chemical process can be automatically corrected for after data reduction.

A schematic diagram for the concept of double-spike technique is adapted from Rudge et al. (2009) and shown in Figure A.3. The double-spike (or tracer) T is a mixture of two single spikes S_1 and S_2 with proportions q to 1-q. The double-spike is then added to a sample N with proportions p to 1-p to form a mixture M which is measured as m in mass spectrometer. For radiogenic isotope work or stable isotope systems conducting mass-independent fractionation, an additional run is the unspiked sample n. For stable isotope work, n is the composition of a standard. The mass fractionation that occurs in the mass spectrometer and in nature will be assumed to follow the same fractionation law.

In order to get a highly precise isotope analysis, it is crucial to optimize the isotopic composition of the double-spike and the sample-spike ratio in the final mixture (Rudge et al., 2009). In this study, the applied double-spike technique is a mixture of ^{61}Ni and ^{62}Ni with a ratio of 25:75 and added into each dissolved sample at a sample : spike ratio of 0.4 before Ni purification according to method developed by Gall et al. (2012).

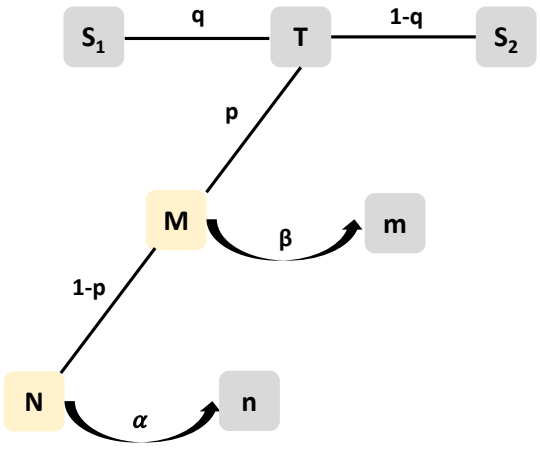


Figure A.3. Schematic diagram of the double-spike technique. Lines without arrows represent mixing and lines with arrows represent mass fractionations. The single spikes S_1 and S_2 are mixed in a proportion of q : 1-q (per mole of element) to form the double-spike (as a tracer T). N is the sample of interest, which is mixed with the double-spike T to form the mixture M with proportions p to 1-p. During isotope analysis in mass spectrometer, the mixture M undergoes instrumental mass fractionation with fractionation factor β, thus a different composition m is measured. Similarly, the composition n represents the instrumental mass fractionation from N with a fractionation factor α. For radiogenic isotope work or stable isotope systems undergoing mass-independent fractionation, n is measured from an unspiked run and α is another instrumental fractionation factor. For stable isotope work, n is the composition of a standard material and α stands for the mass fractionation that has occurred in nature. The double-spike inversion utilizes the parameters in grey (n, m and T) to calculate the unknown α, β, N and M. The figure is adapted from Rudge et al. (2009).

A.6.4.4 Interferences

For samples like sediments and seawater, which typically consist of trace level of Ni and chemically complicated matrices, an accurate, precise and reproducible isotopic analysis using MC-ICP-MS needs careful control on sample processing and analytical approach. Residual elements in the matrices can potentially cause both spectral and non-spectral interferences which can induce significant inaccuracies on interested isotopic ratios during measurements.

Spectral interferences are caused by elemental (singly charged and/or doubly charged) or polyatomic overlap on interested isotope which has similar mass to charge ratio (m/z). This overlap can further influence isotope ratios in a mass-independent fashion.

Many studies have identified and assessed a broad range of potential spectral interferences on Ni isotopes as shown in Table (compiled from May and Wiedmeyer, 1998 and Gall et al., 2012).

There are several possible interferences on the mass of Ni isotopes. One of the critical elemental interferences is the overlap between the masses of ^{58}Fe and ^{58}Ni as ^{58}Ni is commonly used as the denominator isotope of all ratios. The mass resolution (m/Δm) required to separate these two peaks is approximately 28,000 which is not available under current settings with Nu Plasma-HR (R_{low} = m/Δm ≈400; R_{medium} = m/Δm ≈4000; R_{high} = m/Δm ≈8000) (Gall et al., 2012). To solve this problem, Gall et al. (2012) developed an on-line correction by measuring the signal of ^{57}Fe and using it to calculate the theoretical contribution of ^{58}Fe on mass 58. The sources of Fe can be the matrix of solution itself, the desolvator and the internal parts of the mass spectrometer (Gall et al., 2012). To ensure a complete separation of Ni from Fe in samples, Gall et al. (2012) tailored the purification protocol by adding a clean-up step as a third column. This study also suggested Ni isotope composition of samples can be accurately corrected in the presence of Fe in the solution with Fe/Ni ratio up to 2 (Gall et al., 2012). ^{56}Fe also has been measured and used to monitor the potential interference from ^{58}Fe on ^{58}Ni (Vance et al., 2016).

There is also a potential elemental interference of ^{64}Zn on the mass of ^{64}Ni which requires a resolution (m/Δm) of ~55,000 to separate each other. Thus, ratio ^{64}Ni/^{58}Ni is not reported in this thesis.

In addition to singly-charged ions, there are also potential interferences caused by doubly-charged ions such as ^{116}Cd^{++} and ^{116}Sn^{++} on mass 58 and ^{120}Te^{++} and ^{120}Sn^{++} on mass 60 (Table A.6).

Another major interferences for Ni isotopes are the presence of polyatomic $^{40}Ar^{18}O^{+}$ and/or $^{40}Ar^{17}O^{1}H+$ on mass 58 and $^{40}Ar^{17}O^{+}$ and/or $^{40}Ar^{16}O^{1}H^{+}$ on mass 57. Previous Ni isotope studies have tried to use higher resolution on mass spectrometers to monitor and resolve these interferences ($^{40}Ar^{18}O^{+}$ and/or $^{40}Ar^{17}O^{1}H^{+}$) from mass ^{58}Ni (Gall et al., 2012). Since there were no detectable peaks representing to $^{40}Ar^{18}O^{+}$ or $^{40}Ar^{17}O^{1}H^{+}$ on mass 58 in medium resolution mode (pseudo-resolution m/Δm ≈ 4000) on MC-ICP-MS Nu Plasma-HR used in this study, all the Ni isotope measurements were carried out in low resolution mode.

In this study, the intensity of ^{57}Fe, ^{58}Ni, ^{60}Ni, ^{61}Ni and ^{62}Ni are measured under low resolution during Ni isotope analysis on MC-ICP-MS. The potential interference of ^{58}Fe on ^{58}Ni was corrected by simultaneous measurement of ^{57}Fe.

Table A.6. Potential elemental and polyatomic interferences on the mass of five Ni stable isotopes and ^{57}Fe.

	^{57}Fe	^{58}Ni	^{60}Ni	^{61}Ni	^{62}Ni	^{64}Ni
Singly-charged element		$^{58}Fe^{+}$				$^{64}Zn^{+}$
Doubly-charged element		$^{116}Cd^{++}$	$^{120}Te^{++}$	$^{122}Te^{++}$	$^{124}Te^{++}$	
		$^{116}Sn^{++}$	$^{120}Sn^{++}$	$^{122}Sn^{++}$	$^{124}Sn^{++}$	
Polyatomic	$^{40}Ar^{17}O^{+}$	$^{40}Ar^{18}O^{+}$	$^{24}Mg^{36}Ar^{+}$	$^{25}Mg^{36}Ar^{+}$	$^{24}Mg^{38}Ar^{+}$	$^{32}S^{16}O_2^{+}$
	$^{40}Ca^{16}O^{1}H^{+}$	$^{22}Ne^{36}Ar^{+}$	$^{20}Ne^{40}Ar^{+}$	$^{21}Ne^{40}Ar^{+}$	$^{26}Mg^{36}Ar^{+}$	$^{32}S_2^{+}$
	$^{40}Ar^{16}O^{1}H^{+}$	$^{20}Ne^{38}Ar^{+}$	$^{22}Ne^{38}Ar^{+}$	$^{43}Ca^{18}O^{+}$	$^{22}Ne^{40}Ar^{+}$	
	$^{38}Ar^{18}O^{1}H^{+}$	$^{40}Ca^{18}O^{+}$	$^{42}Ca^{18}O^{+}$	$^{44}Ca^{16}O^{1}H^{+}$	$^{44}Ca^{18}O^{+}$	
	$^{38}Ar^{19}F^{+}$	$^{42}Ca^{16}O^{+}$	$^{44}Ca^{16}O^{+}$	$^{45}Sc^{16}O^{+}$	$^{46}Ti^{16}O^{+}$	
		$^{40}Ca^{17}O^{1}H^{+}$	$^{23}Na^{37}Cl^{+}$		$^{23}Na^{39}K^{+}$	
		$^{40}Ar^{17}O^{1}H^{+}$	$^{43}Ca^{16}O^{1}H^{+}$		$^{46}Ca^{16}O^{+}$	
		$^{23}Na^{35}Cl^{+}$				
		$^{29}Si_2^{+}$				

A.6.4.5 Analytical set-up

All Ni isotopic analyses in this study were carried out using a Nu Plasma-HR MC-ICP-MS at the Department of Earth Sciences, University of Oxford.

To clearly illustrate the difference of detector array used in this study than the normal one, the comparison between the normal and adapted alignment of detector is shown in Table A.7. The numbers 0-11 show the placements for the 12 available Faraday cups and IC represents the ion counter. The normal alignment of detectors in Nu Plasma-HR MC-ICP-MS can provide spaces for measuring five isotope masses at a time, which can measure four Ni isotopes without ^{57}Fe. With the adapted detector array, it allows simultaneous determination of six isotope masses in three-spacing intervals which means the instrument is capable of measuring four Ni isotopes of interest and monitoring ^{57}Fe for aforementioned Fe correction at the same time. For this study, only the Faraday detectors were used for Ni isotope measurement. The resistor in a Nu Plasma-HR Faraday detector is around $10^{11}\Omega$, which makes a current of $10^{-11}A$ to be read as an ion beam of 1V. The default resistor setting allows the measurement of current up to $10^{-10}A$ which equals to an ion beam of 10V. One of the resistors can be adjusted using "DVM-offset" function and widen its upper limit of ion beam to 20V at a time. This offset setting can allow the measurement of $^{38}Ar^{+}$ and $^{40}Ar_2^{+}$ which are usually around 10-20V during Normalized Argon Index (NAI) test.

As the peaks for argide interferences on mass 58 and 57 are not detectable, Ni isotope analysis for samples in this study were carried out in low resolution mode on Nu Plasma-HR MC-ICPMS. The sample size of Ni used in this study is usually around 200 ng added with 500 ng of spike in accordance to the sample : spike ratio=0.4 : 1. Samples were

usually run at a total Ni concentration of 200-300 ppb. Sample solutions were introduced to the plasma via a PFA nebulizer (ESI scientific, 50μLmin^{-1}) coupled with an Aridus II Desolvating Nebulizer System (TELEDYNE, CETAC Technologies) which can enhance sensitivity and minimize oxide formation during ionization. In this study, all isotopes were measured simultaneously in static collection mode. Each isotopic measurement consists of 40 cycles which have 10s integration time for acquiring ion beam intensity. The typical instrumental settings for Ni isotope analysis on Nu Plasma-HR are shown in Table A.8.

A set of nickel sampler and skimmer cone was used for Ni isotope analysis. In this study, the background acid 0.3N HNO_3 typically has a total Ni intensity of <1mV, which is negligible compared with 15-16V of total Ni in standards and samples. This background signal with the set of Ni cones has been investigated in Gall et al. (2012) and reported to be constant between analyses when an on-peak-zero background measurement in the blank acid is applied. The result suggests that ~50% of the background comes from the nickel sampler and skimmer cones used and the rest of background presumably originates from other stainless-steel components in the mass spectrometer (Gall et al., 2012).

The total Ni signal received at detectors for ^{58}Ni, ^{60}Ni, ^{61}Ni and ^{62}Ni is usually controlled around 15-16V. As all the samples were bracketed with SRM 986, the total Ni intensity of all samples was adjusted to the intensity of bracketing SRM 986 within 10% difference.

Table A.7. The normal (top) and adapted (bottom) detector array of Nu plasma-HR MC-ICP-MS at the Department of Earth Sciences, University of Oxford. Numbers 57-62 denote the mass ion beams. Numbers 0-11 represent the different Faraday detector (DVM). The grey and blue bars represent the placement of the detectors used in normal and adapted settings, respectively. The numbers of spacing reveal the distance between each detector, the distance between numbers is the same. IC denotes for ion counter. The numbers in red represent the axial detector.

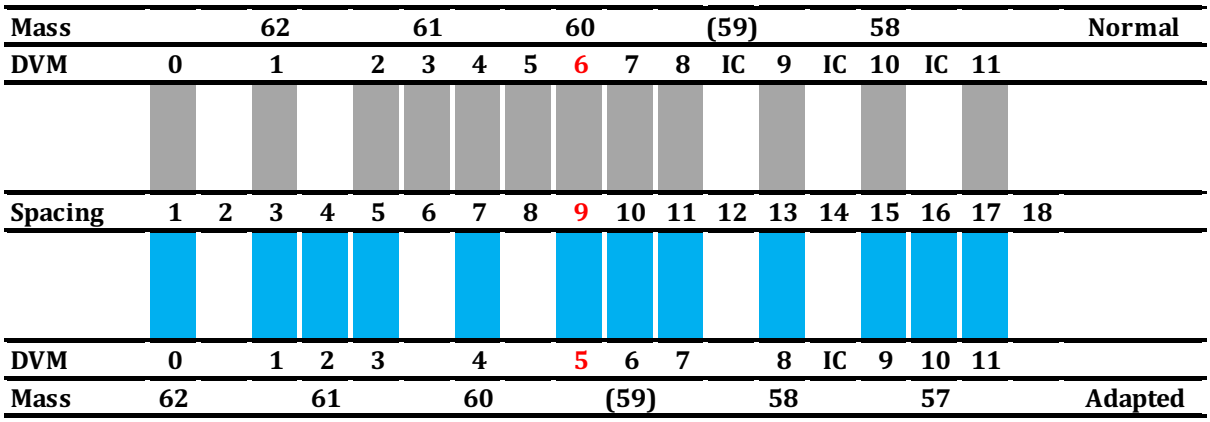


Table A.8. Typical instrumental settings for Ni isotope analysis on Nu Plasma-HR MC-ICP-MS

Parameter	Setting
RF power	1300W
Acceleration voltage	5.85kV
Sampler cone	Ni, 1.0mmØ (Nu Instruments)
Skimmer cone	Ni, 0.7mmØ (Nu Instruments)
Desolvator	Aridus II
Nebulizer	ESI, PFA, 50µLmin^{-1}
Ar gas flow rate_Coolant	13 Lmin^{-1}
Ar gas flow rate _Auxiliary	0.9 Lmin^{-1}
Ar gas flow rate _Nebulizer	20-29 Lmin^{-1}
Sample uptake time	50s
Cycle integration time	10s
Number of cycles per analysis	40
Wash time	300s

A.6.4.6 Introduction of Normalized Argon Index (NAI)

Ni isotopes have been measured by multi-collector thermal ionization mass spectrometry (MC-TIMS) (e.g., Chen et al., 2009) and MC-ICP-MS (e.g., Cameron et al., 2009; Gall et al., 2012; Cameron and Vance, 2014; Porter et al., 2014; Ratié et al., 2015; Ventura et al., 2015; Wasylenki et al., 2015; Vance et al., 2016; Takano et al., 2017; Ciscato et al., 2018; Wang R-M et al., 2019; Wang S-J et al., 2019; Little et al., 2020; Saunders et al., 2020; Gueguen and Rouxel, 2021; Takano et al., 2021). One of the advantages of using MC-ICP-MS is the high temperature of plasma which allows the high ionization efficiency and rapid sample throughput. However, one major concern coming along with MC-ICP-MS is the larger instrumental mass fractionation (IMF) (percent level) than the IMF observed in MC-TIMS (per mil level) (Albarède et al., 2015).

Although the causes of IMF are not fully understood yet, one of the mechanisms has been identified and suggested to cause the IMF is the "space charge effect" (Albarède and Beard, 2004). This effect can result in ions with lower kinetic energy (lower mass to charge ratio) to be more strongly repulsed from the positively charge ion beam than the heavier ions. This preferential loss of lighter ions happens in the interfaces and/or the expansion chamber. The different transmission efficiencies for ions with different mass-to-charge ratio and the non-uniform response across the mass interval result in the preferential transmission of the heavier isotope into the mass spectrometer (Heumann et al., 1998). Maréchal et al. (1999) have suggested that IMF can also originate from the condition of plasma itself. Subtle changes in pumping rate, argon flow rate and plasma temperature supporting the plasma next to the sampler cone where fractionation happens can also influence the result of mass fractionation (Maréchal et al., 1999).

For the induced IMF, a suitable correction method is required and crucial to obtain precise and accurate isotopic compositions on MC-ICP-MS. Three principal techniques, i.e., standard-sample bracketing, internal standard normalization and double-spiking, have been suggested for the correction of IMF induced on MC-ICP-MS (Albarède and Beard, 2004). Standard-sample bracketing and double-spiking have been widely used to correct IMF for Ni isotope analysis on MC-ICP-MS (e.g., Cameron et al., 2009; Gall et al., 2012).

During the IMF correction, non-spectral matrix effect has been observed to influence the precision and accuracy of the correction since the matrix elements in the sample can change the efficiency of ionization and the transmission of analyte element (Yu et al., 2020 and references therein). Although few studies have tried to investigate about non-spectral matrix effect in elemental concentration measurement and specific isotope systems (e.g., Ba isotopes: Yu et al., 2020; Fe isotopes: Kehm et al., 2003; Ag isotopes: Carlson and Hauri, 2001), the connection between IMF and non-spectral matrix effect remains poorly understood (Albarède and Beard, 2004 and references therein; Barling and Weis, 2008; Fietzke and Frische, 2016; Yu et al., 2020).

Albarède and Beard (2004) reviewed the matrix effect observed with both spectral (isobaric) and non-spectral types. Kehm et al. (2003) reported that the IMF can vary with the concentration of analyte Fe in the same sample for Fe isotope analysis, which can be easily solved by controlling the concentration of samples and standards or applying a correction based on a working curve with IMF ($\delta^{56}Fe$) versus intensity (volts of ^{56}Fe). The magnitude and direction of IMFs are variable on different days of measurement with the same matrix element setting, which is attributed to the daily difference of nebulizer gas

flow rates (Kehm et al., 2003). Similar magnitude of isotope offsets has also been observed in Ag isotope system which has 0.3‰ difference in $^{109}Ag/^{107}Ag$ ratio between purified and non-purified pure Ag standard solution (Carlson and Hauri, 2001). As the shift can be the result of non-spectral matrix effect associated with the impurity in the standard solution and/or the fractionation caused by ion exchange process, Carlson and Hauri (2001) did not come to a solid conclusion and implied the difficulty of building connection between IMF and non-spectral matrix effect.

It has been commonly reported that non-spectral matrix effect can lead to inaccurate but highly precise isotope measurement (Carlson and Hauri, 2001; Kehm et al., 2003; Albarède and Beard, 2004; Barling and Weis, 2008; Fietzke and Frische, 2016; Yu et al., 2020). Thus, it is important to develop a quantitative method to address non-spectral matrix effect and sustain a comparable mass-spectrometric condition for measurements at different time and settings. The induced coupled plasma is a flexible and variable ion source, a combination of different adjustable instrumental parameters (e.g., RF power, cone geometry, introduction system, gas flow rate). The thermal condition resulted from the combination of settings would have an impact on the plasma at the region where it is sampled for subsequent mass spectrometry (Fietzke and Frische, 2016). Fietzke and Frische (2016) introduced the normalized argon index (NAI) as a quantitative way to evaluate the thermal condition of plasma (Equation A.7).

$$NAI = 2 \times {}^{38}Ar^{+}/{}^{40}Ar_2^{+} \quad \text{(Equation A.7)}$$

The intensities of both $^{38}Ar^{+}$ and $^{40}Ar_2^{+}$ are dependent on the plasma temperature. However, the density of plasma particles decreases with increasing plasma temperature,

which influences the intensity of both $^{38}Ar^{+}$ and $^{40}Ar_2^{+}$ ions. On the other hand, the abundance of $^{40}Ar_2^{+}$ dimer ions decreases with the increase of plasma temperature as its Ar-Ar bond is more easily broken up with higher temperature (higher energy). Thus, normalizing the intensity of $^{38}Ar^{+}$ to $^{40}Ar_2^{+}$ not only minimize the plasma density effect induced by plasma temperature but also increase the sensitivity of the index to plasma temperature. In brief, the NAI is an indicator of actual thermal condition of plasma at the site sampled for mass-spectrometric analysis regardless of what instrumental settings have been used to achieve this state. Importantly, the NAI also makes it possible to compare the plasma condition from one instrument to the other and quantitatively study the behavior of the IMF induced by non-spectral matrix effect under different plasma conditions coupled with a range of NAIs.

By using the NAI, Fietzke and Frische (2016) found that the volatile/refractory behavior of elements dominates under cool plasma condition (low NAI) and gradually vanishes towards hot plasma condition (high NAI). Under relatively hot plasma condition, a robust and matrix-tolerance environment for isotope analysis seemed to be possibly achieved (Fietzke and Frische, 2016). Later, Yu et al. (2020) applied it on Ba isotope measurement and showed that the matrix effect can be significantly reduced by increasing the NAI. It has also been suggested that this NAI can potentially be applied on other stable isotope systems which have similar non-spectral matrix effects on MC-ICP-MS (Yu et al., 2020).

Thus far, there is no related studies investigating the non-spectral matrix effect on Ni isotopes. Although purification techniques are usually applied prior to isotope analysis, it is still difficult to get quantitative separation of Ni in the situations when trace amount of Ni is accompanied with other abundant elements in biological and geological samples.

A.6.4.7 Application of NAI on Ni isotopic analysis

In this study, the instrumental parts (i.e., cone geometry, introduction system) and the RF power were kept the same through the NAI test. A range of NAI was set by adjusting the Ar flow rate and the rest adjustable parameters (i.e., torch positions, ion lens and nebulizer flow rate). In each set NAI, the Ar flow rate was fixed at value. Then the torch positions (x, y, z), ion lens and nebulizer flow rate were tuned for several cycles separately to optimize the sensitivity of Ni. Finally, the alignment and shape of peaks were examined and optimized.

The relationship between NAIs and set Ar flow rates is shown in Figure A.4. It suggests a clear trend that NAI increases with decreasing Ar flow rate. The relationships between these two parameters based on two attempts agree well with each other. The nebulizer flow rates applied to optimize the sensitivity of Ni also have impacts on the NAI (Figure A.5). In the tests shown in Figure A.5, the nebulizer flow rate was initially set at 21 L/min. A clear trend suggests that the NAI increased when Ar sweep gas flow rate decreased. Later, when the nebulizer flow rate was tuned higher to optimize the sensitivity of Ni, the NAI decreased. The increased nebulizer flow rate seemed to compensate the increased NAI to some extent, but the tuning was useful to compensate the sensitivity lost during the decrease of Ar flow rate.

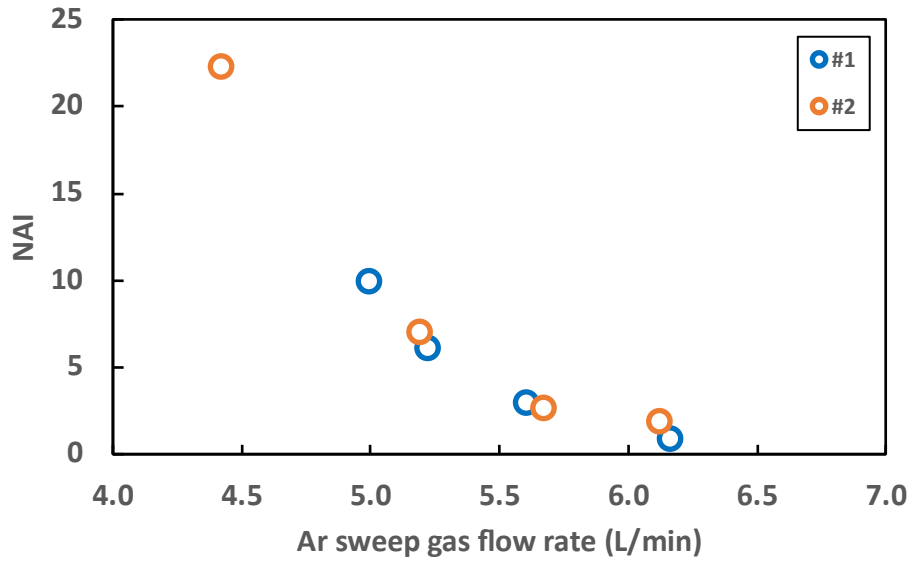


Figure A.4. Relationship between Ar sweep gas flow rate and normalized argon index (NAI) with duplication. Numbers with different colors represent different time of measurement.

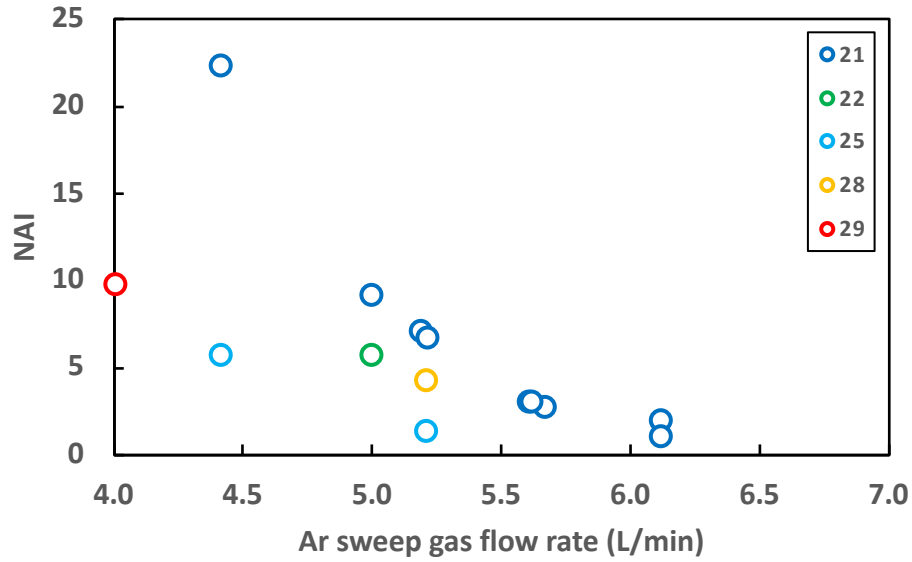


Figure A.5. NAI vs. Ar sweep gas flow rate with different nebulizer Ar gas flow rates. Numbers represent the adjusted nebulizer Ar gas flow rates (L/min).

The sensitivities of ^{58}Ni under different set NAIs for six separate runs are shown in Figure A.6. These six runs were finished separately in roughly seven months. A decreasing trend of ^{58}Ni sensitivity along with increasing NAI is observed in run #1, #2, #3 and #5. While

an increasing trend of ^{58}Ni sensitivity along with increasing NAI is observed in run #4 and #6. It suggests that the daily condition of instrument and the cleanliness of cones and introduction system may also play important roles in controlling the relationship between Ni sensitivity and NAI.

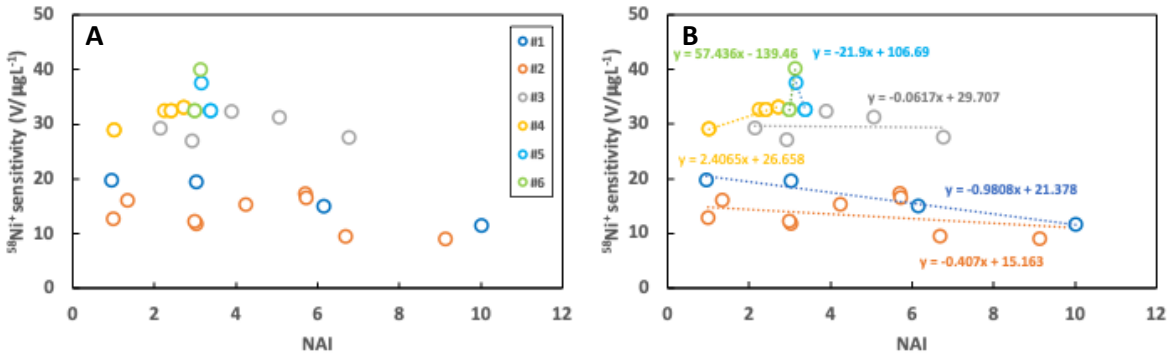


Figure A.6. Analytical sensitivity of ^{58}Ni$^+$ under different NAIs after sensitivity optimization. (A) data only; (B) with slope equations. Numbers with different colors represent different times of measurement.

Standards SRM986, Kam (Ni sulfide, in-house) and Nod-P-1 were used to test the Ni isotope compositions measured under different NAIs (Figure A.7). These standards were measured along with the samples in each individual analysis. The Ni isotope compositions of SRM986 under varying NAIs are all within the long-term average δ^{60}Ni = 0.00±0.05‰ (2SD, n=17). The measured δ^{60}Ni values of Kam fall within the long-term average -0.88±0.06‰ (2SD, n=43) when the NAI is lower than ~9, while a significant drop of δ^{60}Ni (~1‰) can be observed when the NAI increases to ~10. For Nod-P-1, a general decreasing trend of δ^{60}Ni can be observed with the increasing NAI in six separate runs. It suggests that δ^{60}Ni of Nod-P-1 agrees well with published values when NAI is in

a range from 2 to 7. It also indicates that the sweet spot of NAI can shift under different instrument conditions on different days but the range of 2~7 works for Nod-P-1. This range also works for standards SRM986 and Kam.

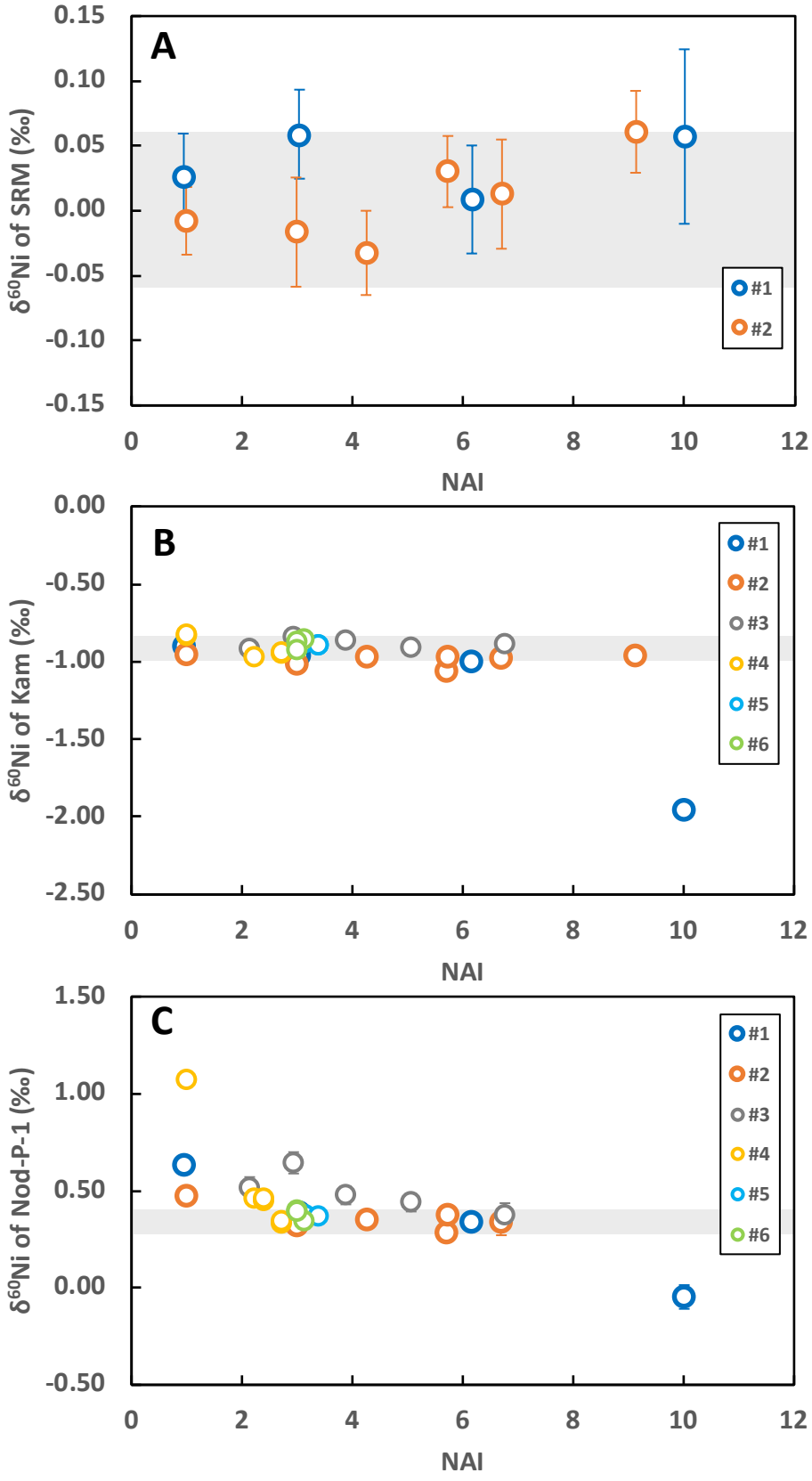


Figure A.7. Ni isotope measurement of standards (A) SRM986, (B) Kambalda (Kam, in-house) and (C) Nod-P-1 under different NAIs for the test of non-spectral matrix effect. The grey shaded areas represent the long-term averaged values, δ^{60}Ni =

0.00±0.05‰ (2SD, n=17) for SRM986; δ^{60}Ni = -0.88±0.06‰ (2SD, n=43) for Kam; δ^{60}Ni = 0.37±0.07‰ (2SD, n=36) for Nod-P-1.

The increasing δ^{60}Ni of Nod-P-1 suggests that either more signal at mass 60 or less signal at mass 58 is detected under lower plasma temperature. This increase was not observed during the measurement of SRM986 and Kam. Referring to Table A.4 shown in section A.5.2, it suggests the processed solution of Nod-P-1 may have more K and Si compared with Kam. However, the presence of either K or Si may not increase the signal at mass 60 but at mass 58 as $^{29}SI_2^+$, which disagrees with the observations.

Importantly, NAI provide a way to quantify the plasma condition during isotopic analysis and a potential solution if an unexpected instrumental bias is observed during the measurement.

A.6.4.8 Reproducibility and accuracy of Ni isotope measurement

In order to validate of sample preparation procedure (i.e., sample digestion and Ni extraction) and assess the accuracy and long-term reproducibility of Ni isotopic analysis carried out in this study, various reference materials (SDO-1, SGR-1b, BHVO-2, BIR-1, AGV-2, Nod-P-1, BCR-414 and BCR-273) and two in-house standards (Kam and Sud) were selected, chemically processed and measured their Ni isotope compositions using MC-ICP-MS in this study (Table A.9 and Figure A.8).

Table A.9. Compilation of reproducibility and accuracy of Ni isotope measurement carried out in this study with published values for various reference materials. "2SD" represents two times of standard deviation. "n" represents the repeated time of measurement for the sample.

Standard Name	Type	Reference	δ^{60}Ni (‰)	2SD	n
SDO-1	Shale (Devonian Ohio)	This study	0.59	0.07	27
		Gueguen et al.(2013)	0.59	0.03	5
		Deng et al. (2014)	0.54	0.05	11
		Estrade et al. (2015)	0.54	0.05	11
		Ventura et al. (2015)	0.58	0.08	–
		Wu et al. (2019)	0.61	0.06	3
SGR-1b	Shale (Green River)	This study	0.46	0.06	5
		Wu et al. (2019)	0.54	0.06	5
BHVO-2	Basalt (Hawaii)	This study	0.02	0.05	3
		Cameron et al. (2009)	0.13	0.03	–
		Gueguen et al.(2013)	0.006	0.041	11
		Deng et al. (2014)	-0.01	0.05	11
		Chernonozhkin et al. (2015)	0.083	0.019	5
		Ratié et al. (2016)	0.05	0.11	–
		Wu et al. (2019)	0.03	0.06	6
		Pašava et al. (2019)	0.015	0.05	5
		Saunders et al. (2020)	0.026	0.059	36
BIR-1	Basalt (Iceland)	This study	0.14	0.04	3
		Gueguen et al.(2013)	0.12	0.035	3
AGV-2	Andesite	This study	0.04	0.07	20
		Wu et al. (2019)	0.02	0.01	3
Nod-P-1	Mn nodule (Pacific)	This study	0.37	0.07	36
		Gueguen et al.(2013)	0.358	0.069	8
		Gueguen et al.(2016)	0.34	0.04	–
		Ratié et al. (2016)	0.39	0.05	–
		Gueguen et al.(2018)	0.328	0.044	4
		Wu et al. (2019)	0.33	0.05	7
BCR-414	Phytoplankton	This study	0.12	0.05	4
		Yang et al. (2020)	0.07	0.06	3
		Takano et al. (2020)	0.11	0.06	10
BCR-273	Single cell	This study	0.17	0.27	3
Kam	Ni sulfide (in-house)	This study	-0.88	0.06	43
Sud	Ni sulfide (in-house)	This study	0.79	0.06	43

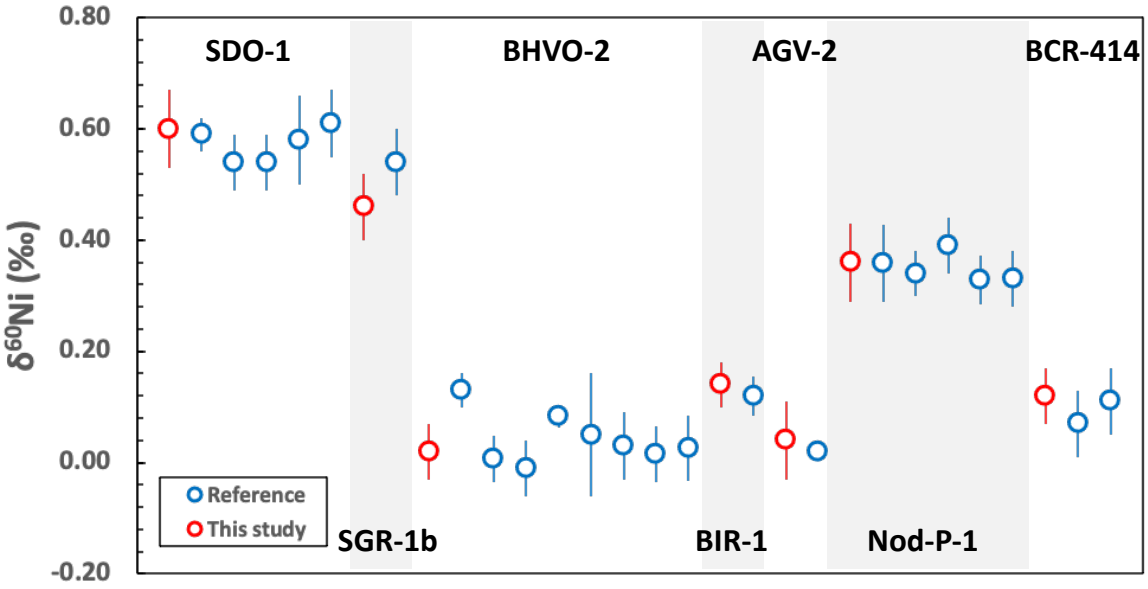


Figure A.8. Comparison of Ni isotope composition for various reference materials between measurements in this study and previously reported values. The error bars represent the 2SD of all measurements done for the sample. The red data points stand for the measurements in this study and the blue data points stand for previously published values.

The average Ni isotope compositions of all standards are all within error of the published values. The reproducibility for each standard is also comparable to previous works. These suggest the chemical procedure and isotopic analysis applied in this study are reliable and robust for various sample types (e.g., shale, basalt, andesite, Mn nodule, phytoplankton, single cell).

The first Ni isotope composition data for single cell standard BCR-273 is reported in this study, though the analytical error is slightly higher than others. It potentially suggests the heterogeneity of the standard itself as the 2SD for other standards are all within the range of 0.04-0.07‰.

For long-term reproducibility, Nod-P-1, Kam and Sud were mainly chosen to be the monitoring standards as they were either easy to acquire or had higher Ni content per unit weight. The long-term monitored δ^{60}Ni values for Kam, Sud and Nod-P-1 are -0.88 ± 0.06‰ (n=43), 0.79 ± 0.06‰ (n=43) and 0.37 ± 0.07‰ (n=36), respectively and shown in Figure A.9. This suggests that the long-term reproducibility in this study is comparable with other studies.

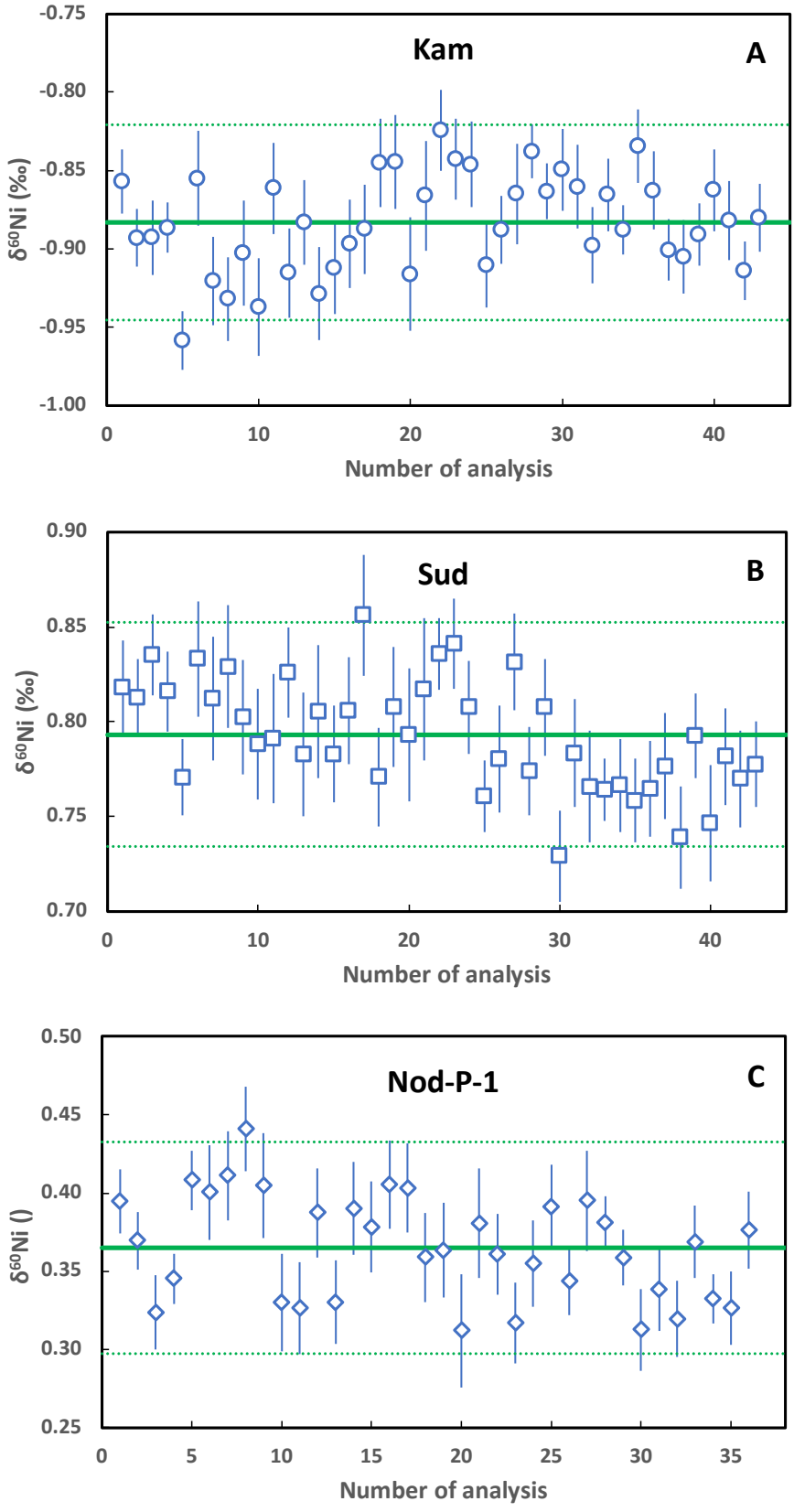


Figure A.9. Long-term instrumental reproducibility monitored by repeatedly measuring in-house sulfide standards (Kam and Sud, (A and B)) and USGS Mn-nodule standard Nod-P-1 I during each run for over 30 months. The error bars of

data points represent the internal errors (2SE) of the individual measurement. The solid green lines represent the long-term average of the standard for repeated measurements and the dotted green lines represent the external errors (2SD) of the standard for repeated measurements. The long-term monitored δ^{60}Ni values for Kam, Sud and Nod-P-1 are -0.88 ± 0.06‰ (n=43), 0.79 ± 0.06‰ (n=43) and 0.37 ± 0.07‰ (n=36), respectively.

A.7 Reference

Aharchaou, I., Rosabal, M., Liu, F., Battaglia, E., Vignati, D.A., Fortin, C., 2017. Bioaccumulation and subcellular partitioning of Cr (III) and Cr (VI) in the freshwater green alga Chlamydomonas reinhardtii. Aquat. Toxicol. 182, 49–57.

Albarède, F., 2015. Metal stable isotopes in the human body: a tribute of geochemistry to medicine. Elements 11, 265-269.

Albarède, F., Beard, B., 2004. Analytical methods for non-traditional isotopes. Rev. Mineral. Geochem. 55, 113–152.

Albarède, F., Telouk, P., Blichert-Toft, J., Boyet, M., Agranier, A., Nelson, B., 2004. Precise and accurate isotopic measurements using multiple-collector ICPMS. Geochim. Cosmochim. Acta 68, 2725-2744.

Andrén, H., Rodushkin, I., Stenberg, A., Malinovsky, D., Baxter, D.C., 2004. Sources of mass bias and isotope ratio variation in multi-collector ICP-MS: optimization of instrumental parameters based on experimental observations. J. Anal. At. Spectrom. 19, 1217–1224.

Balcaen, L., Moens, L., Vanhaecke, F., 2010. Determination of isotope ratios of metals (and metalloids) by means of inductively coupled plasma-mass spectrometry for provenancing purposes — A review. Spectrochim. Acta, Part B 65, 769–786.

Barling, J., Weis, D., 2008. Influence of non-spectral matrix effects on the accuracy of Pb isotope ratio measurement by MC-ICP-MS: implications for the external normalization method of instrumental mass bias correction. J. Anal. At. Spectrom. 23, 1017–1025.

Becker, J., 2007. Inorganic mass spectrometry: principles and applications, Wiley.

Beunon, H., Chernonozhkin, S.M., Mattielli, N., Goderis, S., Doucet, L., Debaille, V., Vanhaecke, F., 2020. Innovative two-step isolation of Ni prior to stable isotope ratio measurements by MC-ICP-MS: application to igneous geological reference materials. J. Anal. At. Spectrom. 35, 2213-2223.

Birck, J.L., Lugmair, G.W., 1988. Nickel and chromium isotopes in Allende inclusions. Earth Planet. Sci. Lett. 90, 131–143.

Bizzarro, M., Ulfbeck, D., Thrane, K., 2006. Nickel isotopes in meteorites: evidence for live ^{60}Fe and distinct ^{62}Ni isotope reservoirs in the early solar system. Lunar Planet. Sci. XXXVII 37.

Carlson, R.W., Hauri, E.H., 2001. Extending the ^{107}Pd-^{107}Ag chronometer to low Pd/Ag meteorites with multicollector plasma-ionization mass spectrometry. Geochim. Cosmochim. Acta 65, 1839-1848.

Cameron, V., Vance, D., 2014. Heavy nickel isotope compositions in rivers and the oceans. Geochim. Cosmochim. Acta 128, 195–211.

Cameron, V., Vance, D., Archer, C., House, C.H., 2009. A biomarker based on the stable isotopes of nickel. Proc. Natl. Acad. Sci. USA 106, 10944–10948.

Chen, J., Papanastassiou, D., Wasserburg, G., 2009. A search for nickel isotopic anomalies in iron meteorites and chondrites. Geochim. Cosmochim. Acta 73, 1461–1471.

Chernonozhkin, S.M., Goderis, S., Lobo, L., Claeys, P., Vanhaecke, F., 2015. Development of an isolation procedure and MC-ICP-MS measurement protocol for the study of stable isotope ratio variations of nickel. J. Anal. At. Spectrom. 30, 1518-1530.

Ciscato, E.R., Bontognali, T.R.R., Vance, D., 2018. Nickel and its isotopes in organic-rich sediments: implications for oceanic budgets and a potential record of ancient seawater. Earth Planet. Sci. Lett. 494, 239–250.

Cook, D.L., Wadhwa, M., Janney, P.E., Dauphas, N., Clayton, R.N., Davis, A.M., 2006. High precision measurements of non-mass-dependent effects in nickel isotopes in meteoritic metal via multicollector ICPMS. Anal. Chem. 78, 8477–84.

Cullen, J.T., Sherrell, R.M., 1999. Techniques for determination of trace metals in small samples of size-fractionated particulate matter: Phytoplankton metals off central California, Mar. Chem. 67, 233-247.

Cutter, G., Casciotti, K., Croot, P., Geibert, W., Heimbürger, L.-E., Lohan, M., Planquette, H., van de Flierdt, T., 2017. Sampling and Sample-handling Protocols for GEOTRACES Cruises. Version 3, August 2017. Toulouse, France, GEOTRACES International Project Office, 139pp. & Appendices.

Dodson, M.H., 1970. Simplified equations for double-spiked isotopic analyses. Geochim. Cosmochim. Acta 34, 1241–1244.

Faure, G., Mensing, T., 2005 Isotopes: principles and applications, Wiley, New York, 3rd edn.

Fietzke, J., Frische, M., 2016. Experimental evaluation of elemental behavior during LA-ICP-MS: influences of plasma conditions and limits of plasma robustness. J. Anal. At. Spectrom. 31, 234–244.

Galer, S.J.G., 1999. Optimal double and triple spiking for high precision lead isotopic measurement. Chem. Geol. 157, 255–274.

Gall, L., 2011. Development and application of nickel stable isotopes as a new geochemical tracer. PhD thesis. University Of Oxford.

Gall L., Williams, H., Siebert, C., Halliday, A., 2012. Determination of mass-dependent variations in nickel isotope compositions using double spiking and MC-ICPMS. J. Anal. At. Spectrometry 27, 137.

Gillson, G.R., Douglas, D.J., Fulford, J.E., Halligan, K.W., Tanner, S.D., 1988. Nonspectroscopic interelement interferences in inductively coupled plasma mass spectrometry. Anal. Chem. 60, 1472–1474.

Gramlich, J.W., Machlan, L.A., Barnes, I.L., Paulsen, P.J., 1989. Absolute isotopic abundance ratios and atomic weight of a reference sample of nickel. J. Res. Natl. Inst. Stand. Technol. 94, 347–356.

Gueguen, B., Rouxel, O., 2021. The Nickel isotope composition of the authigenic sink and the diagenetic flux in modern oceans. Chem. Geol. 563, 120050.

Guinoiseau, D., Galer, S.J.G., Abouchami, W., 2018. Effect of cadmium sulphide pre-282apitation on the partitioning of Cd isotopes: implications for the oceanic Cd cycle. Earth Planet. Sci. Lett. 498, 300–308.

Halliday, A.N., Christensen, J.N., Lee, D.C., Hall, C.M., Luo, X., Rehkämper, M., 2000. Multiple-collector inductively coupled plasma mass spectrometry. Inorganic Mass Spectrometry – Fundamentals and Applications, Marcel Dekker, New York, ch. 8, 291–371.

Hart, S.R., Zindler, A., 1989. Isotope fractionation laws: a test using calcium. Int. J. Mass Spectrom. Ion Processes 89, 287–301.

Heumann, K.G., Gallus, S.M., Radlinger, G., Vogl, J., 1998. Precision and accuracy in isotope ratio measurements by plasma source mass spectrometry. J. Anal. At. Spectrom. 13, 1001–1008.

Hoefs, J., 2004. Stable isotope geochemistry, Springer-Verlag Berlin Heidelbery, New York.

Johnson, C.M., Beard, B.L., 1999. Correction of instrumentally produced mass fractionation during isotopic analysis of Fe by thermal ionization mass spectrometry. Int. J. Mass Spec. 193, 87–99.

Johnson, C.M., Beard, B.L., Albarède, F., 2004. Overview and general concepts. Rev. Mineral. Geochem. 55, 1–24.

Kasemann, S.A., Jeffcoate, A.B., Elliott, T., 2005. Lithium isotope composition of basalt glass reference material. Anal. Chem. 77, 5251–5257.

Kehm, K., Hauri, E.H., Alexander, C.M.O'D., Carlson, R.W., 2003. High precision iron isotope measurements of meteoritic material by cold plasma ICP-MS. Geochim. Cosmochim. Acta 67, 2879-2891.

Laeter, J.D., 1998. Mass spectrometry and geochronology. Mass Spectrom. Rev.17, 97–125.

Little, S.H., Archer, C., McManus, J., Najorka, J., Wegorzewski, A.V., Vance, D., 2020. Towards balancing the oceanic Ni budget. Earth Planet. Sci. Lett. 547, 116461.

Maréchal, C.N., Telouk, P., Albarède, F., 1999. Precise analysis of copper and zinc isotopic compositions by plasma-source mass spectrometry. Chem. Geol. 156, 251–273.

May, T.W., Wiedmeyer, R.H., 1998. A table of polyatomic interferences in ICP-MS. At. Spectrosc. 19, 150-155.

Mellon, F.A., Sandström, B., 1996. Stable isotopes in human nutrition. London: Academic Press.

Millot, R., Guerrot, C., Vigier, N., 2004. Accurate and high precision measurement of lithium isotopes in two reference materials by MC-ICP-MS. Geostand. Geoanal. Res. 28, 153–159.

Morand, P., Allègre, C.J., 1983. Nickel isotopic studies in meteorites. Earth Planet. Sci. Lett. 63, 167–176.

Morel, F. M. M., Rueter, J. G., Anderson, D. M., Guillard, R. R. L., 1979. Aquil: a chemically defined phytoplankton culture medium for trace metal studies. J. Phycol. 15, 135-141.

Nicholls, D., 1974. Complexes and First Row Transition Elements. Macmillan, London.

Ohnemus, D.C., Auro, M.E., Sherrell, R.M., Lagerstrom, M., Morton, P.L., Twining, B.S., Rauschenberg, S., Lam, P.J., 2014. Laboratory intercomparison of marine particulate digestions including Piranha: a novel chemical method for dissolution of polyethersulfone filters. Limnol. Oceanogra., Methods 12, 530-547.

Planquette, H., Sherrell, R.M., 2012. Sampling for particulate trace element determination using water sampling bottles: methodology and comparison to in situ pumps. Limnol. Oceanogr., Methods, 10, 367-388.

Platzner, I.T., 1997. Modern isotope ratio mass spectrometry. Chichester: Wiley.

Porter, S.J., Selby, D., Cameron, V., 2014. Characterising the nickel isotopic composition of organic-rich marine sediments. Chem. Geol. 387, 12-21.

Price, N.M., Harrison, G.I., Hering, J.G., Hudson, R.J., Nirel, P.M.V., Palenik, B., Morel, F. M.M., 1989. Preparation and chemistry of the artificial algal culture medium Aquil. Biol. Oceanogr. 6, 443-61.

Quitté, G., Meier, M., Latkoczy, C., Halliday, A.N., Günther, D., Gunther, D., Günther, D., Gunther, D., Günther, D., 2006. Nickel isotopes in iron meteorites–nucleosynthetic anomalies in sulfides with no effects in metals and no trace of ^{60}Fe. Earth Planet. Sci. Lett. 242, 16–25.

Quitté, G., Oberli, F., 2006. Quantitative extraction and high precision isotope measurements of nickel by MC-ICPMS. J. Anal. At. Spectrom. 21, 1249.

Ratié, G., Jouvin, D., Garnier, J., Rouxel, O., Miska, S., Guimaraes, E., Cruz Vieira, L., Sivry, Y., Zelano, I., Montarges-Pelletier, E., Thil, F., Quantin, C., 2015. Nickel isotope fractionation during tropical weathering of ultramafic rocks. Chem. Geol. 402, 68–76.

Rehkämper, M., Schönbächler, M., Stirling, C., 2001. Multiple collector ICP-MS: introduction to instrumentation, measurement techniques and analytical capabilities. Geostand. Geoanal. Res. 25, 23–40.

Rudge, J., Reynolds, B., Bourdon, B., 2009. The double spike toolbox, Chem. Geol. 265, 420–431.

Russell, W.A., Papanastassiou, D.A., Tombrello, T.A., 1978. Ca isotope fractionation on the Earth and other solar system materials. Geochim. Cosmochim. Acta 42, 1075–1090.

Saunders, N.J., 2018. Nickel stable isotope fractionation in planetary materials. PhD thesis. University Of Oxford.

Saunders, N.J., Barling, J., Harvey, J., Halliday, A.N., 2020. Heterogeneous nickel isotopic compositions in the terrestrial mantle – Part 1: Ultramafic lithologies. Geochim. Cosmochim. Acta 285, 129-149.

Sherrell, R.M., 1991. Collection of suspended oceanic particulate matter for trace metal analysis using a new in-situ pump, in Marine Particles: Analysis and Characterization, Eds. D.C. Hurd and D.W. Spencer, Amer. Geophys. Union, 285-294.

Shimamura, T., Lugmair, G.W., 1983. Ni isotopic compositions in Allende and other meteorites. Earth Planet. Sci. Lett. 63, 177–188.

Shirai, N., Humayun, M., 2011. Mass independent bias in W isotopes in MC-ICP-MS instruments. J. Anal. At. Spectrom. 26, 1414-1420.

Shukolyukov, A., Lugmair, G.W., 1993a. ^{60}Fe in eucrites. Earth Planet. Sci. Lett. 119, 159–166.

Shukolyukov, A., Lugmair, G.W., 1993b. Live Iron-60 in the Early Solar System. Science 259, 1138–1142.

Takano, S., Tanimizu, M., Hirata, T., Shin, K.C., Fukami, Y., Suzuki, K., Sohrin, Y., 2017. A simple and rapid method for isotopic analysis of nickel, copper, and zinc in seawater using chelating extraction and anion exchange. Anal. Chim. Acta 967, 1–11.

Takano, S., Tsuchiya, M., Imai, S., Yamamoto, Y., Fukami, Y., Suzuki, K., Sohrin, Y., 2021. Isotopic analysis of nickel, copper, and zinc in various freshwater samples for source identification. Geochem. J. 55, 171-183.

Tanimizu, M., Hirata, T., 2006. Determination of natural isotopic variation in nickel using inductively coupled plasma mass spectrometry. J. Anal. At. Spectrom. 21, 1423.

Thomas, R., 2003. Practical Guide to ICP-MS: A Tutorial for Beginners (1st ed.). CRC Press.

Vance, D., Little, S.H., Archer, C., Cameron, V., Andersen, M.B., Rijkenberg, M.J.A., Lyons, T.W., 2016. The oceanic budgets of nickel and zinc isotopes: the importance of sulfidic environments as illustrated by the Black Sea. Philos. Trans. R. Soc. A 374, 20150294.

Vanhaecke, F., Balcaen, L., Malinovsky, D., 2009. Use of single-collector and multi-collector ICP-mass spectrometry for isotopic analysis. J. Anal. At. Spectrom. 24, 863-886.

Vanhaecke, F., Moens, L., Dams, R., Papadakis, I., Taylor, P., 1997. Applicability of high-resolution ICP–mass spectrometry for isotope ratio measurement. Anal. Chem. 69, 268-273.

Vanhaecke, F., Moens, L., Dams, R., Allen, L., Georgitis, S., 1999. Evaluation of the isotope ratio performance of an axial time-of-flight ICP mass spectrometer. Anal. Chem. 71, 3297–3303.

Vanhaecke, F., Riondato, J., Moens, L., Dams, R., 1996. Non-spectral interferences encountered with a commercially available high resolution ICP-mass spectrometer. Fresenius J. Anal. Chem. 355, 397–400.

Ventura, G.T., Gall, L., Siebert, C., Prytulak, J., Szatmari, P., Hürlimann, M., Halliday, A.N., 2015. The stable isotope composition of vanadium, nickel, and molybdenum in crude oils. Appl. Geochem. 59, 104–117.

Walder, A.J., Platzner I.T., Freedman, P.A., 1993. Isotope ratio measurement of lead, neodymium and neodymium-samarium mixtures, hafnium and hafnium-lutetium mixtures with a double focusing multiple collector inductively coupled plasma mass spectrometer. J. Anal. At. Spectrom. 8, 19-23.

Wang, R.M., Archer, C., Bowie, A.R., Vance, D., 2019. Zinc and nickel isotopes in seawater from the Indian Sector of the Southern Ocean: the impact of natu- ral iron fertilization versus Southern Ocean hydrography and biogeochemistry. Chem. Geol. 511, 452–464.

Wang, S.J., Rudnick, R.L., Gaschnig, R.M., Wang, H., Wasylenki, L.E., 2019. Methanogenesis sustained by sulfide weathering during the Great Oxidation Event. Nat. Geosci. 12, 296-300.

Wasylenki, L.E., Howe, H.D., Spivak-Birndorf, L.J., Bish, D.L., 2015. Ni isotope fraction-

ation during sorption to ferrihydrite: implications for Ni in banded iron forma- tions. Chem. Geol. 400, 56–64.

Wieser, M.E., Schwieters, J.B., 2005. The development of multiple collector mass spectrometry for isotope ratio measurements. Int. J. Mass Spectrom.242, 97–115.

Wilson, W., Zhang, Q., Rickaby., R.E.M., 2019. Susceptibility of algae to Cr toxicity reveals contrasting metal management strategies. Limnol. Oceanogr. 64, 2271-2282.

Yang, L., 2009. Accurate and precise determination of isotopic ratios by MC-ICP-MS: A review. Mass Spectrom. Rev. 28, 990–1011.

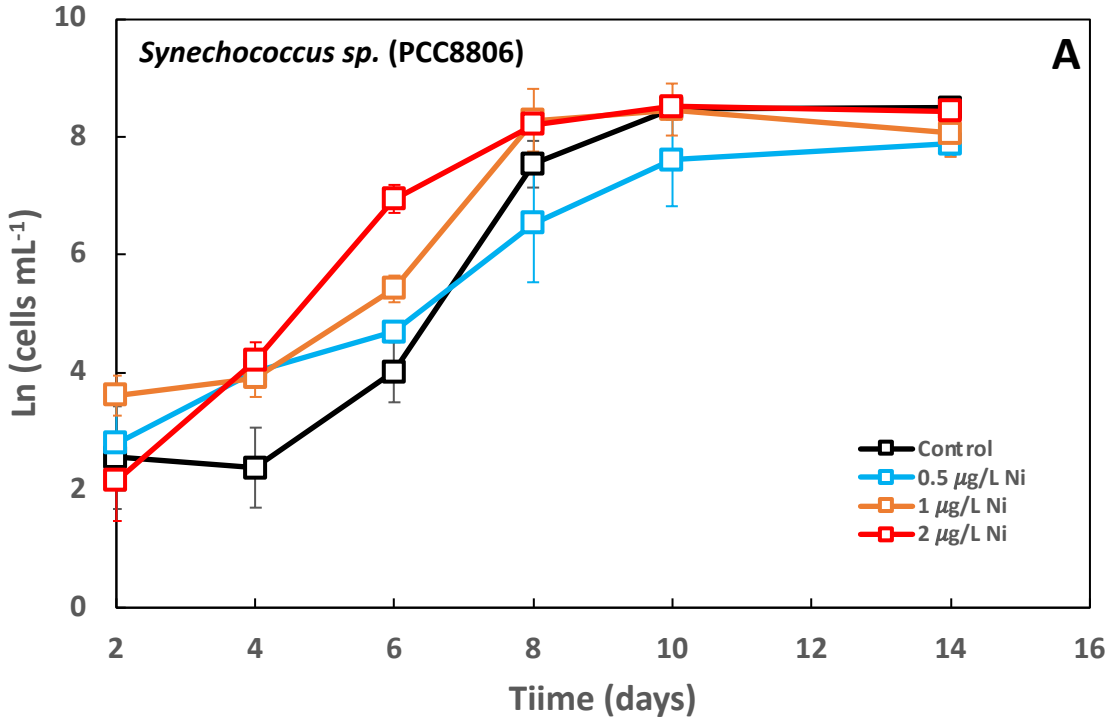
Yang, L., Tong, S., Zhou, L., Hu, Z., Mester, Z., Meija, J., 2018. A critical review on isotopic fractionation correction methods for accurate isotope amount ratio measurements by MC-ICP-MS. J. Anal. At. Spectrom. 33, 1849.

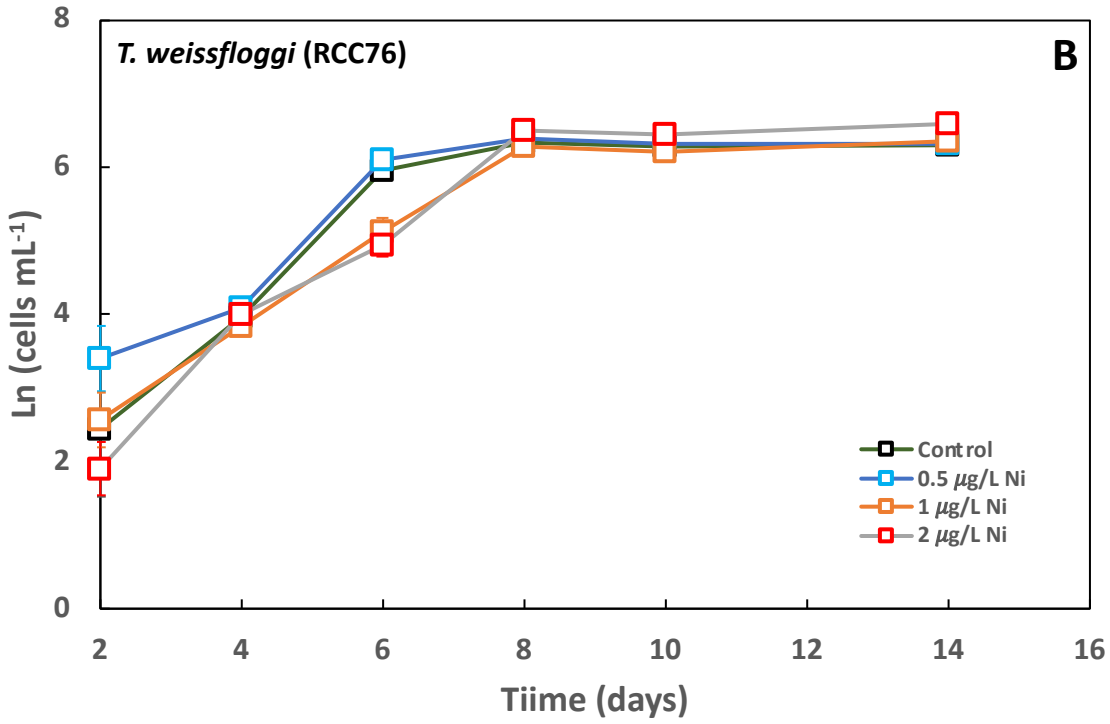
Yu, Y., Siebert, C., Fietzke, J., Goepfert, T., Hathorne, E., Cao, Z., Frank, M., 2020. The impact of MC-ICP-MS plasma conditions on the accuracy and precision of stable isotope measurements evaluated for barium isotopes. Chem. Geol. 549, 119697.

Zhang, Q., Snow, J.T., Holdship, P., Price, D., Watson, P., Rickaby, R.E.M., 2018. Direct measurement of multi-elements in high matrix samples with a flow injection ICP-MS: Application to the extended Emiliania huxleyi Redfield ratio. J. Anal. At. Spectrom. 33, 1196–1208.

Appendix B. Phytoplankton culturing

B.1 Phytoplankton growth rate





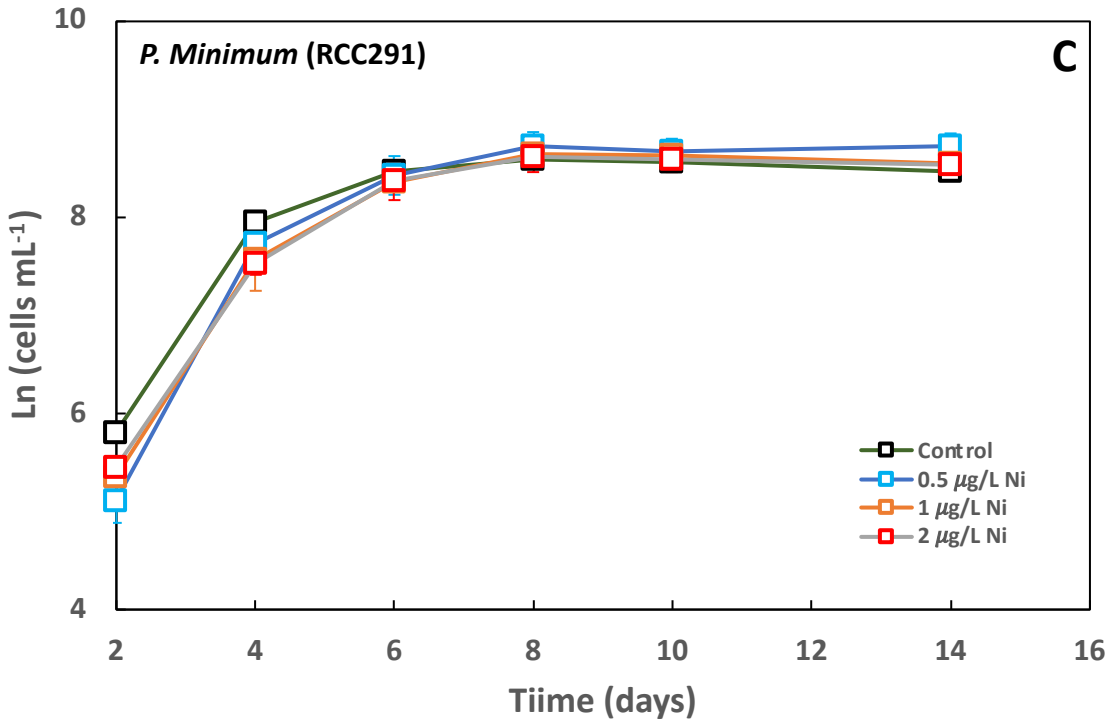
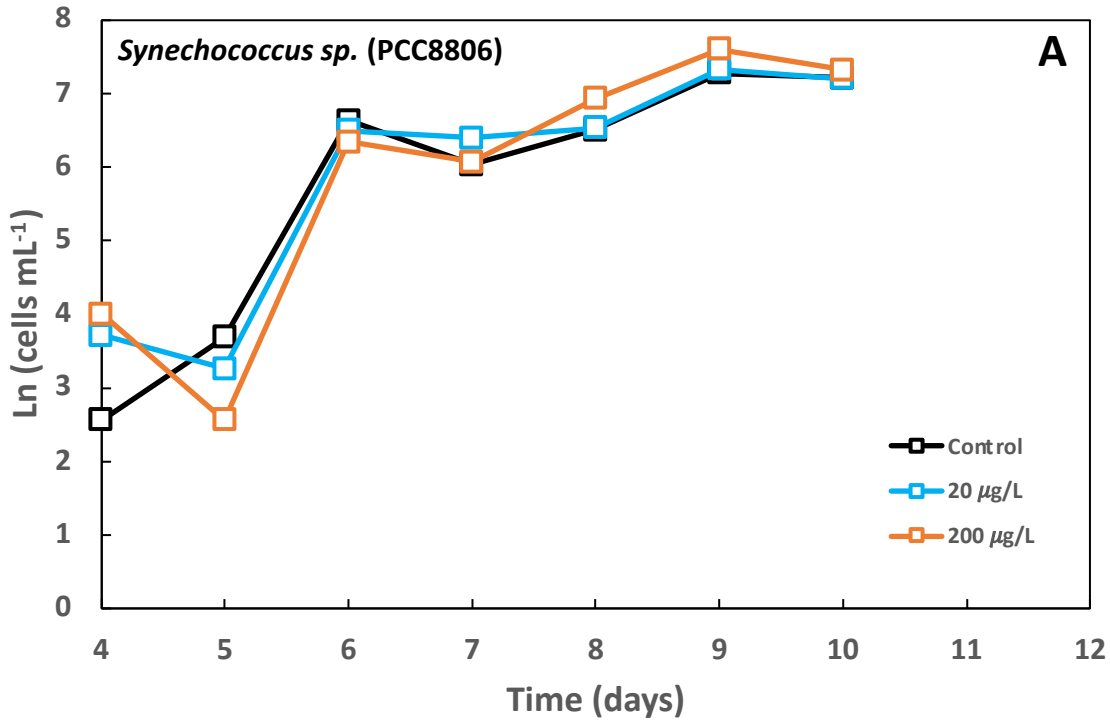


Figure B.1. Growth rates for (A) cyanobacteria Synechococcus sp., (B) diatom T. weissfloggi, and (C) dinoflagellate P. minimum under concentration from 0 to 2 μg/L. The calculation is based on cell number counting.



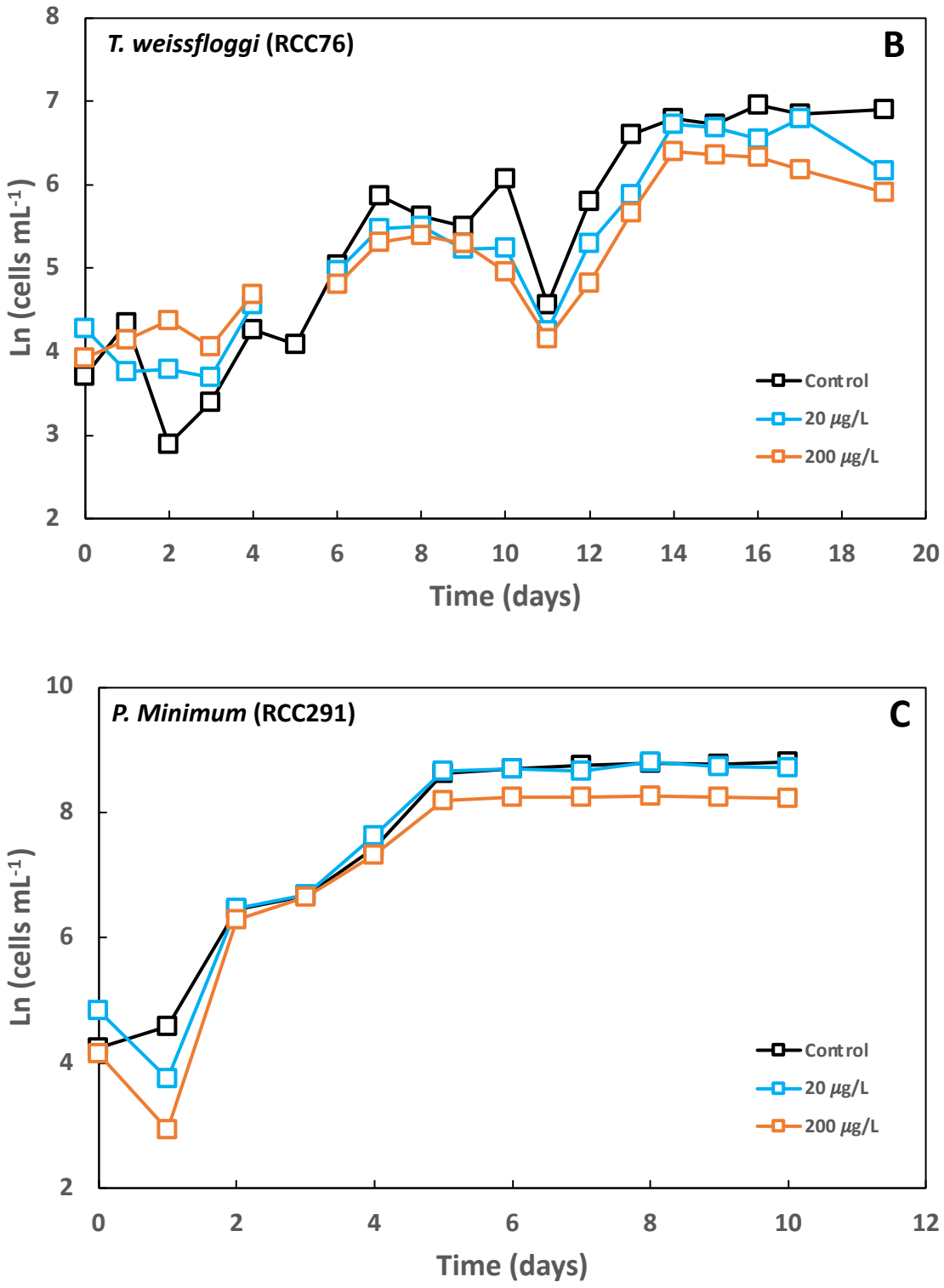


Figure B.2. Growth rates for (A) cyanobacteria Synechococcus sp., (B) diatom T. weissfloggi, and (C) dinoflagellate P. minimum under concentrations of 0, 20 and 200 μg/L. The calculation is based on cell number counting.

Appendix C. Sulfide precipitation experiments

C.1 Ni speciation modelling

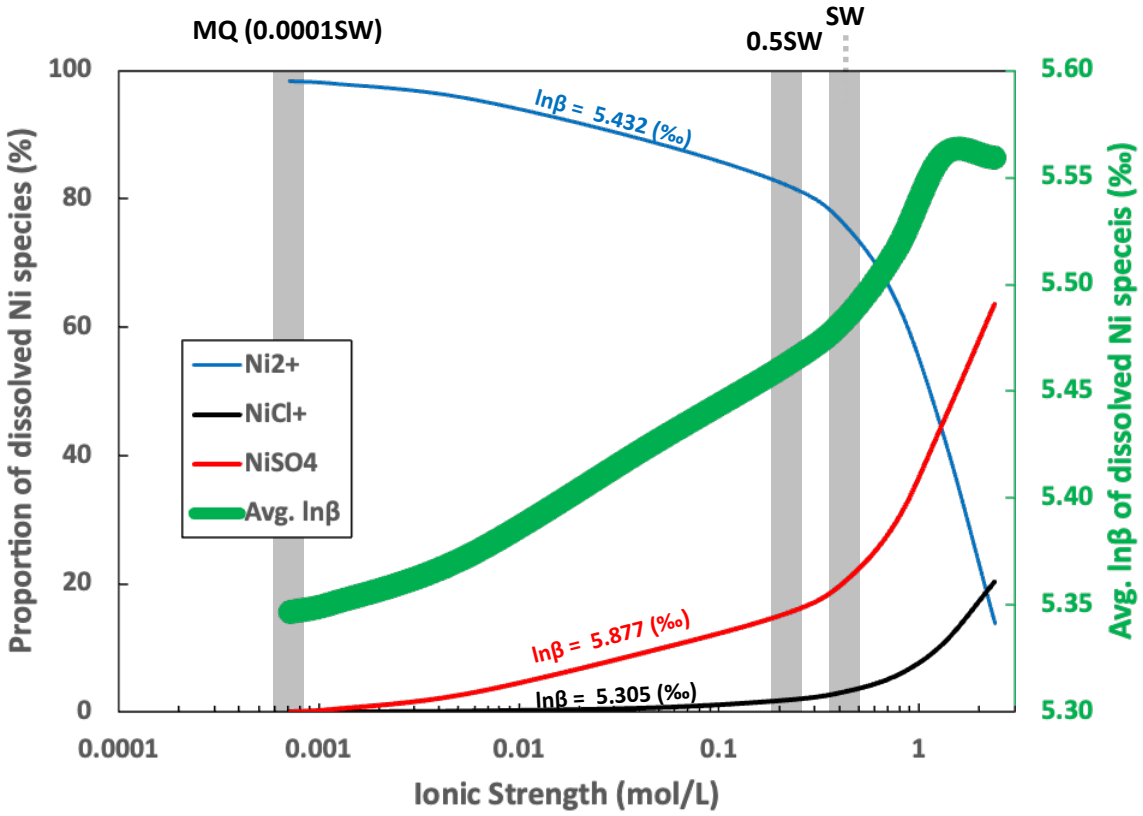


Figure C.1. Proportions of major Ni species and calculated lnβ under varying ionic strengths. Lnβ represents the isotopic enrichment factor for isotope pair $^{60}Ni/^{58}Ni$ at 298K (Fuji et al., 2011).

Appendix D. Namibian samples

D.1. Analytical errors

Table D.1. Analytical results and certified values for river water standard SLRS-6 measured by quadrupole ICP-MS with normal introduction system.

Certified material	Element	Certified value (ng/g)	Measured value (ng/g)	Recovery (%)
SLRS-6	Fe	84.5 ± 3.6	82.896 ± 0.811	98.1
	V	0.352 ± 0.006	0.357 ± 0.012	101.4
	Cr	0.252 ± 0.012	0.249 ± 0.006	99
	Mn	2.12 ± 0.1	2.159 ± 0.036	101.8
	Co	0.053 ± 0.012	0.055 ± 0.001	103.2
	Ni	0.617 ± 0.022	0.603 ± 0.012	97.8
	Cu	24 ± 1.8	24.814 ± 0.366	103.4
	Zn	1.76 ± 0.12	2.17 ± 0.082	123.3
	Ba	14.3 ± 0.48	14.152 ± 0.176	99
	Ca	8770 ± 200	8423.5 ± 355.4	96
	Mo	0.215 ± 0.018	0.198 ± 0.006	92.3
	Cd	0.0063 ± 0.0014	0.011 ± 0.0002	174.2

Table D.2. Analytical results and certified values for seawater standard NASS-7 measured by quadrupole ICP-MS connected with seaFAST preconcentration system.

Ceritified material	Element	Certified value (ng/g)	Measured value (ng/g)	Recovery (%)
NASS-7	Mn	0.74 ± 0.06	0.709 ± 0.010	95.9
	Fe	0.344 ± 0.026	0.438 ± 0.015	127.4
	Co	0.0143 ± 0.0014	0.0168 ± 0.0002	117.3
	Ni	0.243 ± 0.018	0.234 ± 0.002	96.3
	Cu	0.195 ± 0.014	0.206 ± 0.004	105.4
	Zn	0.41 ± 0.08	0.460 ± 0.005	112.3
	Cd	0.0157 ± 0.0016	0.0137 ± 0.0003	87.6

D.2. Particulate data

Table D.3. Elemental concentrations in particulate samples filtered from ~10 m depth seawaters off Namibian margin at stations along transect 20°S and 23°S. The total blank (cassette blank + procedural balnk) and the elemental recovery of digestion method on plankton standard BCR-414 are also provided.

Concentration in the ocean (pM) + blank correction															
Sample ID	**Volume (L)**	**Fe (pM)**	**P (pM)**	**Ti (pM)**	**V (pM)**	**Cr (pM)**	**Mn (pM)**	**Co (pM)**	**Ni (pM)**	**Cu (pM)**	**Zn (pM)**	**Ba (pM)**	**Ca (pM)**	**Mo (pM)**	**Cd (pM)**
20005	3.45	1371	42392	89.1	101	n.a.	45.0	5.68	19.1	19.8	n.a.	41.3	129906	5.44	7.93
20040	8.70	n.a.	19492	n.a.	1.20	n.a.	22.6	4.37	17.4	n.a.	n.a.	28.9	138927	10.8	5.02
20070	4.50	n.a.	54711	n.a.	6.32	n.a.	36.9	11.7	37.7	n.a.	n.a.	43.8	426192	132	7.12
23005	3.15	11022	113405	386	38.0	n.a.	129	15.9	59.2	n.a.	90.2	236	357852	12.0	30.4
23070	2.75	n.a.	82707	n.a.	1.26	n.a.	19.6	12.2	42.3	13.1	n.a.	39.8	516742	12.7	19.6
Cassette blank + procedural blank (ng)															
Sample ID		**Fe (ng)**	**P (ng)**	**Ti (ng)**	**V (ng)**	**Cr (ng)**	**Mn (ng)**	**Co (ng)**	**Ni (ng)**	**Cu (ng)**	**Zn (ng)**	**Ba (ng)**	**Ca (ng)**	**Mo (ng)**	**Cd (ng)**
blank_PES_20005		500	27.1	35.5	0.57	145	8.98	0.18	1.59	14.6	44.0	2.38	2166	0.42	0.29
Recovery of digestion															
Sample ID		**Fe (µg/g)**	**P (µg/g)**	**Ti (µg/g)**	**V (µg/g)**	**Cr (µg/g)**	**Mn (µg/g)**	**Co (µg/g)**	**Ni (µg/g)**	**Cu (µg/g)**	**Zn (µg/g)**	**Ba (µg/g)**	**Ca (µg/g)**	**Mo (µg/g)**	**Cd (µg/g)**
BCR-414		1886	14251	137	8.63	24.9	278	1.4	19.0	27.6	102.5	33	75204	1.62	0.362
Certified (µg/g)					8.1	23.8	299		18.8	29.5	111.6				0.383
Recovery (%)					107	104	93		101	93	92				95

n.a. – the concentration is either under the detection limit or lower than the total blank

D.3. Porewater data

Table D.4. Porewater profiles of trace metals and sulfate in sediment cores collected off Namibian margin along transect 20°S and 23°S. BWO = bottom water oxygen (μmol/kg).

Sample ID	Depth(cm)	Pb (nM)	Cr (nM)	Cu (nM)	Mo (nM)	Ba (nM)	Fe (nM)	V (nM)	Co (nM)	Ni (nM)	Zn (nM)	Cd (nM)	SO_4^{2-} (mM)
Core 20010 (12.858°E, 19.999°S), 91 m water depth, BWO = 14.125 μmol/kg													
20010 3cm	3	0.75	33.3	2.89	11.9	490	104	8.34	5.97	56.0	41.7	0.103	24.3
20010 9cm	9	0.34	27.5	1.86	15.9	650	73.5	7.07	5.18	24.9	34.8	0.032	24.4
20010 14cm	14	0.23	38.7	1.60	32.5	619	65.7	4.19	5.09	14.1	46.1	0.030	24.2
20010 19cm	19	0.17	37.4	3.57	40.7	575	71.7	4.86	5.33	8.63	43.8	0.026	24.3
20010 23.5cm	23.5	0.14	29.4	1.97	43.4	529	63.0	5.94	5.56	7.06	35.3	0.053	24.6
20010 29cm	29	0.15	28.6	2.33	46.7	453	82.9	6.12	5.52	6.02	43.7	0.036	24.2
20010 31cm	31	0.12	37.3	1.85	56.6	430	89.6	6.23	5.57	5.67	30.0	0.055	25.0
Core 20050 (12.148°E, 20.000°S), 277.25m water depth, BWO = 9.387 μmol/kg													
20050 2cm	2	0.31	12.0	8.39	139	121	4897	12.9	0.22	9.02	29.3	0.251	28.4
20050 5.5cm	5.5	0.11	12.1	2.06	124	97.4	6893	2.56	0.08	7.57	65.8	0.080	28.5
20050 8.5cm	8.5	0.19	12.2	3.63	126	91.5	4269	2.04	0.05	5.55	34.8	0.043	28.3
20050 13.5cm	13.5	0.10	10.4	2.00	136	102	1738	1.98	0.03	5.10	64.6	0.039	27.7
20050 17.5cm	17.5	0.13	11.2	2.54	138	92.1	1243						29.0
20050 20.5cm	20.5	0.15	9.28	2.48	133	60.4	138						28.4
20050 25cm	25	0.17	9.59	7.95	166	82.2	550						28.1
Core 23010 (14.226°E, 23.001°S), 102 m water depth, BWO = 2.7 μmol/kg													
23010 1cm	1	0.04	34.8	1.45	31.7	1244	73.4						22.9
23010 3cm	3	0.12	35.4	3.96	29.5	1359	110	99.5	10.9	88.0	23.1	0.305	21.8
23010 5cm	5	0.06	48.7	2.29	26.1	1356	74.3	41.3	12.2	73.4	45.5	0.035	21.1
23010 7cm	7	0.06	48.4	2.11	30.3	1225	93.6						21.2
23010 11cm	11	0.08	53.3	3.34	44.2	1394	109						21.2
23010 17cm	17	0.04	81.1	2.24	41.7	2332	66.7	45.2	12.5	60.2	18.5	0.038	14.6
23010 19cm	19	0.04	84.7	2.43	47.6	2969	64.0						12.4
23010 21cm	21	0.03	106	2.17	61.1	3427	70.5	43.1	10.8	48.8	23.7	0.046	11.0
23010 23cm	23	0.03	117	2.84	69.5	4154	57.2	53.5	10.9	48.3	20.2	0.047	9.52
Core 23030 (13.864°E, 23.000°S), 136.75 m water depth, BWO = 5.262 μmol/kg													
23030 2cm	2	0.15	9.83	3.37	125	95.4	1353	26.9	0.52	9.24	44.2	0.217	28.4
23030 9cm	9	0.06	11.1	2.57	106	115	1294	3.00	0.22	6.53	95.7	0.033	27.8
23030 13cm	13	0.15	10.6	2.76	27.9	89.7	207	2.10	0.17	5.72	90.7	0.008	27.2
23030 19cm	19	0.07	11.5	3.00	12.8	84.9	174	2.05	0.10	3.60	35.5	0.006	28.4
23030 22cm	22	0.05	11.6	2.86	16.8	78.2	197						27.8
23030 29cm	29	0.06	11.1	3.52	26.5	74.6	265						27.7
23030 30cm	30	0.09	13.5	3.48	36.9	83.6	165						28.4
Core 23060 (13.32°E, 23.000°S), 352.5 m water depth, BWO = 67.299 μmol/kg													
23060 2cm	2	0.33	9.90	3.79	109	122	14909	10.7	0.10	11.9	31.5	0.281	28.0
23060 6cm	6	0.25	10.7	2.74	105	121	2505						28.6
23060 9cm	9	0.16	4.74	0.95	37.7	41.6	217						27.1
23060 13cm	13	0.14	8.95	2.40	106	116	164	8.73	-	5.19	68.1	0.020	28.0
23060 17cm	17	0.14	10.4	2.82	127	137	161						27.5
23060 21cm	21	0.17	9.66	3.01	111	112	93.9						28.3
23060 25cm	25	0.12	8.57	2.84	104	113	101						28.2
Mean Ocean (Nozaki, 2001)		0.013	4.039	2.360	104.221	109.228	0.537	39.261	0.020	8.178	5.353	0.623	

D.4. Sediment data

Table D.5. Certified, measured elemental values and elemental recoveries for standard SGR-1b.

Element (µg/g)	Certified value (µg/g)	Measured value (µg/g)						Recovery (%)					
		#1	#2	#3	#4	#5	#6	#1	#2	#3	#4	#5	#6
Fe-56	21192.8	16085	17194	18728	15725	15534	15979	76	81	88	74	73	75
Li-7	147	138	134	145	101	93.7	97.6	94	91	99	69	64	66
Mg-24	26775.1	24782	24200	26141	20341	20427	21329	93	90	98	76	76	80
Na-23	22181.68144				19365	18382	19689				87	83	89
Al-27	34507.6	29593	29062	31149	26333	25903	27865	86	84	90	76	75	81
K-39	13780.5	11436	11225	12080	9950	9848	10233	83	81	88	72	71	74
Ca-43	59891.5	54852	52501	57549				92	88	96			
Ca-44	59891.5				47368	45939	49482				79	77	83
Rb-85		63.2	60.9	65.1	64.0	60.7	63.8						
Sr-88	420	314	305	325	313	299	307	75	73	77	74	71	73
Ba-138	290	239	227	238	238	223	226	82	78	82	82	77	78
Tl-205		1.10	1.08	1.10	0.45	0.44	0.46						
U-238	5.4	5.47	5.30	5.56	4.36	4.17	4.21	101	98	103	81	77	78
Si-28	131818.4	26.8	23.2	25.2									
Ti-48	1516.4	1051	1030	1103	1093	1116	1184	69	68	73	72	74	78
V-51	130	103	100	107	103	99.4	101	79	77	82	79	76	78
Cr-52	30	26.2	25.6	27.3	25.2	23.7	24.4	87	85	91	84	79	81
Mn-55	267	198	195	209	200	190	196	74	73	78	75	71	73
Fe-57	21192.8	15889	15502	16497	15725	15534	15979	75	73	78	74	73	75
Co-59	12	9.69	9.49	10.05	9.62	9.12	9.42	81	79	84	80	76	79
Ni-60	29	24.4	23.7	25.4	32.7	32.4	34.7	84	82	88	113	112	120
Cu-63	66	50.0	49.1	52.0	51.5	49.0	50.2	76	74	79	78	74	76
Zn-66	74	55.8	55.9	59.7	59.0	57.0	58.2	75	75	81	80	77	79
As-75	67	15.6	11.3	16.6	17.9	13.1	16.8	23	17	25	27	20	25
Se-82	3.5	3.92	4.72	4.73	4.98	4.48	1.77	112	135	135	142	128	51
Zr-90	53	14.4	15.3	17.1	13.9	13.0	14.3	27	29	32	26	25	27
Mo-98	35	29.2	28.6	30.2	30.9	29.3	30.0	83	82	86	88	84	86
Ag-107					0.26	0.27	0.27						
Sn-118	1.9	1.48	1.47	1.52	1.44	1.50	1.44	78	78	80	76	79	76
Sb-121	3.4	2.55	2.45	2.56	2.90	2.79	2.92	75	72	75	85	82	86
P-31	1431.5	863	855	918	917	973	1067	60	60	64	64	68	75
Cd-111	0.9	n.a.	n.a.	n.a.	0.8	0.8	0.9				92	92	98
W-183	2.6	2.1	2.1	2.2	2.1	2.0	2.1	82	80	85	80	77	81
Pb-208	38	33.9	33.1	34.8	35.0	33.6	34.2	89	87	91	92	88	90

Table D.6. Certified, measured elemental values and elemental recoveries for standard SDO-1.

Element (µg/g)	Certified value (µg/g)	Measured value (µg/g)						Recovery (%)					
		#1	#2	#3	#4	#5	#6	#1	#2	#3	#4	#5	#6
Fe-56	65326.83312	54092	50235	51566	49314	48153	47576	83	77	79	75	74	73
Li-7	28.6	27.7	30.4	32.7	25.2	24.6	24.6	97	106	115	88	86	86
Mg-24	9286.844978	7687	7751	8151	7184	6742	6752	83	83	88	77	73	73
Na-23	2819.076571				5805	4489	4580				206	159	162
Al-27	64939.82547	55043	54835	57218	49905	48503	47734	85	84	88	77	75	74
K-39	27810.06862	23665	23174	24101	21143	20536	20044	85	83	87	76	74	72
Ca-43	7504.306578	6658	6932	7132				89	92	95			
Ca-44	7504.306578				6315	6004	5973				84	80	80
Rb-85	126	99.7	95.4	97.2	98.8	95.9	95.6	79	76	77	78	76	76
Sr-88	75.1	62.7	59.7	61.4	61.5	58.6	59.6	84	80	82	82	78	79
Ba-138	397	331	311	319	316	310	310	83	78	80	80	78	78
Tl-205		4.78	5.40	5.59	4.86	4.68	4.81						
U-238	48.8	39.3	38.2	40.0	36.6	35.8	36.0	81	78	82	75	73	74
Si-28	230354.996	10.9	18.7	21.8									
Ti-48	4255.377199	3125	2637	2749	2778	2830	2814	73	62	65	65	67	66
V-51	160	137	127	132	131	129	130	86	80	83	82	81	81
Cr-52	66.4	51.5	49.1	51.5	49.4	47.4	48.4	78	74	78	74	71	73
Mn-55	325.2740343	269	253	264	262	254	256	83	78	81	81	78	79
Fe-57	65326.83312	55235	51119	53305	49314	48153	47576	85	78	82	75	74	73
Co-59	46.8	38.1	35.8	37.6	37.6	36.2	36.6	81	76	80	80	77	78
Ni-60	99.5	78.5	75.5	79.1	86.2	82.5	85.0	79	76	80	87	83	85
Cu-63	60.2	42.6	43.0	44.9	46.6	44.5	44.9	71	71	75	77	74	75
Zn-66	64.1	44.4	45.5	49.8	48.8	48.1	51.7	69	71	78	76	75	81
As-75	68.5	30.0	30.3	31.3	34.3	33.4	33.0	44	44	46	50	49	48
Se-82	1.9	3.49	3.43	5.22	n.a.	n.a.	n.a.	184	180	275			
Zr-90	165	89.1	84.4	87.0	87.3	90.2	92.4	54	51	53	53	55	56
Mo-98	134	135	124	128	131	128	129	100	92	95	98	96	96
Ag-107	0.094	n.a.	n.a.	n.a.	0.86	0.59	0.61				914	627	646
Sn-118	3.7	2.25	2.25	2.29	2.35	2.26	2.20	61	61	62	63	61	59
Sb-121	4.1	3.63	3.47	3.50	4.32	3.88	3.79	88	85	85	105	95	92
P-31	480.0694991	335	323	330	502	373	358	70	67	69	105	78	74
Cd-111	2	n.a.	n.a.	n.a.	n.a.	n.a.	n.a.						
W-183	3.3	1.11	1.20	1.28	1.00	1.08	1.10	34	36	39	30	33	33
Pb-208	27.9	21.6	22.7	23.3	24.5	23.4	23.4	77	81	84	88	84	84

Table D.7. Depth profiles of elemental/Al ratios, carbon contents, authigenic fraction estimation and δ^{60}Ni values in Namibian sediment cores 23010 and 23060.

Sample ID	Depth (cm)	Rb/Al ($x10^{-4}$)	Sr/Al ($x10^{-4}$)	Ba/Al ($x10^{-4}$)	V/Al ($x10^{-4}$)	Cr/Al ($x10^{-4}$)	Mn/Al ($x10^{-4}$)	Co/Al ($x10^{-4}$)	Ni/Al ($x10^{-4}$)	Cu/Al ($x10^{-4}$)	Zr/Al ($x10^{-4}$)	Mo/Al ($x10^{-4}$)	Ag/Al ($x10^{-4}$)	Zn/Al ($x10^{-4}$)	As/Al ($x10^{-4}$)	Tl/Al ($x10^{-4}$)	U/Al ($x10^{-4}$)	Se/Al ($x10^{-4}$)	Cd/Al ($x10^{-4}$)	Fe/Al	K/Al	Mg/Al	Ti/Al	Ca/Al	P/Al
Core 23010 (14.226°E, 23.001°S), 102 m water depth, BWO = 2.7 μmol/kg																									
23010_0-1	0.5	19.0	263	454	96.4	69.1	44.9	3.62	36.6	24.5	14.1	30.8	1.43	23.1	180	4.03	8.87	8.08	19.6	1.36	0.80	1.94	0.030	3.57	0.54
23010_1-2	1.5	20.0	264	407	119	66.3	48.2	4.03	37.4	24.6	15.3	35.6	1.56	24.3	105	4.82	10.6	7.58	18.1	1.43	0.74	2.04	0.023	3.66	0.59
23010_2-3	2.5	20.4	261	278	137	58.0	60.4	3.81	35.9	22.0	18.9	39.9	0.88	25.1	30.5	4.71	8.48	6.69	16.6	0.93	0.93	2.46	0.048	3.91	0.26
23010_3-4	3.5	17.0	336	304	165	54.6	42.6	4.00	33.4	22.3	9.10	44.6	1.49	25.4	36.1	5.98	13.7	5.75	14.6	1.28	0.80	2.33	0.021	3.90	0.86
23010_4-5	4.5	20.7	295	444	183	65.1	53.2	4.67	44.8	27.9	18.9	49.1	1.62	26.8	35.5	7.40	12.3	8.76	19.4	1.30	0.92	2.71	0.036	3.65	0.37
23010_5-6	5.5	20.9	281	387	173	61.4	54.7	4.42	39.5	25.6	20.2	46.2	1.43	25.1	28.3	7.28	10.7	8.30	19.6	1.30	0.92	2.47	0.035	3.57	0.34
23010_6-7	6.5		293	342	171	65.5	65.3	3.17	46.9	23.7	26.8	59.9							21.7	0.88	1.02	2.59	0.074	4.02	0.20
23010_7-8	7.5		271	332	166	65.3	58.0	3.20	44.3	23.5	28.5	60.8							20.9	0.81	1.02	2.53	0.059	3.61	0.17
23010_8-9	8.5		241	310	186	60.9	63.9	3.04	45.1	23.3	29.2	63.2							21.8	0.81	0.91	2.11	0.065	3.27	0.14
23010_9-10	9.5		261	286	157	60.5	62.9	2.93	43.1	22.6	25.7	55.6							21.2	0.80	0.91	2.13	0.064	3.74	0.17
23010_10-11	10.5		227	239	113	63.4	60.4	2.71	42.1	21.9	26.4	43.8							22.1	0.80	0.76	1.75	0.063	3.28	0.17
23010_11-12	11.5		210	186	78.3	60.3	56.2	2.44	36.0	20.1	28.2	37.1							21.8	0.77	0.77	1.79	0.061	2.75	0.19
23010_12-13	12.5		137	158	47.5	59.6	55.9	2.34	32.1	17.4	26.2	28.4							19.5	0.76	0.57	1.08	0.063	1.95	0.10
23010_13-14	13.5		144	162	52.5	55.6	53.1	2.26	29.2	17.2	27.1	28.8							18.4	0.77	0.62	1.27	0.061	1.90	0.14
23010_14-15	14.5		131	173	64.3	54.2	51.4	2.23	27.1	15.2	26.2	37.6							18.5	0.77	0.62	1.25	0.060	1.70	0.09
23010_15-16	15.5		101	186	58.6	54.3	54.5	2.33	26.5	15.3	24.9	32.1							17.7	0.75	0.56	1.08	0.062	1.21	0.08
23010_16-17	16.5		107	199	65.6	51.8	55.6	2.29	25.3	15.0	25.8	32.9							18.8	0.76	0.59	1.14	0.064	1.33	0.08
23010_17-18	17.5		109	199	64.0	50.4	56.3	2.36	23.9	14.1	24.7	36.4							17.8	0.76	0.57	1.10	0.063	1.32	0.09
23010_18-19	18.5		107	183	57.2	39.0	65.5	2.52	19.2	11.5	21.9	27.3							12.1	0.74	0.55	0.88	0.070	1.46	0.06
23010_19-20	19.5	19.7	160	271	69.3	50.6	59.9	2.92	28.3	17.1	15.1	35.1	0.56	26.3	6.95	2.72	13.3	4.76	17.7	0.78	0.61	1.19	0.049	2.39	0.11
23010_20-21	20.5	20.1	166	413	86.4	60.5	53.5	3.29	32.3	21.5	17.5	42.7	1.24	28.8	11.6	4.06	14.5	6.17	24.1	1.06	0.70	1.58	0.064	2.08	0.13
23010_21-22	21.5	19.7	221	475	110	65.2	65.0	3.51	38.2	24.6	13.1	52.9	0.94	30.6	9.31	5.18	22.7	7.19	28.3	0.88	0.68	1.47	0.032	3.25	0.12
23010_22-23	22.5	20.0	230	571	121	63.7	57.8	3.56	38.1	24.4	14.2	52.8	0.95	28.0	9.04	4.81	22.6	7.07	25.5	0.95	0.70	1.51	0.020	3.46	0.10
23010_23-24	23.5	19.0	212	803	117	63.1	54.6	3.43	36.7	23.3	14.3	50.8	0.95	29.4	9.69	4.37	22.1	6.95	25.7	0.94	0.65	1.38	0.046	3.21	0.13
23010_24-25	24.5	26.8	200	653	119	66.1	57.6	6.42	41.6	27.4	15.3	53.1	4.08	33.4	11.4	7.42	28.8	5.06	27.6	0.81	0.70	1.53	0.029	2.67	0.11
23010_25-26	25.5	20.4	240	871	120	68.8	63.3	3.62	39.8	25.1	19.9	49.4	1.09	32.1	14.8	4.19	26.1	5.63	21.0	1.17	0.71	1.52	0.065	3.07	0.19
23010_26-27	26.5	19.9	206	639	104	60.9	57.0	3.29	34.7	36.2	14.5	44.1	0.84	35.4	7.78	4.07	19.1	6.20	24.6	0.83	0.63	1.31	0.032	3.02	0.13
23010_27-28	27.5	19.8	199	849	110	66.6	58.5	3.31	36.8	23.5	12.7	44.9	0.76	32.5	7.89	3.91	18.4	6.74	26.0	0.84	0.55	1.06	0.028	2.74	0.12
23010_28-29	28.5	20.9	194	530	111	65.1	58.6	3.39	37.5	23.5	14.0	45.8	0.68	167	8.14	3.89	18.7	7.12	27.5	0.85	0.57	1.06	0.035	2.73	0.13
23010_29-30	29.5	20.2	163	199	99.3	58.1	60.0	3.15	33.3	22.8	15.9	39.2	0.68	30.6	7.66	3.43	18.4	6.13	23.8	0.85	0.51	0.88	0.030	2.45	0.12
Core 23060 (13.32°E, 23.000°S), 352.5 m water depth, BWO = 67.299 μmol/kg																									
23060_0-1	0.5	20.8	1691	85.3	26.7	105	52.0	4.51	63.3	26.7	12.1	3.61	1.03	29.8	18.3	11.4	32.5	4.64	2.81	1.25	0.50	0.73	0.031	43.0	2.83
23060_1-2	1.5	20.1	1413	84.2	20.4	82.4	46.0	3.54	50.5	26.4	20.3	1.89	1.14	27.9	10.6	6.55	18.9	3.47	1.42	1.00	0.48	0.64	0.043	38.2	1.52
23060_2-3	2.5	18.7	1361	82.7	18.6	75.6	48.0	3.09	48.5	25.9	12.4	1.59	0.79	28.5	8.60	5.07	15.5	3.47	1.20	0.81	0.43	0.61	0.023	37.1	1.17
23060_3-4	3.5	18.4	1361	79.3	18.3	72.7	44.6	3.04	47.5	25.7	17.6	1.58	0.78	26.5	8.62	4.83	15.2	3.15	1.10	0.76	0.45	0.61	0.014	37.2	1.19
23060_4-5	4.5	17.8	1341	78.0	18.7	76.0	47.2	3.03	48.1	25.1	16.7	1.83	0.70	26.3	9.22	5.10	15.9	3.47	1.20	0.83	0.42	0.60	0.046	36.1	1.28
23060_5-6	5.5	18.8	1342	79.3	19.0	71.3	46.3	3.17	45.3	25.0	9.34	2.04	1.12	26.3	8.95	4.77	15.1	2.85	0.98	1.02	0.47	0.61	0.021	39.9	1.23
23060_17-18	17.5	18.9	1449	67.8	22.8	77.3	45.4	3.24	51.7	25.7	13.4	3.27	0.70	26.8	12.7	6.35	23.5	3.69	1.67	0.96	0.45	0.61	0.032	39.4	1.60
23060_18-19	18.5	18.1	1393	68.6	23.0	75.2	44.9	3.24	47.0	24.7	16.5	3.15	0.83	26.7	12.4	5.66	21.7	3.59	1.47	0.95	0.46	0.59	0.026	38.1	1.45
23060_19-20	19.5	18.7	1434	69.4	23.0	74.4	44.9	3.13	47.9	24.7	11.1	3.25	0.92	26.1	10.9	5.30	20.5	3.56	1.43	0.89	0.48	0.58	0.027	40.8	1.29
23060_20-21	20.5	18.5	1479	66.9	23.8	83.3	44.5	3.59	52.7	24.0	16.4	3.66	0.65	25.9	15.2	7.85	27.0	4.04	2.01	1.04	0.47	0.61	0.040	39.2	1.99
23060_21-22	21.5	19.3	1398	67.7	24.8	82.2	45.1	3.57	48.7	25.1	18.7	3.88	1.53	25.7	12.8	6.40	24.4	3.87	1.47	1.23	0.40	0.60	0.049	40.9	1.59
23060_22-23	22.5	20.1	1400	77.1	26.4	94.3	49.7	4.10	54.4	25.0	18.8	3.93	1.27	26.7	15.2	8.33	30.8	3.81	1.74	1.35	0.41	0.58	0.034	37.3	2.24
23060_23-24	23.5	18.6	1410	70.1	22.6	75.1	46.7	3.12	47.0	25.7	11.6	3.46	0.96	26.7	10.5	4.76	20.0	3.53	1.29	0.90	0.40	0.59	0.027	39.8	1.16
Average Shale (Heinrichs et al., 1980)		15.836	34	66	14.7	10.2	96	2.15	7.692	5.1	18.1	0.294	0.008	10.7	1.13	0.077	0.42	0.068	0.015	0.55	0.34	0.18	0.053	0.18	0.008
Namibian Mud Lens (Borchers et al., 2005)		22	181	298	126	72	28	2.9	41	32	25	37	0.15	29	11	2.5	29	12.4	25.6	0.8	0.39	0.38	0.08	2	0.17
Doubled Orange River (Garzanti et al., 2012)									9.18																

Table D.7. (continued)

Sample ID	Depth(cm)	TC(%)	TIC(%)	TOC(%)	Authigenic Ni (µg/g)	Authigenic Ni (%)	Authigenic Ni (µg/g)	Authigenic Ni (%)	δ^{60}Ni (‰)	2SE	n	δ^{60}Ni (‰)-dup	2SE	n
					Ni/Al = 3.3 × 10^{-4}		Ni/Al = 9.18 × 10^{-4}							
Core 23010 (14.226°E, 23.001°S), 102 m water depth, BWO = 2.7 µmol/kg														
23010_0-1	0.5	11.4	0.6	10.8	9.5	91.0	7.8	74.9	1.04	0.07	4	0.98	0.19	3
23010_1-2	1.5	9.8	0.6	9.2	8.6	91.2	7.1	75.5	0.97	0.04	4			
23010_2-3	2.5	9.5	0.6	8.9	14.2	90.8	11.6	74.5	0.92	0.02	4			
23010_3-4	3.5	8.9	0.7	8.2	7.6	90.1	6.2	72.5	0.93	0.03	4			
23010_4-5	4.5	8.4	0.5	7.9	9.7	92.6	8.3	79.5	0.91	0.05	4	0.92	0.02	3
23010_5-6	5.5	7.5	0.5	6.9	9.5	91.6	8.0	76.7	0.88	0.06	3			
23010_6-7	6.5								0.90	0.07	3			
23010_7-8	7.5								0.91	0.04	3			
23010_8-9	8.5								0.89	0.04	3			
23010_9-10	9.5								1.14	0.04	4			
23010_10-11	10.5								0.90	0.02	4			
23010_11-12	11.5								0.91	0.04	4			
23010_12-13	12.5								0.98	0.02	4			
23010_13-14	13.5								0.91	0.01	4			
23010_14-15	14.5								0.90	0.04	4			
23010_15-16	15.5								0.89	0.03	4			
23010_16-17	16.5								0.86	0.08	4			
23010_17-18	17.5								0.87	0.05	4			
23010_18-19	18.5								0.82	0.05	4			
23010_19-20	19.5	6.6	0.5	6.0	17.6	88.3	13.4	67.5	0.92	0.05	4			
23010_20-21	20.5	5.4	0.4	5.0	12.9	89.8	10.3	71.6	0.91	0.07	3			
23010_21-22	21.5	5.6	0.6	5.0	19.1	91.4	15.9	76.0	0.91	0.05	3			
23010_22-23	22.5	5.9	0.6	5.2	18.4	91.3	15.3	75.9	0.91	0.02	4			
23010_23-24	23.5	5.6	0.6	5.0	17.1	91.0	14.1	75.0	0.90	0.08	3			
23010_24-25	24.5	5.5	0.5	5.1	21.4	92.1	18.1	77.9	0.93	0.07	3			
23010_25-26	25.5	5.8	0.5	5.3	15.2	91.7	12.7	77.0	0.96	0.02	4			
23010_26-27	26.5	7.0	0.6	6.3	17.9	90.5	14.5	73.6	0.92	0.02	3			
23010_27-28	27.5	7.8	0.6	7.2	22.1	91.0	18.2	75.0	0.91	0.03	3			
23010_28-29	28.5	7.9	0.5	7.4	24.7	91.2	20.4	75.5	0.93	0.03	4			
23010_29-30	29.5	8.0	0.6	7.4	22.7	90.1	18.3	72.4	0.90	0.02	3			
Core 23060 (13.32°E, 23.000°S), 352.5 m water depth, BWO = 67.299 µmol/kg														
23060_0-1	0.5	11.8	8.6	3.2	32.1	94.8	28.9	85.5	0.97	0.02	3			
23060_1-2	1.5	12.2	8.9	3.3	19.4	93.5	17.0	81.8	1.14	0.05	4			
23060_2-3	2.5	12.8	9.2	3.6	26.2	93.2	22.8	81.1	1.16	0.07	3			
23060_3-4	3.5	12.8	9.1	3.6	25.2	93.0	21.8	80.7	1.20	0.06	3			
23060_4-5	4.5	13.0	9.1	3.8	28.7	93.1	25.0	80.9	1.16	0.03	4			
23060_5-6	5.5	13.1	9.3	3.8	16.9	92.7	14.5	79.7	1.17	0.02	3			
23060_17-18	17.5	12.3	9.3	3.0	30.0	93.6	26.3	82.2	1.09	0.03	3			
23060_18-19	18.5	12.1	9.1	2.9	22.9	93.0	19.8	80.5	1.14	0.01	4			
23060_19-20	19.5	12.3	9.1	3.2	22.0	93.1	19.1	80.8	1.15	0.03	3			
23060_20-21	20.5	12.0	9.0	3.0	32.0	93.7	28.2	82.6	1.04	0.02	3			
23060_21-22	21.5	11.9	9.3	2.6	15.9	93.2	13.9	81.2	1.15	0.05	4			
23060_22-23	22.5	12.2	9.1	3.1	19.7	93.9	17.4	83.1	1.00	0.02	3			
23060_23-24	23.5	12.3	9.4	2.9	21.8	93.0	18.9	80.5	1.18	0.05	4			

D.5. Enrichment factors in sediments

Table D.8. Enrichment factors of elements in sediment cores 23010 and 23060. The average elemental/Al ratios in two cores are compared to the ratios in average shale (Heinrichs et al., 1980).

		Average Shale (Heinrichs et al., 1980)	Average_23010	Average_23060	EF_23010	EF_23060
Rb/Al	($x10^{-4}$)	15.84	20.26	18.98	1.3	1.2
Sr/Al	($x10^{-4}$)	34.00	228.80	1420.76	6.7	41.8
Ba/Al	($x10^{-4}$)	66.00	502.76	75.09	7.6	1.1
V/Al	($x10^{-4}$)	14.70	120.00	22.17	8.2	1.5
Cr/Al	($x10^{-4}$)	10.20	62.54	80.35	6.1	7.9
Mn/Al	($x10^{-4}$)	96.00	55.86	46.56	0.6	0.5
Co/Al	($x10^{-4}$)	2.15	3.79	3.41	1.8	1.6
Ni/Al	($x10^{-4}$)	7.69	36.76	50.21	4.8	6.5
Cu/Al	($x10^{-4}$)	5.10	24.49	25.35	4.8	5.0
Zr/Al	($x10^{-4}$)	18.10	15.47	15.00	0.9	0.8
Mo/Al	($x10^{-4}$)	0.29	44.53	2.86	151.5	9.7
Ag/Al	($x10^{-4}$)	0.01	1.25	0.96	155.6	119.5
Zn/Al	($x10^{-4}$)	10.70	36.68	26.90	3.4	2.5
As/Al	($x10^{-4}$)	1.13	30.57	11.85	27.1	10.5
Tl/Al	($x10^{-4}$)	0.08	4.84	6.34	62.9	82.3
U/Al	($x10^{-4}$)	0.42	17.03	21.62	40.5	51.5
Se/Al	($x10^{-4}$)	0.07	6.72	3.62	98.8	53.3
Cd/Al	($x10^{-4}$)	0.02	22.35	1.52	1489.8	101.4
Fe/Al		0.55	1.03	1.00	1.9	1.8
K/Al		0.34	0.71	0.45	2.1	1.3
Mg/Al		0.18	1.67	0.61	9.3	3.4
Ti/Al		0.05	0.04	0.03	0.7	0.6
Ca/Al		0.18	3.14	39.00	17.4	216.7
P/Al		0.01	0.26	1.58	32.0	197.3

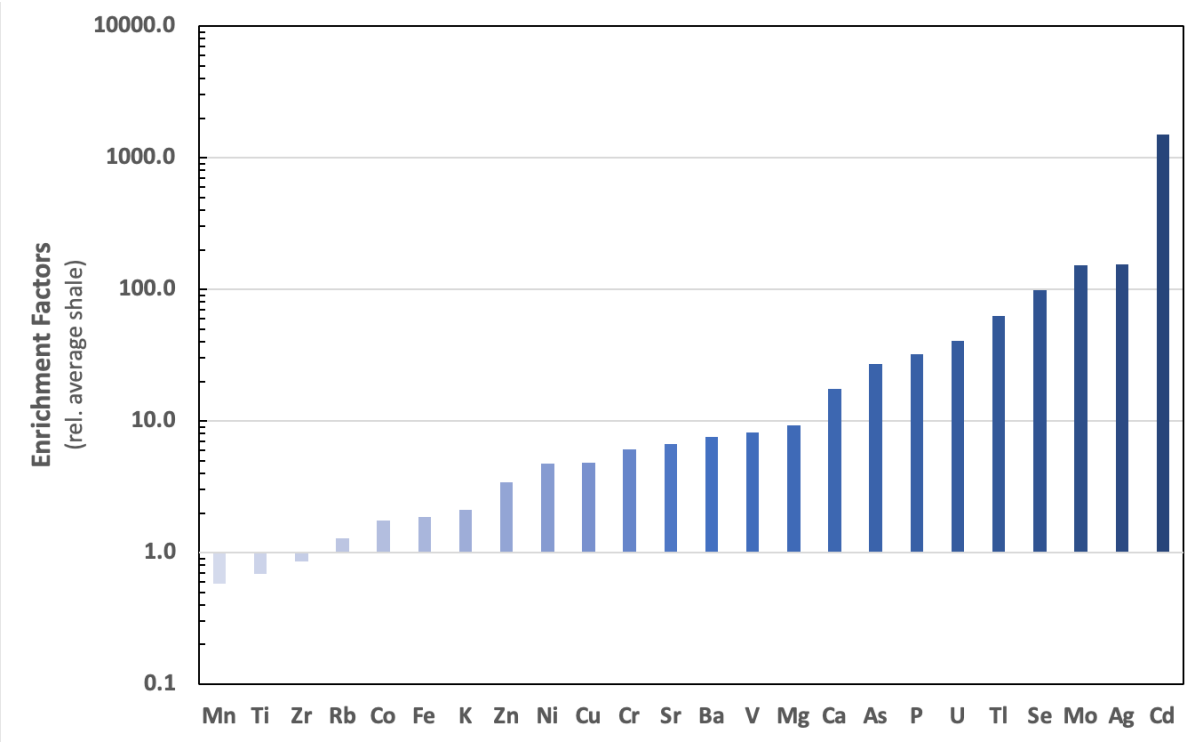


Figure D.1. Enrichment factors for elements in Namibian core 23010.

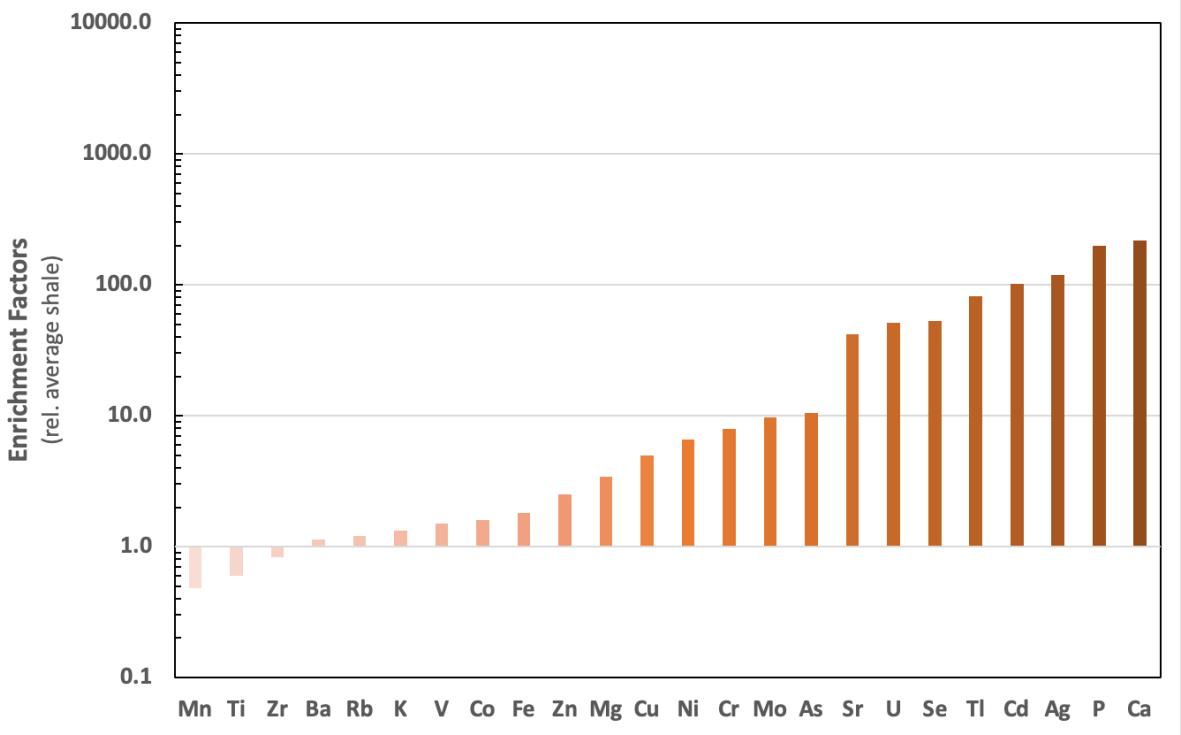


Figure D.2. Enrichment factors for elements in Namibian core 23060.

D.6. Correlations between trace metals and different mineral fractions

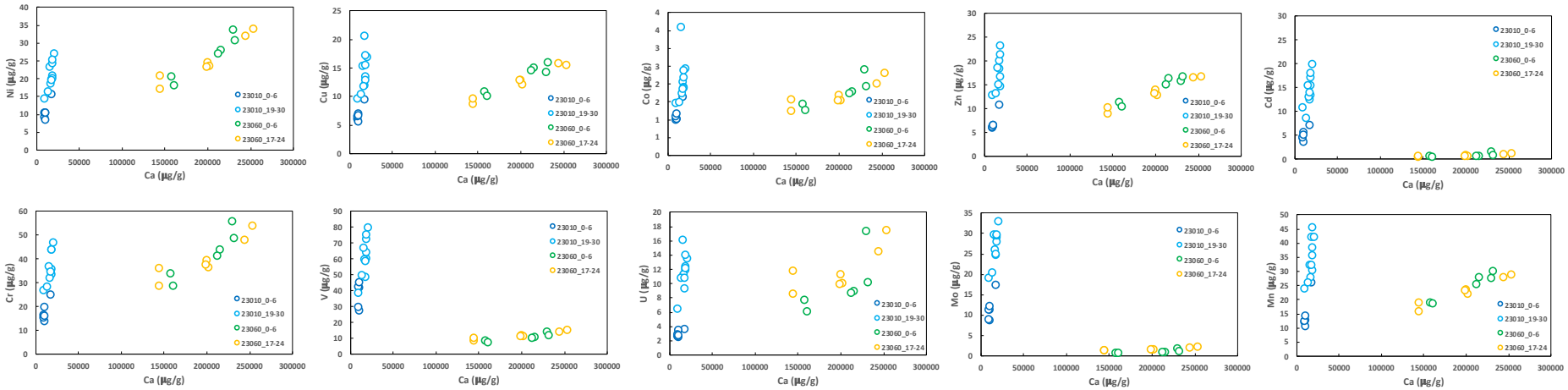


Figure D.3. Correlations between trace metals and Ca (representing carbonate fraction) in Namibian sediments.

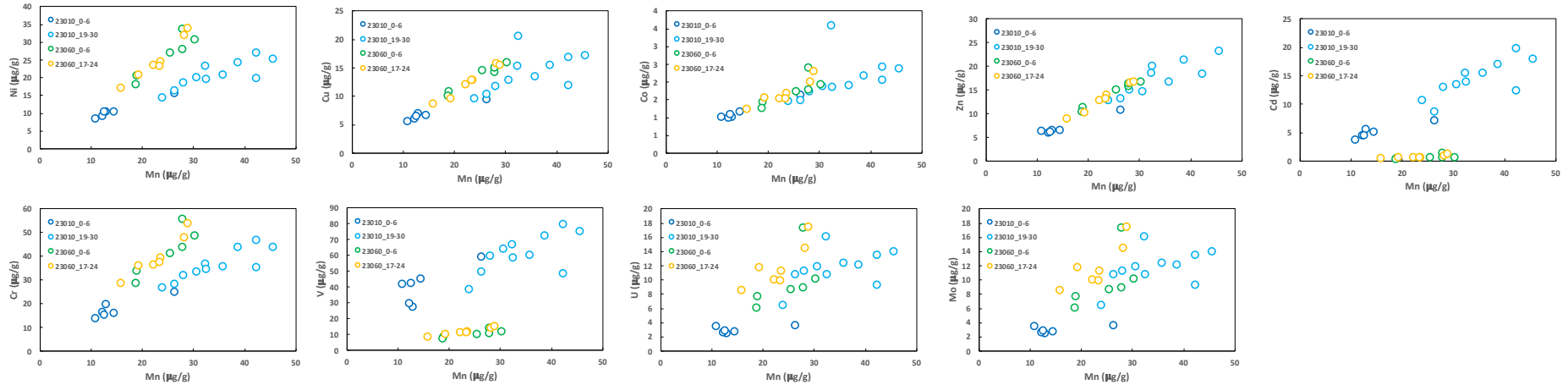


Figure D.4. Correlations between trace metals and Mn (representing Fe-Mn oxyhydroxide fraction) in Namibian sediments.

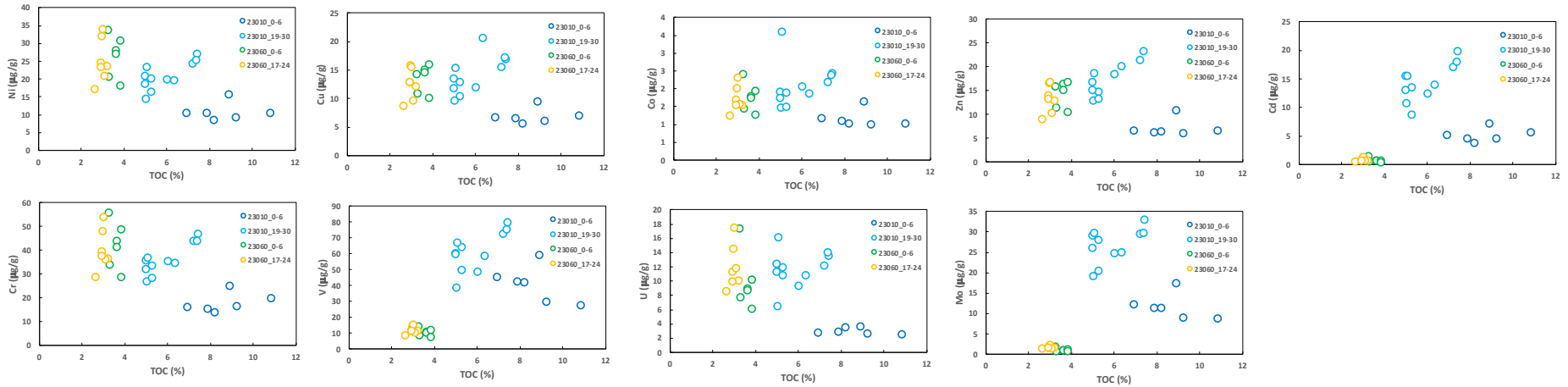


Figure D.5. Correlations between trace metals and TOC (representing organic-sulfide fraction) in Namibian sediments.

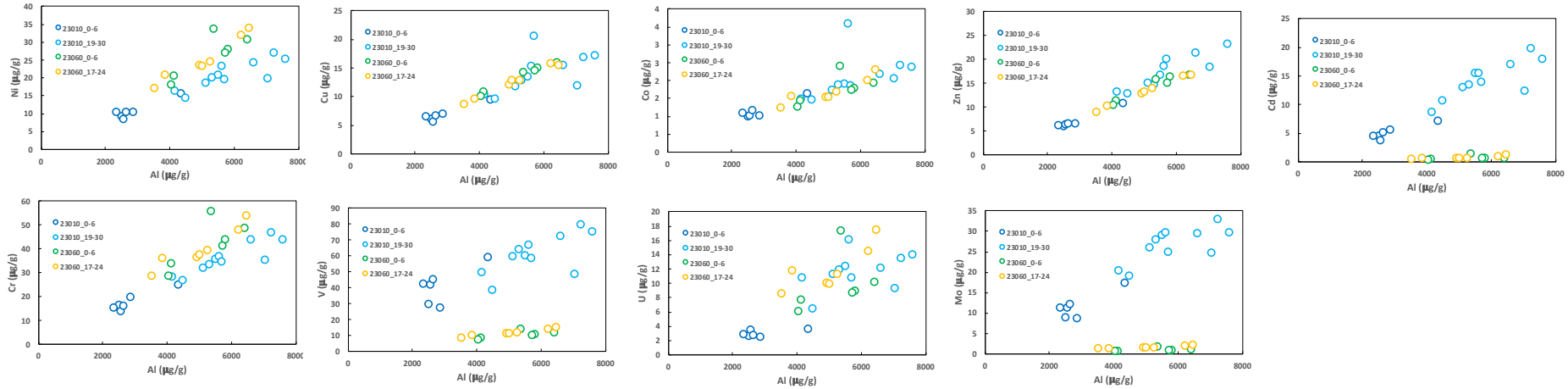
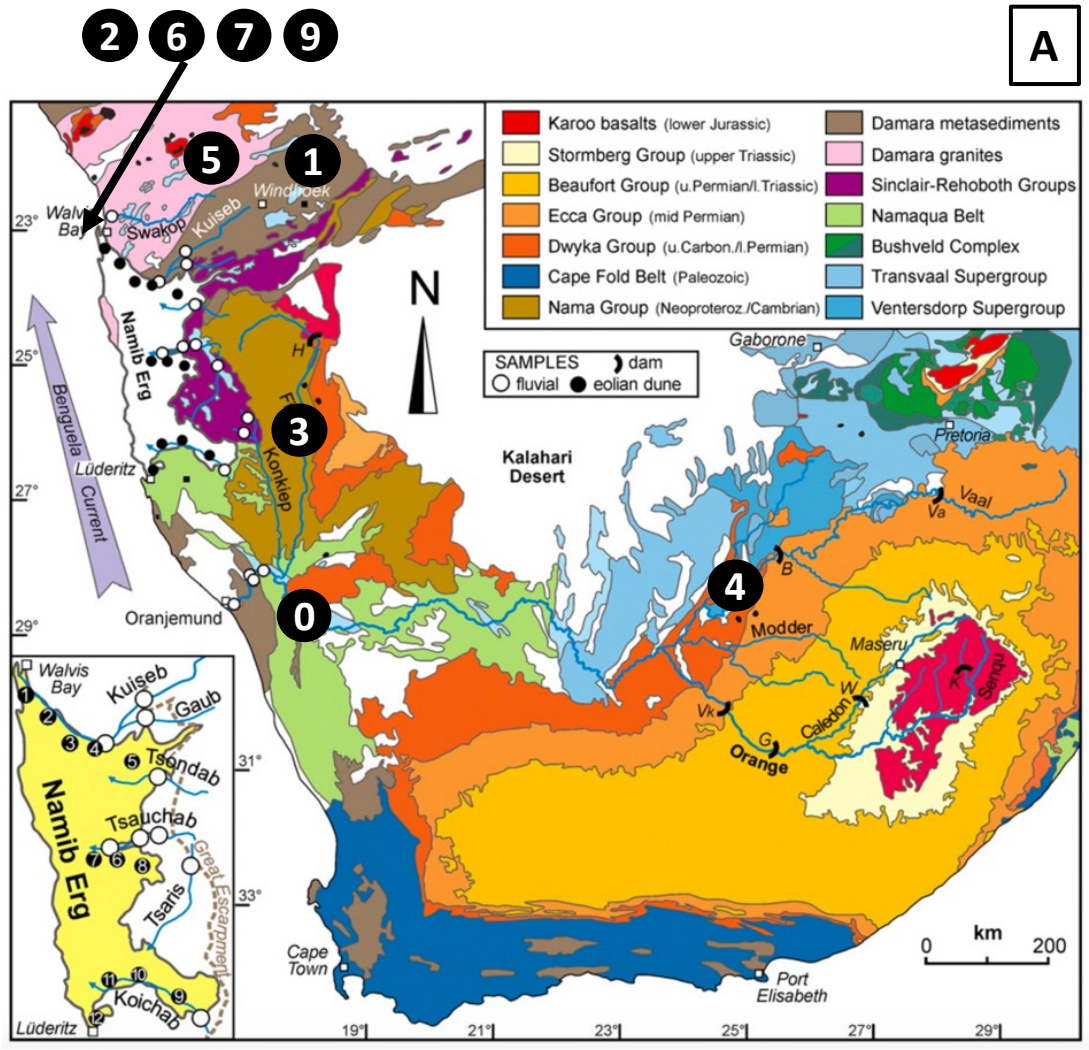


Figure D.6. Correlations between trace metals and Al (representing silicate fraction) in Namibian sediments.

D.7. Local bedrocks



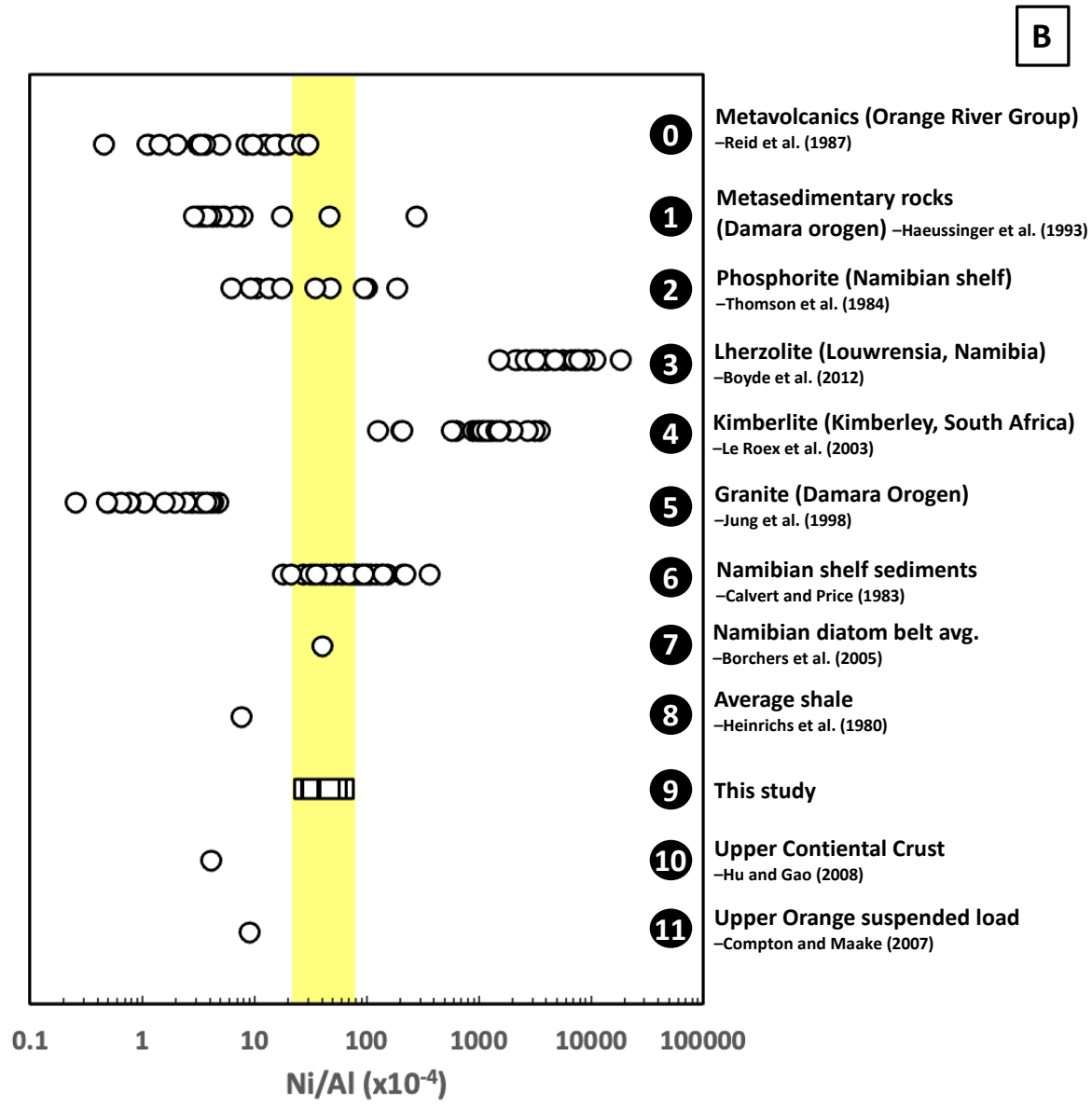


Figure D.7. (A) Geological map of southwest Africa (map is adopted from the Fig.2 in Garzanti et al., 2012) with (B) Ni/Al ratios in local bedrocks and the Namibian sediments collected in this study. Numbers in (B) correspond to the locations noted in (A).